

An Optical Spectroscopic Study of Interacting Galaxies at Low/Intermediate Redshift

INAUGURAL-DISSERTATION

zur
Erlangung des Doktorgrades
der Mathematisch-Naturwissenschaftlichen Fakultät
der Universität zu Köln



vorgelegt von

Persis Thomas Misquitta
aus Vasai, Indien

Köln 2023

This dissertation has been accepted by the Faculty of Mathematics and Natural Sciences of the University of Cologne.

Berichterstatter: Prof. Dr. Andreas Eckart
(Gutachter)

Prof. Dr. Lucas Labadie

Tag der mündlichen Prüfung: 24. Februar 2023

Abstract

Evolution of galaxies, how their central supermassive black holes, stellar populations, and morphology grow and change over cosmic time, is one of the fundamental questions in astrophysics. External and internal processes can bring about this evolution. Interaction of galaxies is an external process where two or more galaxies collide against each other or experience a fly-by. It is important to study galaxies in different phases of interaction and over the electromagnetic spectrum in order to have a concrete understanding of the process.

Within the scope of this thesis, we study a total of 12 pairs/triplets of interacting galaxies. Ten out of twelve of these galaxy pairs/triplets were chosen from a larger sample of 500 SDSS-FIRST selected galaxies. With eight pairs and two triplets, the sample consists of 22 galaxies in total. The remaining two galaxy pairs are SDSSJ134420.86+663717.8 and Mrk231. SDSSJ134420.86+663717.8 is made up of two galaxies, while Mrk231 is in a late stage merger, such that the progenitor galaxies are no longer distinguishable.

All three projects are based on optical long slit spectroscopy of galactic nuclear regions using the Multi-Object Double Spectrographs mounted on the Large Binocular Telescope (LBT) located on Mount Graham in Arizona. Additionally, in the case of Mrk231, six off-nuclear positions were observed.

Archival mid-infrared and radio continuum data were available for the SDSS-FIRST sample. At least one of the two, or three, galaxies involved in an interaction was detected by FIRST at 1.4 GHz. The archival data were used in conjunction with the LBT observations to check for possible correlations between the emission in optical, mid-infrared, and radio regimes. The nuclear ionisation ratios of the radio-detected galaxies in our sample fall in the composite or transition region of the optical diagnostic diagram. Additionally, the radio-detected galaxies in our sample host the more massive supermassive black hole in the pair or triplet of interacting galaxies.

SDSSJ134420.86+663717.8 consists of two galaxies, A and B. Based on the nature of the optical spectra, galaxy A seems to host a Seyfert Type 1 active galactic nucleus,

while the nuclear region of galaxy B seems to have a star-forming nature. Both of the nuclei fall in the composite or transition region of the optical diagnostic diagram. The mass of the supermassive black hole at the centre of galaxy A is $\sim 2 \times 10^7 M_{\odot}$, while the supermassive black hole at the centre of galaxy B has a mass of $\sim 3 \times 10^7 M_{\odot}$. A simple N-body simulation shows that for an almost orthogonal approach of the progenitor galaxies, the resultant model resembles SDSSJ134420.86+663717.8 morphologically and kinematically.

Mrk231 is an ultra-luminous infrared, radio-quiet galaxy that seems to be in a late stage of merger, as evidenced by the existence of two tidal tails. The central region of the galaxy hosts a Seyfert Type 1 active galactic nucleus as well as an extremely intense circum-nuclear starburst. The spectrum of the centre of Mrk231 consists of a continuum originating in the extreme starburst overlaid by emission lines from the active galactic nucleus and broad absorption lines from broad absorption line clouds that are associated with the nucleus but located at a distance from it. The mass of the central supermassive black hole is estimated to be $\sim 2 \times 10^8 M_{\odot}$. Broad $H\alpha$ emission is detected at a distance of ~ 1.7 kpc from the centre of Mrk231. Such high velocities could be attributed to outflows associated with the active galactic nucleus as well as the extreme starburst happening in the circum-nuclear region of Mrk231. Careful examination of acquisition images taken with the LBT as well as archival SDSS and DSS images shows that in addition to the two previously reported tidal tails, there exists a third diffuse tidal tail-like structure that might be indicative of an interaction with a third (dwarf) galaxy.

The study of these 12 pairs/triplets of galaxies shows that interactions lead to energetic phenomena at the centres of at least one of the galaxies involved in the merger. While it is not clear which galaxy gets favoured to be more energetic, it could be connected to the mass of the central supermassive black hole.

Zusammenfassung

Die Entwicklung von Galaxien, wie ihre zentralen supermassereichen Schwarzen Löcher, Sternpopulationen und ihre Morphologie wachsen und sich im Laufe der kosmischen Zeit verändern, ist eine der grundlegenden Fragen der Astrophysik. Externe und interne Prozesse können diese Entwicklung herbeiführen. Die Wechselwirkung von Galaxien ist ein externer Prozess, bei dem zwei oder mehr Galaxien miteinander kollidieren oder aneinander vorbeifliegen. Es ist wichtig, Galaxien in verschiedenen Phasen der Wechselwirkung und über das elektromagnetische Spektrum hinweg zu untersuchen, um den Prozess konkret zu verstehen.

Im Rahmen dieser Arbeit wurden insgesamt 12 Systeme aus jeweils zwei bis drei wechselwirkenden Galaxien untersucht. Zehn von zwölf dieser Galaxiesysteme wurden aus einer größeren Stichprobe von 500 SDSS-FIRST-ausgewählten Galaxien ausgesucht. Mit acht Paaren und zwei Tripeln besteht die Stichprobe aus insgesamt 22 Galaxien. Die verbleibenden zwei Galaxienpaare sind SDSSJ134420.86+663717.8 und Mrk231. SDSSJ134420.86+663717.8 besteht aus zwei Galaxien, während sich Mrk231 in einem Spätstadium der Verschmelzung befindet, sodass die Vorläufergalaxien nicht mehr unterscheidbar sind.

Alle drei Projekte basieren auf optischer Langspaltspektroskopie galaktischer Kernregionen unter Verwendung der Multi-Objekt Doppel Spektrographen (Multi-Object Double Spectrographs), die am Large Binocular Telescope (LBT) auf dem Mount Graham in Arizona montiert sind. Zusätzlich wurden im Fall von Mrk231 sechs außernukleare Positionen beobachtet.

Für die SDSS-FIRST-Probe waren Archivdaten aus dem mittleren Infrarot und Radio-kontinuum verfügbar. Mindestens eine der zwei oder drei an einer Wechselwirkung beteiligten Galaxien wurde von FIRST bei 1,4 GHz erkannt. Die Archivdaten wurden in Verbindung mit den LBT-Beobachtungen verwendet, um mögliche Korrelationen zwischen der Emission im optischen, mittleren Infrarot- und Radiobereich zu überprüfen. Die Kernionisationsverhältnisse der radiodetektierten Galaxien in unserer Probe fallen in den gemischten oder Übergangsbereich des optischen Diagnosedigramms. Darüber

hinaus beherbergen die radiodetektierten Galaxien in unserer Probe das massereichere supermassereiche Schwarze Loch im Paar oder Tripel der wechselwirkenden Galaxien.

SDSSJ134420.86+663717.8 besteht aus zwei Galaxien, A und B. Basierend auf den optischen Spektren scheint Galaxie A einen aktiven Seyfert-Typ-1-Galaxiekern zu beherbergen, während die Kernregion von Galaxie B eine Sternentstehungsnatur zu haben scheint. Beide Kerne fallen in den gemischten oder Übergangsbereich des optischen Diagnosedigramms. Die Masse des supermassereichen Schwarzen Lochs im Zentrum von Galaxie A beträgt $\sim 2 \times 10^7 M_{\odot}$, während das Gegenstück in Galaxie B eine Masse von $\sim 3 \times 10^7 M_{\odot}$ aufweist. Eine einfache N-Körper-Simulation zeigt, dass bei einer nahezu orthogonalen Annäherung der Vorläufergalaxien das resultierende Modell SDSSJ134420.86+663717.8 morphologisch und kinematisch ähnlich ist.

Mrk231 ist eine extrem leuchtende, infrarote, im Radiobereich schwache Galaxie, die sich in einem späten Stadium der Verschmelzung zu befinden scheint, was durch die Existenz von zwei Gezeitenschweifern belegt wird. Die zentrale Region der Galaxie beherbergt einen aktiven Seyfert-Typ-1-Galaxiekern sowie einen extrem intensiven zirkumnuklearen Sternenausbruch. Das Spektrum des Zentrums von Mrk231 besteht aus einem Kontinuum, das seinen Ursprung im extremen Sternenausbruch hat, überlagert von Emissionslinien des aktiven galaktischen Kerns und breiten Absorptionslinien von breiten Absorptionslinienwolken, die mit dem Kern assoziiert sind, sich aber von ihm entfernt befinden. Die Masse des zentralen supermassereichen Schwarzen Lochs wird auf $\sim 2 \times 10^8 M_{\odot}$ geschätzt. In einem Abstand von $\sim 1,7$ kpc zum Zentrum von Mrk231 wird breite $H\alpha$ -Emission detektiert. Solche hohen Geschwindigkeiten könnten Ausströmungen zugeschrieben werden, die mit dem aktiven galaktischen Kern sowie dem extremen Sternenausbruch in der Kernregion von Mrk231 verbunden sind. Eine sorgfältige Untersuchung der mit dem LBT erfassten Bilder, sowie der archivierten SDSS- und DSS-Bilder, zeigt, dass es zusätzlich zu den beiden zuvor genannten Gezeitenschweifern eine dritte diffuse, Gezeitenschweif-ähnliche Struktur gibt, die auf eine Wechselwirkung mit einer dritten (Zwerg-)Galaxie hindeuten könnte.

Die Untersuchung dieser 12 Paare/Tripel von Galaxien zeigt, dass Wechselwirkungen zu energetischen Phänomenen in den Zentren von mindestens einer der an der Verschmelzung beteiligten Galaxien führen. Es ist zwar nicht klar, welche Galaxie als welche Galaxie bevorzugt energiegeladen wird, aber dies könnte mit der Masse des zentralen supermassereichen Schwarzen Lochs in Verbindung gebracht werden.

Contents

Abstract	i
Zusammenfassung	iii
Contents	v
1 Introduction	1
1.1 Early astrophysics	1
1.2 Cosmological models of the universe	3
1.3 Classification of galaxies	5
1.3.1 Elliptical galaxies	5
1.3.2 Spiral galaxies	7
1.3.3 Lenticular galaxies	9
1.3.4 Irregular galaxies	10
1.4 Evolution of galaxies	10
1.5 Interactions of galaxies	11
1.6 Active Galactic Nuclei	13
1.7 Goals and content of this thesis	17
2 Paper I: SDSS-FIRST selected interacting galaxies. An optical long slit spectroscopy study using MODS at the LBT	19
3 Paper II: Interactions among intermediate redshift galaxies. The case of SDSSJ134420.86+663717.8	55
4 Paper III (in prep.): The peculiar optical spectrum of Mrk231	73
5 Summary, conclusions and outlook	91
5.1 Summary	91
5.1.1 SDSS-FIRST-LBT sample	91
5.1.2 SDSS J134420.86+663717.8	94

5.1.3 Markarian 231	96
5.2 Concluding remarks	98
5.2.1 Mergers as a step in galactic evolution	98
5.3 Outlook	100
Bibliography	101
List of Figures	106
List of Acronyms	107
Acknowledgements	109
Declaration	113
Curriculum Vitae	115

1 Introduction

1.1 Early astrophysics

The¹ quest to understand ourselves, and the universe we are a part of, has been a major part of the human psyche over several millennia. Astronomy is a way for us to look beyond the blue planet we call home and try to unravel the processes by which the universe came to be as it is today. Carl Sagan expressed this rather wonderfully in his documentary series, *Cosmos: A Personal Journey*, when he said that humans are a way for the cosmos to understand itself. Whether it truly is possible for someone within a system to completely understand the system is a philosophical debate we shall try to not engage in for the present.

It is no surprise, then, that astronomy is the oldest of the natural sciences, being practised by ancient humans as a part of their religious, cultural, mythological, and astrological beliefs (Krup 2003). In fact, astrology and astronomy have been frequently intertwined over history, with the movement of celestial objects being linked to natural phenomena like rains, drought, change of seasons, etc. One of the first astronomical exercises that the ancient humans engaged in was to record what they observed in the night sky. Records like cave paintings and carvings dating back to approximately 30,000 years ago have been found bearing pictorial representations of astronomical sources such as the constellation Orion, the Pleiades cluster, and the phases of the Moon². Along with such records, remains of structures used for astronomical purposes have also been discovered, like the Kokino site in North Macedonia, discovered in 2001, that is believed to be the site of a Bronze Age astronomical observatory. Other structures like Stonehenge in England and the Goseck Circle in Germany³ seem to have been built in such a way that they would align with the summer and winter solstices.

¹This section derives mainly from the following three websites based on the history of Astronomy: https://en.wikipedia.org/wiki/History_of_astronomy, <http://abyss.uoregon.edu/~js/ast121/lectures/lec02.html>, and <https://www.britannica.com/science/astronomy/History-of-astronomy>.

²<http://news.bbc.co.uk/2/hi/science/nature/2679675.stm>

³<https://www.himmelswege.de/orte/sonnenobservatorium-goseck>

The Babylonians laid the foundations for astronomy that were then built upon by Greek and Hellenistic, Indian, Arabic, Central Asian, and Western astronomers. They catalogued the movements of stars and constellations, with some of them dating all the way back to 1200 BCE, the rising and setting times of planets, and also developed a system to describe the positions of celestial objects using their right ascensions and declinations. Babylonian astronomers were also the first (323-60 BCE) to use records of past movement of planets to predict future phenomena.

The ancient Greeks studied the astronomical works of the Babylonians and used them as a basis to develop further theories about the universe. Heraclides Ponticus put forth the first geocentric model of the universe in the 4th century BCE . In the next century, Aristarchus of Samos proposed the heliocentric model of the universe, which placed the Sun at the centre of the universe with the planets and other celestial bodies revolving around it in concentric circles (Pedersen 1993). However, the adaptation of concentrically circular orbits led to inconsistencies in the paths followed by the planets in the night sky that could not be explained away at that time, and the theory was discarded until it was revived almost a millennium later. With the burning of the great library at Alexandria in 272 CE, much of the astronomical work was destroyed, ushering in the Dark Ages in Europe until the Renaissance brought in a new era of scientific development.

Between these eras, Islamic astronomers made significant contributions to observational astronomy. The Persian astronomer, Abd al-Rahman al-Sufi⁴, observed and recorded movements of several celestial objects in his *Book of Fixed Stars* in the 10th century. He is also one of the first astronomers to record descriptions of the Andromeda galaxy and the Large Magellanic Cloud⁵. The supernova, SN1006, was observed and recorded by an Arabic astronomer, Ali ibn Ridwan.

During the Renaissance, astronomy in Europe underwent a paradigm shift, starting with Nicolaus Copernicus, who re-proposed the heliocentric theory in his seminal work, *De revolutionibus orbium coelestium*, published in 1543 (Westman 2011). The theory, though controversial and in direct opposition to the beliefs held by the Catholic Church at that time, was supported and championed by several notable figures in the scientific community. Scientists like Galileo Galilei, Johannes Kepler, and Isaac Newton provided further support for the heliocentric model by developing theories like Kepler's laws of planetary motion, Newton's laws of motion, and Galileo's observations using a telescope.

In the centuries following the Renaissance and before the invention of photography, the planet Uranus was discovered by Sir William Herschel in 1781 and the idea of cosmic pluralism, that stars are distant suns with their own planetary systems, gained ground. With the invention of photography and the first astronomical photograph of the Moon in 1840, a whole new arena of astronomy opened up. While early photography caught lower amounts of incident photons compared to the human eye, it had a much longer integration time. Advances in technology allowed access to wavelength regimes like X-rays, gamma rays, radio waves, infrared, and ultraviolet radiation which are hidden from the visible eye. The invention of spectroscopy led to further understanding of

⁴<http://messier.obspm.fr/xtra/Bios/alsufi.html>

⁵<http://messier.obspm.fr/xtra/ngc/lmc.html>

astronomical sources, for example, now it could be proved definitely that the Sun is a star like countless others visible in the night sky.

While the Milky Way (MW) had been observed as a white band of stars across the night sky since the times of the ancient Greeks, it wasn't until the 20th century that it was accepted to be a group of stars, and just one amidst several other such groups of stars. This happened in the aftermath of the Shapley-Curtis debate, better known as the *Great Debate*, conducted on April 26, 1920, concerning the nature of alleged spiral nebulae and the size of the universe. While Shapley believed that the nebulae were small in size and were situated within the MW, Curtis proposed that they were independent bodies at large distances from the MW. Several points proposed by both scientists were proven to be true in the aftermath of the debate. Particularly, the observations of Cepheids belonging to the Andromeda galaxy and other nebulae, and the estimation of their distances by Hubble (1925) led to the conclusion that these sources were located at large distances and could not be a part of the MW. This realisation along with the advance of quantum theories opened a whole new era of astrophysics to which we now bear witness.

In the following sections of this chapter, I will introduce some of the terms and ideas associated with astrophysics that will prove to be helpful to gain a better understanding of the work conducted in this thesis. We start by describing the different models of the universe.

1.2 Cosmological models of the universe

This section draws heavily from Chapters 4 and 5 of Ryden (2003).

The universe as we see it today is believed to have been formed by expansion from an infinitesimally small, infinitely dense point of singularity, known as the Big Bang, that occurred almost 14 billion years ago. To understand the geometrical properties of the universe, it is important to understand how the curvature of space-time affects the appearance of cosmological objects at various distances. One of the first field equations to link the curvature of space-time with its mass-energy content was put forth by Albert Einstein in his theory of general relativity in 1915 (Einstein 1915). The cosmological principle states that when viewed on a sufficiently large scale, the universe appears to be homogeneous and isotropic, since the universe is supposed to have expanded uniformly in all directions following the Big Bang, with the same forces in play uniformly, thereby preventing any large scale irregularities. Thus, the spatial extent of the universe must have a uniform curvature, which can be described by the line element, ds , of a metric known as the Robertson-Walker metric:

$$ds^2 = cd^2t^2 - a(t)^2 \left(\frac{dx^2}{1 - \kappa x^2/R^2} + x^2 d\Omega^2 \right) \quad (1.1)$$

where $\kappa (= -1, 0, 1)$ is the curvature constant that gives the sign of the curvature, $a(t)$ is the scale factor that describes how the distances in the universe change with expansion and contraction, c is the speed of light, R scales κ , and $d\Omega^2 = d\theta^2 + \sin^2 \theta d\phi^2$ (θ and ϕ

represent the usual polar and azimuthal angles in the spherical co-ordinate system). The Robertson-Walker metric can be expressed in another form as:

$$ds^2 = cdt^2 - a(t)^2(dr^2 + S_\kappa^2(r)d\Omega^2) \quad (1.2)$$

where

$$S_\kappa = \begin{cases} R \sin r/R & \text{if } \kappa = 1 \\ r & \text{if } \kappa = 0 \\ R \sinh r/R & \text{if } \kappa = -1 \end{cases} \quad (1.3)$$

This shows that for a non-zero κ , the angular lengths would decrease for positive curvature, while for negative curvature, they would increase. Thus, knowing the sign of κ would help to compute the radius of the curvature.

The Friedmann-Lemaître equation provides the solution to the Robertson-Walker metric and has the form:

$$\left(\frac{\dot{a}}{a}\right)^2 = H^2 = \frac{8\pi G}{3}\rho - \frac{\kappa c^2}{R^2} \frac{1}{a^2} + \frac{\Lambda c^2}{3} \quad (1.4)$$

The Friedmann-Lemaître equation describes how the scale factor, $a(t)$, in the Robertson-Walker metric changes with time. H is the Hubble parameter (the Hubble constant, H_0 , is the Hubble parameter estimated by setting the time to the present day), G is the gravitational constant, ρ is the matter-energy density of the universe, $\kappa c^2/R^2$ describes the curvature, and Λ is the cosmological constant.

The cosmological constant, Λ , was already introduced by Einstein as a way to describe a static matter-filled universe, since the cosmic microwave background (CMB) and the expansion of the universe were not discovered by this time, and without an additional factor, the universe would either expand forever or would collapse after an initial expansion to a maximum radius. The CMB is the remnant of the electromagnetic radiation that was emitted approximately 400 thousand years in the aftermath of the Big Bang, which expanded to longer wavelengths with the expansion of the universe and is currently detected in the microwave regime. The CMB has a thermal black body spectrum with a temperature of ~ 2.72 K (Fixsen 2009). Einstein himself was not comfortable with the idea of a cosmological constant, however, it has since been accepted by other cosmologists. While the actual physical mechanism responsible for the existence of the cosmological constant remains unclear, the most popular candidate is *vacuum* or *dark energy*.

The currently most widely accepted model of the universe is the Lambda cold dark matter (Λ CDM) or the standard model. The Λ CDM model is based on three major components: the cosmological constant, Λ , associated with dark energy, cold dark matter, and ordinary matter. Dark energy accounts for the expansion of the universe

against the effects of gravitational force, while the cold dark matter, which is described to be non-baryonic, cold, dissipation-less, and collision-less, accounts for gravitational effects seen in large-scale structures, like the flat rotation curves of spiral galaxies.

1.3 Classification of galaxies

Our current general understanding of the structure of the universe posits that the universe is homogeneous and isotropic, it is expanding, and it had a starting point. It is made up of very large-scale filamentary structures known as galaxy filaments that form wall-like structures of gravitationally-bound superclusters of galaxies, separating large voids in spacetime. Several such walls and superclusters have been discovered since the initial discovery of the Pisces-Cetus Supercluster Complex by [Tully \(1987\)](#). The superclusters are made up of large numbers of galaxy clusters, which are groups of several hundred to thousands of galaxies with masses ranging from 10^{14} - $10^{15} M_{\odot}$ that are bound by gravity. It is estimated that the observable universe contains about 10 million superclusters and about two trillion galaxies. Our galaxy, the MW, is a part of the Local Group, containing the MW, the Andromeda galaxy, the Triangulum galaxy (M33), and their satellite galaxies. The Local Group along with the Virgo Cluster, and several other galaxy clusters, forms the Virgo Supercluster.

The word galaxy is derived from the Greek *galaxias* meaning milky, based on the appearance of the MW as a white band across the night sky. The MW is a barred spiral galaxy with a mass of approximately $10^{12} M_{\odot}$ and a diameter of approximately 27 kpc. The Galactic Centre of our galaxy is located at a distance of ~ 8 kpc from Earth and is shown to host a very compact and intense radio source, the supermassive black hole (SMBH) Sagittarius A* (Sgr A*), with a mass of roughly $4.2 \times 10^6 M_{\odot}$ (e.g., [Eckart et al. 2017](#); [Parsa et al. 2017](#); [GRAVITY Collaboration et al. 2018](#)).

A barred spiral is just one of the morphological types of galaxies observed in space. The most popular scheme used to date to classify galaxies on the basis of their morphological structure was put forth by Edwin Hubble in 1926 ([Hubble 1926](#)). It is colloquially referred to as the Hubble *tuning fork* on the basis of how it is often represented.

Figure 1.1 shows a pictorial representation of the Hubble classification scheme. The Hubble scheme divides galaxies into three main classes: elliptical galaxies being represented as the handle of the fork, and barred and regular spirals as the two tines of the fork. Spherical or lenticular galaxies are placed at the neck of the tuning fork. A brief discussion on each morphological type follows.

1.3.1 Elliptical galaxies

Elliptical galaxies appear like ellipsoids in the sky, they seem to have smooth and featureless profiles, with no discs, spiral arms, dust lanes, or bars. They consist of low amounts of gas and dust, and have older, lower-mass stars. Elliptical galaxies span a large range in mass and can have masses up to $10^{13} M_{\odot}$. In the 1940s, elliptical galaxies were thought to have formed at high redshift, since they appeared to be similar to globular clusters that were formed in the early universe. However, studies using spectroscopy and photometry showed that the spectral energy distributions of elliptical

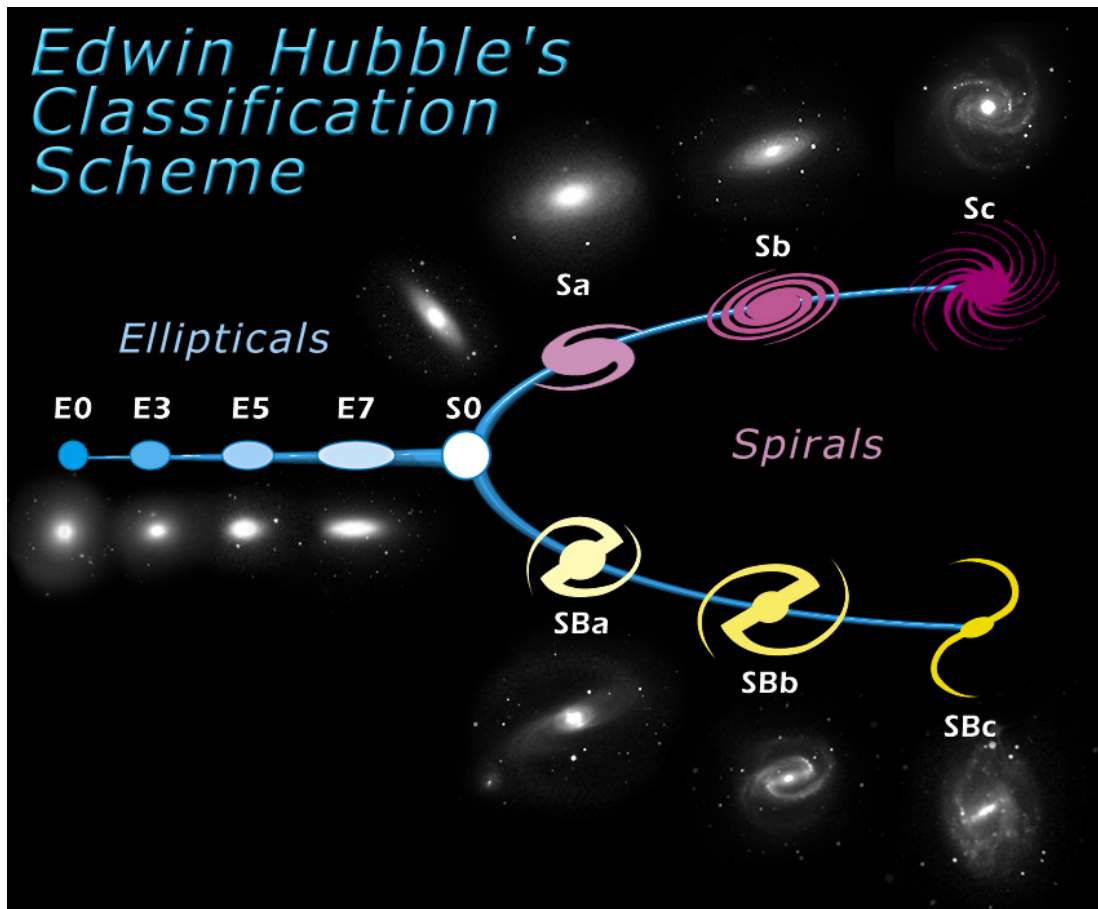


Figure 1.1: Tuning fork style schematic of the Hubble sequence used to classify galaxies morphologically. Credit: Wikipedia

galaxies were very different from that of globular clusters and that elliptical galaxies must have formed over a larger period of time, presumably with contributions from mergers of galaxies. Massive elliptical galaxies are generally found at the centres of galaxy clusters, and elliptical galaxies are more common in dense environments. Against the plane of the sky, some elliptical galaxies appear almost spheroidal while others appear rather elongated. Hubble used the degree of elongation as a way to classify elliptical galaxies. The different classes of elliptical galaxies are indicated by the notation E_n , where n is a measure of the ellipticity of the galaxy, that can be estimated using a simple formula:

$$n = 10 \times \left(1 - \frac{b}{a}\right) \quad (1.5)$$

where a and b refer to the major and minor axis of galaxy's isophotes. Isophotes are contours of constant surface brightness and appear as approximately concentric ellipses with the axis ratio, b/a ranging between 1 and 0.3. Thus, we have elliptical galaxies ranging between type $E0$ to $E7$, where $E0$ galaxies are almost roundish, while $E7$ s are the most elongated. A word of caution that should be mentioned here is that we only

see the projected surface brightness against the plane of the sky.

The brightness profile of most elliptical galaxies can be fit reasonably using the de Vaucouleurs' law (de Vaucouleurs 1948):

$$I(R) = I(0)e^{-kR^{1/4}} \quad (1.6)$$

where $I(R)$ is the surface brightness of the elliptical galaxy as a function of the apparent distance R from the centre of the galaxy. If we define R_e as the effective radius of the isophote containing half of the total luminosity and I_e is the corresponding surface brightness of the isophote at R_e , then the de Vaucouleurs' profile becomes:

$$I(R) = I_e e^{-7.669 \left[\frac{R}{R_e} \right]^{1/4} - 1} \quad (1.7)$$

The de Vaucouleurs's law is a special case of the more general Sersic profile (Sérsic 1963), with a Sersic index of $n = 4$. While the de Vaucouleurs's profile is unable to fit the brightness profiles of some of the elliptical galaxies, the Sersic profile succeeds in doing this. It has the form:

$$I(R) = I(0)e^{-kR^{1/n}} \quad (1.8)$$

where n is the Sersic index of the galaxy, and provides information about the degree of the curvature of the brightness profile. Larger values of n indicate more centrally concentrated brightness profiles.

Elliptical galaxies have a three-dimensional shape which is governed by the behaviour of the stars within them. Disc galaxies maintain their shape with the help of angular momentum due to the rotational motion of their stars, however, in elliptical galaxies, Keplerian rotation is not a dominant factor, and the shape of the system is determined by the stellar velocity dispersion. Therefore, it is difficult to estimate the masses of elliptical galaxies accurately. The correlation between the central stellar velocity dispersion (σ) and the luminosity (L) of an elliptical galaxy is given by the Faber-Jackson relation (Faber & Jackson 1976):

$$L \propto \sigma^\gamma \quad (1.9)$$

where the index, γ , is approximately equal to 4, and can be used to estimate distances to distant elliptical galaxies.

1.3.2 Spiral galaxies

Spiral galaxies have prominent discs made of population I stars, gas, and dust. Population I stars are young, metal-rich, hot, and luminous stars found in discs and spiral arms of galaxies, while population II stars are older, metal-deficient, and found mostly in

globular clusters, galactic bulges, and galaxy halos. These galaxies are also characterised by the presence of spiral arms, which are filamentary structures of stars, gas, and dust, and are most often sites of star formation. The structure of the spiral arms can be used to further categorise spiral galaxies. Some of the spiral galaxies also feature bar-shaped structures in their central regions. Spiral galaxies are most often found in low-density environments. They are some of the brightest galaxies. Spiral galaxies generally have lower masses than elliptical galaxies and span a mass range of 10^9 to $10^{12} M_{\odot}$.

The surface brightness of spiral galaxies can be described by the following exponential law (Freeman 1970):

$$I(r) = I_0 e^{-\frac{r}{h}} \quad (1.10)$$

where h is the disc scale length and I_0 is the central intensity.

Spiral galaxies are rotationally supported. The rotation curves were found to be unexpectedly flat. If only visible matter contributed towards the rotation curve, the curve would drop off as one went further away from the centre. The fact that the rotation curve estimated from neutral hydrogen observations remains flat at radii well beyond the outer edge of the visible galaxy implies the presence of invisible matter that contributes to the rotation curve. This problem is solved by hypothesising the presence of dark matter. The correlation between the mass or the intrinsic luminosity of a spiral galaxy and its rotation velocity is described by the Tully-Fisher relation (Tully et al. 1975):

$$L \propto V_{\text{rot}}^{\alpha} \quad (1.11)$$

where the power index, α , can have values between 3 and 4. Like the Faber-Jackson relation for elliptical galaxies, the Tully-Fisher relation can be used to estimate distances.

The origin of spiral arms has been a matter of much interest to scientists. Originally, the spiral arms were thought to form as a result of matter in the galaxy being condensed into the spiral arms right from the beginning and the pattern would then remain fixed through time. This idea presented unfixable problems (Lindblad 1925), the most significant being that as the matter in the galaxy rotates, the objects farthest from the centre would take a longer period of time to finish a revolution than objects placed closer to the centre. This would result in the arms winding ever tighter until they completely disappeared. This is the *winding problem*.

However, spiral galaxies seem to sustain their spiral structure over time. Two models have been proposed that explain the existence of the sustained spiral structure:

- Density wave model (Lin & Shu 1964; Shu 2016): The model posits that the spiral arms are actually regions of enhanced density that rotate slower compared to the rest of the galaxy. As gas enters this region of enhanced density, it is compressed

and collapses to form new stars. These are hot, high-mass, short-lived blue stars that appear as knots of blue against the spiral arms.

- Stochastic self-propagating star formation model (Mueller & Arnett 1976; Gerola & Seiden 1978; Gerola et al. 1980): Shock waves created by stellar winds and supernovae trigger star formation in the interstellar medium. This starts a cycle of shock waves being formed as a result of star formation and supernova explosions, which then trigger further star formation, making the process self-propagating and self-sustaining. The spiral structure would then be a result of the differential rotation of the galaxy disc.

Depending on how tightly wound the spiral arms are, a galaxy can be classified as Sa, Sb, Sc, and Sd. As we go from Sa to Sd, the spiral arms become more loosely wound, the relative luminosity of the central bulge decreases, and the relative mass of gas increases. The Milky Way appears to be an intermediate between types b and c, and is classified as Sbc.

1.3.3 Lenticular galaxies

The third class of galaxies classified by Hubble are the lenticular galaxies. These are denoted as S0 in the Hubble scheme. They have a prominent disc, but no gas, bright young stars, or spiral arms. They might have significant amounts of dust, though. Like elliptical galaxies, they are smooth and featureless, but follow the exponential surface brightness profile of spiral galaxies. They are rarely found in low-density environments but form a significant portion of highly dense regions. Sometimes, lenticulars might appear as E7 galaxies, and they have also been classified as spiral galaxies sometimes. DeGraaff et al. (2007) present a detailed imaging study of the barred lenticular galaxy, NGC 1533.

The kinematic properties of lenticular galaxies have similarities with both elliptical as well as spiral galaxies. This is because lenticular galaxies have bulge and disc components. The bulge, like elliptical galaxies, is pressure-supported by velocity dispersion, while the disc is rotationally supported. However, it is difficult to conduct kinematic measurements on lenticular galaxies due to their inclination and projection effects caused by the presence of the bulge, the disc, and the random motion of stars. Lenticular galaxies follow the Tully-Fisher relation, but with an offset in the luminosity axis (Blanton & Moustakas 2009).

Several theories regarding the formation of lenticular galaxies exist (DeGraaff et al. 2007; Blanton & Moustakas 2009; van den Bergh 2012; Graham et al. 2015). They could be faded spirals, spiral galaxies that have exhausted their supply of gas and can no longer form new stars (Moore et al. 1998). However, there exist lenticular galaxies with more luminosity than spiral galaxies, so this theory might not explain the existence of all lenticular galaxies. Other theories suggest formation via galaxy mergers or growth via accretion from gas and minor mergers (Sandage 2005; Graham 2013).

1.3.4 Irregular galaxies

The final class of galaxies are the irregular galaxies. Irregular galaxies fall outside the Hubble scheme and encompass all of those galaxies that do not classify as one of the three classes described above. Some of these irregular galaxies are spiral or elliptical galaxies that have undergone galaxy harassment and have distorted shapes as a result of this encounter, but most of irregular galaxies are low-luminosity gas-rich systems. [Gallagher & Hunter \(1984\)](#) provide a review about the structure and evolution of irregular galaxies.

1.4 Evolution of galaxies

This section derives heavily from the review by [Kormendy & Kennicutt \(2004\)](#).

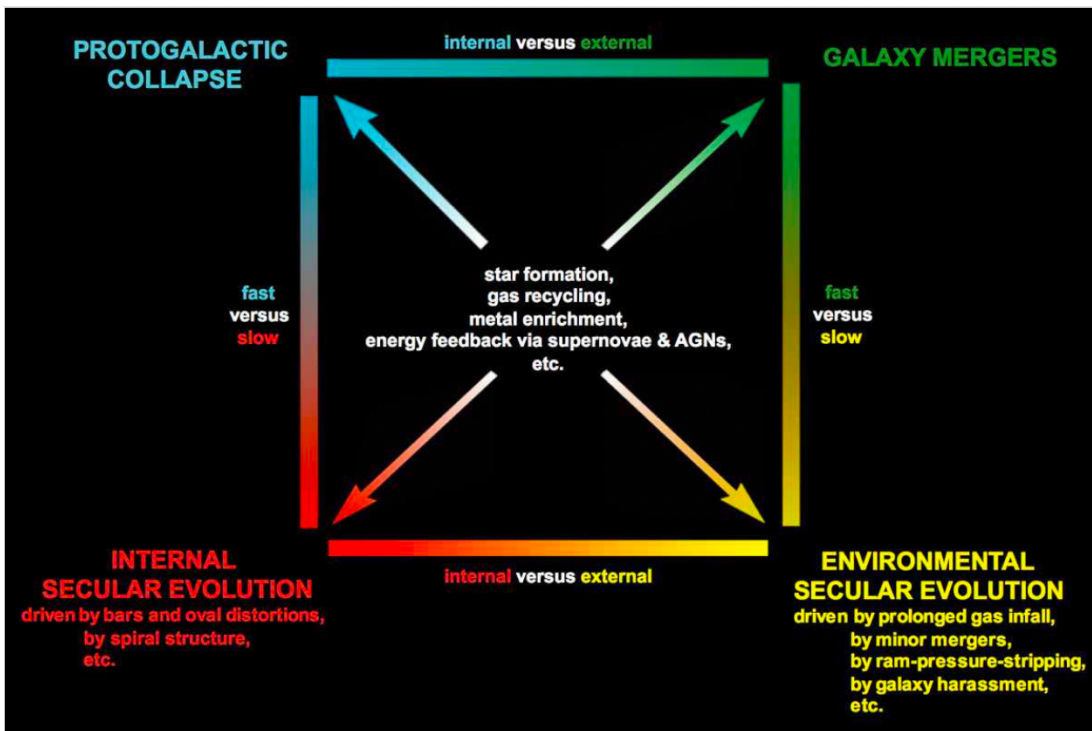


Figure 1.2: Processes of galaxy evolution updated from [Kormendy \(1982\)](#) and from [Kormendy & Kennicutt \(2004\)](#). Processes are divided vertically into fast (top) and slow (bottom). Fast evolution happens on a free-fall (dynamical) timescale. Slow means many galaxy rotation periods. Processes are divided horizontally into ones that happen internally in one galaxy (left) and ones that are driven by environment (right). Credit: [Kormendy \(2013\)](#)

So far, we have understood that the universe has been in transition since the Big Bang. In the early stages of the universe, when the galaxies were in a much denser environment, there was a higher possibility for galaxies to interact and merge. Thus, hierarchical clustering and merging must have been the dominant modes of galaxy evolution in the early universe. However, as the universe expanded and is still expanding, the distance between galaxies is ever increasing, and now secular processes for galaxy evolution are gaining importance.

Figure 1.2 shows a schematic that describes the various processes of galaxy evolution. The top processes in Figure 1.2 describe galaxy evolution via dissipative collapse and interactions of the first galaxies that were formed from the fluctuations of cold dark matter. The timescale of such processes is of the order of the dynamical time of an individual halo, and thus these are fast and violent processes. However, as the universe expands, mergers become less common and slower, internal secular processes become the more dominant mode of galaxy evolution. These processes have timescales much longer than the dynamical time. Some examples of secular processes that could be involved in galaxy evolution would be interactions of stars or gas clouds with galaxy phenomena like bars, spiral structures, and oval distortions. While secular processes are expected to become the dominant mode of galaxy evolution in the distant future, at present, both hierarchical clustering and secular processes play important roles in galaxy evolution.

Since hierarchical clustering is thought to have played an important role in the past, and is still at play in some proportion at low redshift, it is interesting to study systems of interacting galaxies, which is the main goal of this thesis. In the following section, I will briefly introduce some of the characteristics of interacting galaxies.

1.5 Interactions of galaxies

The second law of thermodynamics states that the total entropy of a closed system either increases or stays constant. The stars in spiral galaxies follow ordered orbits. Considering the second law of thermodynamics from an astrophysical perspective, all bodies have the tendency to go from ordered motion towards random/relaxed motion. However, this transition cannot happen without the introduction or presence of some form of instability. The study of galaxy evolution entails the study of how galaxies achieve this transition from ordered to relaxed motion. Intuitively, the most straightforward way to introduce instabilities would be to bring two galaxies close to each other so that their gravitational fields start affecting each other. The perturbation introduced by the gravitational influence of the interacting galaxies would break the conservation of angular momentum of objects in ordered orbits and allow gas and dust to be funnelled through to the central regions of galaxies. The sudden availability of the material in the central region might then trigger the central SMBH to start accreting material, thereby growing, and it might trigger a phase of intense star formation, also known as a starburst phase, around the nucleus of the galaxy. All of this happens within the inner pc to kpc scales at the centre of the galaxy.

Figure 1.3 shows the different stages of interaction between two galaxies. The montage is formed by using images of different sources at different stages of interaction, and it is meant to replicate the interaction between the galaxies Abell 901 and Abell 902. The six stages are briefly described below:

1. As the galaxies start approaching each other and their gravitational fields start interacting, the first subtle signs of tidal disruption start to show up in the form of slight deformation in the outer structure of the galaxies.

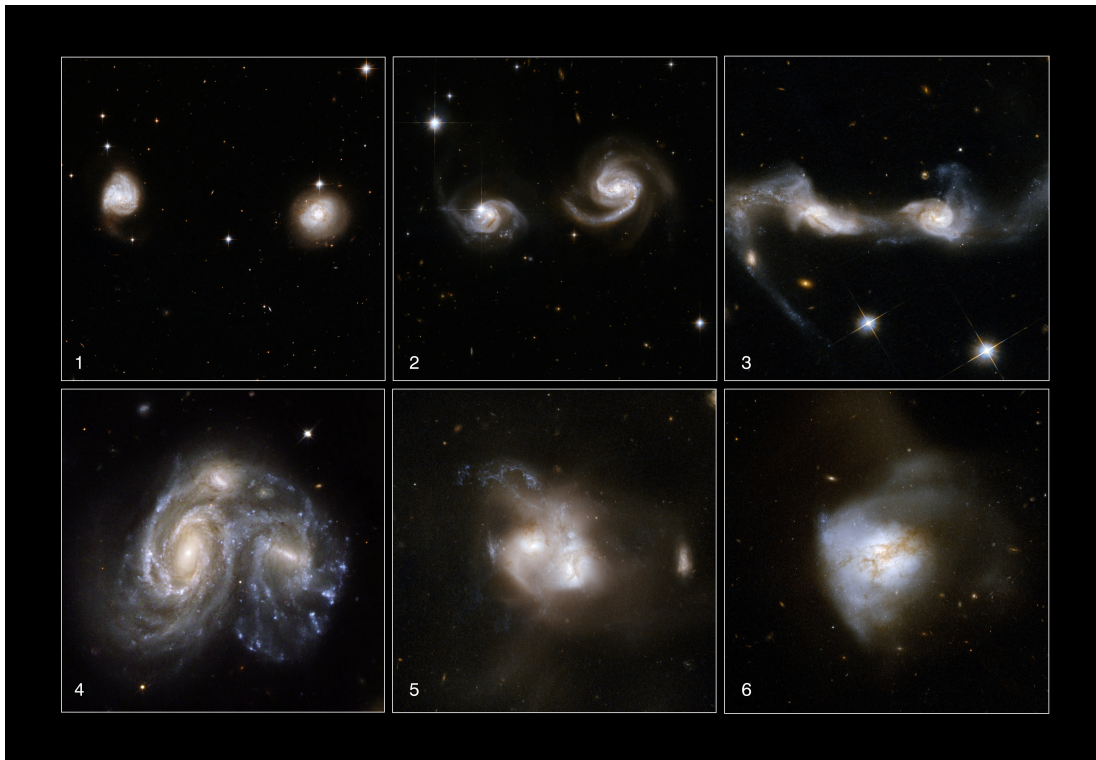


Figure 1.3: Different stages of a merger of galaxies. The images depict the interaction of galaxies Abell 901 and Abell 902, and are illustrated using different images of various galaxies taken by the Hubble Space Telescope. Image credit: NASA, ESA, the Hubble Heritage Team (STScI/AURA)-ESA/Hubble Collaboration and A. Evans (University of Virginia, Charlottesville/NRAO/Stony Brook University), K. Noll (STScI), and J. Westphal (Caltech).

2. As the galaxies come closer to each other, these signs start becoming more prominent. Long filamentary structures of gas and dust, called tidal tails, start stretching out from the galaxies and sweep back to the cores.
3. The tidal tails become more pronounced as the first fly-by takes place. Now the inner structure of the galaxy starts undergoing changes, as well.
4. As the centres of the galaxies start approaching each other, the gas and dust clouds can no longer sustain their ordered motion and start getting accelerated towards the centre of the galaxy. This causes shock waves to ripple through interstellar regions.
5. In later stages of the galaxy interaction, it becomes difficult to distinguish between the two galaxies as their centres approach ever closer. The gas and dust funnelled to the centres of the galaxies might trigger the active phase of the central SMBH as well as fuel bursts of star formation. The centres of such galaxies may be obscured by dust and not appear visible at optical wavelengths. The regions of star formation appear as knots of bright blue against the background of the host galaxy.
6. The final result of a galaxy merger is usually an elliptical or irregular galaxy. Merger products display highly distorted features, with the tidal tails lasting for

a long time after the galaxies have merged. Dust lanes spanning large distances within the galaxy might also be visible. The galaxies might have young stellar clusters formed as a consequence of the interaction. Over time, the gas reservoir in the galaxy gets exhausted and the resulting galaxy is elliptical with an older population of stars and little gas and dust content.

Such violent effects are the consequences of interactions of two equally massive, gas-rich galaxies and are called major mergers. They have a mass ratio of 1:1 to 1:3 (Lotz et al. 2010). If one of the galaxies involved in the interaction has a lower mass and a corresponding mass ratio greater than 1:3, then such an interaction is categorised as a minor merger. While minor mergers do not destroy the spiral structure of the more massive galaxy, they do trigger strong inflows of gas as well as star formation (e.g., Kaviraj 2014). Minor mergers might be more common than major mergers (e.g., Lin et al. 2004; Maller et al. 2006; Stewart et al. 2008; Jogee et al. 2009). The gas content of the progenitor galaxies also plays an important role in how the interaction evolves. If the galaxies are gas-rich, then there is sufficient fuel available for star formation and accretion, and the interaction can be classified as a *wet* merger (e.g., Lambas et al. 2003; Nikolic et al. 2004; Hopkins et al. 2006; Bridge et al. 2007; Lin et al. 2008). However, if the interacting galaxies are gas-poor, then the resulting interaction does not lead to wide-range star formation and is classified as a *dry* merger. While dry mergers do not cause drastic changes in the star formation rate of galaxies, they do significantly influence the stellar mass growth of massive red galaxies at the current epoch (e.g., Tran et al. 2005; Naab et al. 2006; Faber et al. 2007; Lin et al. 2008).

As more information about the nature of interacting galaxies becomes available with increasingly detailed simulations and observations, it becomes ever clearer that mergers of galaxies provide the perfect environment for the central SMBHs of galaxies to grow, for the stellar content of the galaxies to grow and evolve, and for large-scale morphological changes to occur within galaxies. However, many open questions still exist. For example, how often do interactions of galaxies happen? Is the SMBH activity triggered during every interaction? These are some of the interesting questions that are still under debate. I will present some of the findings put forth by various studies over the years in the next section.

1.6 Active Galactic Nuclei

This section derives heavily from Netzer (2013).

Active galactic nuclei (AGN), as the name very aptly suggests, are nuclei of galaxies that are in the process of actively accreting material and thereby growing. A theoretical concept for around half a century, the direct visual evidence for the existence of SMBHs finally became available when the image of the shadow of the SMBH at the centre of the giant elliptical galaxy M87 was published in 2019 by the Event Horizon Telescope Collaboration. This was followed by the publication of the image of the SMBH at the centre of the MW, Sgr A*. Figure 1.4 shows these two images.

The theory of general relativity predicts the existence of points of singularities known

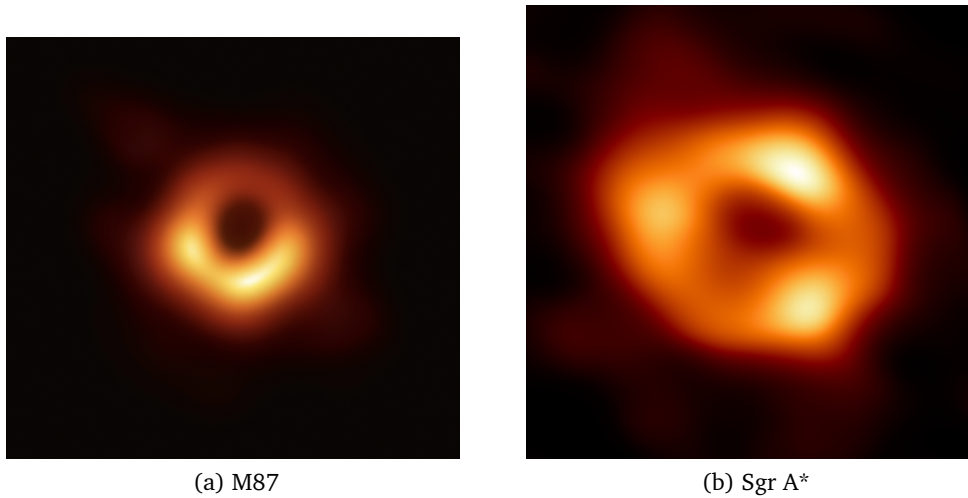


Figure 1.4: Event Horizon Telescope images of the SMBH at the centres of the giant elliptical galaxy M87 (left) and the Milky Way (right). The images show radio emission from a heated accretion ring orbiting the compact object. The dark centre is the event horizon and its shadow. The images were released in 2019 and 2022, respectively, by the Event Horizon Telescope Collaboration.

as black holes (BHs). These are infinitely dense, highly compact objects. They can be broadly classified into three separate classes, based on their mass. The smallest are stellar mass BHs, with masses ranging from 5 to several tens of solar masses, next are intermediate mass BHs, with masses in the range $10^2 - 10^5 M_{\odot}$, and SMBHs with masses ranging from $10^6 - 10^9 M_{\odot}$. Another class, called the primordial or microscopic BHs, are theorised to exist in the early universe. Since radiation does not escape from them and the theorised Hawking radiation has an emission spectrum of a black body with temperature inversely proportional to its mass, it is very difficult to directly detect BHs locally, but their presence can be deduced based on the effect they have on their surroundings. Stellar mass BHs are formed as a result of Supernova Type II explosion of stars with mass exceeding $8 M_{\odot}$. They are generally observed in close binaries with a companion star, with matter from the companion star being accreted onto the stellar BH. The first detection of an isolated stellar mass BH was published in [Sahu et al. \(2022\)](#). Intermediate mass BHs are purported to exist, perhaps as an intermediate evolutionary stage between primordial stellar mass BHs and the SMBHs that appeared hundreds of million years after the Big Bang ([Bañados et al. 2018](#)) (review of intermediate mass BHs: [Greene et al. 2020](#)).

The idea for the existence of SMBHs began with the discovery of the radio source and the optically brightest quasar in the night sky, 3C 273, by [Schmidt \(1963\)](#). It appeared to be a stellar source but spectroscopic analysis showed that the spectrum consisted of Hydrogen emission lines that seemed to be redshifted to a distance of 749 Mpc. The existence of such a luminous source at such a large distance was puzzling. Theories developed over the next decade culminated in the hypothesis that the centres of galaxies host SMBHs. The SMBHs could be quiescent or they could accrete material and thereby radiate brightly. The discovery of the radio source, Sgr A*, at the centre of the Milky Way by [Balick & Brown \(1974\)](#) gave the first observational indication that SMBHs exist.

With the launch of the Hubble Space telescope in 1990, it was possible to study ionised gas in the centres of galaxies other than the Milky Way. It is now a generally accepted idea that the centres of all galaxies host SMBHs.

The level of activity displayed by the SMBH can be used to classify them as either active or quiescent. Quiescent black holes do accrete material, but this is done very ineffectively. They have two sources of fuel, one is the Bondi accretion of diffuse hot gas and the second is the gas released by the stellar population inside the SMBH's sphere of influence. The accretion fractions for quiescent SMBHs range between $\sim 1\% - 10\%$. This means that $\sim 90\% - 99\%$ of the available gas is not accreted by the SMBH (Soria et al. 2006). Quiescent SMBHs are found at the centres of many of the local galaxies. They can be categorised on the basis of their X-ray luminosities, $L_X \leq 10^{40} \text{ ergs s}^{-1}$. This could be due to various factors like low rate of gas inflow inside the SMBH's sphere of influence, low fraction of gas being available for accretion, energy being advected out or in the form of a jet or an outflow, as opposed to being emitted radiatively.

SMBHs whose accretion fractions are $\sim 10\%$ or higher are classified as AGN. A purely observational way to categorise a galactic nucleus as an AGN is if it fulfils at least one of the following criteria:

1. A significantly large amount of energy, more than can be expected from typical stellar processes in a galaxy, is emitted from a compact nuclear region.
2. A spectrum of the central region shows clear non-stellar continuum.
3. Ionisation ratios estimated using strong emission lines from the spectrum are high enough to be indicative of a non-stellar radiation field.
4. The source is variable in line and continuum emission.

AGNs are the compact, luminous centres of many galaxies. Studies of AGNs are a major part of modern astrophysics since this helps in furthering our understanding of how black holes grow and evolve. The activity of the SMBH is also connected to the host galaxy via feedback. The feedback could act in a positive way by, for example, creating shockwaves that ripple through the host galaxy that then causes molecular clouds to collapse and start star formation. However, the feedback can have an opposite effect, for example, by injecting heat into the intergalactic medium (IGM) and preventing cooling, thereby quenching further star formation. AGNs can be classified into further sub-categories on the basis of various factors. The most important among these are the presence or absence of broad emission lines in their spectra, their optical and infrared luminosities, the presence or absence of a radio jet, and their radio luminosities.

The AGN unification scheme proposes that all AGN share similar properties but appear different visually on the basis of the viewing angle (Antonucci 1993; Urry & Padovani 1995). Let us start by describing the schematic of an AGN (see Figure 1.5). At the centre is the SMBH followed by an accretion disc. This is surrounded by a highly dense region called the broad line region (BLR), enveloped by the dusty torus that acts as an obscurer. Low density narrow line regions (NLR) extend out from the centre, sometimes

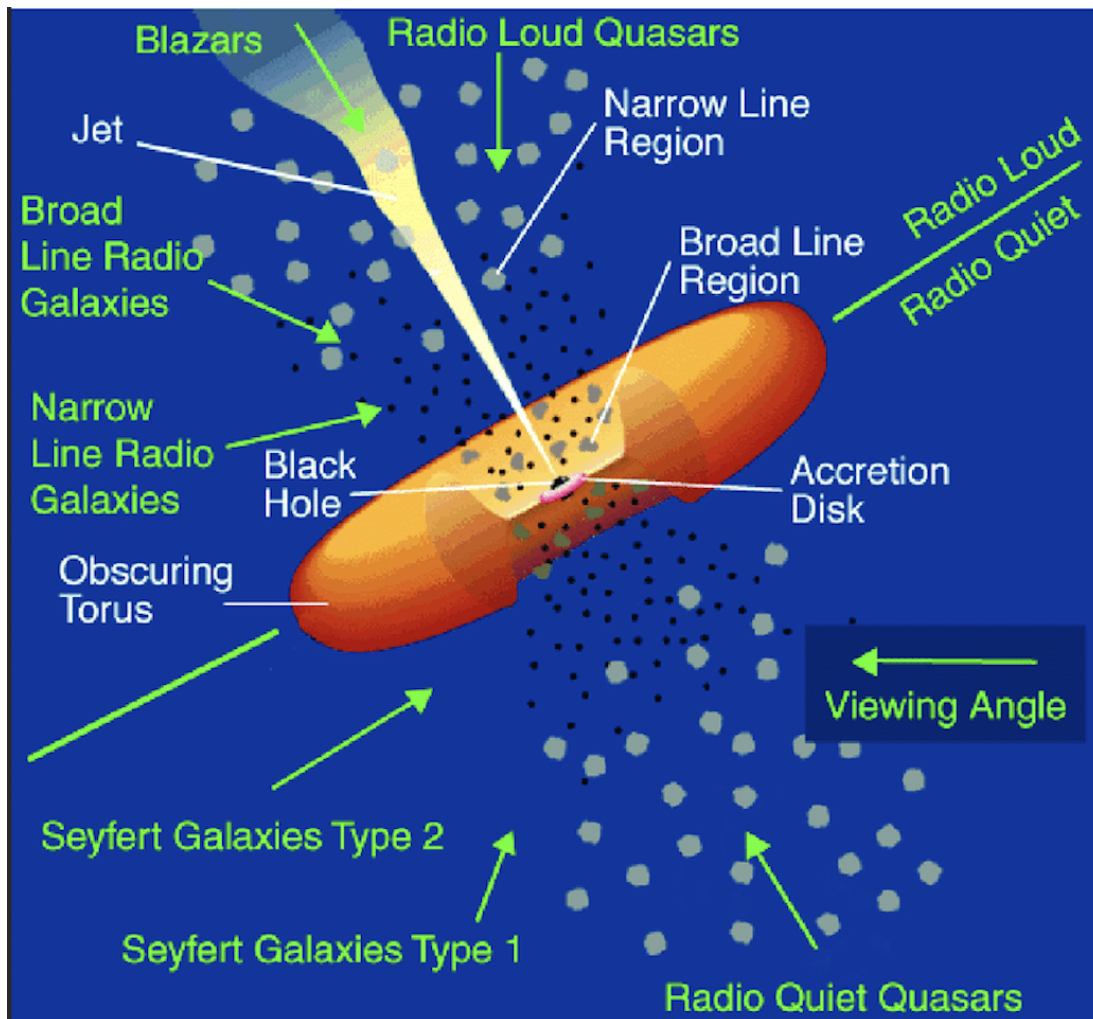


Figure 1.5: The unified AGN model described by [Urry & Padovani \(1995\)](#). The various components of the AGN are indicated. Credit: [Reynolds et al. \(2014\)](#)

spanning kpc-scales. The BLR and NLR are named as such because of the widths of the emission lines that arise within these regions, i.e., emission lines from the BLR are Doppler broadened and have full widths at half maximum (FWHM) $\geq 1000 \text{ km s}^{-1}$, while the lines originating in the NLR have FWHMs $\leq 500 \text{ km s}^{-1}$ (e.g., [Peterson 2006](#)). When viewed face-on, the observer has a view of both the broad and narrow line regions, while an edge-on view blocks the broad line region. The broad lines may still be seen in reflection in polarised light. The presence of a radio jet leads to the classification of *radio loud* (RL) AGNs, although this is no longer strictly true because even the *radio quiet* (RQ) AGNs emit radiation at radio wavelengths, just in lower amounts. The classification of RL and RQ AGNs is currently done on the basis of the ratio of their radio to optical luminosities. Defined as the radio loudness parameter, $R = L_{\text{radio}}/L_{\text{optical}}$, radio loud AGNs are those with $R \geq 10$ ([Kellermann et al. 1989](#)). More recently, [Padovani \(2017\)](#) proposed that instead of RL and RQ, AGNs should be classified as *jetted* and *non-jetted*, based on the presence or absence of strong relativistic jets. He further suggested that jetted and non-jetted AGNs might be intrinsically different from each other since the

RL AGNs emit a large fraction of their energy non-thermally while the RQ emission is pre-dominantly thermal in nature. All of the different components of AGN have intrinsic properties that can be used to determine the physical processes happening in the immediate neighbourhood of an AGN. I wholeheartedly recommend the book *The Physics and Evolution of Active Galactic Nuclei* by [Netzer \(2013\)](#) for a detailed look into AGN.

So far, we have seen that AGNs are extremely energetic phenomena that occur in the centres of many galaxies. The next consequential question is how are AGN triggered? Interactions of galaxies, for one, was long thought to be the most efficient answer. Certainly, interactions show an excess of AGNs, (e.g., [Ellison et al. 2015](#)). However, as the scope of studies increased over the years with better telescopes being built, it was found that this was not usually the case. A significant fraction of AGNs show no signs of previous interaction. The studies conducted to understand the role of interactions in triggering AGNs have contradictory conclusions, with some studies finding positive correlation and some studies finding no significant correlation. The problem seems to stem from the selection criteria adapted while creating the sample to be studied, for example galaxies chosen solely at low redshift, solely at high redshift, or above a cut-off luminosity in a certain wavelength band would present different results. Interestingly, it is the radio loud galaxies, that form a small percentage of all AGNs, that predominantly show signs of past interactions, [Chiaberge et al. \(e.g., 2015\)](#). [Hardcastle & Croston \(2020\)](#) provide a detailed review of radio galaxies. The RL galaxies can be further classified as *low excitation radio galaxies* (LERGs) and *high excitation radio galaxies* (HERGs) ([Laing et al. 1994](#)). Both LERGs and HERGs are jetted, but LERGs have weak or no emission lines in their spectrum, while HERGs have spectra similar to RQ galaxies but additionally possess a radio jet. The difference in the spectral properties of HERGs and LERGs is thought to arise due to the radiative efficiency or inefficiency of the accretion flow ([Hardcastle et al. 2007](#); [Best & Heckman 2012](#); [Pierce et al. 2019](#)). While HERGs were found to be predominantly associated with morphologically disturbed host galaxies ([Ramos Almeida et al. 2012a](#); [Pierce et al. 2019](#)), LERGs show no conclusive evidence either way. Some studies show that LERGs might be influenced by mergers ([Pace & Salim 2014](#); [Sabater et al. 2015](#); [Gordon et al. 2019](#)), but there have also been studies that mergers might not be directly responsible for the radio activity displayed by LERGs ([Ellison et al. 2015](#)).

1.7 Goals and content of this thesis

Based on the discussion presented in this chapter, we can conclude that while much progress has been done in understanding the interplay between interactions of galaxies, triggering of AGNs, and their effect on galaxy evolution, there is still much that is a mystery and needs further work. The work done in this thesis adds to the knowledge that is already available about interacting galaxies.

The thesis consists of three separate projects. Chapter 2 shows the study of a sample of ten pairs/triplets of interacting galaxies and looks at the correlations between their optical, radio, and mid-infrared data. Further, the next two chapters, 3 and 4, focus on a pair of intermediate redshift interacting galaxies, SDSS J134420.86+663717.8,

and the brightest ultra-luminous infra-red galaxy, Markarian 231 (Mrk231), respectively. Summary and concluding remarks are provided in chapter 5. With these three projects, I attempt to understand specific phases in the interaction process as well as to analyse correlations between the properties displayed by the interacting galaxies at different wavelengths, with a main focus on the optical wavelength band.

All three projects are based on long-slit optical spectroscopy data observed using the Multi-Object Double Spectrographs (MODS) at the Large Binocular Telescope (LBT). I was the primary observer for most of the observations used to collect the data for the first and third projects, while also serving as a primary observer for other LBTB projects⁶. The reduction of all MODS data used in this thesis was performed using the MODS CCD reduction pipeline (Pogge 2019), and a Pyraf-based script adapted from the IRAF data reduction manual⁷ and developed as a part of my Master's thesis. The results of the first and second project were presented at conferences like the annual *Astronomische Gesellschaft* meeting in September 2020, the *Spatially Resolved Spectroscopy with the ELTs* conference organised by the University of Oxford in September 2021, and the *Multi-Line Diagnostics of the Interstellar Medium* conference organised by IRAM in April 2022.

⁶The LBTB is a consortium of five German institutes that have a 25% stake in the construction and operation of the Large Binocular Telescope (<https://www.mpia-hd.mpg.de/homes/LBTBWEB/LBT/lbtb.html>)

⁷http://www.astro.iag.usp.br/~jorge/aga5802/spect_iraf_reducao.pdf

Paper I: SDSS-FIRST selected interacting galaxies. An optical long slit spectroscopy study using MODS at the LBT

Interactions of galaxies are thought to trigger the radio-loudness in centres of galaxies (Ramos Almeida et al. 2012a; Pierce et al. 2019). However, it is not clear yet exactly what causes the radio-loud phase in AGN and at what point in the interaction the radio-loud phase is triggered.

In this project, we study a sample of 10 pairs/triplets of interacting galaxies that have been chosen from an SDSS-FIRST sample with the selection criteria of $0.04 \leq z \leq 0.4$ on the redshift, z , and $F_{1.4\text{GHz}} \geq 10$ mJy on the FIRST flux, $F_{1.4\text{GHz}}$ (Vitale et al. 2015; Zajaček et al. 2019). The selection criteria ensures that at least one of the two or three interacting galaxies has sufficient radio continuum emission to be detected at 1.4 GHz by the FIRST survey. The main goal of this project was to study the optical properties of the centres of the interacting galaxies and determine possible correlations between their optical, radio, and mid-infrared properties.

The results of this project are presented in the following peer-reviewed article that has been published in *Astronomy & Astrophysics* (Misquitta et al. 2023).

SDSS-FIRST selected interacting galaxies

An optical long slit spectroscopy study using MODS at the LBT^{*}

Persis Misquitta^{1**}, Andreas Eckart^{1,2}, Michal Zajaček³, Madeleine Yttergren⁴

¹ I. Physikalisches Institut, Universität zu Köln, Zùlpicher Str. 77, 50939, Köln, Germany

² Max-Planck Institut für Radioastronomie (MPIfR), Auf dem Hügel 69, 53121 Bonn, Germany

³ Department of Theoretical Physics and Astrophysics, Faculty of Science, Masaryk University, Kotlářská 2, 611 37 Brno, Czech Republic

⁴ Department of Space, Earth and Environment, Chalmers University of Technology, SE-412 96 Gothenburg, Sweden

Received August 8, 2022; accepted November 29, 2022

ABSTRACT

Context. In the hierarchical model of evolution of the Universe, mergers of galaxies play an important role, especially at high redshift. Interactions of galaxies seem to be associated with incidences of radio loudness in quasars. As a result, it is of interest to study the galaxies that are in the process of interacting with each other and in which at least one nucleus is active in the radio regime.

Aims. In order to understand the various processes taking place within colliding galaxies, it is important to study the radio and optical properties of these sources, as well as any possible correlations that might exist.

Methods. To this end, we present optical long-slit spectroscopy data of ten pairs of SDSS-FIRST selected interacting galaxies at redshift ~ 0.05 , observed using the Multi-Object Double Spectrographs at the Large Binocular Telescope.

Results. We use the line fluxes extracted from the spectra of the nuclear regions of galaxies to plot optical diagnostic diagrams, and estimate masses of the central supermassive black holes as well as their Eddington ratios. Additionally, we use previously published Effelsberg radio telescope data at 4.85 GHz and FIRST survey data at 1.4 GHz to estimate radio spectral slopes and the radio loudness parameters for all of the radio-detected sources, and use WISE data to plot a mid-infrared colour-colour diagram.

Conclusions. We see that while the sample of galaxies covers all of the classes on the optical diagnostic diagrams, the sources that are radio detected fall in the composite/transition region of the diagram. Additionally, we notice a trend that the highest radio loudness parameter in a pair of interacting galaxies is associated with the galaxy that hosts the more massive central supermassive black hole. We do not see any obvious trends with respect to the radio spectral slope, radio loudness parameter, and Eddington ratio. With respect to the mid-infrared data of the galaxies detected by WISE, we see that most of them have contribution from star-formation, but two of them seem to have a significant contribution from an AGN, as well.

Key words. galaxies: interactions - galaxies: active - galaxies: kinematics and dynamics - galaxies: starburst - galaxies: evolution - galaxies: nuclei

1. Introduction

Galaxy evolution has been the subject of study by scientists over many years. According to some of the early studies, galaxies evolve via clustering and merging (Gott & Rees 1975; White 1976; White & Rees 1978). It is generally accepted now that galaxies host super massive black holes (SMBHs) in their centres (Lynden-Bell & Rees 1971; Rees 1984; Kormendy & Richstone 1995; Ferrarese et al. 2001). Several papers have focused on the correlations between the mass of the central SMBHs and the properties of their surrounding galaxies, such as luminosity (Kormendy & Richstone 1995; Marconi & Hunt 2003; Graham 2007; Gültekin et al. 2009), stellar velocity dispersion (Ferrarese & Merritt 2000; Gebhardt et al. 2000; Merritt & Ferrarese 2001;

Tremaine et al. 2002), and bulge mass (Magorrian et al. 1998; McLure & Dunlop 2002; Häring & Rix 2004; Beifiori et al. 2012); implying that there might be co-evolution between the SMBH and its host galaxy. Growth of the central black hole (BH) via accretion of matter also leads to the hypothesis that there must be a link between star-formation and the activity of the SMBH within a galaxy, since both of these processes are fueled by the same material (Heckman et al. 2004; Heckman & Kauffmann 2006; Yesuf et al. 2020).

The star-formation activity of a galaxy is in turn linked to its colour, such that we are led to expect an evolution in galaxy colour as the galaxy undergoes morphological evolution (Kauffmann et al. 2003b). This is supported by galaxy colour bimodality (Strateva et al. 2001; Baldry et al. 2004; Balogh et al. 2004), wherein bulge dominated elliptical galaxies lie in the red peak, while gas rich and disc dominated spiral galaxies can be found in the blue peak. Along with these two prominent types, there are also the green sources associated with mixed morphology,

^{*} This paper uses data taken with the MODS spectrographs built with funding from NSF grant AST-9987045 and the NSF Telescope System Instrumentation Program (TSIP), with additional funds from the Ohio Board of Regents and the Ohio State University Office of Research.

^{**} e-mail: misquitta@ph1.uni-koeln.de

e.g.; early type (red) spirals, that can be found in the regions between the two peaks (Faber et al. 2007; Mendez et al. 2011). These mixed types are called the green valley galaxies. They are found to host a relatively high number of active galactic nuclei (AGN) (e.g.; Nandra et al. (2007); Schawinski (2009); Hickox et al. (2009)). This implies a connection between BH activity and the transitory phase from blue spiral to red elliptical galaxies.

Galaxies can evolve via internal processes, such as formation of bars or spiral arms, i.e.; secular evolution (Courteau et al. 1996; Kormendy & Cornell 2004; Kormendy & Ho 2013; Sellwood 2014; Combes 2014; Méndez-Abreu et al. 2014), or via cataclysmic external processes, like interactions with other galaxies (Toomre & Toomre 1972; Barnes & Hernquist 1996). Interaction between gas rich galaxies is a very efficient way to perturb a system and introduce more gas into the environment. This can lead to triggering of the activity of the central SMBH, causing it to start accretion of material and thereby increase its mass (Springel et al. 2005). The increased gas could also lead to bursts of star-formation. This leads to questions about possible mechanisms that might be involved in making the SMBH become quiescent, as well as in quenching further star formation. One reason could be that the gas reservoir is exhausted, but the process of feedback plays a very important role, as well.

Studies of AGN and star formation activity take into account the process of AGN feedback and its effect on the star formation in the host galaxy. AGN feedback could lead to the gas in the galaxy to either be swept away or heated up due to the influence of a jet, therefore making less fuel available for star formation (Silk & Rees 1998; Benson et al. 2003; Di Matteo et al. 2005; Kaviraj et al. 2007; Khalatyan et al. 2008; Vitale et al. 2015). Broadly, AGN feedback might happen in two different modes. The first is the high-excitation or quasar mode, where a fraction of the material that is being accreted onto the central SMBH is injected back into the surrounding galaxy in the form of thermal energy, thereby heating the gas and quenching star formation (Vitale et al. 2015). Kpc-scale star formation may also be associated with this phase. In the second, low-excitation or radio feedback mode, a smaller fraction of energy is released into the surrounding medium over extended periods of time, preventing cooling flows (Croton et al. 2006; Bower et al. 2006; Khalatyan et al. 2008). AGN and star formation processes are linked to each other in many, complex ways. For example, strong radio jets associated with AGN can lead to shocks and turbulence in the host galaxy, which could in turn induce star formation (Klamer et al. 2004; Gaibler et al. 2012; Ishibashi & Fabian 2012). This interplay between an AGN and its host is still being investigated.

Active galaxies with significantly high radio-to-optical luminosity ratios are considered to be radio loud. As early as the 1960s, it was observed that the radio emission associated with elliptical galaxies was much stronger than radio emission from disc galaxies (Matthews et al. 1964). Additionally, radio-quiet quasars, i.e.; quasars whose radio emission is comparable to their emission in the optical regime, were found to be more frequent than radio loud quasars (Sandage 1965; Strittmatter et al. 1980). This led to the conclusion that there is a bimodality in the nature of radio loudness in AGN, with low-luminosity disc galaxies hosting radio quiet AGN, while high-luminosity radio loud AGN were hosted by elliptical galaxies. Later studies found that there is a large scatter in the radio loudness (Condon et al. 1980). Giant elliptical galaxies were found to host luminous quasars, regardless of their radio loudness, while low-luminosity AGNs were found to have higher than expected values of the radio loudness parameter, placing them in the category of radio loud objects.

Radio galaxies can then be classified as 'low-excitation radio galaxies' (LERGs) and 'high-excitation radio galaxies' (HERGs) (Laing et al. 1994). The spectra of LERGs exhibit weak or no line emission but possess active jets, while HERGs have spectra similar to that of radio-quiet quasars along with a radio jet, and cover all classes of optically selected quasars, such as 'narrow-line radio galaxies' (NLRGs) and 'broad-line radio galaxies' (BLRGs) (Hardcastle & Croston 2020). The difference between LERGs and HERGs is now thought to be a result of the radiative efficiency of the accretion flow to the central SMBH (Hardcastle et al. 2007; Best & Heckman 2012; Pierce et al. 2019). Radiatively efficient (RE) quasars with higher Eddington rates, ($\eta \equiv L_{\text{Bol}}/L_{\text{Edd}}$, greater than a few percent), have sufficient optical luminosity as observed in quasars and BLRGs. LERGs, on the other hand, have lower Eddington rates and accretion happens via the advection dominated, (ADAFs), radiatively inefficient accretion flows (RIAFs), which can launch jets effectively (Ichimaru 1977; Rees et al. 1982; Narayan & Yi 1995). The accretion disc in the case of RIAFs is hot, geometrically thick, and optically thin, while accretion discs associated with higher Eddington ratios and RE accretion flows are colder, optically thick, and geometrically thin (Shakura & Sunyaev 1973). The common factor for all of the objects selected as radio-loud is the non-negligible jet kinetic power. Then, depending on the BH mass and the accretion rate, the accretion flow is either radiatively inefficient (RI) or RE. Although, at low resolution and below a certain jet power, the radio emission from star formation and other processes in the host galaxy may dominate the integrated emission (Gürkan et al. 2019; Hardcastle & Croston 2020).

Another interesting parameter to study, in the case of radio galaxies, along with the Eddington rate, is the spectral index of the emission in the radio regime. The radio continuum spectrum is dominated by the non-thermal synchrotron emission at frequencies ≤ 10 GHz (Duric et al. 1988). The non-thermal synchrotron emission can be described by the characteristic power-law, $S_\nu \propto \nu^\alpha$, where α is the power-law slope or the spectral index. For the compact structures of radio galaxies with jets, the spectral slopes corresponding to the synchrotron self-absorbed radio cores have positive values ~ 0.4 , while secondary components like jets have negative (steep) spectral indices with values ~ -0.7 (Eckart et al. 1986). The latter are consistent with optically thin synchrotron emission. The superposition of self-absorbed synchrotron spectra, typical of an integrated radio spectrum associated with radio jets, results in a flat spectral slope (Zajaček et al. 2019). Thus, the value of α can help to distinguish between the emission mechanisms at play.

Combining the Eddington ratios of quasars with their spectral slopes helps to reach a clearer picture. Laor et al. (2019) found that for a sample of 25 radio quiet (RQ) quasars, high Eddington ratios were associated with steep spectral slopes, while sources with lower Eddington ratios were associated with flat or inverted spectral slopes. On the other hand, for a sample of 16 radio loud (RL) quasars, the correlation is exhibited between the spectral slope and black hole mass. It is, therefore, of interest to study the optical properties of radio galaxies, to understand better the correlation between emission in the radio and optical domains.

It is also interesting to consider what could trigger the radio emission in AGNs and has been the subject of several studies. Chiaberge et al. (2015) measured the merger fraction of Type 2 RQ and RL AGN at redshifts greater than one, using the infrared channel Wide Field Camera 3 on the Hubble Space Telescope (HST) and compared it with the 3CR sample of radio galaxies at similar redshift as well as a sample of non-active galaxies. They

found that almost 92% RL galaxies at $z > 1$ are associated with a recent or an on-going merger, while only 38% of the RQ galaxies are connected to merging systems, similar to the fraction of mergers in the non-active sample. They concluded that mergers could be the triggering mechanism for RL AGN, along with the launching of relativistic jets from the SMBH. [Hardcastle & Croston \(2020\)](#) discuss the role of mergers in triggering various types of radio AGN. While HERGs definitely seem to be associated with host galaxies with disturbed morphologies ([Ramos Almeida et al. 2012](#); [Pierce et al. 2019](#)), LERGs also show some evidence of being influenced by mergers ([Pace & Salim 2014](#); [Sabater et al. 2015](#); [Gordon et al. 2019](#)), although there have been studies suggesting that mergers might not be directly responsible for the radio activity in LERGs ([Ellison et al. 2015](#)).

Along with optical and radio wavelengths, the mid-infrared (MIR) region could also be taken into consideration while studying interacting galaxies. The MIR emission of galaxies is influenced by multiple processes that must be taken into consideration before any conclusions are drawn on its basis. Very small dust grains heated by star-formation and evolved stellar populations (e.g., [Rowan-Robinson & Crawford \(1989\)](#), [Desert et al. \(1990\)](#), [Draine & Li \(2001\)](#), [Groves et al. \(2012\)](#)), along with excited Polycyclic Aromatic Hydrocarbons (PAHs) (e.g., [Draine & Li \(2007\)](#), [da Cunha et al. \(2008\)](#)), indicative of the presence of warm dust associated with star formation, emit in this wavelength range. The extreme ultra-violet radiation from RE AGNs gets absorbed by the dust and gas in the vicinity of the SMBH as well as in the host galaxy, and is re-emitted at MIR wavelengths by the dust. As a result, both the nuclear source as well as star-formation contribute towards the MIR radiation of a galaxy.

With its four bands, namely W1, W2, W3, and W4 corresponding to 3.4 μm , 4.6 μm , 12 μm , and 22 μm respectively, the Wide-field Infrared Survey Explorer (WISE, [Wright et al. \(2010\)](#)) is able to map contributions from the various processes that emit in the MIR region. W1 and W2 are dominated by stellar emission (e.g., [Meidt et al. \(2012\)](#), [Cluver et al. \(2014\)](#)), while W3 detects strong PAH emission bands ([Jarrett et al. 2011](#)). W4, while noisier than W3, has no contribution from PAHs but is able to map warm dust ([Herpich et al. 2016](#)).

There have been some attempts to study the correlation between the optical and radio properties of galaxies. The Faint Images of the Radio Sky at Twenty-centimeters Survey (FIRST, [Becker et al. \(1995\)](#)) covered $\sim 10\,000\text{deg}^2$ in the north Galactic cap, partially overlapping with the region mapped by SDSS. The observations were performed at 1.4 GHz by the Very Large Array (VLA) in its B-configuration and up to $\sim 10^6$ sources were observed. Peak as well as integrated flux densities are provided by the survey. Up to a sensitivity of $\sim 1\text{ mJy}$ and an angular scale of $2'' - 30''$, one third of the sources are resolved with structures. [Vitale et al. \(2012\)](#) found that, for a cross-matched SDSS-FIRST sample, the radio luminosity increases from star-forming galaxies to composite/transitioning, Seyfert, and LINER galaxies, while the $H\alpha$ luminosity decreases to reach a minimum in LINER galaxies. Optical emission-line ratios can be used to identify AGN by using low-ionisation emission-line diagnostic diagrams. These diagrams use emission lines that are close to each other in wavelength and whose strength is a function of the strength and shape of the ionising radiation field, as well as the physical properties of the line emitting gas such as metallicity, gas density, dust, and cloud thickness. AGNs have a stronger ionising field, and therefore give rise to strong [N II], [S II], and [O I] emission lines.

[Vitale et al. \(2015\)](#) presented the radio spectral index trends in optical diagnostic diagrams. For a limited sample of 119

SDSS-FIRST selected sources at intermediate redshift ($0.04 \leq z \leq 0.4$), they performed radio continuum observations at 4.85 GHz and 10.45 GHz, and found a weak trend of spectral-index flattening in the [N II]-based diagnostic diagram along the star-forming-composite-Seyfert branch. In a follow-up study, [Zajaček et al. \(2019\)](#) extended the sample towards lower radio flux densities at 1.4 GHz, with integrated flux densities in the range $10\text{mJy} \leq F_{1.4} \leq 100\text{ mJy}$. They observed the additional 381 sources at 4.85 GHz and 10.45 GHz using the 100-m Effelsberg radio telescope. They found that as the radio spectral index steepens for the sources, the ionisation ratio and radio loudness increase, and this trend is consistent with the transition through the Seyfert-LINER division in the [N II]-based diagnostic diagram.

In this paper, we will focus on a small sub-sample of the sources from [Zajaček et al. \(2019\)](#): the interacting galaxies. This consists of eight pairs and two triplets of interacting galaxies. Figure 1 shows the SDSS images of all of the sources. The one arcsec slit used for the observations, along with the position angle of the observation, is marked. We performed optical long-slit spectroscopy for all of the sources. We present our results based on the study of the optical properties of these radio galaxies. We were primarily interested in checking whether the trends from [Zajaček et al. \(2019\)](#) were also applicable for the case of interacting galaxies, or whether the process of interaction leads to outlying behaviour in the galaxies. Furthermore, we wanted to check if we could find any more correlations between the radio and optical properties of the galaxies.

This paper is organised as follows. We present details about the observations and data reduction in Section 2. In Section 3, we present all of the sources from the sample and their one dimensional optical spectra, while the radio data is discussed in Section 4. We discuss our findings in Section 6, and draw conclusions and summarise in Section 7.

2. Observations and data reduction

Optical long slit spectroscopy was conducted for all of the sources using the Multi Object Double Spectrographs (MODS) mounted on the Large Binocular Telescope (LBT) ([Pogge et al. 2010](#)). The LBT has two 8.4 m mirrors. They are located side-by-side and have a centre-to-centre distance of 14.4 m. MODS are a pair of seeing-limited, two channel, identical spectrographs. They have low-to-medium resolution. They are mounted on the twin mirrors of the LBT. A dichroic splits the light into blue and red optimised spectrograph channels, such that when used in binocular mode, there are four sets of two-dimensional spectra for each exposure. The LBT has a field of view of $6' \times 6'$, while the wavelength coverage of MODS extends from 3000 Å to 10000 Å.

The observations of the ten sources were carried out over several months, starting in January 2020 and ending in May 2021. Table 1 gives an overview over the dates of observations, exposure times and position angles of the observations. All sources, except L127 had one position angle; with the slit being centred across both of the nuclei. At each slit position, we took two exposures; one at the zeroth position of the vertical axis and one with a dither of $10''$ along the slit to account for any loss of data due to the struts between the slits. Each exposure was 1200 s long. L127 consists of three galaxies. We used two different slit positions to ensure that we could observe the centres of all of them. There were two 900 s exposures at each of the slit position, centred on the nuclei of the galaxies. L170

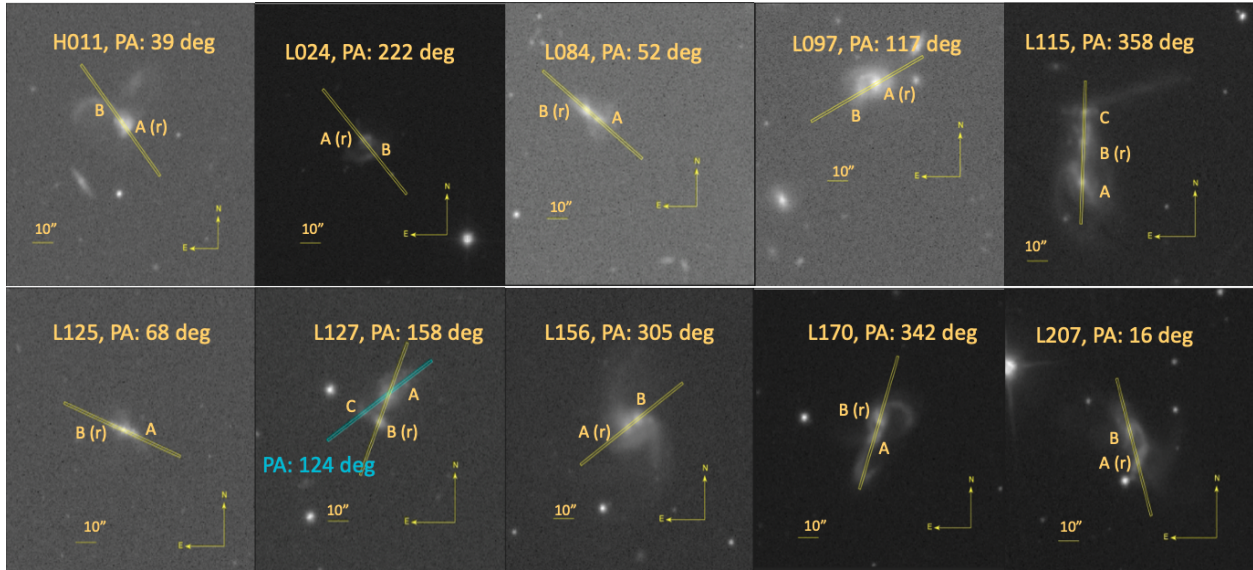


Fig. 1: SDSS images of the sample: H011, L024, L084, L097, L115, L125, L127, L156, L170, and L207. The 1 arcsec slit used for the observation is illustrated and the position angle used for each of the observations is marked. Scale is mentioned in each image. North is up and East is to the left. The radio detected galaxy is marked with an 'r'.

has three 600 s exposures centred across the nuclei of both of the galaxies, two exposures at the zeroth position of the vertical axis and one exposure with a dither of $1''$ along the vertical axis of the slit. For all of the observations, the slit used was $1''$ wide, with spectral resolution of 150 km s^{-1} and spatial resolution of $0.627''$.

The observed two-dimensional spectra were flat-fielded and bias corrected using the MODS CCD Reduction pipeline (Pogge 2019) provided by the observatory. Wavelength calibration, background subtraction, flux calibration, and one-dimensional spectral extraction was performed using pyraf routines adapted from the iraf manual, A User's Guide to Reducing Slit Spectra with IRAF by Phil Massey, Frank Valdes and Jeannette Barnes¹. Along with science sources, calibration spectra were also observed. Mercury, Neon, Argon, Xenon, and Krypton lamps were observed with the telescope dome closed and used for wavelength calibration. Spectrophotometric standard stars were observed at the start or the end of the night and used for flux calibration. The lamp and spectrophotometric standard star spectra were treated to same data reduction procedures as the science spectra. Fresh calibration data was recorded for each observing run.

3. Spectra of galaxies

In the following section, we present a brief introduction to each of our interacting sources. One-dimensional spectra, with the prominent emission lines marked, for each of the galactic centre are presented. The values of the flux of each prominent emission line, along with their full widths at half maximum (FWHMs) and line centres, are tabulated. The projected pair separations between the nuclei and the redshift calculated from the emission lines can be found tabulated in Tables 2 and 3, respectively.

¹ <https://www.mn.uio.no/astro/english/services/it/help/visualization/iraf/spect.pdf>

3.1. H011

We cross-identified H011 with the archival names of CGCG1033.9+0237, VIII Zw 090, MCG +01-27-019, AKARI J1036322+022144, and CGCG 037-089 using the NASA/IPAC Extragalactic Database². Located at a Hubble distance of 226.9 Mpc, the galaxy pair appears to have experienced first passage of both of the galaxies already. Prominent tidal tails are clearly visible in the SDSS image. The two nuclei seem to be very close to each other in projection with a projected pair separation of 2.49 kpc. H011 is the source with the shortest projected pair separation in our sample. We designate the brightest centre of the source as H011B and the comparatively less bright source to the south-west of H011B as H011A. The source was observed with a position angle such that both of the nuclei fell on the slit. The slit position has been marked in figure 1, along with the positions of the nuclei A and B. The one-dimensional spectra of nuclei A and B are shown in Figures 2 and 3. Both of the nuclei have several strong emission lines. The emission lines have been marked in the spectra. We used the lmfits module of Python to perform Gaussian fitting for all of the strong emission lines, thereby letting us estimate line centres, FWHMs, and fluxes of the lines. These have been tabulated for nuclei A and B in Tables 4 and 5, respectively.

We note two interesting points in the spectra of the two nuclei. First, while the $H\alpha$ emission line of H011B has a broad component, the broad component is conspicuously missing in the case of the $H\beta$ emission line. Second, while nuclei A and B have comparably similar flux values in the blue channel, with the values of nucleus A being slightly larger than nucleus B, the fluxes of the various emission lines of nucleus B in the red channel are much larger than nucleus A. It could be that the nucleus of H011B is enshrouded in dust, thereby preventing an unimpeded view to the centre.

² https://ned.ipac.caltech.edu/byname?objname=CGCG1033.9%2B0237&hconst=67.8&omegam=0.308&omegav=0.692&wmap=4&corr_z=1

Table 1: Observational details

Source	RA	Dec	Date of observations	Exposure time	No. of exposures	Position Angle
					s	degrees
H011	10:36:31.87	02:21:44.00	15.11.2020	1200	2	39
L024	12:13:46.11	02:48:41.42	22.03.2021	1200	2	222
L084	09:05:47.35	37:47:38.26	19.01.2020	1200	2	52
L097	11:26:28.29	54:47:14.06	17.05.2021	1200	2	117
L115	08:53:54.54	35:09:01.20	15.11.2020	1200	2	358
L125	09:16:59.97	09:26:48.61	16.11.2020	1200	2	68
L127	09:43:21.62	10:05:01.83	17.11.2020	900	2	158
L127	09:43:21.62	10:05:01.83	17.11.2020	900	2	124
L156	09:19:54.54	32:55:59.81	23.01.2020	1200	2	305
L170	15:18:06.13	42:44:45.07	13.06.2020	600	3	342
L207	07:54:32.20	16:48:32.56	23.01.2020	1200	2	16

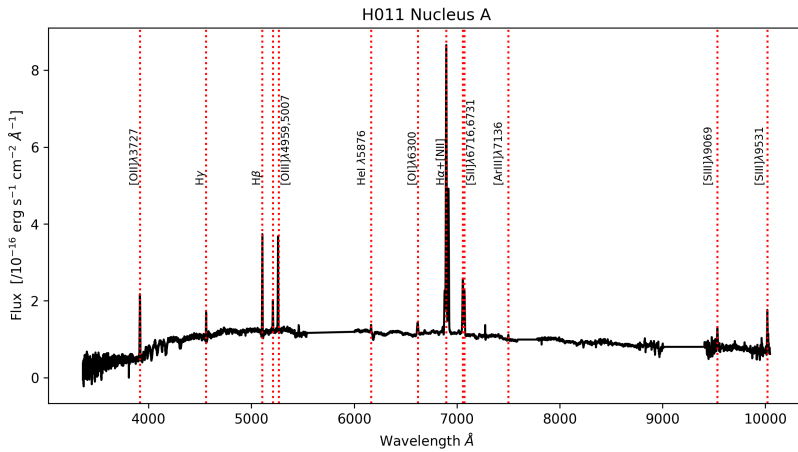


Fig. 2. One-dimensional optical spectrum of the H011A nucleus, extracted over an aperture of ~ 1.2 arcsec (~ 1.2 kpc at given redshift). Prominent emission lines are marked and named. The x-axis represents the wavelength in Angstroms, while the y-axis depicts the flux in units of $\text{erg s}^{-1} \text{cm}^{-2} \text{Å}^{-1}$. The flattened part of the spectrum between 5500 and 6000 Å is the region where the end of the blue channel overlaps with the beginning of the red channel of MODS. Two additional sections beyond 7500 Å have been normalised. They coincide with a sky absorption line and a noisy part of the spectrum.

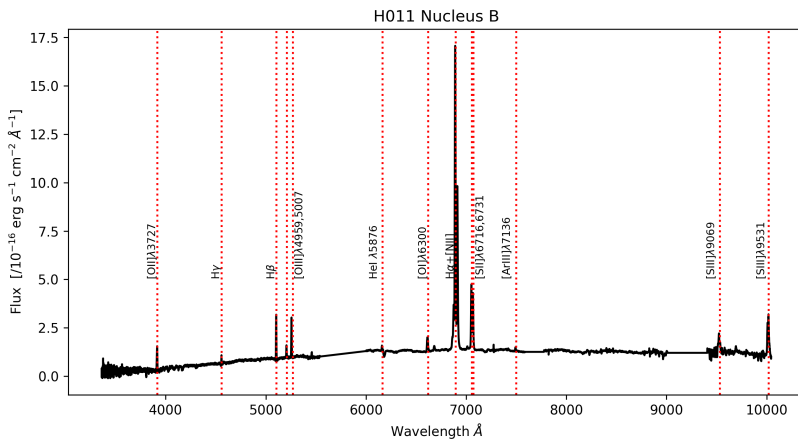


Fig. 3. One-dimensional optical spectrum of the H011B nucleus, extracted over an aperture of ~ 1.2 arcsec (~ 1.2 kpc at given redshift). Prominent emission lines are marked and named. The x-axis represents the wavelength in Angstroms, while the y-axis depicts the flux in units of $\text{erg s}^{-1} \text{cm}^{-2} \text{Å}^{-1}$. The flattened part of the spectrum between 5500 and 6000 Å is the region where the end of the blue channel overlaps with the beginning of the red channel of MODS. Two additional sections beyond 7500 Å have been normalised. They coincide with a sky absorption line and a noisy part of the spectrum.

3.2. L024

L024 can be cross-identified as SDSS J121346.07+024841.4 and IRAS 12112+0305NE using the NASA/IPAC Extragalactic Database³. The source is made up of at least two galaxies and seems to be in a phase post the first passage of the galaxies. Prominent tidal tails are visible in the optical SDSS image, with one tidal tail seemingly going northwards and then turning downwards to the south, while the second tidal tail seems to extend towards the observer inclined edge-on to our line-of-

³ https://ned.ipac.caltech.edu/byname?objname=SDSS+J121346.07%2B024841.4&hconst=67.8&omega_m=0.308&omega_v=0.692&wmap=4&corr_z=1

sight, before turning and extending away from our line-of-sight. The planes described by the tidal tails appear to be mutually perpendicular. The projected pair separation between the nuclei is 5.10 kpc. The brightest centre is designated as L024A, while the source to the south-west of L024A is designated as L024B. Figure 1 shows the slit position used to observe this source, so that both of the nuclei fell on the slit. Approximate positions of nuclei A and B are marked, as well. The one-dimensional spectra of nuclei A and B are shown in Figures A.1 and A.2, respectively. Several emission lines are visible in the spectra of both of the nuclei. However, it is clear at close inspection that the spectrum of L024B is slightly noisier than the spectrum of L024A. The various emission lines are marked in the spectra. The values of

Table 2: Projected pair separations

Source	Pair Separation (kpc)		
	A-B	B-C	A-C
H011	2.5	NA	NA
L024	5.1	NA	NA
L084	6.3	NA	NA
L097	7.2	NA	NA
L115	19.0	14.6	33.9
L125	4.5	NA	NA
L127	13.3	9.0	15.2
L156	5.5	NA	NA
L170	4.9	NA	NA
L207	12.3	NA	NA

Notes. Approximate estimates of the projected pair separations between the nuclei of the individual galaxies. 'NA' denotes 'not applicable'; for sources consisting of two galaxies.

Table 3: Redshifts

Source	Redshift (z)			Uncertainty		
	A	B	C	A	B	C
H011	0.0507	0.0498	NA	0.0002	0.0001	NA
L024	0.0730	0.0730	NA	0.0002	0.0003	NA
L084	0.0477	0.0479	NA	0.0002	0.0002	NA
L097	0.0469	0.0466	NA	0.0001	0.0002	NA
L115	0.0556	0.0569	0.0570	0.0002	0.0001	0.0002
L125	0.0466	0.0480	NA	0.0002	0.0001	NA
L127	0.0536	0.0548	0.0540	0.0002	0.0001	0.0001
L156	0.0485	0.0497	NA	0.0004	0.0002	NA
L170	0.0405	0.0402	NA	0.0005	0.0001	NA
L207	0.0469	0.0456	NA	0.0004	0.0002	NA

Notes. Redshift of galaxies estimated using the centres of the $H\alpha$ recombination line. 'NA' denotes 'not applicable'; for sources consisting of two galaxies. The uncertainties quoted are the 1σ error values.

line centres, FWHMs and fluxes obtained by performing Gaussian fitting of the emission lines have been tabulated and can be found in Tables 6 and 7, respectively.

We note that two narrow components are required to get a good Gaussian fit of the $H\alpha$ + [NII] complex corresponding to the L024A nucleus. Since we are already past the first passage of the galaxies, it is possible that the massive movement of gas and dust associated with the turbulence of such a major event causes structure in the narrow line region. It could also be possible that narrow line regions corresponding to two nuclei are being probed in the slit position due to the chaotic movement of gas and closeness of the nuclei. Another point of interest is that there seems to be a blue-ward wing associated with the [O III] λ 5007 emission line. This could be due to outflows, taking into consideration that the [O III] λ 5007 emission line is associated with outflows (Weedman 1970; Heckman et al. 1981; Veilleux & Osterbrock 1987; Harrison et al. 2014).

3.3. L084

L084 was cross-identified with 2MASX J09054734+3747374, WISEA J090547.34+374738.1 and SDSS J090547.33+374738.2 using the NASA/IPAC Extragalactic Database⁴. The optical SDSS image shows two galaxies. We designate the brightest centre in the source as L084B. The centre of the bluish source to the south-west of L084B we designate as L084A, although we note that it is not very distinguishable from

⁴ https://ned.ipac.caltech.edu/byname?objname=2MASX+J09054734%2B3747374&hconst=67.8&omegam=0.308&omegav=0.692&wmap=4&corr_z=1

L084B in the SDSS fits file. L084 seems to be in the phase past the first passage of the individual galaxies, as well, but the tidal tails seem to be in the planes along the line-of-sight and are thus not very pronounced. The projected pair separation between the nuclei is estimated to be 6.31 kpc. Figure 1 shows the slit position used to observe L084, along with the approximate positions of L084A and L084B.

The one-dimensional spectra of L084A and L084B are shown in Figures A.3 and A.4, respectively. The spectra of both of the nuclei show several emission lines. However, L084A has a noisier spectrum. Several strong Calcium H+K band absorption features are visible in the wavelength range 4000-4300 Å. Additionally, we note that L084A has a bump in the continuum around 4100 Å. We have truncated the spectrum at wavelength 7100 Å since the spectrum is very noisy beyond this and no emission lines are visible. L084B has several more emission lines compared to L084A. The continuum is almost flat for the entirety of the visible wavelength range. The values of the line centres, FWHMs and fluxes obtained from the Gaussian fitting of both of the nuclei can be found in the Tables 8 and 9, respectively. The fluxes of the emission lines belonging to the spectrum of L084A are at least an order of magnitude smaller than those of L084B. In the case of L084B, both [O III] λ 4959 and [O III] λ 5007 have wings. These could be associated with stellar winds or outflows. Additionally, the $H\alpha$ emission line belonging to L084B has a broad component.

3.4. L097

L097 can be cross-identified as SBS 1123+550, CGCG 268-035, CGCG 1123.6+5503, WISEA J112628.37+544713.8, and 2MASX J11262822+5447138 using the NASA/IPAC Extragalactic Database⁵. The source is made up of two galaxies that seem to be approaching each other. A bluish spiral galaxy seems to host the brightest centre of the source, which we have designated as L097A. The second nucleus, designated L097B, is hosted in a yellowish seemingly spheroidal galaxy to the south-east of L097A. Along with these two galaxies, there are two other sources that appear to be close to L097 in projection; a spiral bluish galaxy to the north-west of L097A and a yellow spheroidal galaxy to the west of L097A. In this work, we focus only on L097 and the two nuclei associated with it. L097A and L097B have a projected pair separation of 7.19 kpc. Figure 1 shows the slit position used to observe L097, with the approximate positions of the two nuclei being marked, as well.

The one-dimensional spectra of L097A and L097B are shown in Figures A.5 and A.6, respectively. L097A has several strong emission lines. Some Calcium H+K band absorption features are visible, as well. Several emission lines corresponding to the Balmer recombination series are visible. Compared with $H\beta$, the [O III] λ 4959 and [O III] λ 5007 lines seem to be quite weak. L097B has a less bright spectrum. It is also noisier in comparison with L097A and has fewer emission lines. The $H\alpha$ recombination line seems to be weaker than the [N II] λ 6583 emission line. The ratio of the fluxes of $H\beta$ recombination line to the [O III] λ 5007 emission line for L097B would be higher than a similar ratio for L097A. The ratio $H\alpha/H\beta$, ~ 0.86 , is lower than

⁵ https://ned.ipac.caltech.edu/byname?objname=2MASX+J11262822%2B5447138&hconst=67.8&omegam=0.308&omegav=0.692&wmap=4&corr_z=1

Table 4: H011 Nucleus A Emission Line Data

Emission Line	Observed Wavelength (Å)	Uncertainty in Wavelength (Å)	Flux Value (10^{-16} erg s $^{-1}$ cm $^{-2}$)	Uncertainty in Flux (10^{-16} erg s $^{-1}$ cm $^{-2}$)	FWHM (km s $^{-1}$)	Uncertainty in FWHM (km s $^{-1}$)
[O II] λ 3727	3916.05	0.05	11.33	0.20	474.20	2.30
H γ	4559.88	0.06	2.67	0.11	237.51	9.87
H β	5106.66	0.03	11.30	0.14	249.09	3.52
[O III] λ 4959	5209.02	0.09	3.58	0.15	282.20	12.67
[O III] λ 5007	5259.37	0.03	12.47	0.15	277.79	3.99
He I λ 5876	6163.96	0.53	1.57	0.24	349.94	60.35
[O I] λ 6300	6617.67	0.45	4.44	0.31	584.80	47.60
[N II] λ 6548	6880.74	0.12	12.43	0.31	432.08	12.64
H α	6895.72	0.02	70.73	0.29	380.24	1.74
[N II] λ 6583	6916.93	0.03	39.18	0.27	425.48	3.47
[S II] λ 6716	7056.90	0.09	15.23	0.29	407.69	9.35
[S II] λ 6731	7072.25	0.10	11.10	0.27	361.41	10.60
[Ar III] λ 7136	7499.00	0.90	0.65	0.21	230.43	85.21
[S III] λ 9069	9533.38	0.21	4.20	0.24	242.11	15.73
[S III] λ 9531 _{comp1}	10019.22	0.19	5.56	0.42	167.98	11.68
[S III] λ 9531 _{comp2}	10026.70	0.56	2.51	0.44	201.96	37.10

Notes. All uncertainties are the 1σ standard error values. The values stated are calculated for an aperture of 1 arcsec.

Table 5: H011 Nucleus B Emission Line Data

Emission Line	Observed Wavelength (Å)	Uncertainty in Wavelength (Å)	Flux Value (10^{-16} erg s $^{-1}$ cm $^{-2}$)	Uncertainty in Flux (10^{-16} erg s $^{-1}$ cm $^{-2}$)	FWHM (km s $^{-1}$)	Uncertainty in FWHM (km s $^{-1}$)
[O II] λ 3727	3914.26	0.06	8.51	0.19	488.98	11.50
H γ _{narrow}	4557.09	0.05	1.77	0.07	229.75	9.22
H β _{narrow}	5103.39	0.02	10.35	0.09	248.66	2.35
[O III] λ 4959	5205.88	0.07	3.30	0.09	293.32	9.22
[O III] λ 5007	5256.17	0.02	10.73	0.09	287.66	2.85
[He I] λ 5876	6159.35	0.41	1.28	0.23	229.41	31.44
[O I] λ 6300	6614.04	0.22	8.30	0.35	488.05	23.13
[N II] λ 6548	6874.65	0.09	10.99	0.45	304.16	10.45
H α _{narrow}	6890.22	0.01	136.61	0.74	379.23	1.31
H α _{broad}	6894.79	0.42	76.85	1.64	2463.60	40.30
[N II] λ 6583	6912.21	0.02	69.63	0.58	380.20	2.68
[S II] λ 6716	7051.87	0.05	31.93	0.34	376.92	4.68
[S II] λ 6731	7067.03	0.05	29.32	0.35	401.16	5.52
[Ar III] λ 7136	7492.50	0.45	1.15	0.23	188.59	42.84
[S III] λ 9069	9524.92	0.26	18.36	0.48	647.56	19.53
[S III] λ 9531 _{comp1}	10007.89	0.14	7.63	0.64	180.16	10.19
[S III] λ 9531 _{comp2}	10017.69	0.18	24.02	0.73	361.76	11.98

Notes. All uncertainties are the 1σ standard error values. The values stated are calculated for an aperture of 1 arcsec.

Table 6: L024 Nucleus A Emission Line Data

Emission Line	Observed Wavelength (Å)	Uncertainty in Wavelength (Å)	Flux Value (10^{-16} erg s $^{-1}$ cm $^{-2}$)	Uncertainty in Flux (10^{-16} erg s $^{-1}$ cm $^{-2}$)	FWHM (km s $^{-1}$)	Uncertainty in FWHM (km s $^{-1}$)
[O II] λ 3727	4001.20	0.05	94.97	1.40	509.84	8.25
[Ne III] λ 3869	4151.77	0.80	14.78	2.45	906.12	148.85
H γ	4659.77	0.27	3.09	0.52	210.52	40.56
H β	5218.35	0.07	17.99	0.60	252.38	9.77
[O III] λ 4959	5323.21	0.13	10.95	0.63	266.00	17.47
[O III] λ 5007	5374.58	0.05	30.83	0.64	277.42	6.70
[O I] λ 6300	6759.63	0.17	22.50	0.92	409.64	18.64
[N II] λ 6548	7026.96	0.17	58.56	1.52	603.25	17.08
H α _{narrow1}	7042.20	0.02	237.61	1.52	367.64	2.56
H α _{narrow2}	7054.31	0.29	19.41	2.29	307.90	29.77
[N II] λ 6583	7063.72	0.09	100.46	2.16	397.95	8.07
[S II] λ 6716	7207.51	0.08	65.11	1.09	423.72	8.32
[S II] λ 6731	7222.54	0.10	47.21	1.07	400.83	10.38

Notes. All uncertainties are the 1σ standard error values. The values stated are calculated for an aperture of 1 arcsec.

the theoretically expected value of 2.8 for case B recombination in HII regions (Miller 1974). We have truncated the spectrum of L097B at approximately 7100 Å, since the spectrum becomes very noisy and no emission lines are visible. The strongest emission line in the spectrum of L097B is the [O II] λ 3727 emission line, with the ratio $\log([\text{O II}]\lambda 3727/\text{H}\alpha) \sim 0.47$. In general, the blue channel spectrum of L097B is brighter than the red chan-

nel spectrum. The values of the line centres, FWHMs and fluxes obtained from the Gaussian fitting of both of the nuclei can be found in the Tables 10 and 11, respectively.

Table 7: L024 Nucleus B Emission Line Data

Emission Line	Observed Wavelength (Å)	Uncertainty in Wavelength (Å)	Flux Value (10^{-16} erg s $^{-1}$ cm $^{-2}$)	Uncertainty in Flux (10^{-16} erg s $^{-1}$ cm $^{-2}$)	FWHM (km s $^{-1}$)	Uncertainty in FWHM (km s $^{-1}$)
[O II] λ 3727	3999.79	0.13	37.67	1.56	537.03	24.75
H β	5216.92	0.15	11.28	0.54	388.73	20.70
[O III] λ 4959	5322.81	0.17	8.22	0.57	337.60	24.23
[O III] λ 5007 _{blue wing}	5372.51	0.66	12.96	2.44	462.35	37.97
[O III] λ 5007	5375.08	0.08	13.57	2.20	217.11	16.18
[O I] λ 6300	6759.18	0.30	8.77	0.65	372.83	31.51
[N II] λ 6548	7027.94	0.34	54.44	2.30	710.31	29.45
H α	7042.23	0.07	106.68	2.16	445.60	5.54
[N II] λ 6583	7063.47	0.06	72.84	0.78	496.50	5.95
[S II] λ 6716	7206.99	0.14	29.85	0.84	433.74	14.57
[S II] λ 6731	7222.18	0.16	22.53	0.80	393.79	16.61
[S III] λ 9069	9732.37	0.21	38.36	0.96	555.77	15.72

Notes. All uncertainties are the 1σ standard error values. The values stated are calculated for an aperture of 1 arcsec.

Table 8: L084 Nucleus A Emission Line Data

Emission Line	Observed Wavelength (Å)	Uncertainty in Wavelength (Å)	Flux Value (10^{-17} erg s $^{-1}$ cm $^{-2}$)	Uncertainty in Flux (10^{-17} erg s $^{-1}$ cm $^{-2}$)	FWHM (km s $^{-1}$)	Uncertainty in FWHM (km s $^{-1}$)
[O II] λ 3727	3905.23	0.08	33.77	1.67	407.91	17.67
H β	5092.64	0.09	6.10	0.41	156.11	11.78
[O III] λ 4959	5194.99	0.16	6.14	0.50	232.15	21.94
[O III] λ 5007	5245.09	0.05	17.45	0.49	212.20	6.86
[N II] λ 6548	6860.99	0.20	6.07	0.43	258.42	20.55
H α	6876.03	0.02	44.56	0.39	214.66	2.18
[N II] λ 6583	6897.78	0.09	11.68	0.40	227.03	8.70
[S II] λ 6716	7037.37	0.09	11.46	0.41	222.10	8.95
[S II] λ 6731	7052.52	0.13	7.89	0.42	229.28	13.61

Notes. All uncertainties are the 1σ standard error values. The values stated are calculated for an aperture of 1 arcsec.

Table 9: L084 Nucleus B Emission Line Data

Emission Line	Observed Wavelength (Å)	Uncertainty in Wavelength (Å)	Flux Value (10^{-16} erg s $^{-1}$ cm $^{-2}$)	Uncertainty in Flux (10^{-16} erg s $^{-1}$ cm $^{-2}$)	FWHM (km s $^{-1}$)	Uncertainty in FWHM (km s $^{-1}$)
[O II] λ 3727	3904.72	0.02	20.47	0.19	511.69	4.61
H δ	4296.87	0.13	1.37	0.08	315.58	20.95
H γ	4546.82	0.05	4.44	0.09	364.87	8.58
H β	5092.42	0.02	15.78	0.09	364.66	2.36
[O III] λ 4959 _{blue wing}	5193.97	0.15	5.98	0.26	458.03	11.55
[O III] λ 4959	5196.17	0.14	0.88	0.23	176.09	25.98
[O III] λ 5007 _{blue wing}	5240.04	0.56	5.52	0.46	892.55	36.64
[O III] λ 5007	5244.91	0.02	18.33	0.41	379.80	4.58
[He I] λ 5876	6152.12	0.58	3.34	0.35	546.64	66.32
[O I] λ 6300	6600.43	0.18	7.92	0.32	415.88	19.09
[N II] λ 6548	6861.61	0.11	14.41	1.07	340.15	15.30
H α _{narrow}	6877.39	0.02	112.71	1.20	348.10	2.18
H α _{broad}	6871.30	0.38	49.24	2.18	1315.03	35.80
[N II] λ 6583	6898.73	0.03	63.39	0.51	401.38	3.04
[S II] λ 6716	7037.96	0.05	30.83	0.35	399.41	5.54
[S II] λ 6731	7053.15	0.06	25.66	0.34	382.81	5.95
[S III] λ 9069	9505.27	0.09	33.69	0.42	496.46	6.94
[S III] λ 9531	9991.77	0.05	87.49	0.46	558.76	3.30

Notes. All uncertainties are the 1σ standard error values. The values stated are calculated for an aperture of 1 arcsec.

3.5. L115

Cross-identified as UGC 04653, ARP 195, VV 243, CGCG 180-018, and CGCG 0850.7+3520 using the NASA/IPAC Extragalactic Database⁶, L115 is made up of three galaxies that are interacting with each other. The brightest nucleus is hosted by the central galaxy and is designated as L115B by us. The nucleus of the galaxy to the south of L115B is designated as L115A, while the nucleus to the north of L115B is L115C. The

galaxy hosting L115A is a face-on spiral galaxy with a bright core. The host galaxy of L115B seems to be edge-on and it is unclear whether this is an early or late type galaxy. The galaxy hosting L115C seems to be a late type spiral, with a prominent tidal tail extending far out in the north-west direction from the host galaxy. The projected pair separation between L115A and L115B is 19.00 kpc, between L115B and L115C is 14.56 kpc, and between L115A and L115C is 33.92 kpc. Figure 1 shows the slit position used to observe the source. The approximate positions of L115A, L115B and L115C are marked therein, as well. The one dimensional spectra of the three nuclei can be

⁶ https://ned.ipac.caltech.edu/byname?objname=UGC04653&hconst=67.8&omegam=0.308&omegav=0.692&wmap=4&corr_z=1

Table 10: L097 Nucleus A Emission Line Data

Emission Line	Observed Wavelength (Å)	Uncertainty in Wavelength (Å)	Flux Value (10^{-16} erg s $^{-1}$ cm $^{-2}$)	Uncertainty in Flux (10^{-16} erg s $^{-1}$ cm $^{-2}$)	FWHM (km s $^{-1}$)	Uncertainty in FWHM (km s $^{-1}$)
[O II] λ 3727	3903.16	0.04	7.54	0.14	431.19	7.69
H γ	4544.14	0.07	2.32	0.10	218.52	10.56
H β	5091.03	0.02	10.03	0.11	235.12	2.95
[O III] λ 4959	5193.51	0.62	0.78	0.14	406.08	84.91
[O III] λ 5007	5243.77	0.15	1.82	0.12	276.33	20.60
[He I] λ 5876	6151.74	0.51	2.68	0.30	461.33	59.50
[O I] λ 6300	6597.12	0.51	1.60	0.25	305.59	55.02
[N II] λ 6548	6856.56	0.07	14.34	0.27	339.97	7.44
H α	6872.13	0.01	72.74	0.27	335.27	1.31
[N II] λ 6583	6893.65	0.03	38.39	0.27	332.04	2.61
[S II] λ 6716	7032.99	0.10	11.09	0.28	336.98	9.81
[S II] λ 6731	7048.04	0.11	9.21	0.27	327.32	11.07
[S III] λ 9531	9981.26	0.10	14.57	0.31	299.66	7.21

Notes. All uncertainties are the 1σ standard error values. The values stated are calculated for an aperture of 1 arcsec.

Table 11: L097 Nucleus B Emission Line Data

Emission Line	Observed Wavelength (Å)	Uncertainty in Wavelength (Å)	Flux Value (10^{-17} erg s $^{-1}$ cm $^{-2}$)	Uncertainty in Flux (10^{-17} erg s $^{-1}$ cm $^{-2}$)	FWHM (km s $^{-1}$)	Uncertainty in FWHM (km s $^{-1}$)
[O II] λ 3727	3901.94	0.08	34.81	1.52	424.40	16.91
H γ	4542.43	0.14	2.97	0.34	172.37	22.45
H β	5088.98	0.05	13.78	0.38	198.07	6.48
[O III] λ 4959	5191.69	0.51	2.60	0.50	318.97	69.34
[O III] λ 5007	5241.60	0.11	8.09	0.44	249.54	15.45
[N II] λ 6548	6854.47	0.22	9.52	0.45	439.86	23.63
H α	6868.91	0.08	11.82	0.34	261.61	8.73
[N II] λ 6583	6891.08	0.06	20.78	0.37	331.30	6.53
[S II] λ 6716	7030.75	0.15	7.42	0.36	290.58	15.79
[S II] λ 6731	7045.62	0.19	5.30	0.34	264.42	19.16

Notes. All uncertainties are the 1σ standard error values. The values stated are calculated for an aperture of 1 arcsec.

studied in Figures A.7, A.8, and A.9, respectively.

L115A and L115B have several strong emission lines. While, L115B has a relatively strong [S III] λ 9069 emission line towards the end of the red channel, this is not visible in the L115A spectrum, which has been truncated here since the spectrum becomes very noisy beyond 7500 Å. L115B has a stronger red component compared to its blue component. This is less pronounced in the case of L115A. L115C has a very faint spectrum in comparison with L115A and L115B. Fewer emission lines are visible over the noisy continuum, H α and [O II] λ 3727 being the strongest emission lines in the spectrum. The edge-on view to the centre of the galaxy might be responsible for enshrouding the central regions, thereby giving rise to a noisy and faint spectrum. The process of interacting with other galaxies also causes violent movement of gas and dust within the galaxies, which might lead to the obscuration of the central object. The values of the line centres, FWHMs and fluxes obtained from the Gaussian fitting of all three of the nuclei can be found in the Tables 12, 13, and 14, respectively.

3.6. L125

We cross-identified L125 with 2MASX J09170001+0926486, SDSS J091659.97+092648.6, GALEXASC J091659.82+092648.0, IRAS 09143+0939, and IRAS F09143+0939 using the NASA/IPAC Extragalactic Database⁷. L125 is made up of two edge-on disk galaxies with a projected

⁷ https://ned.ipac.caltech.edu/byname?objname=IRAS09143%2B0939&hconst=67.8&omegam=0.308&omegav=0.692&wmap=4&corr_z=1

pair separation of 4.48 kpc. The brightest nucleus in the source is designated as L125B, while the second nucleus to the south-west of L125B is designated as L125A. The optical SDSS image in Figure 1 shows the approximate positions of the two nuclei. The slit position used to observe the source is drawn, as well. L125A sits in the centre of a rather blue host galaxy, while L125B is hosted by a redder galaxy. This is reflected in the one-dimensional optical spectra of L125A and L125B, shown in Figures A.10 and A.11, respectively.

L125A has a rather flat continuum with very strong emission lines. The emission lines in the blue channel are stronger than the emission lines in the red channel. L125A shows very weak [N II] λ 6548 and [N II] λ 6583 emission lines along with very strong [O III] λ 4959 and [O III] λ 5007 emission lines and recombination lines up to H8 in the Hydrogen Balmer series. L125B has a more typical spectrum, with a slight rise in the continuum towards longer wavelengths. Several strong emission lines are visible. The red channel has a stronger emission than the blue channel. The [N II] λ 6548 and [N II] λ 6583 emission lines are relatively stronger in L125B compared to L125A. In the blue channel of L125B, the [O III] λ 4959 and [O III] λ 5007 emission lines are weaker than the H β recombination line. Both of the nuclei have clearly distinguishable [S III] λ 9069 and [S III] λ 9531 emission lines at the end of the red channel. The values of the line centres, FWHMs and fluxes obtained from the Gaussian fitting of both of the nuclei can be found in the Tables 15 and 16, respectively.

Table 12: L115 Nucleus A Emission Line Data

Emission Line	Observed Wavelength (Å)	Uncertainty in Wavelength (Å)	Flux Value (10^{-16} erg s $^{-1}$ cm $^{-2}$)	Uncertainty in Flux (10^{-16} erg s $^{-1}$ cm $^{-2}$)	FWHM (km s $^{-1}$)	Uncertainty in FWHM (km s $^{-1}$)
[O II] λ 3727	3934.43	0.03	18.61	0.18	572.64	5.34
H γ	4579.94	0.18	1.52	0.17	222.06	27.51
H β	5129.62	0.06	6.78	0.19	265.52	8.77
[O III] λ 4959	5233.52	0.76	1.75	0.29	558.32	103.75
[O III] λ 5007	5284.55	0.22	3.59	0.24	395.68	30.09
[O I] λ 6300	6650.65	0.44	3.17	0.30	448.83	47.81
[N II] λ 6548	6912.67	0.11	12.05	0.30	412.29	12.15
H α	6928.02	0.03	43.69	0.30	388.42	3.03
[N II] λ 6583	6950.27	0.04	39.07	0.30	448.47	3.88
[S II] λ 6716	7091.09	0.13	11.29	0.35	396.41	13.96
[S II] λ 6731	7105.95	0.18	10.28	0.37	451.31	19.00

Notes. All uncertainties are the 1σ standard error values. The values stated are calculated for an aperture of 1 arcsec.

Table 13: L115 Nucleus B Emission Line Data

Emission Line	Observed Wavelength (Å)	Uncertainty in Wavelength (Å)	Flux Value (10^{-16} erg s $^{-1}$ cm $^{-2}$)	Uncertainty in Flux (10^{-16} erg s $^{-1}$ cm $^{-2}$)	FWHM (km s $^{-1}$)	Uncertainty in FWHM (km s $^{-1}$)
[O II] λ 3727	3939.82	0.05	6.52	0.15	519.31	9.90
H γ	4587.57	0.08	1.27	0.06	235.42	12.43
H β	5137.98	0.02	7.10	0.06	254.57	2.34
[O III] λ 4959	5241.27	0.12	1.47	0.07	295.35	16.03
[O III] λ 5007	5291.76	0.04	4.25	0.07	274.39	5.10
[O I] λ 6300	6657.62	0.65	1.55	0.21	447.46	69.84
[N II] λ 6548	6921.62	0.08	12.40	0.22	420.42	8.67
H α	6936.73	0.01	73.45	0.20	342.96	1.30
[N II] λ 6583	6958.46	0.02	32.93	0.19	353.96	2.15
[S II] λ 6716	7099.21	0.08	11.05	0.20	367.22	8.03
[S II] λ 6731	7114.46	0.09	8.20	0.19	333.55	9.28
[S III] λ 9069	9588.77	0.07	8.41	0.18	220.88	5.32

Notes. All uncertainties are the 1σ standard error values. The values stated are calculated for an aperture of 1 arcsec.

Table 14: L115 Nucleus C Emission Line Data

Emission Line	Observed Wavelength (Å)	Uncertainty in Wavelength (Å)	Flux Value (10^{-16} erg s $^{-1}$ cm $^{-2}$)	Uncertainty in Flux (10^{-16} erg s $^{-1}$ cm $^{-2}$)	FWHM (km s $^{-1}$)	Uncertainty in FWHM (km s $^{-1}$)
[O II] λ 3727	3940.99	0.12	2.71	0.18	450.65	26.64
H β	5139.55	0.26	0.13	0.04	101.56	35.61
[O III] λ 4959	5242.41	0.49	0.34	0.07	293.57	66.38
[O III] λ 5007	5292.59	0.22	0.43	0.06	199.52	29.48
[N II] λ 6548	6921.60	0.07	0.73	0.07	319.00	29.47
H α	6937.37	0.05	4.14	0.06	316.98	5.19
[N II] λ 6583	6959.45	0.09	2.48	0.07	343.56	9.48
[S II] λ 6716	7100.30	0.23	0.92	0.06	322.80	23.24
[S II] λ 6731	7115.56	0.25	0.86	0.06	330.12	26.14

Notes. All uncertainties are the 1σ standard error values. The values stated are calculated for an aperture of 1 arcsec.

3.7. L127

L127 consists of three galaxies interacting with each other. It has been cross-identified with CGCG 063-051, CGCG 0940.7+1019, MCG +02-25-024, 2MASX J09432129+1005128, and 2MASS J09432131+1005129 using the NASA/IPAC Extragalactic Database⁸. The brightest centre in the source is designated as L127B. The source to its north-west is designated as L127A, while the source to its north-east is designated as L127C. We managed to perform long-slit spectroscopy on all three sources using two different slit positions. Figure 1 shows the optical SDSS image of L127 with the two slit positions drawn and the approximate positions of all three nuclei marked. The projected pair separation between L127A and L127B is 13.26 kpc, between L127B and L127C

is 8.99 kpc, and between L127A and L127C is 15.21 kpc, respectively. L127A is hosted by a face-on spiral galaxy. The host galaxy of L127B seems to be a red spheroid, while L127C sits at the centre of a very blue irregularly shaped galaxy. It might be that L127C has already suffered distortions due to previous encounters. The optical one-dimensional spectra of L127A, L127B and L127C are shown in Figures A.12, A.13, and A.14, respectively.

L127A has a weak optical spectrum. Few emission lines are visible, primarily the H α + [NII] complex, the [O II] λ 3727 emission line, the [S II] λ 6716, [S II] λ 6731 doublet and the H β recombination line. The [O III] λ 4959 and [O III] λ 5007 emission lines are very weak. The continuum seems to be rise towards longer wavelengths. The spectrum has been truncated around 7100 Å as there are no emission lines visible beyond this point and the spectrum becomes noisy. The spectrum of L127B is the brightest. Several strong emission lines are visible, with the H α + [NII]

⁸ https://ned.ipac.caltech.edu/byname?objname=CGCG+063-051&hconst=67.8&omegam=0.308&omegav=0.692&wmap=4&corr_z=1

Table 15: L125 Nucleus A Emission Line Data

Emission Line	Observed Wavelength (Å)	Uncertainty in Wavelength (Å)	Flux Value (10^{-16} erg s $^{-1}$ cm $^{-2}$)	Uncertainty in Flux (10^{-16} erg s $^{-1}$ cm $^{-2}$)	FWHM (km s $^{-1}$)	Uncertainty in FWHM (km s $^{-1}$)
[O II] λ 3727	3900.93	0.02	11.66	0.08	389.14	3.08
[Ne III] λ 3869	4048.54	0.05	1.92	0.06	223.78	8.15
H8	4069.43	0.09	0.95	0.06	207.15	14.74
H ϵ	4153.35	0.10	1.36	0.07	288.20	17.33
H δ	4291.94	0.06	1.58	0.06	215.29	9.79
H γ	4541.32	0.03	3.98	0.07	224.60	3.96
H β	5085.99	0.01	8.67	0.07	203.50	1.77
[O III] λ 4959	5188.09	0.01	12.24	0.07	197.18	1.16
[O III] λ 5007	5238.26	0.01	38.73	0.07	195.87	0.57
[O I] λ 6300	6593.16	0.73	0.48	0.09	252.99	53.24
[N II] λ 6548	6855.99	0.33	1.29	0.21	515.02	123.40
H α	6868.51	0.02	17.53	0.14	207.91	1.75
[N II] λ 6583	6890.21	0.33	1.27	0.14	271.69	33.53
[S II] λ 6716	7029.84	0.16	2.33	0.13	246.66	16.22
[S II] λ 6731	7044.74	0.23	1.67	0.13	251.25	23.00
[Ar III] λ 7136	7469.54	0.62	0.23	0.05	122.10	38.56
[S III] λ 9069	9492.39	0.06	5.68	0.13	171.29	4.42
[S III] λ 9531	9978.80	0.08	14.97	0.22	216.16	21.04

Notes. All uncertainties are the 1σ standard error values. The values stated are calculated for an aperture of 1 arcsec.

Table 16: L125 Nucleus B Emission Line Data

Emission Line	Observed Wavelength (Å)	Uncertainty in Wavelength (Å)	Flux Value (10^{-16} erg s $^{-1}$ cm $^{-2}$)	Uncertainty in Flux (10^{-16} erg s $^{-1}$ cm $^{-2}$)	FWHM (km s $^{-1}$)	Uncertainty in FWHM (km s $^{-1}$)
[O II] λ 3727	3904.91	0.05	10.06	0.17	476.32	9.22
H γ	4548.04	0.07	4.07	0.14	277.04	11.21
H β	5093.49	0.02	19.46	0.16	292.14	2.94
[O III] λ 4959 _{blue wing}	5189.86	0.26	0.89	0.09	183.82	35.84
[O III] λ 4959	5195.67	0.12	3.98	0.20	292.17	17.32
[O III] λ 5007 _{blue wing}	5240.06	0.11	2.64	0.20	198.66	14.89
[O III] λ 5007	5245.82	0.04	13.23	0.23	301.95	6.29
[O I] λ 6300	6601.62	0.28	5.18	0.39	341.28	29.99
[N II] λ 6548	6862.75	0.04	40.58	0.42	368.95	4.37
H α	6878.21	0.01	152.89	0.40	335.84	0.87
[N II] λ 6583	6899.81	0.02	100.09	0.40	340.01	1.74
[S II] λ 6716	7038.81	0.06	31.75	0.44	375.06	5.97
[S II] λ 6731	7054.14	0.06	28.67	0.43	351.71	5.95
[S III] λ 9069	9509.25	0.09	21.57	0.44	297.82	6.94
[S III] λ 9531	9994.15	0.07	41.75	0.51	370.42	5.10

Notes. All uncertainties are the 1σ standard error values. The values stated are calculated for an aperture of 1 arcsec.

complex in the red channel being the strongest lines. The Hydrogen recombination Balmer series is visible until H ϵ . The continuum seems to be flat. L127C has a bright spectrum, as well. It is stronger in the blue channel as compared to the red channel. Several strong emission lines are visible, the [O III] λ 5007 emission line being the strongest throughout the spectrum. In the red channel, the H α + [NII] complex is the strongest. The Hydrogen recombination Balmer series is visible clearly until H8. The continuum seems to be flat throughout the spectrum. The [S III] λ 9069 emission line is clearly visible for L127B and L127C at the end of the red channel. The values of the line centres, FWHMs and fluxes obtained from the Gaussian fitting of all three of the nuclei can be found in the Tables 17, 18, and 19, respectively.

3.8. L156

L156 can be cross-identified as UGC 04947, CGCG 181-026, CGCG 0916.9+3308, MCG +06-21-016, and B2 0916+33 using the NASA/IPAC Extragalactic Database⁹. The source (see

⁹ https://ned.ipac.caltech.edu/byname?objname=UGC+4947&hconst=67.8&omegam=0.308&omegav=0.692&wmap=4&corr_z=1

Figure 1) consists of two spiral galaxies interacting with each other. We designate the brightest centre of the galaxy as L156B, with the other centre to the south-east of it being designated as L156A. Prominent tidal tails are visible, such that the system might be in the phase post the first passage of the individual galaxies. The projected pair separation between the nuclei is 5.50 kpc. The one-dimensional optical spectra of L156A and L156B are shown in Figures A.15 and A.17, respectively.

The spectrum of L156A has several strong emission lines, with the H α + [NII] complex being the strongest lines in the spectrum. Interestingly, the H α recombination line needs two narrow Gaussian components for the fit to be good. A zoom-in view to the Gaussian fit of the H α + [NII] complex of L156A can be seen in Figure A.16. We also note that both the [O III] λ 4959 and the [O III] λ 5007 emission lines show a blue-ward asymmetry. The continuum rises towards the longer wavelengths in the blue channel before flattening in the red channel. L156B has a brighter spectrum than L156A, especially with respect to the H α + [NII] complex. The Hydrogen recombination Balmer series extends up to H δ for both of the nuclei in the blue channel, however unlike L156A, L156B does not show asymmetry in the structures of the [O III] λ 4959 and the [O III] λ 5007 emission lines. Similar to L156A, the H α recombination line must be fit using

Table 17: L127 Nucleus A Emission Line Data

Emission Line	Observed Wavelength (Å)	Uncertainty in Wavelength (Å)	Flux Value (10^{-17} erg s $^{-1}$ cm $^{-2}$)	Uncertainty in Flux (10^{-17} erg s $^{-1}$ cm $^{-2}$)	FWHM (km s $^{-1}$)	Uncertainty in FWHM (km s $^{-1}$)
[O II] λ 3727	3929.15	0.14	15.22	0.89	388.63	25.20
H β	5122.57	0.08	10.75	0.45	236.01	11.13
[O III] λ 5007	5276.29	0.32	3.11	0.49	254.16	44.35
[N II] λ 6548	6899.31	0.21	11.87	0.74	306.12	21.74
H α	6914.88	0.03	93.91	0.77	327.55	3.04
[N II] λ 6583	6936.81	0.06	43.25	0.77	327.82	6.49
[S II] λ 6716	7077.29	0.18	12.71	0.75	280.62	18.23
[S II] λ 6731	7092.50	0.22	10.56	0.76	285.09	22.42

Notes. All uncertainties are the 1σ standard error values. The values stated are calculated for an aperture of 1 arcsec.

Table 18: L127 Nucleus B Emission Line Data

Emission Line	Observed Wavelength (Å)	Uncertainty in Wavelength (Å)	Flux Value (10^{-17} erg s $^{-1}$ cm $^{-2}$)	Uncertainty in Flux (10^{-17} erg s $^{-1}$ cm $^{-2}$)	FWHM (km s $^{-1}$)	Uncertainty in FWHM (km s $^{-1}$)
[O II] λ 3727	3933.75	0.02	181.63	1.27	446.14	3.81
[Ne III] λ 3869	4080.34	0.86	29.36	2.48	1577.07	150.72
H ϵ	4189.77	0.26	4.78	0.88	204.78	43.68
H δ	4328.46	0.12	17.31	1.05	283.47	20.10
H γ	4580.17	0.05	51.20	1.15	320.29	8.51
H β	5129.46	0.02	154.89	1.27	340.97	2.92
[O III] λ 4959	5232.02	0.11	35.54	1.31	356.08	14.91
[O III] λ 5007	5282.66	0.04	105.64	1.30	343.58	4.54
[O I] λ 6300	6644.50	0.29	28.56	2.03	381.07	31.15
[N II] λ 6548	6907.44	0.05	169.78	2.01	354.83	4.78
H α	6922.85	0.01	1083.40	1.88	311.58	0.43
[N II] λ 6583	6944.70	0.01	500.06	1.93	328.74	1.30
[S II] λ 6716	7085.32	0.04	172.57	1.86	301.47	3.81
[S II] λ 6731	7100.54	0.05	136.21	1.85	295.33	4.65
[S III] λ 9069	9570.67	0.09	91.84	2.02	262.05	6.58

Notes. All uncertainties are the 1σ standard error values. The values stated are calculated for an aperture of 1 arcsec.

Table 19: L127 Nucleus C Emission Line Data

Emission Line	Observed Wavelength (Å)	Uncertainty in Wavelength (Å)	Flux Value (10^{-17} erg s $^{-1}$ cm $^{-2}$)	Uncertainty in Flux (10^{-17} erg s $^{-1}$ cm $^{-2}$)	FWHM (km s $^{-1}$)	Uncertainty in FWHM (km s $^{-1}$)
[O II] λ 3727	3930.43	0.01	130.22	0.72	390.80	2.29
[Ne III] λ 3869	4079.11	0.06	15.55	0.57	236.82	10.30
H8	4100.24	0.06	15.06	0.57	236.33	10.24
H ϵ	4185.28	0.08	14.11	0.63	280.27	14.34
H δ	4324.43	0.04	18.85	0.54	201.88	6.94
H γ	4575.90	0.02	40.21	0.56	203.24	3.28
H β	5124.96	0.01	95.56	0.57	191.42	1.17
[O III] λ 4959	5227.84	0.01	86.13	0.58	193.39	1.72
[O III] λ 5007	5278.34	0.01	248.56	0.59	195.52	0.57
[O I] λ 6300	6641.21	0.55	9.08	1.02	463.02	59.18
[N II] λ 6548	6901.61	0.12	21.08	0.80	282.11	12.17
H α	6917.29	0.01	412.92	0.86	323.54	0.87
[N II] λ 6583	6939.02	0.04	69.85	0.86	318.20	4.32
[S II] λ 6716	7080.06	0.07	39.30	0.84	299.57	7.20
[S II] λ 6731	7095.10	0.09	31.14	0.84	300.63	9.30
[Ar III] λ 7136	7521.93	0.17	11.65	0.74	223.75	16.35
[S III] λ 9069	9561.41	0.06	30.67	0.72	162.21	4.39

Notes. All uncertainties are the 1σ standard error values. The values stated are calculated for an aperture of 1 arcsec.

two narrow Gaussian components to get a good fit. The optical image of L156 shows that the two galaxies are quite close to each other in projection and it is difficult to distinguish between them in the regions between the two nuclei. The movement of gas and dust caused by the interaction between the two galaxies could be responsible for the dual components of the narrow H α recombination line. The values of line centres, FWHMs and fluxes obtained by performing Gaussian fitting of the emission lines have been tabulated and can be found in Tables 20 and 21, respectively.

3.9. L170

We cross-identified L170 as VV 705, MRK 0848, I Zw 107, CGCG 221-050, and CGCG 1516.2+4255 using the NASA/IPAC Extragalactic Database¹⁰. It consists of two spiral galaxies that have already finished the first passage against each other. We denote the brightest nucleus in the source as L170B, while the second nucleus to the south-east of L170B, we denote as L170A. The tidal tails associated with both of the galaxies

¹⁰ https://ned.ipac.caltech.edu/byname?objname=Mrk848&hconst=67.8&omegam=0.308&omegav=0.692&wmap=4&corr_z=1

Table 20: L156 Nucleus A Emission Line Data

Emission Line	Observed Wavelength (Å)	Uncertainty in Wavelength (Å)	Flux Value (10^{-16} erg s $^{-1}$ cm $^{-2}$)	Uncertainty in Flux (10^{-16} erg s $^{-1}$ cm $^{-2}$)	FWHM (km s $^{-1}$)	Uncertainty in FWHM (km s $^{-1}$)
[O II] λ 3727	3910.36	0.03	19.87	0.15	557.75	4.60
[Ne III] λ 3869	4057.98	0.25	1.02	0.12	341.55	44.36
H δ	4302.99	0.26	1.08	0.12	339.53	42.53
H γ	4553.48	0.12	3.09	0.13	391.35	19.11
H β	5100.46	0.04	9.21	0.14	371.14	6.47
[O III] λ 4959 _{blue wing}	5200.43	0.70	2.93	0.51	735.52	89.41
[O III] λ 4959	5202.33	0.21	1.81	0.49	284.30	40.94
[O III] λ 5007 _{blue wing}	5251.29	0.24	7.76	0.71	672.41	38.28
[O III] λ 5007	5252.55	0.07	5.97	0.72	291.86	15.42
[O I] λ 6300	6607.28	0.50	3.10	0.33	442.69	54.03
[N II] λ 6548	6866.47	0.23	13.89	0.57	514.24	23.59
H α _{comp1}	6881.42	0.23	53.09	3.41	398.03	16.13
H α _{comp2}	6888.16	0.20	30.73	3.18	309.23	10.45
[N II] λ 6583	6905.42	0.04	57.60	0.40	560.43	4.78
[S II] λ 6716	7046.34	0.20	24.47	0.72	615.21	19.58
[S II] λ 6731	7061.84	0.23	13.90	0.67	463.90	19.97
[S III] λ 9069	9513.00	0.19	10.26	0.36	359.19	14.19
[S III] λ 9531	10003.82	0.17	22.25	0.44	517.60	11.69

Notes. All uncertainties are the 1σ standard error values. The values stated are calculated for an aperture of 1 arcsec.

Table 21: L156 Nucleus B Emission Line Data

Emission Line	Observed Wavelength (Å)	Uncertainty in Wavelength (Å)	Flux Value (10^{-16} erg s $^{-1}$ cm $^{-2}$)	Uncertainty in Flux (10^{-16} erg s $^{-1}$ cm $^{-2}$)	FWHM (km s $^{-1}$)	Uncertainty in FWHM (km s $^{-1}$)
[O II] λ 3727	3914.71	0.06	15.39	0.36	421.49	11.49
H δ	4307.73	0.23	2.48	0.30	270.91	38.30
H γ	4558.20	0.10	7.66	0.33	308.67	15.14
H β	5104.95	0.04	24.16	0.36	316.75	5.29
[O III] λ 4959	5207.28	0.65	1.09	0.33	259.25	89.30
[O III] λ 5007	5257.47	0.17	5.44	0.36	308.13	23.39
[O I] λ 6300	6613.06	0.68	1.27	0.31	260.85	72.58
[N II] λ 6548	6875.26	0.06	18.22	0.34	286.68	6.11
H α _{comp1}	6889.19	0.10	95.34	3.79	322.68	2.61
H α _{comp2}	6891.35	0.03	58.08	3.74	197.64	3.92
[N II] λ 6583	6911.94	0.02	70.25	0.34	299.05	1.74
[S II] λ 6716	7051.74	0.06	21.36	0.34	299.93	5.53
[S II] λ 6731	7066.92	0.06	16.96	0.33	284.42	6.37
[S III] λ 9069	9522.58	0.40	14.82	0.59	653.71	29.93
[S III] λ 9531	10010.08	0.12	22.47	0.45	364.73	8.39

Notes. All uncertainties are the 1σ standard error values. The values stated are calculated for an aperture of 1 arcsec.

are very prominent. The tidal tail of L170A seems to move southwards before turning north-westwards. Meanwhile, the tidal tail associated with L170B moves up and out westwards from the galaxy before turning southwards and then to the east behind the host galaxy of L170B. The optical SDSS image of L170, along with the slit position and the approximate positions of L170A and L170B are shown in Figure 1. The projected pair separation between the two nuclei is estimated to be approximately 4.86 kpc. Figures A.18 and A.19 show the one-dimensional optical spectra of L170A and L170B, respectively.

The optical spectra of both L170A and L170B show several strong emission lines. The spectrum of L170B is brighter than that of L170A. Both of the nuclei have distinguishable Balmer emission until H γ . Both of the nuclei have broad components in the H α recombination line. However, in the case of L170B, both the [O III] λ 4959 and the [O III] λ 5007 emission lines show asymmetry in their structure, unlike L170A. The [S III] λ 9069 and the [S III] λ 9531 emission lines are stronger for L170B as compared to L170A. The continuum seems to rise towards longer wavelengths for L170A, while it is flatter for L170B. The values of line centres, FWHMs and fluxes obtained by performing Gaus-

sian fitting of the emission lines have been tabulated and can be found in Tables 22 and 23, respectively.

3.10. L207

L207 can be cross-identified as UGC 04090, CGCG 087-046 NED2, MCG +03-02-016 NED02, and 2MASX J0754322+164835 using the NASA/IPAC Extragalactic Database¹¹. The source (see Figure 1) consists of a face-on spiral galaxy interacting with a seemingly edge-on disc galaxy. We designate the first galaxy along the slit, the southern-most galaxy, as L207A. The brighter galaxy to the north-east, we designate as L207B. The projected pair separation between the nuclei is 13.34 kpc. The galaxies seem to already be in the process of interacting with each other, as evidenced by the presence of strong tidal tails, that are ubiquitous in the case of such events. The one-dimensional optical spectra of L207A and L207B are shown in Figures A.20 and A.21, respectively.

Both 207A and L207B have similarly noisy spectra, but display several emission lines. For the case of L207A, the

¹¹ https://ned.ipac.caltech.edu/byname?objname=ugc+4090&hconst=67.8&omegam=0.308&omegav=0.692&wmap=4&corr_z=1

Table 22: L170 Nucleus A Emission Line Data

Emission Line	Observed Wavelength (Å)	Uncertainty in Wavelength (Å)	Flux Value (10^{-16} erg s $^{-1}$ cm $^{-2}$)	Uncertainty in Flux (10^{-16} erg s $^{-1}$ cm $^{-2}$)	FWHM (km s $^{-1}$)	Uncertainty in FWHM (km s $^{-1}$)
[O II] λ 3727	3879.47	0.06	4.23	0.10	391.29	10.05
H γ	4517.61	0.26	0.39	0.07	194.57	41.17
H β	5059.78	0.05	3.19	0.09	240.72	7.11
[O III] λ 4959	5161.20	0.43	0.68	0.09	337.13	53.48
[O III] λ 5007	5210.98	0.12	2.33	0.10	333.33	16.70
[O I] λ 6300	6555.95	0.31	3.19	0.23	391.25	32.95
[N II] λ 6548	6813.70	0.13	6.78	0.42	334.18	15.85
H α _{narrow}	6828.54	0.03	31.03	0.48	323.35	3.51
H α _{broad}	6832.00	1.55	19.45	1.15	2000.59	84.75
[N II] λ 6583	6850.77	0.04	27.93	0.44	393.68	5.25
[S II] λ 6716	6988.78	0.11	10.94	0.28	380.32	11.16
[S II] λ 6731	7003.49	0.15	9.61	0.30	439.49	16.28
[S III] λ 9069	9434.42	0.14	3.52	0.19	170.44	10.18
[S III] λ 9531	9920.91	0.10	14.87	0.27	346.84	7.26

Notes. All uncertainties are the 1σ standard error values. The values stated are calculated for an aperture of 1 arcsec.

Table 23: L170 Nucleus B Emission Line Data

Emission Line	Observed Wavelength (Å)	Uncertainty in Wavelength (Å)	Flux Value (10^{-16} erg s $^{-1}$ cm $^{-2}$)	Uncertainty in Flux (10^{-16} erg s $^{-1}$ cm $^{-2}$)	FWHM (km s $^{-1}$)	Uncertainty in FWHM (km s $^{-1}$)
[O II] λ 3727	3877.31	0.07	17.18	0.35	553.99	12.38
H γ	4515.05	0.10	4.43	0.24	240.53	15.28
H β	5057.09	0.03	21.48	0.27	255.09	3.56
[O III] λ 4959 _{blue wing}	5153.00	4.73	3.23	0.96	530.95	59.38
[O III] λ 4959	5158.55	0.25	6.19	0.83	291.36	37.80
[O III] λ 5007 _{blue wing}	5203.76	0.57	15.29	1.07	673.36	39.20
[O III] λ 5007	5208.58	0.05	18.14	1.19	288.56	10.94
[O I] λ 6300	6553.00	0.37	8.29	0.81	356.17	40.29
[N II] λ 6548	6811.29	0.06	36.76	1.30	270.43	7.93
H α _{narrow}	6827.09	0.01	230.33	1.51	277.72	1.32
H α _{broad}	6826.11	0.43	132.97	3.21	1597.98	39.55
[N II] λ 6583	6848.13	0.02	154.10	1.33	305.34	2.19
[S II] λ 6716	6987.02	0.08	38.49	0.84	345.21	8.59
[S II] λ 6731	7001.76	0.08	33.24	0.79	305.49	8.57
[S III] λ 9069	9433.80	0.03	83.07	0.71	190.48	1.91
[S III] λ 9531	9914.98	0.02	175.81	0.81	230.86	1.21

Notes. All uncertainties are the 1σ standard error values. The values stated are calculated for an aperture of 1 arcsec.

Table 24: L207 Nucleus A Emission Line Data

Emission Line	Observed Wavelength (Å)	Uncertainty in Wavelength (Å)	Flux Value (10^{-16} erg s $^{-1}$ cm $^{-2}$)	Uncertainty in Flux (10^{-16} erg s $^{-1}$ cm $^{-2}$)	FWHM (km s $^{-1}$)	Uncertainty in FWHM (km s $^{-1}$)
[O II] λ 3727	3903.97	0.05	5.97	0.16	1797.04	10.54
H β _{narrow}	5091.33	0.05	2.21	0.08	262.80	8.13
[O III] λ 4959	5192.49	0.40	1.19	0.13	468.97	55.46
[O III] λ 5007	5242.78	0.10	2.80	0.11	334.65	14.34
[O I] λ 6300	6594.21	0.34	1.06	0.11	326.76	36.87
[N II] λ 6548	6854.53	0.11	5.23	0.12	434.34	11.82
H α _{narrow}	6870.90	0.02	13.86	0.10	290.09	2.44
[N II] λ 6583	6891.65	0.04	11.26	0.11	337.15	3.71
[S II] λ 6716	7031.39	0.07	4.69	0.11	300.86	7.66
[S II] λ 6731	7046.37	0.10	3.23	0.10	289.81	10.52

Notes. All uncertainties are the 1σ standard error values. The values stated are calculated for an aperture of 1 arcsec.

H α + [NII] complex is the brightest, followed by the [O II] λ 3727 emission line. Several stellar absorption lines are visible in the spectrum of L207A, especially in the wavelength range 3910-4350 Å. The spectrum of L207B displays emission lines similar to L207A with the notable addition of a broad H α recombination line component. In contrast to L207A, the [O III] λ 4959 and the [O III] λ 5007 emission lines are stronger than the H β recombination line. L207B displays stronger levels of ionisation compared to L207A. The values of line centres, FWHMs and fluxes obtained by performing Gaussian fitting of the emission lines have

been tabulated and can be found in Tables 24 and 25, respectively.

3.11. General comments on spectra of sample galaxies

The optical spectra of the nuclear regions of all galaxies in our sample show several emission lines, some more so than others. The most common, and usually the most prominent lines are the H α and the H β recombination lines, along with the [O II] λ 3727 and the [O III] λ 5007 ionisation lines. These line emissions trace star formation, but could also indicate the activity of the central

Table 25: L207 Nucleus B Emission Line Data

Emission Line	Observed Wavelength (Å)	Uncertainty in Wavelength (Å)	Flux Value (10^{-16} erg s $^{-1}$ cm $^{-2}$)	Uncertainty in Flux (10^{-16} erg s $^{-1}$ cm $^{-2}$)	FWHM (km s $^{-1}$)	Uncertainty in FWHM (km s $^{-1}$)
[O II] λ 3727	3898.86	0.07	7.54	0.21	552.61	14.48
H β _{narrow}	5085.08	0.22	1.32	0.15	235.51	31.54
[O III] λ 4959	5185.48	0.14	7.79	0.25	552.50	19.54
[O III] λ 5007	5235.97	0.04	21.58	0.23	464.91	5.51
[O I] λ 6300	6587.15	0.48	1.78	0.19	428.11	51.74
[N II] λ 6548	6847.02	0.12	8.46	0.25	454.80	13.49
H α _{broad}	6854.88	0.73	81.03	1.30	6554.25	101.54
H α _{narrow}	6862.37	0.04	12.06	0.18	281.26	4.43
[N II] λ 6583	6883.58	0.03	22.46	0.22	384.61	3.83
[S II] λ 6716	7023.46	0.18	4.22	0.19	362.64	18.79
[S II] λ 6731	7038.36	0.18	4.21	0.20	366.99	19.61

Notes. All uncertainties are the 1σ standard error values. The values stated are calculated for an aperture of 1 arcsec.

BH. We study this in some detail by using diagnostic diagrams in Section 6.2.

H011B, L084B, L170A, L170B, and L207B have broad H α components in their spectra. However, the broad components appear to be missing from the H β line. It could be that the broad component is masked by an absorption feature that overlays the emission line. The presence of the broad component in the spectra of these galaxies indicates the presence of a broad line region (BLR) associated with an active SMBH.

The asymmetric [O III] λ 5007 emission line is known to be a tracer of outflows. Outflows are seen to be present in galaxies hosting AGNs as well as star forming regions (Harrison et al. 2014; Bae & Woo 2016; Cicone et al. 2016; Kakkad et al. 2016; Zakamska et al. 2016; Matzko et al. 2022). Since mergers cause movement of material within galaxies, it would not be surprising to see a large incidence of outflows within our sample. However, this is not exactly the case. Amongst our sample, we see that L024B, L084B, L125B, L156A, and L170B have winged [O III] λ 5007 emission line. All of these galaxies with the asymmetric [O III] λ 5007 emission are detected at 1.4 GHz in the FIRST survey (see Section 4 for a detailed discussion on the radio data of the sample). However, not all of the radio detected galaxies have asymmetric [O III] λ 5007 emission. This result is consistent with, e.g., Matzko et al. (2022), who find that the merging environment does not predominantly impact the incidence of outflows in galaxies.

Another point of interest is the presence of [S III] λ 9069 and [S III] λ 9531 emission lines in the spectra of some of the galaxies. We are able to detect these emission lines due to the wavelength coverage of the LBT that extends up to 10,000 Å in the red channel. [S III] λ 9069 is detected in H011A, H011B, L024B, L084B, L115B, L125A, L125B, L127B, L127C, L156A, L156B, L170A, and L170B, while [S III] λ 9531 is seen in H011A, H011B, L084B, L097A, L125A, L125B, L156A, L156B, L170A, and L170B.

The continua underlying the spectra may be analysed to understand the nature of the host galaxies. Most of the galaxies in our sample show a mild increase towards the red part of the spectrum. This is most likely due to contributions from the obscuring dust and starlight. This can be seen most prominently in the case of L115C, and to some degree in the spectra of L097B, L127A, L207A, and L207B. The spectrum of L084A stands out in the sample, since this is the only galaxy whose spectrum shows a quasar-like shape, especially with a feature that closely resembles the big blue bump. Linearly fitting the blue and red continua separately and using the expression, $\alpha_\lambda = -(\alpha_\nu + 2)$, from Vanden Berk et al. (2001) to convert from wavelength to frequency regime, gives a slope of -1.9834 ± 0.0002 for the blue part and

Table 26: Radio loudness and spectral indices

Source	$\alpha_{1.4/4.85}$	$R_{1.4\text{GHz}/g\text{-band}}$	$R_{1.4\text{GHz}/5100\text{\AA}(LBT)}$	$R_{1.4\text{GHz}/5100\text{\AA}(SDSS)}$
H011A	-0.5414	2.146	22.342	5.895
L024A	-0.4724	1.868	1.420	1.847
L084B	-0.3961	1.712	2.331	0.625
L097A	0.1742	0.733	1.919	0.329
L115B	-0.6644	0.998	8.048	1.47
L125B	-0.3365	1.377	1.566	0.637
L127B	-0.5679	1.827	4.600	1.355
L156A	0.3451	0.897	3.332	0.963
L170B	-0.3282	1.042	3.449	0.627
L207A	-0.2824	0.759	1.994	-

Notes. Spectral indices of sources estimated as the ratio of radio fluxes at 1.4 GHz and 4.85 GHz, along with radio loudness parameters of each source, estimated with respect to the SDSS g-band magnitude and the luminosity at 5100 Å, from the LBT spectra and the SDSS spectra, respectively.

-1.9949 ± 0.0003 for the red part. Comparing this to power law fitting and spectral slopes of -0.44 and -2.45 quoted by Vanden Berk et al. (2001) for the blue ($\sim 3000 - 5000\text{\AA}$) and red ($\geq 5000\text{\AA}$) parts of the spectrum, we see that while the spectral slopes are very different for the blue part, they are consistent for the red part. Additionally, the overall shape of the spectrum of L084A resembles the composite quasar spectrum. The difference in the spectral slopes might arise from contributions from starlight.

4. Radio data

While we don't perform any fresh radio observations, we had access to previously conducted continuum observations using the Effelsberg radio telescope at 4.85 GHz and 10.45 GHz. Additionally, for each of the sources, we made use of observations at 1.4 GHz from the FIRST survey. We adopted the spectral slope values from the continuum observations done using the Effelsberg radio telescope as quoted in Zajaček et al. (2019). Details about the SDSS-FIRST cross identification, as well as the Effelsberg observations at 4.85 GHz and 10.45 GHz can be found in Vitale et al. (2012, 2015) and Zajaček et al. (2019). Figure 4 shows the SDSS images of all of the sources with arbitrarily defined SDSS contours in red, overlaid by arbitrarily defined FIRST contours in green. The FIRST database lists the closest SDSS source within a radius of $30''$ of the radio source. This helped us to determine which galaxy or nucleus to associate with the dominant radio emission. Exact identification is tricky in the cases of H011 and L024, since these sources are compact enough at optical wavelengths that the radio map at 1.4 GHz encapsu-

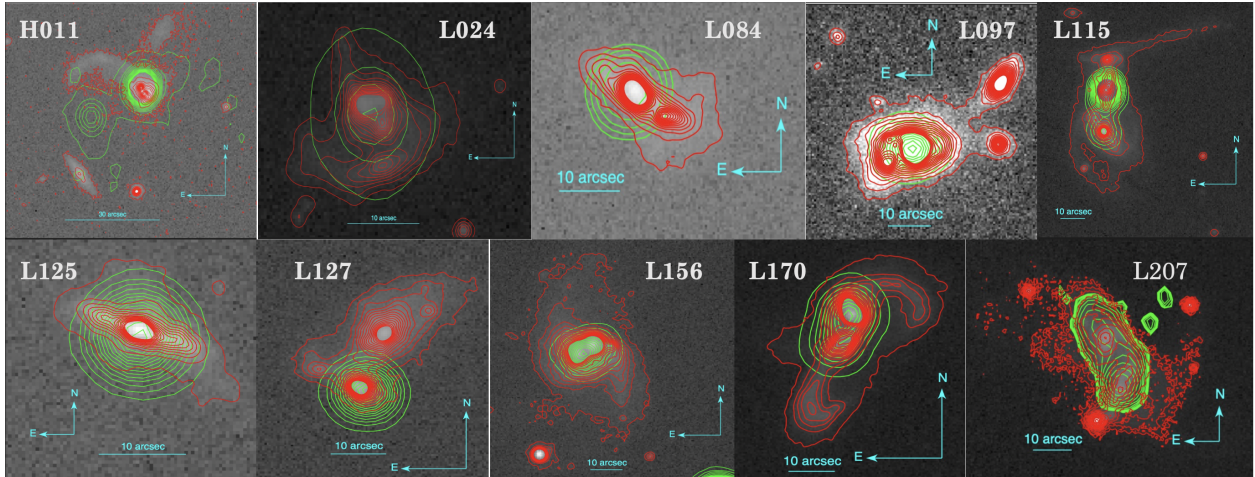


Fig. 4: SDSS (aperture size $\sim 3''$) contour images of all sources overplotted with FIRST (angular resolution $\sim 5''$ contours). The contour levels are chosen arbitrarily. SDSS contours are in red, while the FIRST contours are indicated with the colour green. North is up and east is to the left. Scale is indicated in each image.

lates both of the galaxies when they are overlaid, as can be seen from the Figure 4. We have associated the radio emission with the galaxy identified by FIRST to be the closest to the radio detection. The radio spectral index of each source estimated from their flux densities at 1.4 GHz and 4.85 GHz can be found in the second column of Table 26. We used the following convention to classify the sources as steep, flat, or inverted, based on the values of their radio spectral slopes:

- (i) $\alpha \leq -0.7$: steep
- (ii) $-0.7 \leq \alpha \leq -0.4$: flat
- (iii) $\alpha \geq -0.4$: inverted.

We do not consider the Effelsberg observations at 10.45 GHz studied in Vitale et al. (2015) and Zajaček et al. (2019) in this work, since only H011 and L170 are detected at this frequency. Following the discussion in Zajaček et al. (2019), we define the radio loudness parameter of a source as the ratio of the radio flux density to the optical flux density. We used the flux density values of the galaxies at 20 cm ($F_{1.4}$), which are available from the FIRST survey, and converted the radio flux density into the AB_r -radio magnitude system (Oke & Gunn 1983), using the following conversion (Ivezić et al. 2002),

$$m_{1.4} = -2.5 \log(F_{1.4}/3631 \text{ Jy}), \quad (1)$$

where 3631 Jy is the wavelength independent zero point. The radio loudness parameter, R_g can then be estimated as,

$$R_g \equiv \log(F_{\text{radio}}/F_{\text{optical}}) = 0.4(g - m_{1.4}), \quad (2)$$

where g signifies the optical g -band magnitude for each source, as quoted in the SDSS-DR7 catalogue. The radio loudness parameter values for each galaxy, estimated using this method, can be found in the third column of Table 26.

However, with an aperture size of 3 arcsec, the optical flux density from SDSS corresponds to the host galaxy and not just the nucleus of the galaxy. As a result, the radio loudness parameter thus defined represents the ratio of the radio emission from the centres of the galaxies to the optical g -band emission from

the host galaxies. In a bid to understand how the radio emission behaves with respect to the optical emission from the centres of the galaxies, we estimated radio loudness as the ratio of the luminosity of the source at 1.4 GHz to its optical continuum luminosity at 5100 Å. The optical luminosity is estimated over an aperture of 1.2 arcsec. The radio loudness parameters estimated with this method can be found in the fourth column in the Table 26. As a comparison, we estimated the corresponding radio loudness parameter using the optical continuum luminosity at 5100 Å from the SDSS spectra, these can be found in the fifth column of the Table 26. For the purpose of analysis, we use $R > 10$ (e.g., (Kellermann et al. 1989)) as the criterion to classify a source as radio loud based on LBT data.

The values of the radio loudness parameter estimated using the continuum luminosity from the SDSS spectra are comparatively lower than the values calculated using the LBT spectra. The reason for this is that the aperture size of SDSS is more than twice that used to extract the LBT spectra. This in turn leads to higher luminosity estimates for the SDSS spectra, and thus lower values of R . On the basis of the adapted criterion, H011A is the only radio loud galaxy, while the others, while being radio detected, have lower radio loudness parameters.

5. Mid-infrared data

In order to take into consideration the MIR properties of the galaxies within our sample, we made use of the data observed by WISE in the W1, W2, W3, and W4 bands, corresponding to 3.4 μm , 4.6 μm , 12 μm , and 22 μm respectively.

Further, we compute source flux density in Jansky (Jy) units from the WISE Vega magnitude of the galaxies in the W3 band, $m_{12\mu\text{m}}$, using the following equation:

$$F_\nu[\text{Jy}] = F_{\nu,0} \times 10^{(-m_{12\mu\text{m}}/2.5)} \quad (3)$$

where $F_{\nu,0}$ is the zero magnitude flux density corresponding to the constant that gives the same response as that of Vega, and has the value 31.674 for the W3 band. We use the computed flux density to further estimate the 12 μm luminosity of the galaxies in the units of erg s^{-1} .

Table 27 lists all of the galaxies detected by WISE, their Vega magnitudes in the four bands, and luminosity at $12\mu\text{m}$. With the exception of L170A, all galaxies that either host a nuclear region that has broad emission line components in its spectrum or are detected at 1.4 GHz in the FIRST survey are also detected by WISE.

6. Discussion

All of the galaxies presented in Section 3 have emission lines that can be analysed to study the nature of the regions where they originate. In this section, we discuss the properties showcased by the interacting systems in our sample. We start by briefly describing our estimates for the masses of the SMBHs hosted by the galaxies. We follow by plotting diagnostic diagrams, such as the BPT diagram proposed by Baldwin, Phillips, and Terlevich (Baldwin et al. 1981). The diagnostic diagrams are used to identify if the emission lines arise in a hard ionising field associated with AGNs or a softer ionising field that characterises star formation, based on the ratios of emission lines that are placed close to each other in the spectrum, such that we may safely disregard reddening and do not need to correct for interstellar and galactic extinction (Kewley et al. 2019). Furthermore, we will discuss the optical and radio properties of the galaxies in the context of their luminosities, ionisation ratios, Eddington ratios, radio loudness parameters and radio spectral indices.

6.1. Masses of the central super massive black holes

Optical spectra of nuclear regions of a galaxy are useful in the estimation of the masses of the central SMBH. This can be accomplished either by estimating the stellar velocity dispersion of the galaxy, or, given the presence of broad emission lines in the spectrum, by making use of the virial theorem.

We used the penalised pixel-fitting (pPXF) method (Cappellari & Emsellem 2004; Cappellari 2017) to fit stellar components (Sánchez-Blázquez et al. 2006; Vazdekis et al. 2010; Falcón-Barroso et al. 2011) to our galaxy spectra, thereby estimating the values of their stellar velocity dispersion. The values of the stellar velocity dispersion corresponding to each of the galaxy can be found in the Table 28. For H011B, L024B, L125A, and L127C, pPXF was not able to fit a reasonable stellar component, either because the continuum was too strong or because the spectrum was too noisy or attenuated.

We use the M - σ relation presented by Gültekin et al. (2009):

$$\log(M_{\text{SMBH}}) = 8.12 + \left[4.24 \times \log\left(\frac{\sigma}{200}\right) \right] \quad (4)$$

to estimate the masses of the SMBHs at the centres of the galaxies with an estimated stellar velocity dispersion value. These can be found tabulated in the Table 29.

While we could not determine a stellar velocity dispersion for H011B, it has a broad $H\alpha$ component, we used the FWHM of this broad component to estimate mass of the central SMBH using the virial theorem (Greene & Ho 2005; Peterson 2010; Woo et al. 2015):

$$M_{\text{SMBH}} = f \times 10^{6.544} \left(\frac{L_{H\alpha}}{10^{42} \text{ erg s}^{-1}} \right)^{0.46} \left(\frac{FWHM_{H\alpha}}{10^3 \text{ km s}^{-1}} \right)^{2.06} M_{\odot}. \quad (5)$$

We adopt the value of 1.12 for the factor f (Woo et al. 2015) and estimate the black hole mass to be $(1.027 \pm 0.051) \times 10^7 M_{\odot}$. The

value in its logarithmic form is also listed in Table 29. L207 B has a broad $H\alpha$ component as well as stellar absorption features. As a result of this, we were able to estimate the black hole mass for this nucleus using both of the methods. The logarithm of the BH mass using stellar velocity dispersion is estimated to be $(5.834 \pm 0.052) \times 10^7 M_{\odot}$, while it is $(4.188 \pm 0.262) \times 10^7 M_{\odot}$ using the FWHM of the broad $H\alpha$ component. For consistency with the method of mass estimation for most of the sample of galaxies, we state the value estimated using the stellar velocity dispersion in Table 29.

A look at the values in Table 29 shows that almost all of the SMBHs have masses in the range $10^6 - 10^8 M_{\odot}$, which is the typical range for BH masses in quasars. Especially, all of the galaxies associated with radio emission, with the exception of L084B, host central SMBHs with values of mass in the multiples of $10^8 M_{\odot}$.

Amongst the galaxies not detected in the radio regime, there is one exception; L084A has a BH mass of $(9.19 \pm 0.021) \times 10^5 M_{\odot}$, which is on the low end of the mass range of SMBHs. L084A appears extremely blue in the optical SDSS images, and has strong [O III] emission and $H\alpha$ recombination lines. So, L084A could be a compact, young, star-forming galaxy, with the gas reservoir being used mostly for star-formation as opposed to accretion on to the central BH, leading to a less massive BH. We note that it is difficult to understand properly the morphology of the pair, since the region between the two galaxies is rather ambiguous. As a result, it could be that we underestimate the value of the mass of the SMBH.

6.2. Diagnostic diagrams

For our analysis, we use the [O III] λ 5007/ $H\beta$ vs. the [N II] λ 6583/ $H\alpha$ plot (Baldwin et al. 1981), better known as the BPT plot, along with the [O III] λ 5007/ $H\beta$ vs. [S II] λ 6716 + [S II] λ 6731/ $H\alpha$ and the [O III] λ 5007/ $H\beta$ vs. the [O I] λ 6300/ $H\alpha$ plots (Veilleux & Osterbrock 1987). Figure 5 shows all three diagnostic diagram plots for the sample of ten interacting sources. Equations 6, 7, and 8 (Groves & Kewley 2008),

$$\log([\text{O III}]/H\beta) = 0.61/(\log([\text{N II}]/H\alpha) - 0.47) + 1.19, \quad (6)$$

$$\log([\text{O III}]/H\beta) = 0.72/(\log([\text{S II}]/H\alpha) - 0.32) + 1.30, \quad (7)$$

$$\log([\text{O III}]/H\beta) = 0.73/(\log([\text{O I}]/H\alpha) + 0.59) + 1.33. \quad (8)$$

are used to define the demarcation curve that separates the line ratios arising from AGNs from the line ratios associated with star forming regions.

The [O III] λ 5007/ $H\beta$ vs. the [N II] λ 6583/ $H\alpha$ plot has in addition to the delineation curve defined by Equation 6, another demarcation curve, proposed by Kauffmann et al. (2003a), called the 'pure star-forming' line. This curve can be defined by Equation 9 as follows

$$\log([\text{O III}]/H\beta) = 0.61/(\log([\text{N II}]/H\alpha) - 0.05) + 1.3. \quad (9)$$

The pure star-forming line is based on observational data, whereas the curve described by Equation 6 is based on theoretical modelling presented in Kewley et al. (2001) and called the 'maximum starburst' line. If a source falls above the maximum starburst curve, the source of ionisation is very strong and could

Table 27: Mid infrared luminosity data

Source	W1	δ W1	W2	δ W2	W3	δ W3	W4	δ W4	$\log L_{12\mu\text{m}}$
	$m_{3.4\mu\text{m}}$		$m_{4.6\mu\text{m}}$		$m_{12\mu\text{m}}$		$m_{22\mu\text{m}}$		
H011A	11.575	0.006	10.301	0.006	6.232	.006	2.786	0.006	44.19
L024A	12.188	0.009	11.417	0.010	6.949	0.008	3.591	0.011	44.24
L084B	11.810	0.006	10.644	0.007	6.880	0.007	3.795	0.010	44.88
L097A	11.423	0.006	11.064	0.007	6.736	0.006	4.270	0.010	43.92
L115A	11.580	0.006	11.405	0.008	7.863	0.011	4.870	0.017	43.63
L115B	11.200	0.006	10.850	0.006	6.843	0.007	4.485	0.012	44.05
L125B	12.172	0.008	11.679	0.014	7.170	0.008	4.055	0.011	43.77
L127A	12.744	0.009	12.410	0.016	8.006	0.013	4.530	0.015	43.53
L127B	12.267	0.009	11.676	0.011	7.200	0.008	4.327	0.013	43.88
L156A	11.196	0.006	10.800	0.007	6.551	0.006	3.813	0.010	44.04
L156B	11.196	0.006	10.800	0.007	6.551	0.006	3.813	0.010	44.04
L170B	11.019	0.006	10.326	0.006	5.627	0.005	2.163	0.006	44.25
L207A	11.431	0.007	11.075	0.007	7.303	0.008	4.907	0.025	43.70
L207B	11.410	0.006	11.143	0.007	7.284	0.008	4.909	0.018	43.68

Notes. 3.4 μm , 4.6 μm , 12 μm , and 22 μm Vega magnitudes of galaxies and log values of their 12 μm luminosity, mapped by WISE.

Table 28: Stellar velocity dispersions

Source	Stellar velocity dispersion ($\sigma \text{ km s}^{-1}$)			Uncertainty ($d\sigma \text{ km s}^{-1}$)		
	A	B	C	A	B	C
H011	285	-	NA	55	-	NA
L024	345	-	NA	84	-	NA
L084	62	177	NA	3	7	NA
L097	226	106	NA	46	66	NA
L115	251	221	200	29	62	120
L125	-	279	NA	-	62	NA
L127	151	314	-	50	100	-
L156	197	257	NA	32	39	NA
L170	156	195	NA	24	54	NA
L207	197	165	NA	32	20	NA

Notes. Stellar velocity dispersion of galaxies, estimated by fitting stellar templates to the galaxy spectra by using the pPXF fitting method. The uncertainties quoted are the 1σ values. 'NA' is used to denote 'not applicable', for the case of sources where there are just two galaxies. '-' represents galaxies for which we could not determine a value of the stellar velocity dispersion.

Table 29: Masses of the supermassive black holes

Source	$\log(M_{\text{SMBH}})$			Uncertainty		
	A	B	C	A	B	C
H011	8.772	7.012	NA	0.084	0.015	NA
L024	8.960	-	NA	0.106	-	NA
L084	5.963	7.895	NA	0.021	0.017	NA
L097	8.344	6.951	NA	0.088	0.270	NA
L115	8.538	8.303	8.121	0.050	0.122	0.260
L125	-	8.733	NA	-	0.096	NA
L127	7.603	8.951	-	0.144	0.138	-
L156	8.093	8.582	NA	0.070	0.066	NA
L170	7.662	8.072	NA	0.067	0.120	NA
L207	8.092	7.766	NA	0.003	0.002	NA

Notes. Log values of the masses of the central supermassive black holes and the uncertainty in their values. The uncertainties quoted are the 1σ values. 'NA' is used to denote 'not applicable', for the case of sources where there are just two galaxies. '-' represents galaxies for which we could not determine a value of the SMBH mass.

be from the extremely energetic AGN. If the source falls below the pure star-forming curve, the ionising field is soft and could arise from star-forming regions. If an object falls in the region between the two curves on the BPT diagram, the ionisation field could have contributions from an AGN as well as star-forming regions, and is therefore declared to be a composite or a transitioning object.

Article number, page 18 of 34

The AGN region of all three diagnostic diagrams can be further divided into two separate sub-regions, line ratios arising from the Seyfert type II sources and those ionised by low ionisation nuclear emission-line regions (LINERs). These lines are defined by Equations 10 and 11 as follows,

$$\log([\text{O III}]/\text{H}\beta) = 1.89 \log([\text{S II}]/\text{H}\alpha) + 0.76, \quad (10)$$

$$\log([\text{O III}]/\text{H}\beta) = 1.18 \log([\text{O I}]/\text{H}\alpha) + 1.30. \quad (11)$$

The topmost panel in Figure 5 shows the $[\text{O III}]\lambda 5007/\text{H}\beta$ vs. the $[\text{N II}]\lambda 6583/\text{H}\alpha$ plot for all of our nuclei. 13 out of 22 of our nuclei fall in the composite region on this plot. All of them show signs of previous interactions, with the presence of prominent tidal tails. The sources with low line ratios, L127 A, L097 A, and L156 B are hosted by face-on spiral galaxies. In the case of L127, especially, it is difficult to ascertain whether previous interactions have taken place. The source does not exhibit any overt signs of tidal interactions yet. The galaxies are close to each other in projection and redshift, though, so we might be looking at a system that is about to start interacting, with the first processes just starting. L127B and L127C look like there might be some interaction happening already. While L127 A sits below the purely star-forming line, L127 B straddles the line between the line distinguishing the star-forming region from the composite region. L127 C, which appears extremely blue in the optical SDSS image, meanwhile falls below the pure star-forming line, as well, but with a relatively higher $[\text{O III}]\lambda 5007/\text{H}\beta$ line ratio.

In the case of L097, the nucleus B, lies well inside the LINER region. Its $[\text{N II}]\lambda 6583$ emission line appears to be stronger than the $\text{H}\alpha$ recombination line in its spectrum, as seen in Figure A.6. The source appears to have reddish centres in the optical SDSS image and might have low amounts of gas to be ionised. Shocks could also be responsible for driving the line ratios that fall in the LINER region (e.g., (Farage et al. 2010)).

L156 certainly presents tidal tails and a seemingly chaotic environment. It is difficult to gauge whether there are two or three galaxies interacting with each other here. We have studied the nuclear regions of two, but not the third core that appears to the west of nucleus B. It would be interesting to study this and check whether it is really a part of the interaction or whether it is a foreground object. While the nucleus B has a low $[\text{O III}]\lambda 5007/\text{H}\beta$ line ratio and lies in the star-forming region of the BPT diagram, nucleus A seems to have sufficiently high line ratios to be a composite.

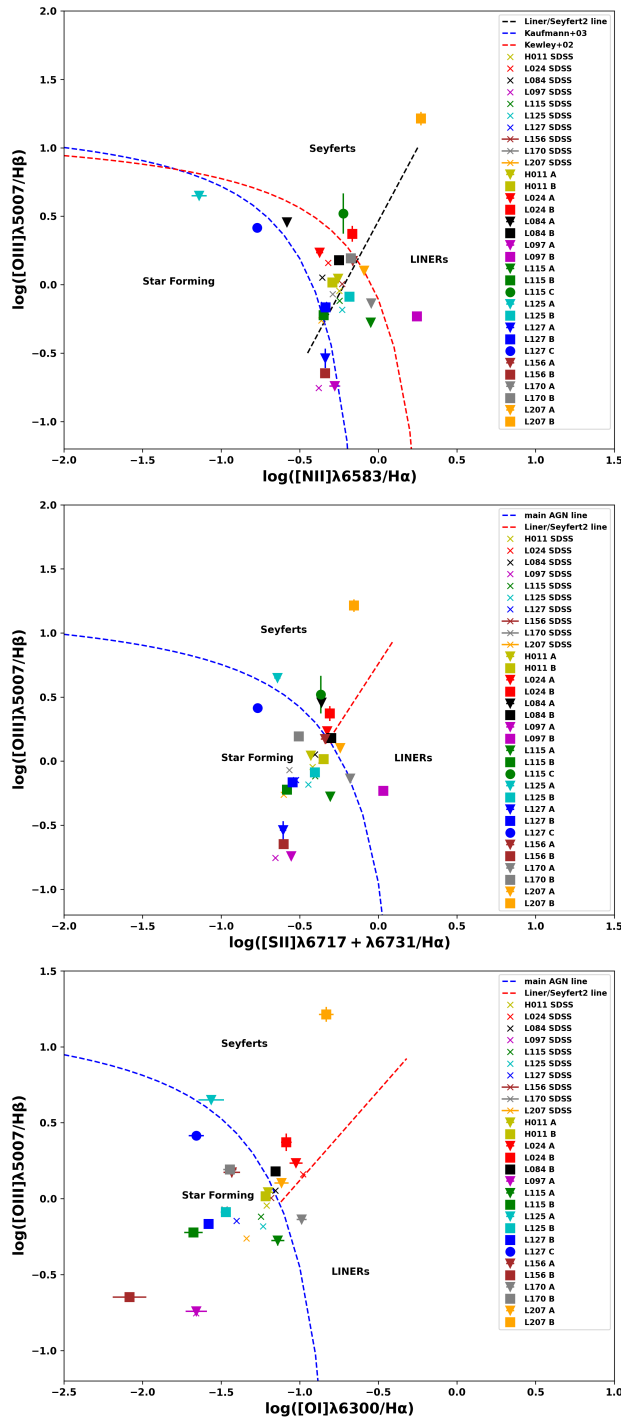


Fig. 5: Plots of $\log([\text{O III}]\lambda 5007/\text{H}\beta)$ vs $\log([\text{N II}]\lambda 6583/\text{H}\alpha)$, $\log([\text{O III}]\lambda 5007/\text{H}\beta)$ vs $\log([\text{S II}](\lambda 6717 + \lambda 6731)/\text{H}\alpha)$ and $\log([\text{O III}]\lambda 5007/\text{H}\beta)$ vs $\log([\text{O I}]\lambda 6300/\text{H}\alpha)$. Each colour marks a particular interacting pair or group. The inverted triangles represent the data points corresponding to nucleus A of a given source, whereas the squares represent the nucleus B, filled circles represent nucleus C, where applicable, and the crosses mark the data point derived from the SDSS spectrum of the source. The data points have been calculated for an aperture of 1 arcsec. The error bars have been derived from the 1σ standard uncertainty values.

The middle and the bottom panels of Figure 5 show the $[\text{O III}]\lambda 5007/\text{H}\beta$ vs. $[\text{S II}]\lambda 6716 + [\text{S II}]\lambda 6731/\text{H}\alpha$ and the $[\text{O III}]\lambda 5007/\text{H}\beta$ vs. the $[\text{O I}]\lambda 6300/\text{H}\alpha$ plots, respectively. The $[\text{O III}]\lambda 5007/\text{H}\beta$ vs. $[\text{S II}]\lambda 6716 + [\text{S II}]\lambda 6731/\text{H}\alpha$ plot is perhaps the more reliable of the two, since the $[\text{S II}]\lambda 6716$ and the $[\text{S II}]\lambda 6731$ emission lines are strong and well-defined for all of our sources. All except the data point associated with L125 A lie in regions similar to the ones in the $[\text{O III}]\lambda 5007/\text{H}\beta$ vs. the $[\text{N II}]\lambda 6583/\text{H}\alpha$ plot. This could be because the $[\text{N II}]\lambda 6583$ emission line is curiously stunted in the L125 A spectrum. The galaxy appears very blue in the optical SDSS image. Moreover, it is partially obscured by its companion, L125 B. As a result, it is uncertain whether we are actually probing the nuclear region of L125 A.

The $[\text{O III}]\lambda 5007/\text{H}\beta$ vs. the $[\text{O I}]\lambda 6300/\text{H}\alpha$ plot has fewer data points than the other two plots. This is because the $[\text{O I}]\lambda 6300$ emission line is not sufficiently well defined in the spectra of some of the sources. The data points on the plot correspond to the information gleaned from the $[\text{O III}]\lambda 5007/\text{H}\beta$ vs. $[\text{S II}]\lambda 6716 + [\text{S II}]\lambda 6731/\text{H}\alpha$ plot, though.

6.3. Diagnostic diagrams: trend with radio spectral indices

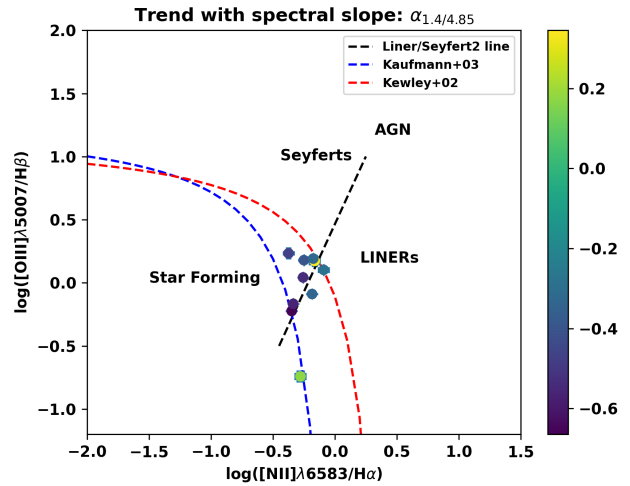


Fig. 6: Plot of $\log([\text{O III}]\lambda 5007/\text{H}\beta)$ vs $\log([\text{N II}]\lambda 6583/\text{H}\alpha)$ with a colour map based on the radio spectral indices of the sources derived from radio fluxes of the sources at 1.4 GHz and 4.85 GHz.

Figure 6 shows the $[\text{O III}]\lambda 5007/\text{H}\beta$ vs. the $[\text{N II}]\lambda 6583/\text{H}\alpha$ plot of the radio detected nuclei with the data points marked by the values of their corresponding spectral indices. Table 26 lists the spectral indices of all of the sources. These values are estimated using the radio fluxes at 1.4 GHz and 4.85 GHz. Almost all of the data points lie in the composite or transitioning region of the BPT diagram, except for the data points corresponding to L097A, which straddles the line separating the pure star-forming region, and L207 A, which straddles the line separating the composite region from the LINER region.

Focusing, for now, on the sources that fall in the composite region, we see that most of them, with the exception of L156A, have flat spectral indices. Flat radio spectral indices are associated with a mixture of optically thin and self-absorbed synchrotron emission, associated with radio jets and lobes, respectively. It is difficult to distinguish between the contribution of

AGN and star-formation activity towards the overall radio luminosity of a galaxy, since the spectral indices associated with synchrotron emission of supernova remnants are similar to those typical of the radio lobe+jet structures. However, since all of these sources have chaotic environments, typical for interactions of galaxies, there is a good possibility of contribution from an AGN. It would be interesting to see if the AGN is already in a 'switched-on' state before the first approach of galaxies or whether the first passage and the movement of gas and dust associated with it is responsible for the switching-on of the central SMBH.

Coming now to L156A and L097A, we see that L156A has the highest spectral index in the sample with a value of 0.3451, while L097A follows with a value of 0.1742. Both of these values fall well in the inverted spectral index range and could be indicative of AGN core components, emanating from self-absorbed synchrotron emission. In the case of L156A, this is reflected in the position of the nucleus on the diagnostic diagram, since it falls very close to the maximum starburst line in the composite region of the BPT diagram (see Figure 5a), and on the curve dividing the star-forming region from the AGN region on the $[\text{O III}]\lambda 5007/\text{H}\beta$ vs. $[\text{S II}]\lambda 6716 + [\text{S II}]\lambda 6731/\text{H}\alpha$ plot (see Figure 5b). L097A, though, has very low ionisation ratios, especially very low $[\text{O III}]\lambda 5007$ emission. A look at the spectrum of L097A shows that while the Hydrogen recombination line, $\text{H}\beta$, is quite strong, the $[\text{O III}]\lambda 4959$ and the $[\text{O III}]\lambda 5007$ emission lines are quite weak. The centre of L097A seems quite red, which might be indicative of extinction, or the source might have low amounts of ionised material.

The study of interacting galaxies based on the radio spectral index and the optical diagnostic diagrams has some interesting implications. Galaxies in the post-passage phase seem to have flat spectral indices, which are indicative of optically thin synchrotron structures and self-absorbed synchrotron emission, generally associated with the emission from supernova remnants. An increase in star-formation might be linked to the availability of material brought about by the increased movement of gas and dust as the galaxies start interacting with each other. In some cases, perhaps, as in the case of L156A, the AGN is already ignited when the galaxies approach each other, or perhaps the age of the interaction is such that the AGN was ignited by the passage and we observe it in the time succeeding the ignition. It could also be that the dusty environment around the centres of the interacting galaxies causes enough obscuration that the diagnostic diagrams are not very reliable, in which case taking into consideration the radio data of the galaxies could help to understand the nature of the nuclei.

6.4. Diagnostic diagrams: Eddington ratio trend

In order to understand the trend of our galaxies with respect to their Eddington ratio, $\eta \equiv L_{\text{Bol}}/L_{\text{Edd}}$ (Cavaliere & Padovani 1988), we estimated their bolometric luminosity, L_{Bol} , using the equation $L_{\text{Bol}} = k_{\text{Bol}} \times L_{5100\text{\AA}}$, where k_{Bol} is the bolometric correction factor given by $k_{\text{Bol}} = 40 \times [L_{5100\text{\AA}}/10^{42}\text{erg s}^{-1}]^{-0.2}$ (Netzer 2019), and Eddington luminosity, L_{Edd} , where $L_{\text{Edd}} = 4\pi GM_* m_p c / \sigma_T = 1.3 \times 10^{38} (M_*/M_\odot) \text{erg s}^{-1}$ (Lightman 1982). The logarithmic values of L_{Bol} , L_{Edd} , and η can be found in the Table 30. We find that all of the radio galaxies, irrespective of their spectral index, have $\log \eta$ values in the range [-4,-2], while the non-radio galaxies span the range [0, -3]. Netzer (2019) uses an optically thick, geometrically thin accretion disc to calculate the optical bolometric correction factor. In the case of H011B,

Table 30: Eddington ratios

Source	$\log(L_{\text{Edd}})$ erg s ⁻¹	$\delta \log(L_{\text{Edd}})$ erg s ⁻¹	$\log(L_{\text{Bol}})$ erg s ⁻¹	$\log(\delta L_{\text{Bol}})$ erg s ⁻¹	$\log \eta$	$\delta \log \eta$
H011A	46.886	0.004	44.074	0.025	-2.812	0.025
H011B	45.125	0.001	43.997	0.024	-1.128	0.024
L024A	47.074	0.005	44.559	0.018	-2.515	0.019
L024B	NA	NA	44.845	0.015	NA	NA
L084A	44.077	0.001	43.666	0.008	-0.411	0.008
L084B	46.009	0.001	43.804	0.033	-2.205	0.033
L097A	46.458	0.005	43.918	0.037	-2.540	0.037
L097B	45.065	0.017	43.374	0.016	-1.691	0.023
L115A	46.652	0.002	44.180	0.028	-2.472	0.028
L115B	46.417	0.006	43.813	0.060	-2.604	0.060
L115C	46.234	0.014	43.885	0.068	-2.349	0.069
L125A	NA	NA	43.449	0.115	NA	NA
L125B	46.847	0.005	44.119	0.016	-2.728	0.017
L127A	45.717	0.008	43.696	0.009	-2.021	0.012
L127B	47.065	0.007	43.835	0.008	-3.230	0.011
L127C	NA	NA	43.334	0.024	NA	NA
L156A	46.207	0.004	43.932	0.028	-2.275	0.028
L156B	46.696	0.003	44.188	0.023	-2.508	0.023
L170A	45.776	0.004	43.457	0.011	-2.319	0.012
L170B	46.186	0.006	43.911	0.032	-2.275	0.033
L207A	46.206	0.002	43.924	0.030	-2.282	0.030
L207B	45.880	0.001	44.030	0.031	-1.850	0.031

Notes. Log values of the Eddington luminosity, Bolometric luminosity, and the Eddington ratio of each galaxy. The uncertainties quoted are the 1σ values.

L084B, L170A, L170B, and L207B, the assumption of a standard thin accretion disc is applicable since they show broad components in their spectra, which are typically associated with standard thin discs (Czerny et al. 2004; Czerny & Hryniewicz 2011). In addition, there seems to be no significant trend in the values of Eddington ratios of radio detected and non-detected sources. Therefore, we conclude that all of our sources might, in principle, have standard discs or discs with mixed properties such that the thin disc transitions to ADAF in the inner regions for lower accretion rates due to the classical ADAF approach (i.e., the hot flow forms whenever it can, see Abramowicz et al. 1995; Honma 1996; Kato & Nakamura 1998) or the disc evaporation model (Liu et al. 1999; Różańska & Czerny 2000; Meyer-Hofmeister & Meyer 2003). In fact, changing-look AGN, which can be associated with the radiation-pressure instability operating in a radially narrow zone between the ADAF and the thin disc (Sniegowska et al. 2020), have the median Eddington ratios of ~ -2 (Panda & Śniegowska 2022). Standard thin accretion discs associated with lower accretion rates have been previously reported in, e.g., Bianchi et al. (2019), where a very broad $\text{H}\alpha$ component is found in the spectrum of NGC3137 and the inferred Eddington ratio for this source is $\log \eta \sim -4$.

Figure 7 shows the plot of the ionisation ratios, $\log([\text{O III}]\lambda 5007/\text{H}\beta)$, against the Eddington ratios, $\log \eta$, for the radio detected galaxies. The colour map is defined by using the values of the spectral slope of each of the source. We see that there is no significant trend in the distribution of the spectral indices, as well as Eddington ratios. However, a very weak trend of higher ionisation ratios corresponding to higher values of the Eddington ratio is visible.

This becomes clearer in Figure 8, which shows the BPT plot of the radio detected galaxies, with a colour map defined by the logarithmic values of the Eddington ratios.

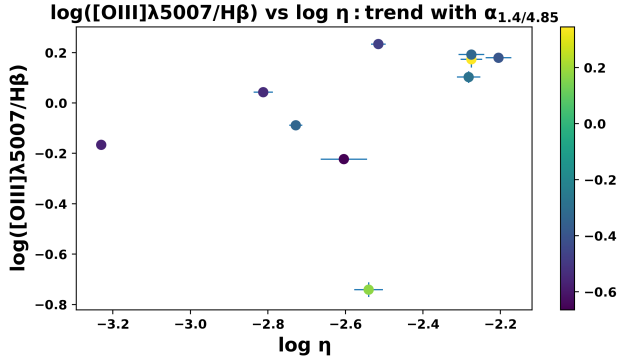


Fig. 7: Plot of $\log([\text{O III}]\lambda 5007/\text{H}\beta)$ vs $\log \eta$. The colour bar is defined by the value of the spectral index of the source.

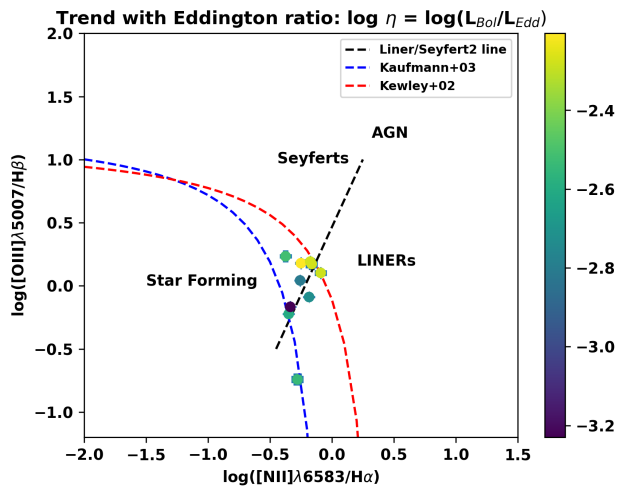


Fig. 8: Plot of $\log([\text{O III}]\lambda 5007/\text{H}\beta)$ vs $\log([\text{N II}]\lambda 6583/\text{H}\alpha)$ with a colour map based on the value of the Eddington ratio of each source.

6.5. Ionisation ratio vs. radio loudness parameter

Figure 9 is the plot of the line ratios $\log([\text{O III}]\lambda 5007/\text{H}\beta)$ vs radio loudness ($L_{1.4 \text{ GHz}}/L_{5100 \text{ \AA}} (LBT)$) parameters of all the radio galaxies. The red dots represent galaxies with inverted spectral indices and green dots indicate galaxies with flat spectral indices. H011A has the highest value of radio loudness at 22.342, with L115B being second highest at 8.048. L024A and L125B are the lowest at 1.420 and 1.566, respectively.

If we exclude, for now, H011A from our analysis, we are left with nine radio quiet galaxies. Three of these have flat spectral slopes, while six have inverted spectral slopes. Considering just the flat sources for now, we see that the ionisation ratio decreases with increasing radio loudness parameter, with the spectral slope steepening with increasing radio loudness parameter. The sources with inverted spectral slopes do not seem to follow a trend with the ionisation ratio and radio loudness parameter with respect to their spectral slope, but they do seem to cluster at the lower end of the radio loudness parameter axis.

Coming back to H011A now, it is the only galaxy with flux density ≥ 100 mJy in our sample. It also has the highest radio loudness parameter, $R_{1.4\text{GHz}/5100\text{\AA}}(LBT) \sim 22$, considering both LBT and SDSS data (see Table 26), and is the only radio loud

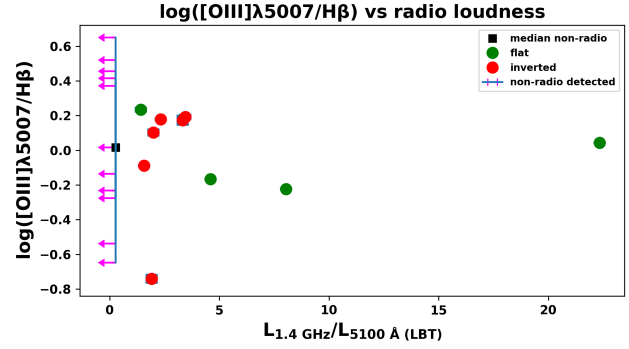


Fig. 9: Plot of $\log([\text{O III}]\lambda 5007/\text{H}\beta)$ vs radio loudness parameter ($L_{1.4 \text{ GHz}}/L_{5100 \text{ \AA}} (LBT)$). Green dots represent galaxies with flat radio spectral index ($-0.7 \leq \alpha_{1.4/4.85} \leq -0.4$), while red dots represent galaxies with inverted radio spectral index ($\alpha > -0.4$). The vertical blue line represents the median value of the radio loudness parameter for the non-radio detected galaxies from Table 31 and the magenta arrows indicate that this is the upper limit of the radio loudness at the $\log([\text{O III}]\lambda 5007/\text{H}\beta)$ values for each of the galaxies.

galaxy in our sample. Marecki et al. (2006) studied H011 using observations with MERLIN at 5 GHz, as a candidate for double-double or X-shaped structures. They refer to the source as TXS 1033+026, and present FIRST and MERLIN maps at 1.4 GHz and 5 GHz, respectively, along with an SDSS image of the source. They infer that the most likely scenario to explain the morphology of the sources is a rapid repositioning of the central engine. Such rapid repositioning of the central engine could be most likely caused by a merger. They present the following interpretations for the radio maps. In the case of the FIRST map, there is a core that coincides with H011A in the optical domain, and a dominant lobe to the southeast along with either a jet pointing to a second lobe almost 3.5 times away from the core than the southeastern lobe or the protrusion to the northwest itself being the lobe. At 5 GHz, a core and a jet pointing in the northeast direction can be seen clearly, along with shorter protrusions to the southeast and northwest, which could be the indicators or 'remains' of the flux from the two lobes, or the lobe and jet, visible in the FIRST map. The jet at 5 GHz is at an angle of almost 80° relative to the direction of the southeastern lobe at 1.4 GHz¹².

Figure 9 can be explained using a simple physical source model as depicted in Figure 10. Here we show a possible arrangement of different source components. The radio components are depicted by black contour lines. Radio continuum radiation is indicated by blue arrows, while the ionising optical line emission is indicated by red arrows. The excitation and radio strength parameters are largely independent of each other. The inverted radio flux is due to a compact optically thick jet component typically located (due to optical depth effects) a bit upstream from the ionising nucleus (red circle). Excess flat to steep spectrum radio flux density is due to contributions from extended source components like a jet. Steep spectrum contributions could be due to radio lobes or non-thermal supernova remnant emission, as well.

In Figure 11 we make use of the fact that the excitation and radio strength parameters are assumed to be independent of each other, and show a figure rather similar to Figure 9 but the relative contributions of ionising and/or radio detected components

¹² See Figure 2 in Marecki et al. (2006).

Table 31: Radio loudness parameters and ionisation ratios

ID (*-non-radio)	$\log(L_{5100})$ (SDSS)	$\log(L_{5100})$ (LBT)	$\log(L_{1.4\text{GHz}})$	$R_{1.4/5100}$ (SDSS)	$R_{1.4/5100}$ (LBT)	$\log([\text{O III}]\lambda 5007/\text{H}\beta)$
H011A	39.461	38.883	40.232	5.895	22.343	0.04279
L024A	39.375	39.489	39.642	1.847	1.420	0.23394
L084B	39.116	38.545	38.912	0.625	2.331	0.17938
L097A	39.453	38.688	38.971	0.329	1.919	-0.74123
L115B	39.295	38.556	39.462	1.470	8.048	-0.22287
L125B	39.330	38.937	39.134	0.637	1.566	-0.08857
L127B	39.115	38.584	39.247	1.355	4.601	-0.16620
L156A	39.244	38.705	39.228	0.963	3.333	0.17341
L170B	39.418	38.678	39.216	0.627	3.448	0.19210
median				0.963	3.333	0.04279
mean				1.528	5.445	
H011B*	NA	38.786	<39.176	NA	<2.780	0.01566
L024B*	NA	39.396	<38.623	NA	<0.173	0.37143
L084A*	38.871	38.373	<37.903	<0.109	<0.343	0.45647
L097B*	38.567	38.007	<38.363	<0.633	<2.300	-0.23130
L115A	NA	39.015	~38.948	NA	~0.857	-0.27613
L115C*	39.088	38.646	<38.431	<0.163	<0.451	0.51952
L125A*	NA	38.101	<38.079	NA	<0.792	0.65003
L127A*	38.941	38.41	<38.208	<0.114	<0.389	-0.53865
L127C*	38.431	37.957	<38.204	<0.371	<1.104	0.41516
L156B*	NA	39.025	<38.751	NA	<0.532	-0.64749
L170A	38.583	38.111	~38.965	<2.410	~7.147	-0.13643
median				0.267	0.792	0.01566
mean				0.633	1.533	
				$R_{\text{LBT}}/R_{\text{SDSS}}$		
median				3.46		
mean				3.56		

Notes. Continuum luminosities at 5100 Å corresponding to the SDSS and LBT spectra, radio luminosity at 1.4 GHz, radio loudness parameters estimated using the SDSS and LBT continuum luminosities, and the $\log([\text{O III}]\lambda 5007/\text{H}\beta)$ ionisation ratios for all of the galaxies in our sample. 'NA' is used as the placeholder for galaxies that do not have a published SDSS spectrum. Luminosities are quoted in units of ergs s^{-1} .

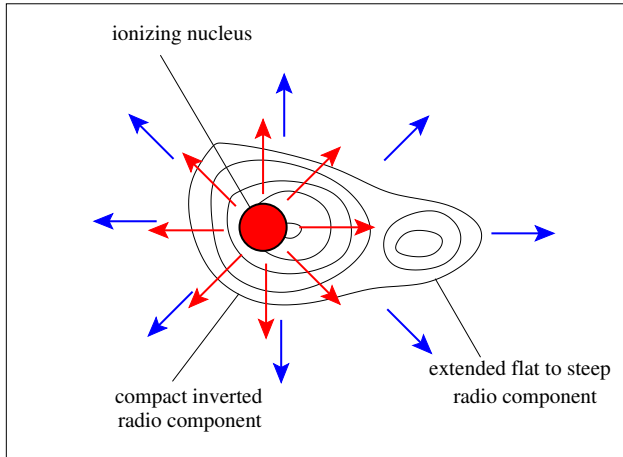


Fig. 10: Underlying physical source model of our interpretation. A detailed description is given in Section 6.5.

are shown continuously in heat colors and black contours. The relative contributions were derived from the median and the approximate extent of the region covered by data shown in Figure 9. The median position of the radio detected sources is indicated by a black dot. An upper limit of the median position of the radio

weak/non-detected sources is shown by a red hexagram (see also data in the Table 31). The trend indicated here is that the higher ionising sources are also associated with radio bright emission, i.e., high values of R . However, the medians also show that the ionising radiation of the radio detected and weak sources are rather similar, demonstrating that the ionising radiation as such cannot be the only reason for the radio emission of the sources.

We can compare our LBT source sample with SDSS reference data as presented by Vitale et al. (2015) and Zajaček et al. (2019). For the radio detected sources presented there the corresponding scatter plot of ionisation ratio versus radio loudness is shown in Figure 12. The median position of the distribution is compatible with the median distribution found in our LBT sub-sample of these sources.

In Figure 13 we show the same data as in Figure 12 but collapsed onto the R -parameter axis. We plot the square-root of the number of sources against the radio loudness parameter using a bin-size of 0.5. The red line shows that there is an excess of radio loud sources similar to what we find in our sub-sample, albeit at a lower magnitude. The radio loud sources well above the median position in R are highlighted here by the hashed area. The lower magnitude of the excess is mainly due to the fact that the optical continuum luminosity the radio luminosity is referenced to, is taken in a larger aperture for the SDSS data (approximately 3'') in comparison to the LBT slit width (1''). In the SDSS data, the optical continuum represents the luminosity of the bulge or even the inner section of the host galaxy. In our LBT data we

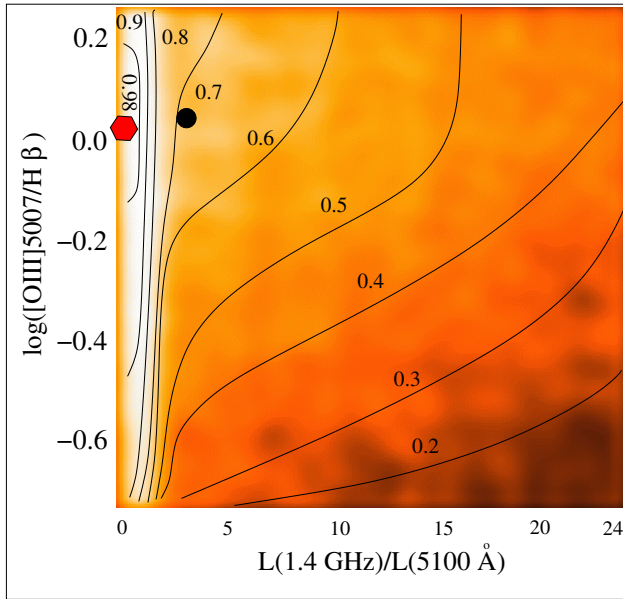


Fig. 11: Same as Figure 9 but relative contributions of ionising and/or radio detected components in heat colours and black contours. The radio loudness parameter is estimated using the 5100 Å luminosity from LBT spectra.

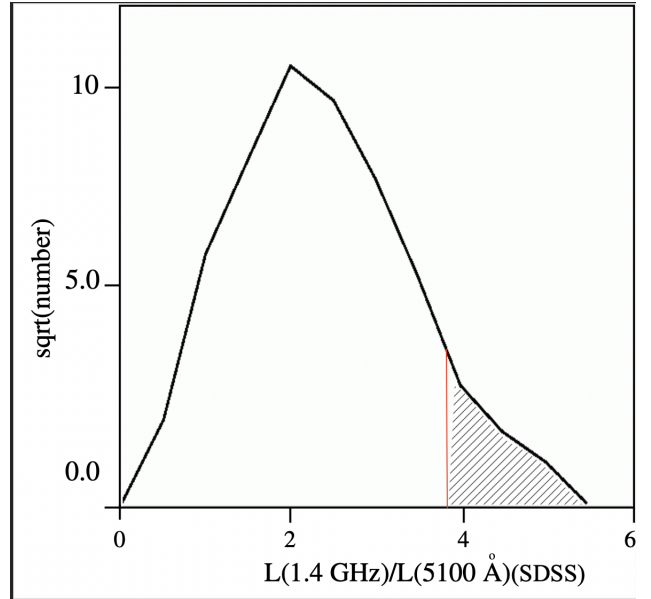


Fig. 13: Scatter diagram shown in Figure 12 but collapsed onto the radio loudness axis (see text in Section 6.5). The radio loudness parameter is estimated using the 5100 Å luminosity from SDSS spectra.

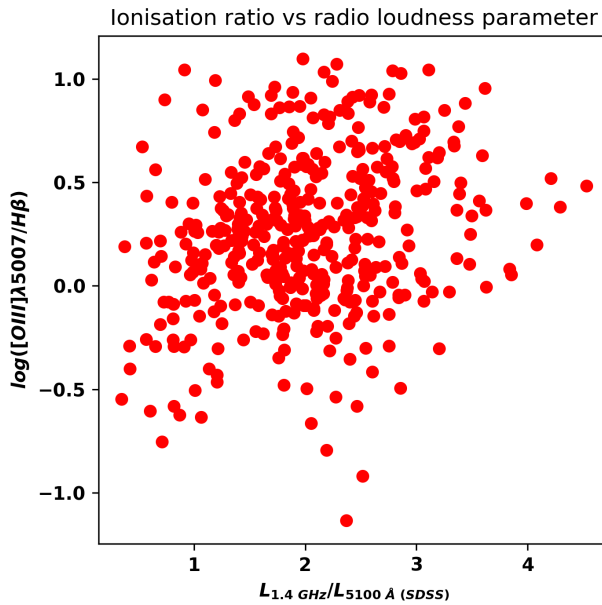


Fig. 12: Scatter plot of the reference radio detected source data presented by Vitale et al. (2015) and Zajaček et al. (2019). The radio loudness parameter is estimated using the 5100 Å luminosity from SDSS spectra.

reference the radio luminosity to the nuclear optical continuum within the slit. In fact, multiplying the ratio between the R -values of the radio detected sources to the corresponding limits for the radio weak sources with the upper limit of the excess shown in the distribution in Figure 13 we obtain a value of about 19. This

is in good agreement with the highest R -value of about 22 as obtained for our SDSS-FIRST-LBT sample.

6.6. Correlations with black hole mass

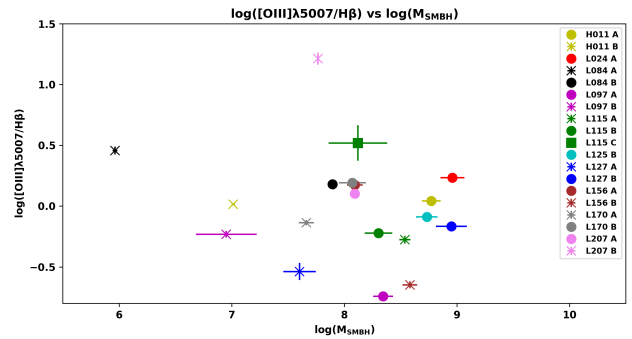


Fig. 14: Plot of the ionisation ratio of each galactic nuclear region versus the mass of the central SMBH. The crosses and square represent the masses of the non-radio detected galaxies, while the dots represent the radio detected galaxies. Each interacting pair is represented by a specific colour, as described in the legend of the plot.

Next, we looked at any possible correlation between the ionisation ratio of the nuclear regions and the mass of the central SMBHs. Figure 14 shows a scatter plot of the ionisation ratio, represented by $\log([O\text{III}]\lambda 5007/H\beta)$, versus the logarithmic values of the masses of the central SMBHs. We see no specific correlation between the ionisation ratio and masses of the SMBHs. However, we note that for all of the interacting pairs, with the exception of L156 and L115, it is the galaxy that hosts the more massive SMBH that is associated with the radio detection at 1.4 GHz. In the cases where both of the galaxies are detected

at 1.4 GHz, the galaxy with a more massive SMBH has a higher flux density.

This correlation could be attributed to a more massive circum-nuclear disc being associated with the more massive SMBH, thus providing more material for star-formation and ultimately, radio emission. Additionally, the more massive SMBH could cause stronger emission in the radio regime. It is interesting to note that the values of the radio loudness parameters of the radio detected sources do not seem to give rise to any correlation in this figure. This can be seen clearly in Figure 15, which shows the plot of the radio loudness parameter, estimated using the 5100 Å continuum luminosity from the LBT spectra, against the mass of the central SMBH for all of the radio detected galaxies. We see that there is no obvious correlation between the two properties. It could be related to the stage of the galaxy interaction, with later stages of the collision being associated with stronger radio emission from the AGN, while the earlier phases have weaker radio emission.

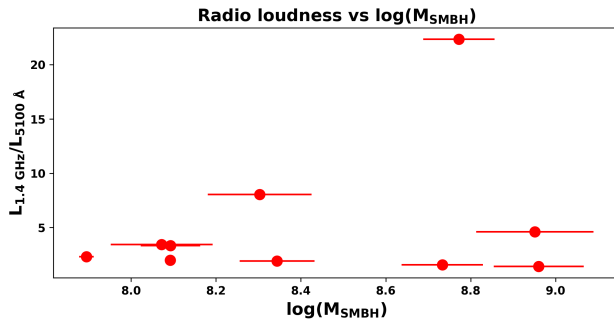


Fig. 15: Plot of the radio loudness parameter of each galactic nuclear region versus the mass of the central SMBH.

6.7. Correlation with mid-infrared luminosity

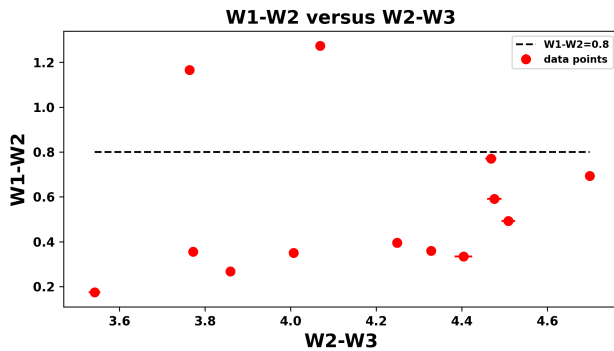


Fig. 16: W1-W2 versus W2-W3 colour-colour diagram based on the WISE magnitudes at 3.4 μm, 4.6 μm, and 12 μm. The red dots are the data points for the galaxies in our sample. The dashed black line shows the $W1 - W2 > 0.8$ criterion proposed by Stern et al. (2012).

Finally, we look at the MIR properties of the galaxies in our sample, and study their behaviour with respect to their radio properties.

In order to understand the nature of the MIR emission of the galaxies in our sample, we first looked at their $W2 - W3$ colour,

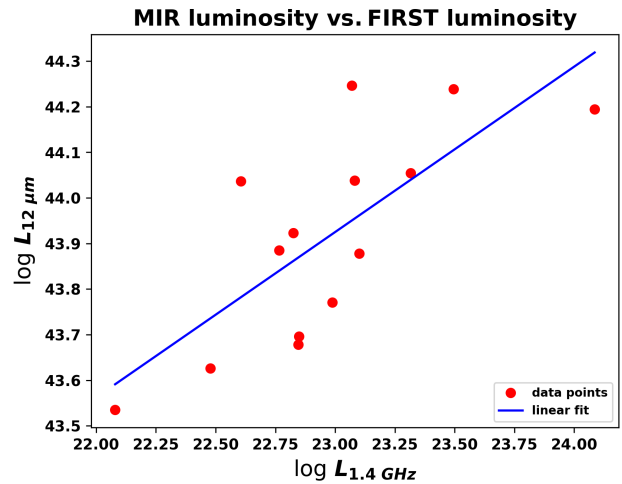


Fig. 17: Plot of log values of the 12 μm luminosity, in erg s^{-1} units, of the galaxies detected by the WISE W3 band versus the log values of the 1.4 GHz luminosity, in W Hz^{-1} units, observed in the FIRST survey. The red dots are the data points for the galaxies in our sample. The solid blue line shows the linear regression fit to the data, described by $L_{12\mu\text{m}} = 0.36L_{1.4\text{ GHz}} + 35.58$.

since it is sensitive to the contribution from star-formation. Figure 16 shows the colour-colour plot of $W1 - W2$ versus $W2 - W3$. The $W2 - W3$ values of all of the detected galaxies fall in the range [3.5-4.8], while the $W1 - W2$ values lie in the range [0.1-1.3]. Herpich et al. (2016) found that the colour $W2 - W3 = 2.5$ is the best divisor between actively star-forming galaxies and retired galaxies. Galaxies whose star-formation has stopped for a long period of time are classified as retired. Additionally, Stern et al. (2012) showed that the criterion $W1 - W2 > 0.8$ can be used to identify both unobscured and obscured AGNs. Considering the criteria proposed by Herpich et al. (2016) and Stern et al. (2012) to select AGNs based on the MIR emission, we see that while all of our galaxies have $W2 - W3 > 2.5$, and are thus likely actively forming stars, only two of them satisfy $W1 - W2 > 0.8$, namely H011A and L084B. L084B shows broad $H\alpha$ emission line in its optical nuclear spectrum and as such, already qualifies as a prospective Seyfert 1 galaxy. H011 shows only narrow emission lines in its optical nuclear spectrum and could be a Seyfert 2 galaxy. Alternatively, it could be that the MIR emission is actually associated with H011B, which also has a broad $H\alpha$ emission line in its optical nuclear spectrum. H011B is separated from H011A by $\sim 2.4''$, while the angular resolution of WISE is 6.1'', 6.4'', 6.5'', and 12'' at 3.4 μm, 4.6 μm, 12 μm, and 22 μm, respectively. The rest of our galaxies seem to lie in the region corresponding to contributions from both star-formation and AGN, including L170B and L207B, both of which have broad $H\alpha$ emission lines in their nuclear spectra.

Further, we plot the 12 μm luminosity against the 1.4 GHz luminosity from FIRST data of all WISE-detected galaxies to check for any trend (Figure 17). We plot the linear regression fitted to this data in a solid blue line. The fit has a positive gradient of 0.36 and an intercept of 35.58. Comparing our plot with the left panel of Figure 3 in Rosario et al. (2013), we see that our galaxies fall in Branch A, populated by Seyferts and star-forming galaxies, as opposed to Branch B, which is mostly populated by LINERs.

7. Conclusions and summary

In this paper, we presented the optical spectra of a sample of eight pairs and two triplets of interacting galaxies that have been selected from an SDSS-FIRST parent sample studied in Vitale et al. (2015) and Zajaček et al. (2019). We observed a total of 22 galaxies using MODS at the LBT, focusing on their central regions. We used continuum data at 4.85 GHz from the Effelsberg telescope as well as FIRST data at 1.4 GHz to estimate spectral slopes and radio loudness parameters for all of the radio-detected sources. Additionally, we used WISE MIR images at 3.4 μm , 4.6 μm , and 12 μm of the 14 galaxies detected at these wavelengths to plot a $W1 - W2$ versus $W2 - W3$ colour-colour diagram and a $L_{\mu\text{m}}$ versus $L_{1.4 \text{ GHz}}$ plot.

The properties of each pair/triplet are briefly summarised below:

1. H011/CGCG 1033.9+0237: The galaxy pair H011 has strongly ionised nuclear spectra. While H011A shows narrow emission lines only, H011B has both broad and narrow components. The pair has the shortest projected pair separation in our sample. Both of the nuclei lie close to each other in the composite region of the BPT diagram. The FIRST radio emission encapsulates both of the galaxies but is centred closest to the H011A nucleus. H011 is the only galaxy pair in our sample with FIRST flux greater than 100 mJy and can be classified as hosting an AGN on the basis of its $W1 - W2$ colour.
2. L024/SDSS J121346.07+024841.4: The galaxy pair L024 shows prominent emission lines in the spectra of both of the nuclear regions. The FIRST radio emission encapsulates both of the galaxies but is centred closest to the L024A nucleus. L024A has two narrow components corresponding to the $H\alpha$ emission line. L024B shows a blue wing in its $[\text{O III}]\lambda 5007$ emission line. L024A lies in the composite region of the BPT diagram while L024B falls in the Seyfert region.
3. L084/ 2MASX J09054734+3747374: The galaxy pair L084 consists of a blue galaxy L084A in the process of interacting with a red galaxy L084B. The FIRST radio emission is associated with L084B. L084A has a continuum that is quasar, with a blue bump like feature around 4100 Å, along with emission lines. L084B has a flat continuum spectrum, with prominent emission lines. Both $[\text{O III}]\lambda 4959$ and $[\text{O III}]\lambda 5007$ emission lines have blue wings and there is broad $H\alpha$ component present in the case of L084B. L084B is the only other galaxy other than H011 that can be classified as hosting an AGN on the basis of its $W1 - W2$ colour. Both of the nuclear regions lie in the composite region of the BPT diagram.
4. L097/ 2MASX J11262822+5447138: The galaxy pair L097 is an interacting system consisting of a spiral galaxy L097A and a spheroidal galaxy L097B. L097A is associated with FIRST radio emission. The spectrum of the nuclear region associated with L097A has a flat continuum with prominent emission lines but very weak $[\text{O III}]\lambda 5007$ emission, while L097B has a noisier spectrum. Consequently, L097A lies in the star-forming region of the BPT diagram, while L097B lies well within the LINER region.
5. L115/ UGC 04653: L115 is a triplet consisting of galaxies L115A, L115B, and L115C in the process of interaction with each other. L115B is detected at 1.4 GHz in the FIRST survey. The spectra of the nuclear regions of L115A and L115B have flat continua with prominent emission lines, while the spectrum of the L115C nucleus is noisy and reddened with weak emission lines. L115A and L115B fall in the composite region of the BPT diagram, while L115C lies in the Seyfert region.
6. L125/ 2MASX J09170001+0926486: The galaxy pair L125 consists of a blue galaxy L125A and the red spiral galaxy L125B. The FIRST radio emission can be associated with L125B. L125A shows a very flat continuum, while the continuum of L125B shows some reddening. Both the nuclear spectra have prominent emission lines, and show Balmer series lines up to H8 for L125A and H δ for L125B. Both $[\text{O III}]\lambda 4959$ and $[\text{O III}]\lambda 5007$ emission lines display blue wings in the nuclear spectrum of L125B. L125A falls in the star forming region in the BPT diagram, while L125B lies in the composite region.
7. L127/ CGCG 063-051: The triplet L127 is made up of a spiral L127A, a spheroidal galaxy L127B, and a blue irregular galaxy L127C interacting with each other. L127B is detected at 1.4 GHz in the FIRST survey. The spectrum of the nuclear region of L127A shows reddening and has weak $[\text{O III}]\lambda 5007$ emission. The nuclear spectra of L127B and L127C have very flat continua. The emission lines in the red part of the spectrum are especially strong for L127B, while the blue band is more prominent in the case of L127C. L127A and L127C lie in the star forming region in the BPT diagram, while L127B falls in the composite region.
8. L156/ UGC 04947: L156 is a galaxy pair consisting of a spiral galaxy L156A and a spheroidal galaxy L156B. L156A is visible at 1.4 GHz in the FIRST survey. The nuclear spectrum of L156A displays some reddening along with prominent emission lines, while the nuclear spectrum of L156B is flat with prominent emission lines in the red band but weak $[\text{O III}]\lambda 5007$ emission. Both $[\text{O III}]\lambda 4959$ and $[\text{O III}]\lambda 5007$ emission lines display blue wings in the nuclear spectrum of L156A. Moreover, the $H\alpha$ emission lines of both L156A and L156B show two narrow components each. L156A lies in the composite region and L156B in the star-forming region of the BPT diagram.
9. L170/ MRK 0848: The galaxy pair L170 is made up of two spiral galaxies. Both of the galaxies are visible in the FIRST survey, but L170B has a more prominent radio emission. The nuclear spectrum of L170A shows some reddening and prominent emission lines, along with a broad $H\alpha$ emission line. L170B displays a flat continuum in its nuclear spectrum and has prominent emission lines. L170B has the most prominent $[\text{S III}]\lambda 9069$ and the $[\text{S III}]\lambda 9531$ emission lines in our sample. It also displays a broad $H\alpha$ component and has blue wings in both $[\text{O III}]\lambda 4959$ and $[\text{O III}]\lambda 5007$ emission lines. Both L170A and L170B lie in the composite region on the BPT diagram.
10. L207/ UGC 04090: L207 is a galaxy pair made up of two spiral galaxies. While both L207A and L207B are detected at 1.4 GHz by the FIRST radio survey, L207A has the stronger radio emission of the two. Both L207A and L207B show reddening in their nuclear spectra and display absorption lines, but only L207B has a broad $H\alpha$ component. L207A straddles the line between composite and LINER regions on the BPT diagram, while L207B lies in the Seyfert region of the plot.

The galaxies in this sample appear to be at various stages of interaction but none of them are yet close to merging, except for H011, which has the shortest projected pair separation. H011 has the highest flux density in the sample at 1.4 GHz and has been detected at 4.85 GHz as well as 10.45 GHz by the Effelsberg radio telescope. This could be attributed to various reasons, one amongst them hosting an AGN. The presence of broad

line components in the spectrum of one of the two nuclei further strengthens the connection with an AGN. Whether this AGN was triggered by the process of interaction is an interesting question to consider, but this is yet to be determined.

All interactions do not necessarily generate a radio loud AGN (Chiaberge et al. 2015). It is, therefore, difficult to ascertain whether the other sources in the sample would have stronger radio emission at later stages of interaction. Timescales would also likely play an important role in the observation of radio activity, since the radio loud phase of an AGN is most probably significantly shorter than the lifetime of an interaction (Chiaberge et al. 2015).

Our main findings are listed below:

1. By plotting diagnostic diagrams using low ionisation emission line ratios, we see that while the entire sample of galaxies covers all the regions on the plot, almost all of the galactic nuclei associated with radio emission at 1.4 GHz and 4.85 GHz fall in the composite or transitioning region. This implies that the ionising field in the nuclear regions probed in these galaxies might arise from a combination of star-formation and an AGN.
2. The spectral slope, $\alpha_{1.4/4.85}$, of all of the radio detected galaxies is ≥ -0.7 , which can be classified as either flat or inverted, according to the convention adopted in this paper, as described in Section 4. This implies that the radio emission arises either from self-absorbed cores and jets. Star-forming regions are a less likely origin of the radiation, since they are likely to be fainter than nuclear emission and dominated by thin steep spectrum synchrotron emission. At the redshifts covered by the sample, flat spectrum Bremsstrahlung is much fainter than the overall non-thermal emission and can be excluded.
3. All of the radio detected galaxies host SMBHs of mass in the range $10^7 - 10^8 M_{\odot}$, which is the typical BH mass for Seyferts. The galaxy with the highest radio loudness parameter in a pair is almost always associated with the galaxy which hosts the more massive central SMBH.
4. All of the radio detected galaxies have an Eddington ratio, $\log \eta$ in the range $[-4, -2]$, while the Eddington ratios of non-radio detected galaxies span the range $[0, -3]$, which is indicative of the transition from the standard optically thick, geometrically thin accretion disc to the ADAF regime in the inner regions for lower accretion rates.
5. MIR data of the galaxies detected by WISE suggests that while most of the galaxies have dominant contribution to their emission at this wavelength from star-formation, at least two galaxies, i.e. H011A/B and L084B, have significant contribution from an AGN.

In conclusion, the radio detected galaxies in our sample display the trend of being classified as composite at optical wavelengths and generally host the higher mass SMBH in their centre, as compared to their companions. The galaxies have flat or inverted spectral slopes. We see no other specific trend with the spectral index, radio loudness parameter, or the Eddington ratio.

Acknowledgements. Study of the conditions for star formation in nearby AGN and QSOs is carried out within the Collaborative Research Centre 956, sub-project [A02], funded by the Deutsche Forschungsgemeinschaft (DFG) – project ID 184018867.

We made use of the Mods CCD Reduction package to reduce this data. ModsCCDRed was developed for the MODS1 and MODS2 instruments at the Large Binocular Telescope Observatory, which were built with major support provided by grants from the U.S. National Science Foundation’s Division of Astronomical Sciences Advanced Technologies and Instrumentation (AST-9987045), the NSF/NOAO TSIP Program, and matching funds provided by the Ohio State

University Office of Research and the Ohio Board of Regents. Additional support for modsCCDRed was provided by NSF Grant AST-1108693. We made use of the NASA/IPAC Extragalactic Database (NED) and of the HyperLeda database.

M.Z. acknowledges the financial support by the GAČR-LA grant No. GF22-04053L.

M.Y. acknowledges support via research grants from the Knut and Alice Wallenberg Foundation.

References

- Abramowicz, M. A., Chen, X., Kato, S., Lasota, J.-P., & Regev, O. 1995, *ApJ*, 438, L37
- Bae, H.-J. & Woo, J.-H. 2016, *ApJ*, 828, 97
- Baldry, I. K., Glazebrook, K., Brinkmann, J., et al. 2004, *ApJ*, 600, 681
- Baldwin, J. A., Phillips, M. M., & Terlevich, R. 1981, *PASP*, 93, 5
- Balogh, M. L., Baldry, I. K., Nichol, R., et al. 2004, *ApJ*, 615, L101
- Barnes, J. E. & Hernquist, L. 1996, *ApJ*, 471, 115
- Becker, R. H., White, R. L., & Helfand, D. J. 1995, *ApJ*, 450, 559
- Beifiori, A., Courteau, S., Corsini, E. M., & Zhu, Y. 2012, *MNRAS*, 419, 2497
- Benson, A. J., Bower, R. G., Frenk, C. S., et al. 2003, *ApJ*, 599, 38
- Best, P. N. & Heckman, T. M. 2012, *MNRAS*, 421, 1569
- Bianchi, S., Antonucci, R., Capetti, A., et al. 2019, *MNRAS*, 488, L1
- Bower, R. G., Benson, A. J., Malbon, R., et al. 2006, *MNRAS*, 370, 645
- Cappellari, M. 2017, *MNRAS*, 466, 798
- Cappellari, M. & Emsellem, E. 2004, *PASP*, 116, 138
- Cavaliere, A. & Padovani, P. 1988, *ApJ*, 333, L33
- Chiaberge, M., Gilli, R., Lotz, J. M., & Norman, C. 2015, *ApJ*, 806, 147
- Cicone, C., Maiolino, R., & Marconi, A. 2016, *A&A*, 588, A41
- Cluver, M. E., Jarrett, T. H., Hopkins, A. M., et al. 2014, *ApJ*, 782, 90
- Combes, F. 2014, *A&A*, 571, A82
- Condon, J. J., O’Dell, S. L., Puschell, J. J., & Stein, W. A. 1980, *Nature*, 283, 357
- Courteau, S., de Jong, R. S., & Broeils, A. H. 1996, *ApJ*, 457, L73
- Croton, D. J., Springel, V., White, S. D. M., et al. 2006, *MNRAS*, 365, 11
- Czerny, B. & Hryniewicz, K. 2011, *A&A*, 525, L8
- Czerny, B., Rózańska, A., & Kuraszek, J. 2004, *A&A*, 428, 39
- da Cunha, E., Charlot, S., & Elbaz, D. 2008, *MNRAS*, 388, 1595
- Desert, F. X., Boulanger, F., & Puget, J. L. 1990, *A&A*, 237, 215
- Di Matteo, T., Springel, V., & Hernquist, L. 2005, *Nature*, 433, 604
- Draine, B. T. & Li, A. 2001, *ApJ*, 551, 807
- Draine, B. T. & Li, A. 2007, *ApJ*, 657, 810
- Duric, N., Bourneuf, E., & Gregory, P. C. 1988, *AJ*, 96, 81
- Eckart, A., Witzel, A., Biermann, P., et al. 1986, *A&A*, 168, 17
- Ellison, S. L., Patton, D. R., & Hickox, R. C. 2015, *MNRAS*, 451, L35
- Faber, S. M., Willmer, C. N. A., Wolf, C., et al. 2007, *ApJ*, 665, 265
- Falcón-Barroso, J., Sánchez-Blázquez, P., Vazdekis, A., et al. 2011, *A&A*, 532, A95
- Farage, C. L., McGregor, P. J., Dopita, M. A., & Bicknell, G. V. 2010, *ApJ*, 724, 267
- Ferrarese, L. & Merritt, D. 2000, *ApJ*, 539, L9
- Ferrarese, L., Pogge, R. W., Peterson, B. M., et al. 2001, *ApJ*, 555, L79
- Gaibler, V., Khochfar, S., Krause, M., & Silk, J. 2012, *MNRAS*, 425, 438
- Gebhardt, K., Bender, R., Bower, G., et al. 2000, *ApJ*, 539, L13
- Gordon, Y. A., Pimbblet, K. A., Kaviraj, S., et al. 2019, *ApJ*, 878, 88
- Gott, J. R., I. & Rees, M. J. 1975, *A&A*, 45, 365
- Graham, A. W. 2007, *MNRAS*, 379, 711
- Greene, J. E. & Ho, L. C. 2005, *ApJ*, 630, 122
- Groves, B. & Kewley, L. 2008, in *Astronomical Society of the Pacific Conference Series*, Vol. 390, *Pathways Through an Eclectic Universe*, ed. J. H. Knapen, T. J. Mahoney, & A. Vazdekis, 283
- Groves, B., Krause, O., Sandstrom, K., et al. 2012, *MNRAS*, 426, 892
- Gültekin, K., Richstone, D. O., Gebhardt, K., et al. 2009, *ApJ*, 698, 198
- Gürkan, G., Hardcastle, M. J., Best, P. N., et al. 2019, *A&A*, 622, A11
- Hardcastle, M. J. & Croston, J. H. 2020, *New A Rev.*, 88, 101539
- Hardcastle, M. J., Evans, D. A., & Croston, J. H. 2007, *MNRAS*, 376, 1849
- Häring, N. & Rix, H.-W. 2004, *ApJ*, 604, L89
- Harrison, C. M., Alexander, D. M., Mullaney, J. R., & Swinbank, A. M. 2014, *MNRAS*, 441, 3306
- Heckman, T. M. & Kauffmann, G. 2006, *New A Rev.*, 50, 677
- Heckman, T. M., Kauffmann, G., Brinchmann, J., et al. 2004, *ApJ*, 613, 109
- Heckman, T. M., Miley, G. K., van Breugel, W. J. M., & Butcher, H. R. 1981, *ApJ*, 247, 403
- Herpich, F., Mateus, A., Stasińska, G., Cid Fernandes, R., & Vale Asari, N. 2016, *MNRAS*, 462, 1826
- Hickox, R. C., Jones, C., Forman, W. R., et al. 2009, *ApJ*, 696, 891
- Honma, F. 1996, *PASJ*, 48, 77

- Ichimaru, S. 1977, *ApJ*, 214, 840
- Ishibashi, W. & Fabian, A. C. 2012, *MNRAS*, 427, 2998
- Ivezic, Ž., Menou, K., Knapp, G. R., et al. 2002, *AJ*, 124, 2364
- Jarrett, T. H., Cohen, M., Masci, F., et al. 2011, *ApJ*, 735, 112
- Kakkad, D., Mainieri, V., Padovani, P., et al. 2016, *A&A*, 592, A148
- Kato, S. & Nakamura, K. E. 1998, *PASJ*, 50, 559
- Kauffmann, G., Heckman, T. M., Tremonti, C., et al. 2003a, *MNRAS*, 346, 1055
- Kauffmann, G., Heckman, T. M., White, S. D. M., et al. 2003b, *MNRAS*, 341, 54
- Kaviraj, S., Kirkby, L. A., Silk, J., & Sarzi, M. 2007, *MNRAS*, 382, 960
- Kellermann, K. I., Sramek, R., Schmidt, M., Shaffer, D. B., & Green, R. 1989, *AJ*, 98, 1195
- Kewley, L. J., Dopita, M. A., Sutherland, R. S., Heisler, C. A., & Trevena, J. 2001, *ApJ*, 556, 121
- Kewley, L. J., Nicholls, D. C., & Sutherland, R. S. 2019, *ARA&A*, 57, 511
- Khalatyan, A., Cattaneo, A., Schramm, M., et al. 2008, *MNRAS*, 387, 13
- Klamer, I. J., Ekers, R. D., Sadler, E. M., & Hunstead, R. W. 2004, *ApJ*, 612, L97
- Kormendy, J. & Cornell, M. E. 2004, in *Astrophysics and Space Science Library*, Vol. 319, *Penetrating Bars Through Masks of Cosmic Dust*, ed. D. L. Block, I. Puerari, K. C. Freeman, R. Groess, & E. K. Block, 261
- Kormendy, J. & Ho, L. C. 2013, *ARA&A*, 51, 511
- Kormendy, J. & Richstone, D. 1995, *ARA&A*, 33, 581
- Laing, R. A., Jenkins, C. R., Wall, J. V., & Unger, S. W. 1994, in *Astronomical Society of the Pacific Conference Series*, Vol. 54, *The Physics of Active Galaxies*, ed. G. V. Bicknell, M. A. Dopita, & P. J. Quinn, 201
- Laor, A., Baldi, R. D., & Behar, E. 2019, *MNRAS*, 482, 5513
- Lightman, A. P. 1982, *Space Sci. Rev.*, 33, 335
- Liu, B. F., Yuan, W., Meyer, F., Meyer-Hofmeister, E., & Xie, G. Z. 1999, *ApJ*, 527, L17
- Lynden-Bell, D. & Rees, M. J. 1971, *MNRAS*, 152, 461
- Magorrian, J., Tremaine, S., Richstone, D., et al. 1998, *AJ*, 115, 2285
- Marconi, A. & Hunt, L. K. 2003, *ApJ*, 589, L21
- Marecki, A., Thomasson, P., Mack, K. H., & Kunert-Bajraszewska, M. 2006, *A&A*, 448, 479
- Matthews, T. A., Morgan, W. W., & Schmidt, M. 1964, *ApJ*, 140, 35
- Matzko, W., Satyapal, S., Ellison, S. L., et al. 2022, *MNRAS*[arXiv:2205.13668]
- McLure, R. J. & Dunlop, J. S. 2002, *MNRAS*, 331, 795
- Meidt, S. E., Schinnerer, E., Knapen, J. H., et al. 2012, *ApJ*, 744, 17
- Mendez, A. J., Coil, A. L., Lotz, J., et al. 2011, *ApJ*, 736, 110
- Méndez-Abreu, J., Debattista, V. P., Corsini, E. M., & Aguerri, J. A. L. 2014, *A&A*, 572, A25
- Merritt, D. & Ferrarese, L. 2001, *ApJ*, 547, 140
- Meyer-Hofmeister, E. & Meyer, F. 2003, *A&A*, 402, 1013
- Miller, J. S. 1974, *ARA&A*, 12, 331
- Nandra, K., Georgakakis, A., Willmer, C. N. A., et al. 2007, *ApJ*, 660, L11
- Narayan, R. & Yi, I. 1995, *ApJ*, 444, 231
- Netzer, H. 2019, *MNRAS*, 488, 5185
- Oke, J. B. & Gunn, J. E. 1983, *ApJ*, 266, 713
- Pace, C. & Salim, S. 2014, *ApJ*, 785, 66
- Panda, S. & Śniegowska, M. 2022, arXiv e-prints, arXiv:2206.10056
- Peterson, B. M. 2010, in *Co-Evolution of Central Black Holes and Galaxies*, ed. B. M. Peterson, R. S. Somerville, & T. Storchi-Bergmann, Vol. 267, 151–160
- Pierce, J. C. S., Tadhunter, C. N., Ramos Almeida, C., Bessiere, P. S., & Rose, M. 2019, *MNRAS*, 487, 5490
- Pogge, R. 2019, rwpogge/modsCCDRed 2.0, modsCCDRed was developed for the MODS1 and MODS2 instruments at the Large Binocular Telescope Observatory, which were built with major support provided by grants from the U.S. National Science Foundation's Division of Astronomical Sciences Advanced Technologies and Instrumentation (AST-9987045), the NSF/NOAO TSIP Program, and matching funds provided by the Ohio State University Office of Research and the Ohio Board of Regents. Additional support for modsCCDRed was provided by NSF Grant AST-1108693.
- Pogge, R. W., Atwood, B., Brewer, D. F., et al. 2010, in *Society of Photo-Optical Instrumentation Engineers (SPIE) Conference Series*, Vol. 7735, *Proc. SPIE*, 77350A
- Ramos Almeida, C., Bessiere, P. S., Tadhunter, C. N., et al. 2012, *MNRAS*, 419, 687
- Rees, M. J. 1984, *ARA&A*, 22, 471
- Rees, M. J., Begelman, M. C., Blandford, R. D., & Phinney, E. S. 1982, *Nature*, 295, 17
- Rosario, D. J., Burtscher, L., Davies, R., et al. 2013, *ApJ*, 778, 94
- Rowan-Robinson, M. & Crawford, J. 1989, *MNRAS*, 238, 523
- Róžańska, A. & Czerny, B. 2000, *A&A*, 360, 1170
- Sabater, J., Best, P. N., & Heckman, T. M. 2015, *MNRAS*, 447, 110
- Sánchez-Blázquez, P., Peletier, R. F., Jiménez-Vicente, J., et al. 2006, *MNRAS*, 371, 703
- Sandage, A. 1965, *ApJ*, 141, 1560
- Schawinski, K. 2009, in *American Institute of Physics Conference Series*, Vol. 1201, *The Monster's Fiery Breath: Feedback in Galaxies, Groups, and Clusters*, ed. S. Heinz & E. Wilcots, 17–20
- Sellwood, J. A. 2014, *Reviews of Modern Physics*, 86, 1
- Shakura, N. I. & Sunyaev, R. A. 1973, *A&A*, 24, 337
- Silk, J. & Rees, M. J. 1998, *A&A*, 331, L1
- Śniegowska, M., Czerny, B., Bon, E., & Bon, N. 2020, *A&A*, 641, A167
- Springel, V., Di Matteo, T., & Hernquist, L. 2005, *ApJ*, 620, L79
- Stern, D., Assef, R. J., Benford, D. J., et al. 2012, *ApJ*, 753, 30
- Strateva, I., Ivezic, Ž., Knapp, G. R., et al. 2001, *AJ*, 122, 1861
- Strittmatter, P. A., Hill, P., Pauliny-Toth, I. I. K., Steppe, H., & Witzel, A. 1980, *A&A*, 88, L12
- Toomre, A. & Toomre, J. 1972, *ApJ*, 178, 623
- Tremaine, S., Gebhardt, K., Bender, R., et al. 2002, *ApJ*, 574, 740
- Vanden Berk, D. E., Richards, G. T., Bauer, A., et al. 2001, *AJ*, 122, 549
- Vazdekis, A., Sánchez-Blázquez, P., Falcón-Barroso, J., et al. 2010, *MNRAS*, 404, 1639
- Veilleux, S. & Osterbrock, D. E. 1987, *ApJS*, 63, 295
- Vitale, M., Fuhrmann, L., García-Marín, M., et al. 2015, *A&A*, 573, A93
- Vitale, M., Zuther, J., García-Marín, M., et al. 2012, *A&A*, 546, A17
- Weedman, D. W. 1970, *ApJ*, 159, 405
- White, S. D. M. 1976, *MNRAS*, 177, 717
- White, S. D. M. & Rees, M. J. 1978, *MNRAS*, 183, 341
- Woo, J.-H., Yoon, Y., Park, S., Park, D., & Kim, S. C. 2015, *ApJ*, 801, 38
- Wright, E. L., Eisenhardt, P. R. M., Mainzer, A. K., et al. 2010, *AJ*, 140, 1868
- Yesuf, H. M., Faber, S. M., Koo, D. C., et al. 2020, *ApJ*, 889, 14
- Zajaček, M., Busch, G., Valencia-S., M., et al. 2019, *A&A*, 630, A83
- Zakamska, N. L., Hamann, F., Pâris, I., et al. 2016, *MNRAS*, 459, 3144

Appendix A: Optical long slit spectra of central 1''

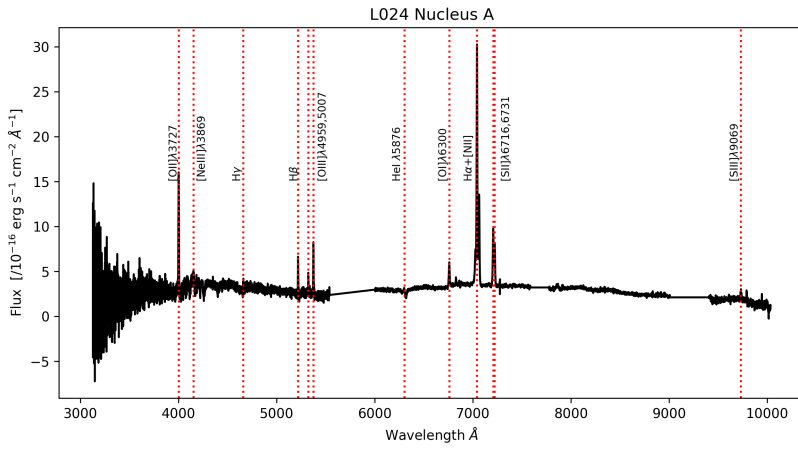


Fig. A.1. One-dimensional optical spectrum of the L024A nucleus, extracted over an aperture of ~ 1.2 arcsec (~ 1.7 kpc at given redshift). Prominent emission lines are marked and named. The x-axis represents the wavelength in Angstroms, while the y-axis depicts the flux in units of $\text{ergs s}^{-1} \text{cm}^{-2} \text{\AA}^{-1}$. The flattened part of the spectrum between 5500 and 6000\AA is the region where the end of the blue channel overlaps with the beginning of the red channel of MODS. Two additional sections beyond 7500\AA have been normalised. They coincide with a sky absorption line and a noisy part of the spectrum.

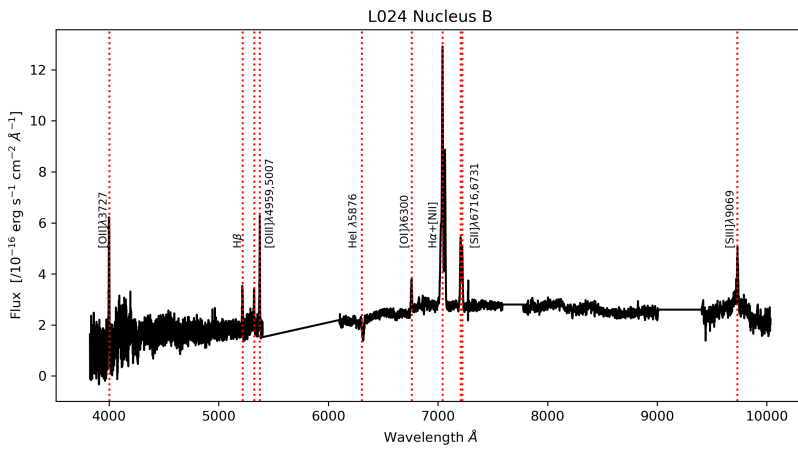


Fig. A.2. One-dimensional optical spectrum of the L024B nucleus, extracted over an aperture of ~ 1.2 arcsec (~ 1.7 kpc at given redshift). Prominent emission lines are marked and named. The x-axis represents the wavelength in Angstroms, while the y-axis depicts the flux in units of $\text{ergs s}^{-1} \text{cm}^{-2} \text{\AA}^{-1}$. The flattened part of the spectrum between 5500 and 6000\AA is the region where the end of the blue channel overlaps with the beginning of the red channel of MODS. Two additional sections beyond 7500\AA have been normalised. They coincide with a sky absorption line and a noisy part of the spectrum.

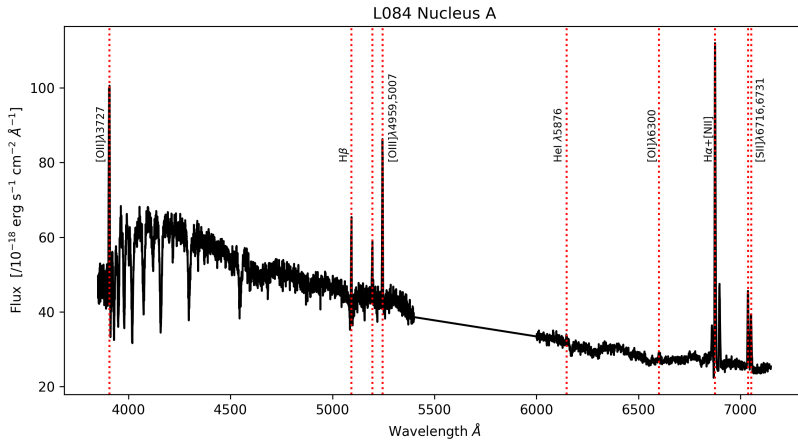


Fig. A.3. One-dimensional optical spectrum of the L084A nucleus, extracted over an aperture of ~ 1.2 arcsec (~ 1.2 kpc at given redshift). Prominent emission lines are marked and named. The x-axis represents the wavelength in Angstroms, while the y-axis depicts the flux in units of $\text{ergs s}^{-1} \text{cm}^{-2} \text{\AA}^{-1}$. The flattened part of the spectrum between 5500 and 6000\AA is the region where the end of the blue channel overlaps with the beginning of the red channel of MODS.

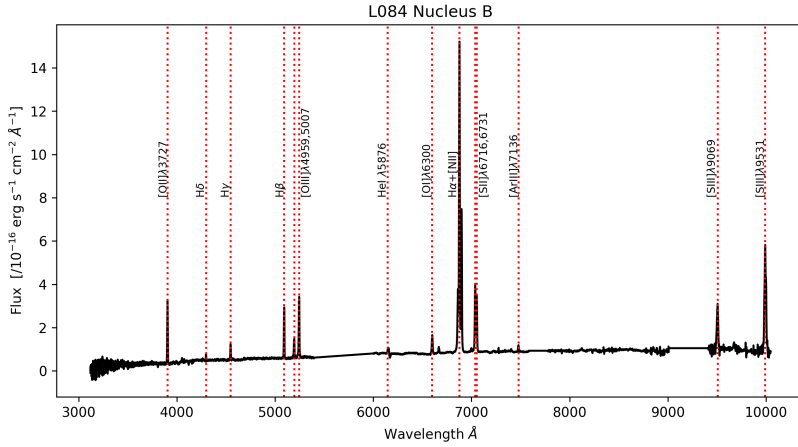


Fig. A.4. One-dimensional optical spectrum of the L084B nucleus, extracted over an aperture of ~ 1.2 arcsec (~ 1.2 kpc at given redshift). Prominent emission lines are marked and named. The x-axis represents the wavelength in Angstroms, while the y-axis depicts the flux in units of $\text{ergs s}^{-1} \text{cm}^{-2} \text{Å}^{-1}$. The flattened part of the spectrum between 5500 and 6000 Å is the region where the end of the blue channel overlaps with the beginning of the red channel of MODS. Two additional sections beyond 7500 Å have been normalised. They coincide with a sky absorption line and a noisy part of the spectrum.

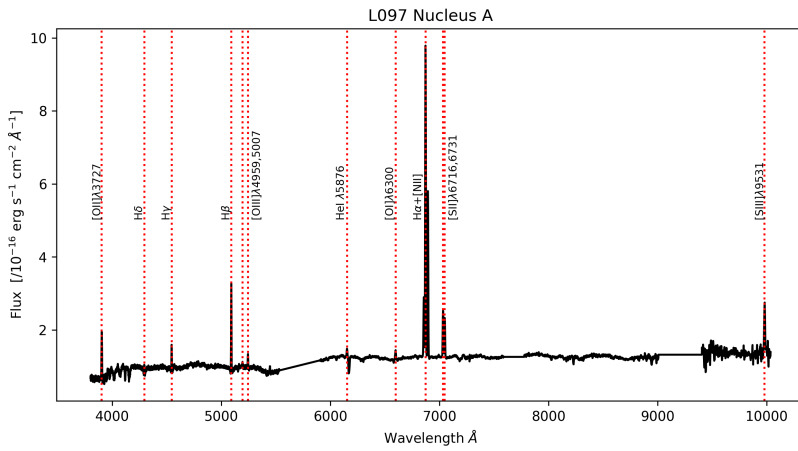


Fig. A.5. One-dimensional optical spectrum of the L097A nucleus, extracted over an aperture of ~ 1.2 arcsec (~ 1.1 kpc at given redshift). Prominent emission lines are marked and named. The x-axis represents the wavelength in Angstroms, while the y-axis depicts the flux in units of $\text{ergs s}^{-1} \text{cm}^{-2} \text{Å}^{-1}$. The flattened part of the spectrum between 5500 and 6000 Å is the region where the end of the blue channel overlaps with the beginning of the red channel of MODS. Two additional sections beyond 7500 Å have been normalised. They coincide with a sky absorption line and a noisy part of the spectrum.

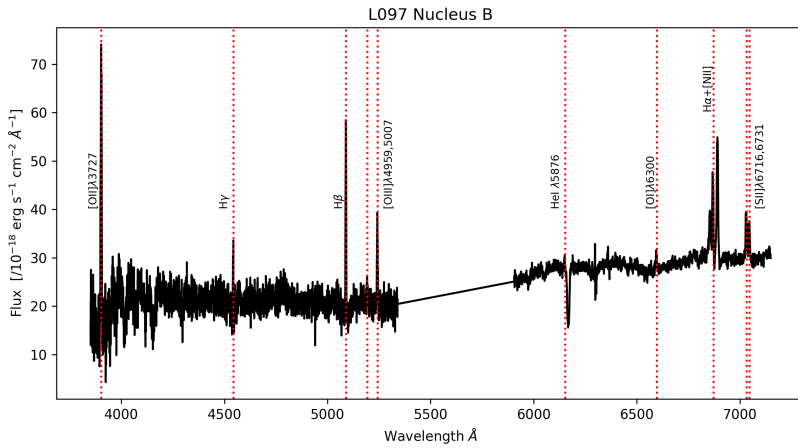


Fig. A.6. One-dimensional optical spectrum of the L097B nucleus, extracted over an aperture of ~ 1.2 arcsec (~ 1.1 kpc at given redshift). Prominent emission lines are marked and named. The x-axis represents the wavelength in Angstroms, while the y-axis depicts the flux in units of $\text{ergs s}^{-1} \text{cm}^{-2} \text{Å}^{-1}$. The flattened part of the spectrum between 5500 and 6000 Å is the region where the end of the blue channel overlaps with the beginning of the red channel of MODS.

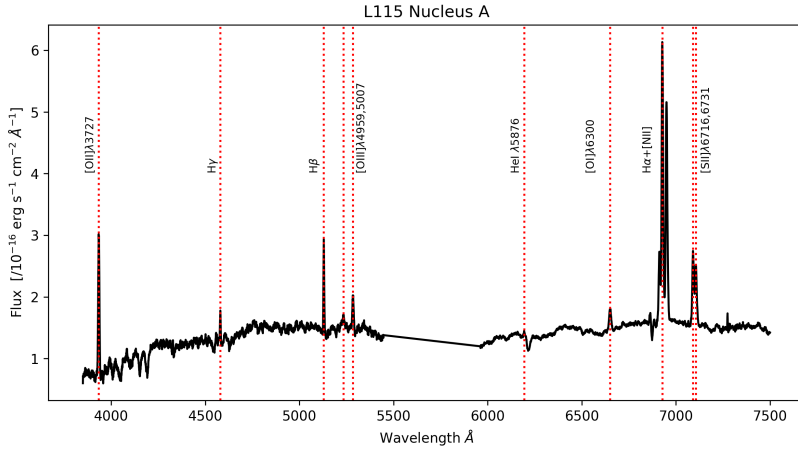


Fig. A.7. One-dimensional optical spectrum of the L115A nucleus, extracted over an aperture of ~ 1.2 arcsec (~ 1.3 kpc at given redshift). Prominent emission lines are marked and named. The x-axis represents the wavelength in Angstroms, while the y-axis depicts the flux in units of $\text{ergs s}^{-1} \text{cm}^{-2} \text{\AA}^{-1}$. The flattened part of the spectrum between 5500 and 6000 \AA is the region where the end of the blue channel overlaps with the beginning of the red channel of MODS.

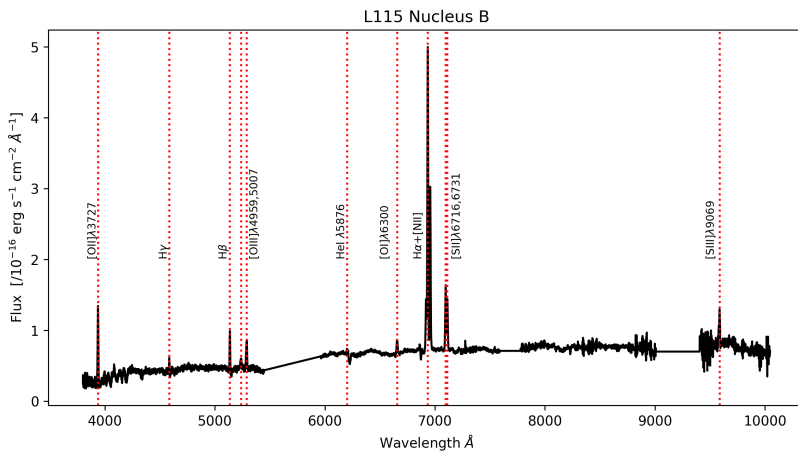


Fig. A.8. One-dimensional optical spectrum of the L115B nucleus, extracted over an aperture of ~ 1.2 arcsec (~ 1.4 kpc at given redshift). Prominent emission lines are marked and named. The x-axis represents the wavelength in Angstroms, while the y-axis depicts the flux in units of $\text{ergs s}^{-1} \text{cm}^{-2} \text{\AA}^{-1}$. The flattened part of the spectrum between 5500 and 6000 \AA is the region where the end of the blue channel overlaps with the beginning of the red channel of MODS. Two additional sections beyond 7500 \AA have been normalised. They coincide with a sky absorption line and a noisy part of the spectrum.

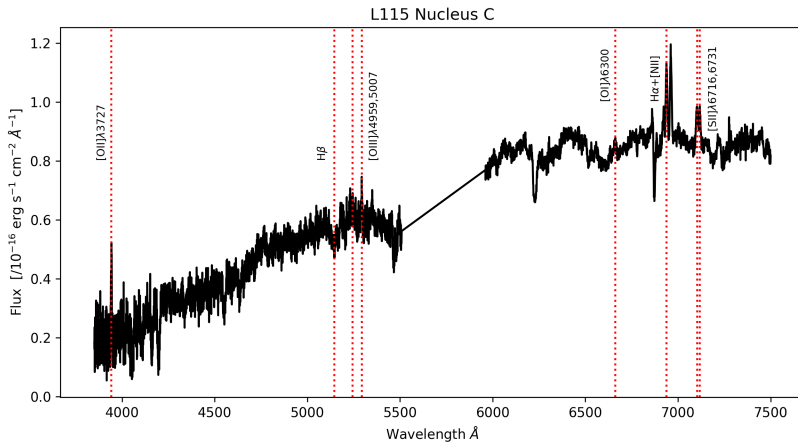


Fig. A.9. One-dimensional optical spectrum of the L115C nucleus, extracted over an aperture of ~ 1.2 arcsec (~ 1.4 kpc at given redshift). Prominent emission lines are marked and named. The x-axis represents the wavelength in Angstroms, while the y-axis depicts the flux in units of $\text{ergs s}^{-1} \text{cm}^{-2} \text{\AA}^{-1}$. The flattened part of the spectrum between 5500 and 6000 \AA is the region where the end of the blue channel overlaps with the beginning of the red channel of MODS.

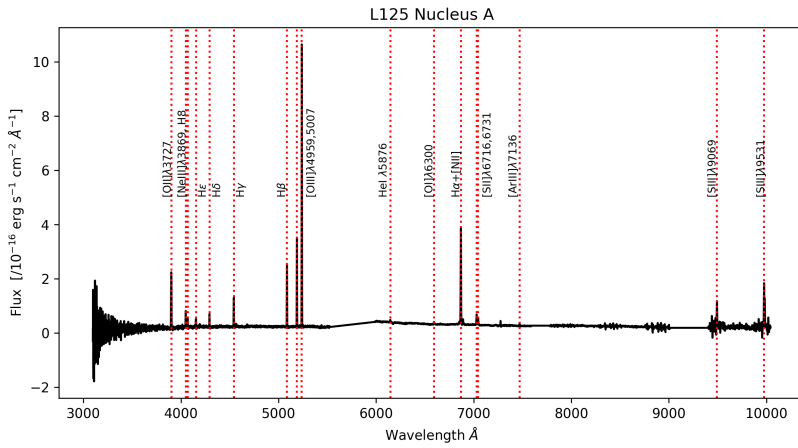


Fig. A.10. One-dimensional optical spectrum of the L125A nucleus, extracted over an aperture of ~ 1.2 arcsec (~ 1.1 kpc at given redshift). Prominent emission lines are marked and named. The x-axis represents the wavelength in Angstroms, while the y-axis depicts the flux in units of $\text{ergs s}^{-1} \text{cm}^{-2} \text{Å}^{-1}$. The flattened part of the spectrum between 5500 and 6000 Å is the region where the end of the blue channel overlaps with the beginning of the red channel of MODS. Two additional sections beyond 7500 Å have been normalised. They coincide with a sky absorption line and a noisy part of the spectrum.

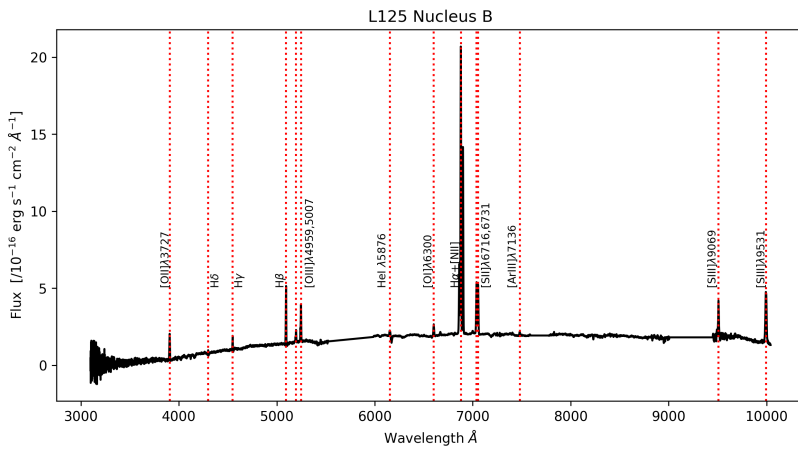


Fig. A.11. One-dimensional optical spectrum of the L125B nucleus, extracted over an aperture of ~ 1.2 arcsec (~ 1.2 kpc at given redshift). Prominent emission lines are marked and named. The x-axis represents the wavelength in Angstroms, while the y-axis depicts the flux in units of $\text{ergs s}^{-1} \text{cm}^{-2} \text{Å}^{-1}$. The flattened part of the spectrum between 5500 and 6000 Å is the region where the end of the blue channel overlaps with the beginning of the red channel of MODS. Two additional sections beyond 7500 Å have been normalised. They coincide with a sky absorption line and a noisy part of the spectrum.

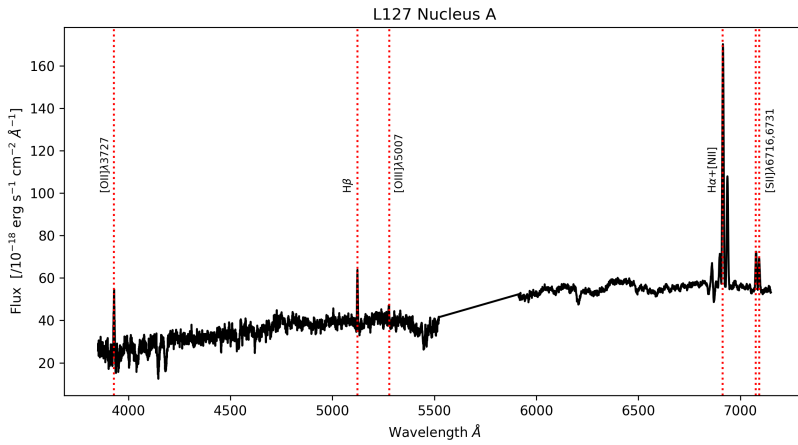


Fig. A.12. One-dimensional optical spectrum of the L127A nucleus, extracted over an aperture of ~ 1.2 arcsec (~ 1.3 kpc at given redshift). Prominent emission lines are marked and named. The x-axis represents the wavelength in Angstroms, while the y-axis depicts the flux in units of $\text{ergs s}^{-1} \text{cm}^{-2} \text{Å}^{-1}$. The flattened part of the spectrum between 5500 and 6000 Å is the region where the end of the blue channel overlaps with the beginning of the red channel of MODS.

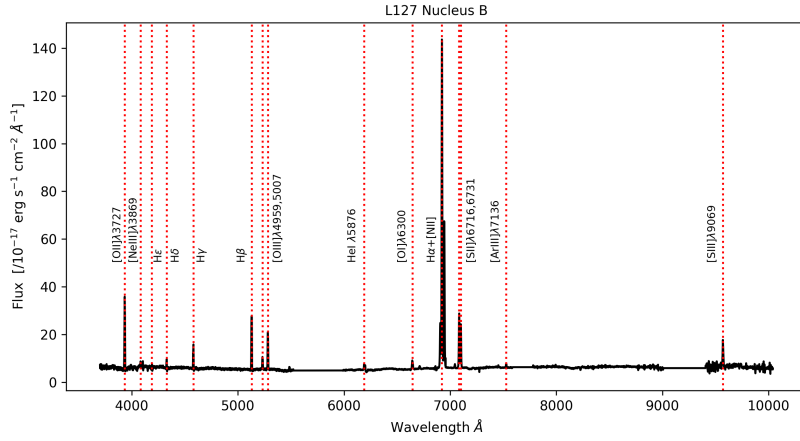


Fig. A.13. One-dimensional optical spectrum of the L127B nucleus, extracted over an aperture of ~ 1.2 arcsec (~ 1.3 kpc at given redshift). Prominent emission lines are marked and named. The x-axis represents the wavelength in Angstroms, while the y-axis depicts the flux in units of $\text{ergs s}^{-1} \text{cm}^{-2} \text{\AA}^{-1}$. The flattened part of the spectrum between 5500 and 6000 \AA is the region where the end of the blue channel overlaps with the beginning of the red channel of MODS. Two additional sections beyond 7500 \AA have been normalised. They coincide with a sky absorption line and a noisy part of the spectrum.

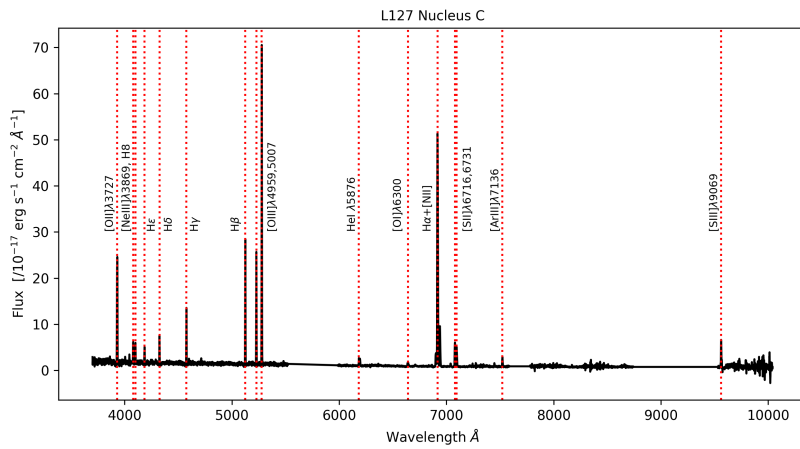


Fig. A.14. One-dimensional optical spectrum of the L127C nucleus, extracted over an aperture of ~ 1.2 arcsec (~ 1.3 kpc at given redshift). Prominent emission lines are marked and named. The x-axis represents the wavelength in Angstroms, while the y-axis depicts the flux in units of $\text{ergs s}^{-1} \text{cm}^{-2} \text{\AA}^{-1}$. The flattened part of the spectrum between 5500 and 6000 \AA is the region where the end of the blue channel overlaps with the beginning of the red channel of MODS. Two additional sections beyond 7500 \AA have been normalised. They coincide with a sky absorption line and a noisy part of the spectrum.

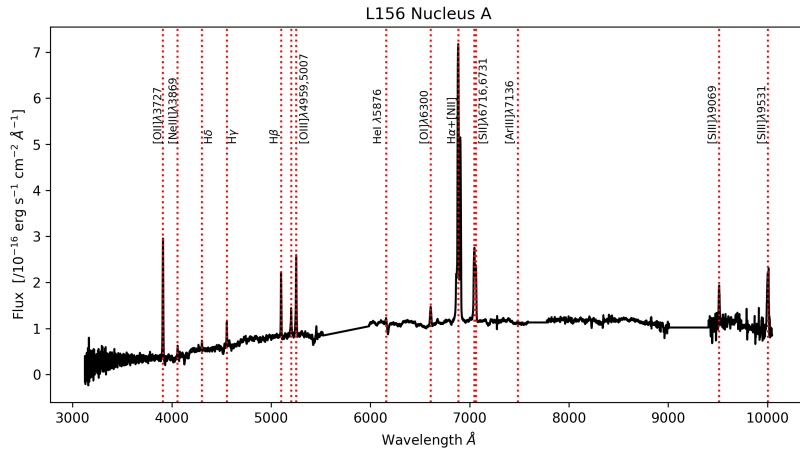


Fig. A.15. One-dimensional optical spectrum of the L156A nucleus, extracted over an aperture of ~ 1.2 arcsec (~ 1.2 kpc at given redshift). Prominent emission lines are marked and named. The x-axis represents the wavelength in Angstroms, while the y-axis depicts the flux in units of $\text{ergs s}^{-1} \text{cm}^{-2} \text{\AA}^{-1}$. The flattened part of the spectrum between 5500 and 6000 \AA is the region where the end of the blue channel overlaps with the beginning of the red channel of MODS. Two additional sections beyond 7500 \AA have been normalised. They coincide with a sky absorption line and a noisy part of the spectrum.

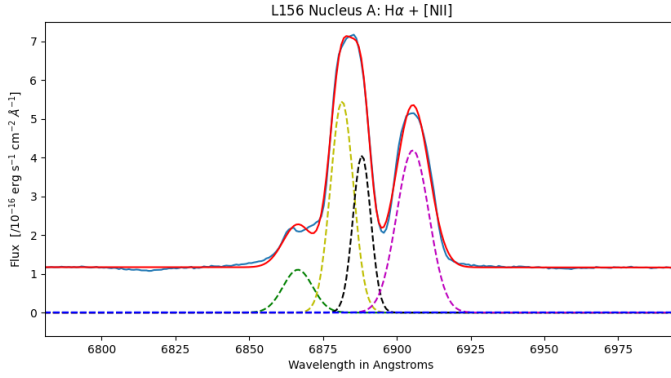


Fig. A.16. One-dimensional optical spectrum of the L156A nucleus, showing the Gaussian fitting performed over the $H\alpha+[NII]$ component. The four narrow components used to perform the fitting are marked by green, yellow, black, and magenta dashed lines, while the best fit is represented by a red line.

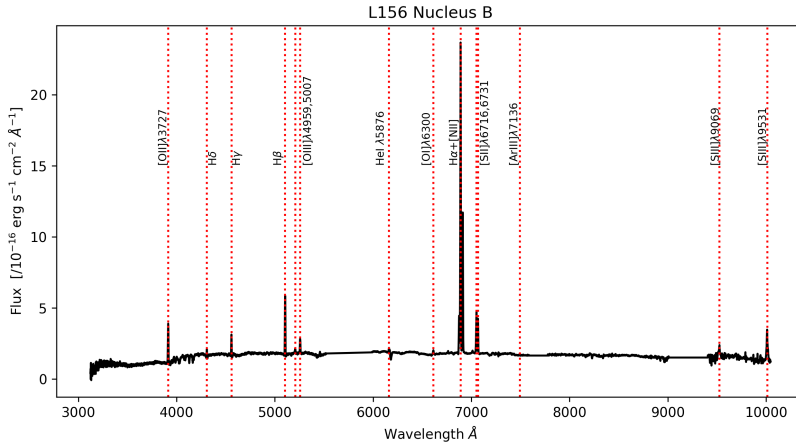


Fig. A.17. One-dimensional optical spectrum of the L156B nucleus, extracted over an aperture of ~ 1.2 arcsec (~ 1.2 kpc at given redshift). Prominent emission lines are marked and named. The x-axis represents the wavelength in Angstroms, while the y-axis depicts the flux in units of $\text{ergs s}^{-1} \text{cm}^{-2} \text{Å}^{-1}$. The flattened part of the spectrum between 5500 and 6000 Å is the region where the end of the blue channel overlaps with the beginning of the red channel of MODS. Two additional sections beyond 7500 Å have been normalised. They coincide with a sky absorption line and a noisy part of the spectrum.

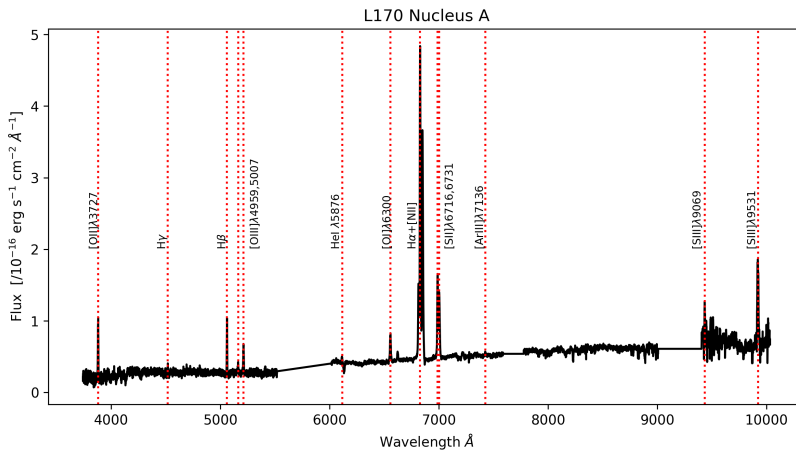


Fig. A.18. One-dimensional optical spectrum of the L170A nucleus, extracted over an aperture of ~ 1.2 arcsec (~ 1.0 kpc at given redshift). Prominent emission lines are marked and named. The x-axis represents the wavelength in Angstroms, while the y-axis depicts the flux in units of $\text{ergs s}^{-1} \text{cm}^{-2} \text{Å}^{-1}$. The flattened part of the spectrum between 5500 and 6000 Å is the region where the end of the blue channel overlaps with the beginning of the red channel of MODS. Two additional sections beyond 7500 Å have been normalised. They coincide with a sky absorption line and a noisy part of the spectrum.

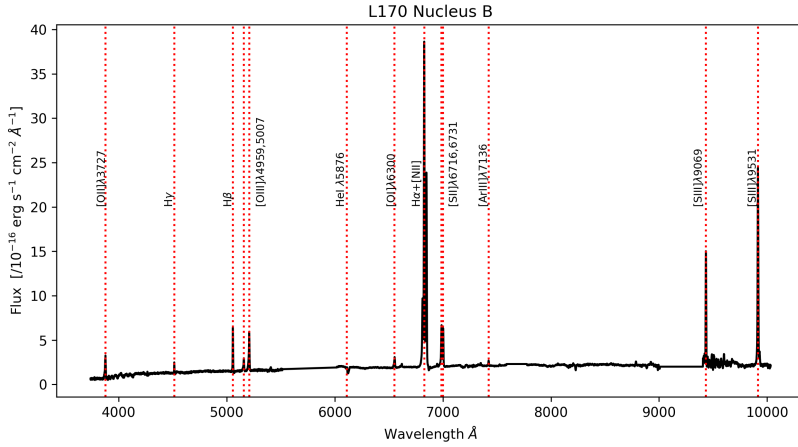


Fig. A.19. One-dimensional optical spectrum of the L170B nucleus, extracted over an aperture of ~ 1.2 arcsec (~ 1.0 kpc at given redshift). Prominent emission lines are marked and named. The x-axis represents the wavelength in Angstroms, while the y-axis depicts the flux in units of $\text{ergs s}^{-1} \text{cm}^{-2} \text{\AA}^{-1}$. The flattened part of the spectrum between 5500 and 6000 \AA is the region where the end of the blue channel overlaps with the beginning of the red channel of MODS. Two additional sections beyond 7500 \AA have been normalised. They coincide with a sky absorption line and a noisy part of the spectrum.

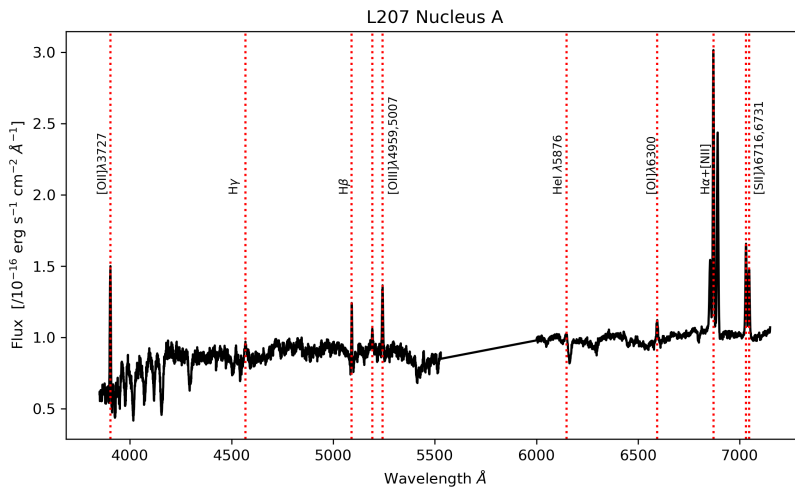


Fig. A.20. One-dimensional optical spectrum of the L207A nucleus, extracted over an aperture of ~ 1.2 arcsec (~ 1.1 kpc at given redshift). Prominent emission lines are marked and named. The x-axis represents the wavelength in Angstroms, while the y-axis depicts the flux in units of $\text{ergs s}^{-1} \text{cm}^{-2} \text{\AA}^{-1}$. The flattened part of the spectrum between 5500 and 6000 \AA is the region where the end of the blue channel overlaps with the beginning of the red channel of MODS.

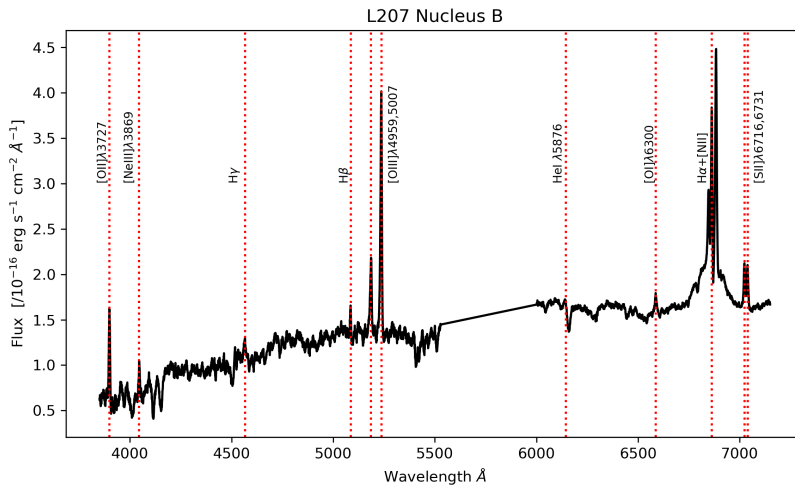


Fig. A.21. One-dimensional optical spectrum of the L207B nucleus, extracted over an aperture of ~ 1.2 arcsec (~ 1.1 kpc at given redshift). Prominent emission lines are marked and named. The x-axis represents the wavelength in Angstroms, while the y-axis depicts the flux in units of $\text{ergs s}^{-1} \text{cm}^{-2} \text{\AA}^{-1}$. The flattened part of the spectrum between 5500 and 6000 \AA is the region where the end of the blue channel overlaps with the beginning of the red channel of MODS.

Paper II: Interactions among intermediate redshift galaxies. The case of SDSSJ134420.86+663717.8

Several elliptical and irregular galaxies display signs of morphological disturbance. It is now generally accepted that interactions played an important role in the evolution of galaxies around the cosmic noon. Therefore, it is important to study the various stages of interaction in individual galaxies to help further our understanding of the process.

In this project, we analyse the optical long-slit spectroscopy data of a pair of interacting galaxies, SDSSJ134420.86+663717.8. The individual galaxies, named A and B, seem to be at a stage of interaction where their centres are still distinctly distinguishable, however, prominent and long tidal tails have arched out from the host galaxies. Along with spectral analysis, we attempted a simple N-body simulation to understand the nature of the progenitor galaxies.

The results of this project are presented in the following peer-reviewed article published in *Astronomy & Astrophysics* reproduced with permission © ESO (Misquitta et al. 2020).

Interactions among intermediate redshift galaxies

The case of SDSSJ134420.86+663717.8^{*}

Persis Misquitta^{1**}, Micah Bowles¹, Andreas Eckart^{1,2}, Madeleine Yttergren^{1,2***}, Gerold Busch¹, Monica Valencia-S.^{1,3}, Nastaran Fazeli¹

¹ I. Physikalisches Institut, Universität zu Köln, Zùlpicher Str. 77, 50939, Köln, Germany

² Max-Planck Institut für Radioastronomie (MPIfR), Auf dem Hügel 69, 53121 Bonn, Germany

³ Regional Computer Center (RRZK), Universität zu Köln, Weyertal 121, 50931, Köln, Germany

Received October 28, 2019; accepted May 9, 2020

ABSTRACT

We present the properties of the central supermassive black holes and the host galaxies of the interacting object SDSSJ134420.86+663717.8. We obtained optical long slit spectroscopy data from the Large Binocular Telescope (LBT) using the Multi Object Double Spectrograph (MODS). Analysing the spectra revealed several strong broad and narrow emission lines of ionised gas in the nuclear region of one galaxy, whereas only narrow emission lines were visible for the second galaxy. The optical spectra were used to plot diagnostic diagrams, deduce rotation curves of the two galaxies, and calculate the masses of the central supermassive black holes. We find that the galaxy with broad emission line features has Seyfert 1 properties, while the galaxy with only narrow emission line features seems to be star-forming in nature. Furthermore, we find that the masses of the central supermassive black holes are almost equal at a few times $10^7 M_{\odot}$. Additionally, we present a simple N-body simulation to shed some light on the initial conditions of the progenitor galaxies. We find that for an almost orthogonal approach of the two interacting galaxies, the model resembles the optical image of the system.

Key words. galaxies: interactions - galaxies: active - galaxies: kinematics and dynamics - galaxies: starburst - galaxies: evolution - methods: numerical

1. Introduction

Interactions play an important role in the evolution of galaxies. It is generally accepted that smaller galaxies in the past merged to form larger galaxies (White & Rees 1978; Kauffmann et al. 1993; Cole et al. 2000; Casteels et al. 2014). The gas content in these galaxies was affected as a result of this process. Gas-rich galaxies interacted with one another, causing the gas and dust content to get funneled through to the center, leading to bursts of star formation and enabling the black holes in the centers of galaxies to start accreting material (Barnes & Hernquist 1991, 1996; Mihos & Hernquist 1994, 1996; Di Matteo et al. 2005; Hopkins et al. 2005a,b; Cox et al. 2008; Lotz et al. 2008, 2010a,b; Di Matteo et al. 2012; Ellison et al. 2013; Torrey et al. 2014; Casteels et al. 2014). Accretion onto the central super massive black hole (SMBH) and the starburst phase leads to the depletion of gas in the progenitor galaxies and the merger remnants end up gas-poor (Springel et al. 2005; Johansson et al. 2009; Hopkins et al. 2010a).

^{*} This paper uses data taken with the MODS spectrographs built with funding from NSF grant AST-9987045 and the NSF Telescope System Instrumentation Program (TSIP), with additional funds from the Ohio Board of Regents and the Ohio State University Office of Research.

^{**} e-mail: misquitta@ph1.uni-koeln.de

^{***} Member of the International Max Planck Research School (IMPRS) for Astronomy and Astrophysics at the Universities of Bonn and Cologne.

Early surveys and catalogs by Vorontsov-Velyaminov (1959); Arp (1966); Zwicky et al. (1968) list many galaxies as distorted or irregular. Pfeiderer & Siedentopf (1961); Pfeiderer (1963); Yabushita (1971); Toomre & Toomre (1971); Clutton-Brock (1972a,b); Wright (1972); Eneev et al. (1973); Barnes & Hernquist (1992) showed that the distortions could be caused by the influence of the gravitational potential of one galaxy on the gas and dust content of the other galaxy using simple models and three-body interactions. Over the years, many attempts have been made to study the merger rate over cosmic time. For example: Mantha et al. (2018) analysed a sample of 9800 massive ($M_{\text{stellar}} \geq 2 \times 10^{10} M_{\odot}$) galaxies spanning $0 < z < 3$, and found that the merger rate fraction increases from $z \approx 0$ to $0.5 < z < 1$ before decreasing at $2.5 < z < 3$, indicating a turnover at $z \approx 1$. Hopkins et al. (2010b) provides a good review of the different models used to study merger rates theoretically.

Another interesting point to consider while studying interacting galaxies is the influence they have on triggering active galactic nuclei (AGN). While traditionally, the theoretical view has been that mergers are the predominant mechanism responsible for black hole growth and AGN activity, some theoretical studies predict the requirement of other processes along with merging to drive nuclear activity (Fanidakis et al. 2012; Hirschmann et al. 2012). Steinborn et al. (2018) conclude that while mergers increase the probability for nuclear activity, the role of mergers causing nuclear activity in the overall AGN population is still

minor (<20 %). This is also the case with observational studies, with some of them finding that mergers play a minor role in triggering luminous AGN (Villforth et al. 2017; Hewlett et al. 2017), while other studies find that mergers are the dominant mechanism for driving AGN activity (Urrutia et al. 2008; Hopkins & Hernquist 2009; Treister et al. 2012; Glikman et al. 2015; Fan et al. 2016).

The highly energetic phenomena known as AGN emit brightly over the entire electromagnetic spectrum. They can be broadly classified as Type 1 and Type 2 AGN based on the respective presence or absence of broad emission lines in their spectra. Antonucci (1993) put forth an AGN unification model, wherein Type 1 and Type 2 AGN are the same type of object, with the difference appearing relative to the orientation of the observer. If the unification scheme holds true, there should be no significant difference in the external environment of Type 1 and Type 2 AGN. However, Dultzin-Hacyan et al. (1999); Koulouridis et al. (2006); Jiang et al. (2016) found more Type 2 galaxies than Type 1 galaxies in close galaxy pairs, leading to the suggestion that instead of a unified AGN model, galaxy interactions could result in evolution of galaxies from star-forming to Type 2 and finally to Type 1. Gordon et al. (2017) find that upto a pair separation of 50 kpc h^{-1} , there is no difference in the AGN found in pairs based on the AGN type, with an excess of Type 2 AGN at separations lesser than 20 kpc h^{-1} . They suggest that either the unified model breaks down in the case of close gravitational interactions or that the interaction between galaxies drives more dust towards the nucleus, causing the obscuration to be more probable. Additionally, Ricci et al. (2017) find that the fraction of Compton-thick AGN in late merger galaxies is higher compared to the local hard X-ray selected AGN. They conclude that late stage mergers of galaxies suffer greater obscuration as material is most efficiently funneled to the inner parsecs from the outer scales and the classical AGN unification model cannot sufficiently explain this phenomenon.

The lifetimes of interactions among galaxies are measured in the order of 10^8 years (Struck 1999). It is, therefore, impossible for us to study a particular case in the entirety of the process. Every case available to us is a cosmic ‘snapshot’ of a particular phase in the long series of interactive events, and as such, yields information and helps to better our understanding of galaxy mergers. Studying different pairs of galaxies at different stages in their interaction aids in putting together a coherent picture of the series of events. Another important tool that helps in increasing our knowledge is simulations of galaxy interactions. Observations help make the simulations more detailed while simulations help to interpret the observations.

SDSSJ134420.86+663717.8 is a pair of interacting galaxies that is located at an intermediate redshift of approximately $z \sim 0.128$ ¹. The pair derives its name from the Sloan Digital Sky Survey catalogue number. Previously, they were cataloged as a clumpy source by several surveys like the Infrared Astronomical Satellite (IRAS), the Wide-field Infrared Survey Explorer (WISE), the Two Micron All Sky Survey (2MASS), the ROentgen SATellite (ROSAT) survey, and the Palomar Schmidt 48-inch telescope survey. Table 1 presents the literature values of luminosity and photometry for SDSSJ134420.86+663717.8. The Sloan Digital Sky Survey (SDSS) provides a significantly improved picture of the galaxies. The two nuclei are well resolved and tidal distortions are clearly visible (see Figure 1). The orientation and size of the tidal tails hints at an orthogo-

nal interaction between the progenitor galaxies. The SDSS website lists some information about the larger of the two nuclei, which we shall call nucleus A, but provides no information for nucleus B. Nucleus A is classified as a quasi-stellar object (QSO) by SDSS (Schneider et al. 2003), as a Seyfert 1 galaxy by Zuther et al. (2012), and as a Seyfert 1.5 galaxy by Paturel et al. (2003) and Moran et al. (1996). Zuther et al. (2012) also note that SDSSJ134420.87+663717.6 is an interacting galaxy and the pair shows 2.70 ± 0.40 mJy peak flux at 20 cm (taken from the NVSS 20 cm survey), $L_{\text{FIR}} \approx 5 \times 10^{11} L_{\odot}$, and $\log M_{\text{BH}} = 7.6$ (taken from Greene & Ho (2007)). However, they could not detect any compact flux density at 18 cm with the Multi-Element Radio Linked Interferometer Network (MERLIN). They conclude that the radio emission was likely dominated by extended star formation since it is an infrared (IR) luminous galaxy. Moran et al. (1996) provide values for the flux and luminosity of SDSSJ134420.86+663717.8 (or IRASF13429+6652, after its IRAS catalogue name) in the X-ray and far infrared (FIR) regions to be $F_{\text{X}} = 4.88 \times 10^{-13}$ erg s^{-1} cm^{-2} , $L_{\text{X}} = 3.87 \times 10^{43}$ erg s^{-1} , $F_{\text{FIR}} = 2.18 \times 10^{-11}$ erg s^{-1} cm^{-2} , and $L_{\text{FIR}} = 1.73 \times 10^{45}$ erg s^{-1} , respectively. The X-ray luminosity was calculated using ROSAT observations over the energy range between 0.1-2.4 keV.

As an on-going merger of two intermediate redshift, almost orthogonal galaxies, SDSSJ134420.86+663717.8 is a subject of interest as a case study for orthogonal interactions of galaxies. This work focuses on studying the spectra of the two nuclei in the optical wavelength regime and analysing this data. In addition, we use a simple N-body simulation to infer the initial conditions of the host galaxies before the interaction, based on their morphology.

This paper is organised as follows. We present details about the observations and data reduction in Section 2. In Section 3, we detail the process of spectral extraction and present the optical spectra of the two nuclei. Further on, we mention the results from emission line fits. We analyse the spectra in detail and list some of the properties of the galaxies in Section 4 and present an N-body simulation to model a SDSS J1334420.86+663717.8 look-alike in Section 5. Finally, we summarise the paper and provide some concluding remarks in Section 6.

2. Observations and data reduction

SDSSJ134420.86+663717.8 was observed using the Multi-Object Double Spectrograph (MODS) at the Large Binocular Telescope (LBT)² located at an altitude of approximately 3,200 m on Mount Graham, United States (Pogge et al. 2010). The LBT has a binocular design and consists of two 8.4 m wide mirrors mounted side-by-side with a centre-to-centre distance of 14.4 m, such that it has a combined collecting area of an 11.8 m telescope. MODS are a pair of seeing-limited low to medium resolution, two-channel, identical spectrographs: MODS1 and MODS2. They are mounted at the direct Gregorian foci of the twin LBT mirrors. A dichroic splits the light into red and blue optimised spectrograph channels, such that the data corresponding to an object is obtained from four different channels:

² The LBT is an international collaboration among institutions in the United States, Italy, and Germany. LBT Corporation partners are: The University of Arizona on behalf of the Arizona Board of Regents; Istituto Nazionale di Astrofisica, Italy; LBT Beteiligungsgesellschaft, Germany, representing the Max-Planck Society, The Leibniz Institute for Astrophysics Potsdam, and Heidelberg University; The Ohio State University, and The Research Corporation, on behalf of The University of Notre Dame, University of Minnesota, and University of Virginia.

¹ <http://skyserver.sdss.org/dr15/en/tools/explore/Summary.aspx?id=1237651273514745920>

Table 1: Photometry Values for SDSSJ134420.86+663717.8

Spectral Region	Band	Apparent Mag or Flux	Reference
Ultraviolet	NUV (GALEX) AB	17.0747±0.0326211 mag	1
Visual	i (SDSS Petrosian) AB	15.546±0.012 asinh mag	2
Near-Infrared	K _s	12.747±0.079 mag	3
Mid-Infrared	12 microns (IRAS)	<5.397e-02 Jy	3
Far-Infrared	60 microns (IRAS)	4.074e-01 ±9 % Jy	4
Radio	1.4 GHz	3.2±0.5 mJy	5

References. (1) Seibert et al. (2012); (2) Schneider et al. (2002); (3) Cutri et al. (2013); (4) Moshir & et al. (1990); (5) Condon et al. (1998)

Notes. Credit:NED

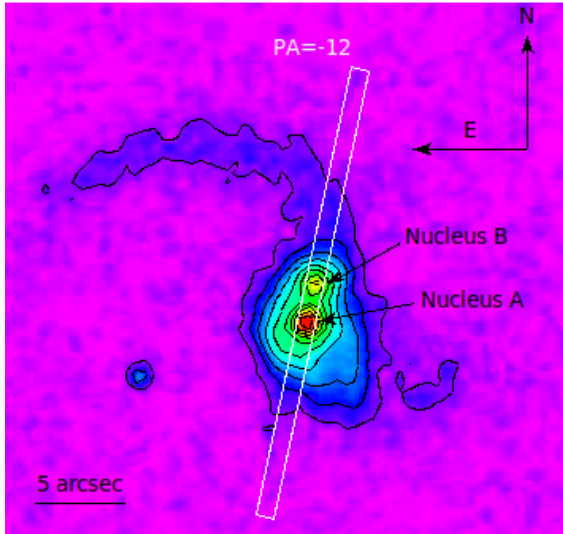


Fig. 1: SDSS image of the galaxy pair SDSSJ134420.86+663717.8. North is up and left is East. The central bulge hosts the two nuclei: nucleus A, which is at the bottom of the bulge, and nucleus B, at the top of the bulge. Clearly visible is the tidal arm to the north-east of nucleus B, while the tidal arm to the south-west of nucleus A appears quite foreshortened. The position angle in degrees (measured from the North to the East) and the 1 arcsec slit used for long-slit spectroscopy with LBT/MODS are illustrated. Credit: SDSS Skyserver Data Release 15.

MODS1 B, MODS1 R, MODS2 B, and MODS2 R. MODS can be used for imaging, long-slit and multi-object spectroscopy. It has a field-of-view of $6' \times 6'$. The wavelength range for MODS is from 3000 Å to 10000 Å. We used MODS in long slit spectroscopy mode to obtain the data on May 13, 2016. The exposure time for each spectrum was 600 seconds, and the object was observed thrice, with a total exposure time of 1800 seconds. In total, we had twelve spectra, corresponding to three spectra each from MODS1 B, MODS1 R, MODS2 B and MODS2 R, respectively. The slit width was 1 arcsec, with spectral resolution of 150 km s^{-1} , and a spatial resolution of 0.627 arcsec.

The observed frames were bias corrected and combined using the MODS CCD Reduction pipeline (Pogge 2019). Wavelength and flux calibration, and background subtraction was done using Pyraf routines developed by us, yielding two-dimensional spectra that were used to extract one-dimensional spectra. Hg, Ne, Ar, Xe, and Kr lamps were used for wavelength calibration while data from a standard star, BD+33d2642, was used for flux calibration. BD+33d2642 is a spectrophotometric standard star of spectral type B2IV with an established spec-

trum (Oke 1990). It was observed using MODS during the same night as the target, SDSS J134420.86+663717.8. The standard star data underwent the same procedures as the science data in that it was bias corrected, combined and wavelength calibrated using the same methods. The data from MODS1 and MODS2 was reduced separately but was combined after reduction to improve the signal-to-noise ratio (S/N).

3. Emission line fits and results

We extracted one-dimensional spectra of nuclei A and B from the reduced two-dimensional spectra. This was done by choosing an aperture of approximately 1 arcsec on the spatial axis for each nucleus and then extracting along the wavelength axis. Additionally, we chose an aperture of approximately 8 arcsec and extracted spectra along each pixel row (1 pixel = 0.123 arcsec for MODS Red and 1 pixel = 0.120 arcsec for MODS Blue) in order to study the intensity distribution of the two nuclei. The continuum was fit with a line and all broad emission lines were fit using multiple Gaussian functions, while the narrow emission lines were fit using single Gaussian functions using the Levenberg-Markwardt algorithm, non-linear least-squares minimisation and curve-fitting for Python (LMFIT) (Markwardt 2009; Newville et al. 2016).

3.1. Optical spectrum of Nucleus A

Figures 2 and 3 show the optical spectrum of nucleus A. The continuum emission is overlaid by several emission lines. Stellar absorption features are not detected. Broad H_I emission features are clearly visible. The break in the wavelength axis reproduces the split between the blue and red beams due to the dichroic. Gaussian fits to the emission lines helped in determining the full width at half maximum (FWHM) of the various emission lines (see Figure 4 for an example of the spectrum fit with Gaussian functions). In order to determine the number of Gaussian components to be fit, we started with, for example, three narrow Gaussian components and one broad component for the case of the H α + [N II] complex. We used visual inspection as well as the χ^2 values of the Gaussian fitting module³ and determined the number that was the best fit to the data, which in our case was two broad H α components and three narrow components corresponding to [N II] λ 6548, H α , and [N II] λ 6583, respectively. The choice was obvious: an additional broad component is required to fit the extended [N II] λ 6548, H α , and [N II] λ 6583 wing towards longer wavelengths. The three narrow components are needed to fit the three narrow line features related to the [N II] λ 6548, H α , and [N II] λ 6583 lines, respectively. Hence,

³ The χ^2 value for only one broad component is 1.19, whereas we find a χ^2 value of 0.32 for two broad components.

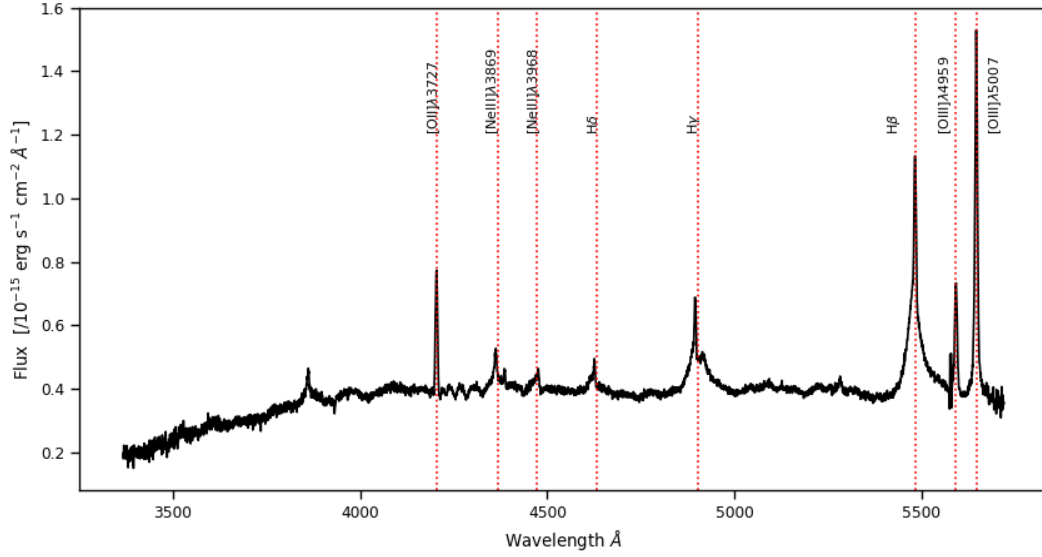


Fig. 2: One-dimensional observed optical spectrum of SDSSJ134420.86+663717.8 nucleus A in the wavelength range 3500–5700 Å. The emission lines observed have been marked by vertical red dotted lines and named. The aperture size for spectral extraction is 1 arcsec. The wavelength axis depicts the observed wavelength.

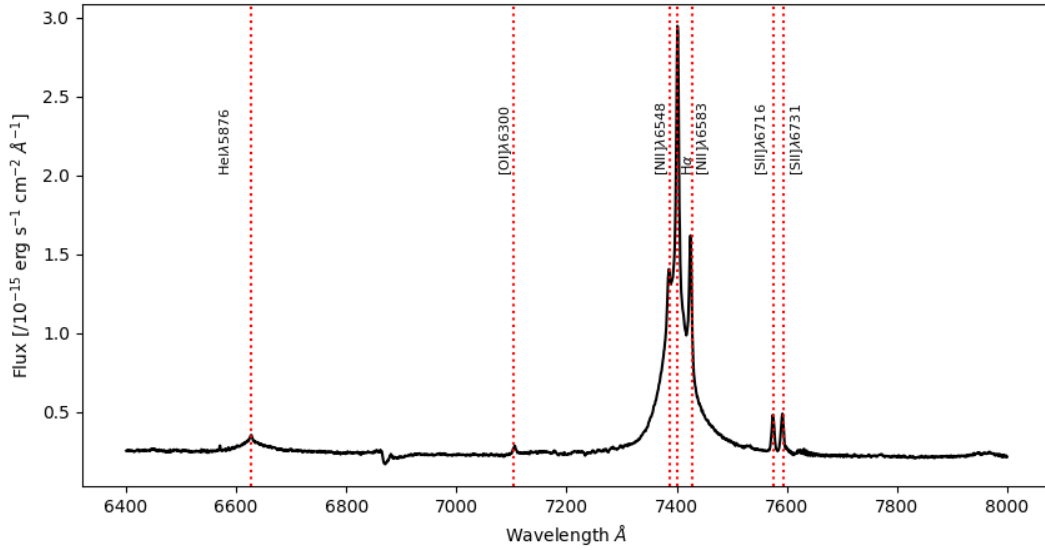


Fig. 3: One-dimensional observed optical spectrum of SDSSJ134420.86+663717.8 nucleus A in the wavelength range 6400–8000 Å. The emission lines observed have been marked by vertical red dotted lines and named. The aperture size for spectral extraction is 1 arcsec. The wavelength axis depicts the observed wavelength.

our choice comprises only the most necessary components. Table 2 lists the different emission lines observed in the spectrum, their flux values and FWHM. The average redshift of nucleus A, as calculated using the central positions of various emission lines is 0.1279 ± 0.0002 ($\sim 38370 \text{ km s}^{-1}$). The velocity corresponding to the redshift is the cz value. The FWHM

of the broad components of the $H\alpha$ and $H\beta$ recombination lines are $1715 \pm 14 \text{ km s}^{-1}$, $5317 \pm 56 \text{ km s}^{-1}$, $1944 \pm 55 \text{ km s}^{-1}$, and $2507 \pm 31 \text{ km s}^{-1}$, respectively. The FWHM of the narrow components of the $H\alpha$ and $H\beta$ recombination lines are $256 \pm 3 \text{ km s}^{-1}$ and $335 \pm 6 \text{ km s}^{-1}$, respectively. These FWHM values fall in the range of 1000 – 6000 km s^{-1} for broad HI lines

in Seyfert 1 galaxies, and $300 - 800 \text{ km s}^{-1}$ for narrow lines in both classes of Seyfert galaxies, as specified in [Osterbrock & Pogge \(1985\)](#).

3.2. Optical spectrum of Nucleus B

Figures 5 and 6 show the optical spectrum of nucleus B. Several stellar absorption features are clearly visible along with some emission lines. Nucleus B shows fewer emission lines compared to nucleus A. No broad emission features are noticeable. Table 3 lists the different emission lines, their flux and FWHM values. The FWHM of the narrow $H\alpha$ and $H\beta$ recombination lines are $250 \pm 2 \text{ km s}^{-1}$ and $256 \pm 16 \text{ km s}^{-1}$, respectively. Some stellar absorption can be seen at the $H\beta$ line. The stellar absorption lines were fit using the 'penalised Pixel-Fitting' (pPXF, ([Cappellari 2017](#); [Cappellari & Emsellem 2004](#)) method, and were taken into consideration while estimating emission line fluxes (see also, Section 4.3.2). The average redshift calculated from the central positions of various emission lines is 0.1285 ± 0.0001 . The plots of spatial position versus intensity for $H\alpha$ and the continuum show that both of them peak at the same point, which we consider to be the position of the central nucleus. We use this to estimate that the systemic redshift of Nucleus B is the redshift value displayed by the Hydrogen recombination lines at the central position of Nucleus B, that is, 0.1285. However, interestingly, the redshift of the $[\text{O III}]\lambda 5007$ is smaller at 0.1282 ($\sim 38460 \text{ km s}^{-1}$), whereas the redshift of the $[\text{O II}]\lambda 3727$ line is larger at 0.1288 ($\sim 38640 \text{ km s}^{-1}$) compared to the mean redshift of 0.1285 ($\sim 38550 \text{ km s}^{-1}$). The velocities corresponding to the redshifts are the cz values. $[\text{O II}]\lambda 3727$ is considered to be a good tracer for star formation. However, [Yan et al. \(2018\)](#) state that $[\text{O II}]$ emission in galaxies could have other possible sources like AGN, fast shock waves, post-asymptotic giant branch (AGB) stars, and cooling flows. The comparatively higher value of redshift could arise from star formation in cool molecular clouds accumulated due to cooling flows. [Boller et al. \(1998\)](#) categorise SDSSJ134420.86+663727.8 as a source of diffuse X-ray emission. The X-ray emission is suggested to be indicative of cooling flows. If the cooling flow is rapid, an inflow of gas is created to satisfy the condition of hydrostatic equilibrium. The lower redshift associated with the $[\text{O III}]\lambda 5007$ line could arise due to emission resulting from an outflow. On checking the value of its FWHM, we notice that it is $429 \pm 35 \text{ km s}^{-1}$, which is higher than the FWHM values of the $H\alpha$ and $H\beta$ lines. The $[\text{O III}]\lambda 5007$ emission line is usually associated with outflows in the narrow line region (NLR). In such cases, the $[\text{O III}]\lambda 5007$ profile exhibits a blue asymmetry, in that the peak of the line is skewed blueward. However, in our case, the $[\text{O III}]\lambda 5007$ line is not reliable since it falls towards the end of the blue spectrum, and is very noisy and weak. Thus, we refrain from drawing any concrete conclusions based on the redshift and shape of the $[\text{O III}]\lambda 5007$ line.

4. Discussion

Once we obtained the optical spectra of both the galaxies along with the flux values of the different emission lines, we could use this information to deduce some properties associated with the individual galaxies. We discuss our findings in the subsections below. Having this knowledge at hand is useful to reconstruct the picture of the interaction (e.g., while using simulations).

4.1. Diagnostic diagrams

We use the diagnostic diagram originally proposed by Baldwin, Phillips and Terlevich ([Baldwin et al. 1981](#)), along with two other diagnostic diagrams which are discussed by ([Veilleux & Osterbrock 1987](#)). The diagnostic diagrams are essentially a set of three different plots of the ratios of the fluxes of emission lines that are close enough to each other in wavelength to render reddening ineffective. They are used to determine the excitation mechanisms of the gas, and thereby they help us to distinguish between AGN and star-forming galaxies ([Kewley et al. 2019](#)). The different excitation mechanisms responsible for line emission could be normal H II regions, planetary nebulae, objects photoionised by a harder radiation field, AGN, shocks, and low-ionisation nuclear emission-line region (LINER) emission. The Equations (1, 2, and 3) ([Groves & Kewley 2008](#)) define the curves in the diagrams which separate the AGN from star-forming galaxies (see the plots in Figure 7). The emission lines used are $[\text{O III}]\lambda 5007$, $H\beta$, $[\text{N II}]\lambda 6583$, $H\alpha$, $[\text{O I}]\lambda 6300$, $[\text{S II}]\lambda 6716$ and $[\text{S II}]\lambda 6731$.

$$\log([\text{O III}]/H\beta) = 0.61/(\log([\text{N II}]/H\alpha) - 0.47) + 1.19. \quad (1)$$

$$\log([\text{O III}]/H\beta) = 0.72/(\log([\text{S II}]/H\alpha) - 0.32) + 1.30. \quad (2)$$

$$\log([\text{O III}]/H\beta) = 0.73/(\log([\text{O I}]/H\alpha) + 0.59) + 1.33. \quad (3)$$

Additionally, there is a curve (Equation 4) proposed by [Kauffmann et al. \(2003\)](#), which provides another delineation between AGN and star-forming galaxies. The curve (Equation 1) proposed by [Kewley et al. \(2001\)](#) is called the maximum starburst line and is based on theoretical modelling, while the curve (Equation 4) put forth by [Kauffmann et al. \(2003\)](#) is called the pure star-forming line and is based on observational data. If an object falls in the space between these two curves, they are considered to be composite or transitioning objects.

$$\log([\text{O III}]/H\beta) = 0.61/(\log([\text{N II}]/H\alpha) - 0.05) + 1.3. \quad (4)$$

To further classify the AGN as Seyferts or LINERS, there are two more curves (Equations 5 and 6). The LINER region can also be populated by regions of shocked gas ([Rich et al. 2014](#)).

$$\log([\text{O III}]/H\beta) = 1.89 \log([\text{S II}]/H\alpha) + 0.76. \quad (5)$$

$$\log([\text{O III}]/H\beta) = 1.18 \log([\text{O I}]/H\alpha) + 1.30. \quad (6)$$

Figure 7 shows the three different plots. We can see from the first plot in Figure 7 that while both nuclei lie in the composite/transition phase, nucleus A is very close to the AGN part, and nucleus B lies very close to the star forming part of the composite or transition phase. This could be due to the interaction of the galaxies. Interactions of galaxies cause huge amounts of gas and dust to get funneled through to the centers of the galaxies causing star-formation and might make the super-massive black holes (SMBH) at the centres of galaxies active, in the sense that they start accreting gas and dust. The position of the two galaxies in the transitioning phase is further bolstered by the remaining two figures (see the second and third plot in Figure 7), where nucleus A lies in the star-forming region close to the dividing curve, while nucleus B lies much further down, with low ionisation values. The $[\text{O III}]\lambda 5007$ lying at the red-ward end of the MODS

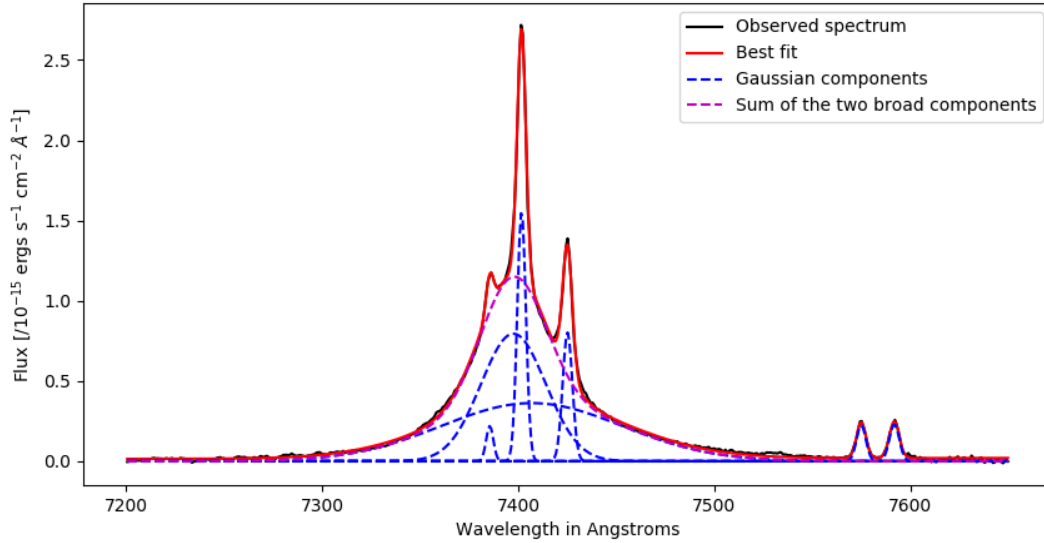


Fig. 4: One-dimensional observed optical spectrum in the wavelength range 7200-7650 Å of SDSSJ134420.86+663717.8 nucleus A overlaid with the Gaussian fits. Two broad components along with three narrow components are fit to the H α + N II complex. The black line represents the observed spectrum, the red line is the best fit, the dotted blue lines are the individual Gaussian components, and the dotted magenta line is the sum of the two broad components. The wavelength axis depicts the observed wavelength.

Table 2: Values for Nucleus A

Emission Line	Observed Wavelength (Å)	Uncertainty in Wavelength (Å)	Flux Value (10^{-16} erg s $^{-1}$ cm $^{-2}$)	Uncertainty in Flux (10^{-16} erg s $^{-1}$ cm $^{-2}$)	FWHM (km sec $^{-1}$)	Uncertainty in FWHM (km sec $^{-1}$)
[O II] λ 3727	4204.01	0.05	7.45	0.44	438	9
H γ _{narrow}	4894.82	0.09	3.55	0.54	330	16
H γ _{broad}	4903.44	0.52	2.01	0.43	3652	86
H β _{narrow}	5482.47	0.04	8.99	0.49	335	6
H β _{broad1}	5477.49	0.24	9.84	0.28	1944	55
H β _{broad2}	5510.64	0.29	4.84	0.06	2507	31
[O III] λ 4959	5591.68	0.06	6.27	0.55	407	8
[O III] λ 5007	5645.88	0.02	20.1	0.23	430	3
[He I] λ 5876	6630.27	1.09	4.35	0.04	3022	94
[O I] λ 6300	7105.775	0.51	0.79	0.07	202	49
[N II] λ 6548	7385.54	0.09	6.89	0.15	287	14
H α _{narrow}	7401.65	0.01	31.9	0.16	256	3
H α _{broad1}	7397.88	0.10	38.42	0.42	1715	14
H α _{broad2}	7410.05	0.45	41.88	0.86	5317	56
[N II] λ 6583	7425.12	0.03	14.2	0.68	192	5
[S II] λ 6716	7574.90	0.09	4.39	0.21	235	17
[S II] λ 6731	7591.79	0.09	4.45	0.05	248	18

Notes. All uncertainties are the 1σ standard error values. The values stated are calculated for an aperture of 1 arcsec.

Blue spectrum for nucleus B is very noisy, this is reflected in the uncertainty in the positions of the data points. Similarly, the [O I] λ 6300 line has very low flux values and has a higher uncertainty in its measurement. Thus, we can conclude that while nucleus A has definite AGN like properties, nucleus B is quiescent, with low ionisation levels, and could be star-forming. This is in agreement with the conclusions we drew in Section 3 from looking at the emission lines displayed by both the nuclei.

4.2. Gas rotation curve

The rotation curve of a galaxy is the plot of line-of-sight (LOS) velocity against the radial distance from the centre of the same

(Jog 2002). The rotation curve helps in understanding the distribution of mass as a function of the distance from the centre of the galaxy.

Figure 8 shows the gas rotation curves for the nuclei A and B along the aperture of approximately 8 arcsec on the slit. Additionally, we mark the velocities obtained from our simulation with dashed green lines, to aid in comparing the results of our simulation with the observational data. See Section 5.3.2 for more details about the velocity field of the simulated model. It can be seen from the SDSS image of SDSS J134420.86+663717.8 (see Figure 1) that the galaxies appear to be significantly overlapping. As a result, the extended gas disks associated with the galaxies might overlap in projec-

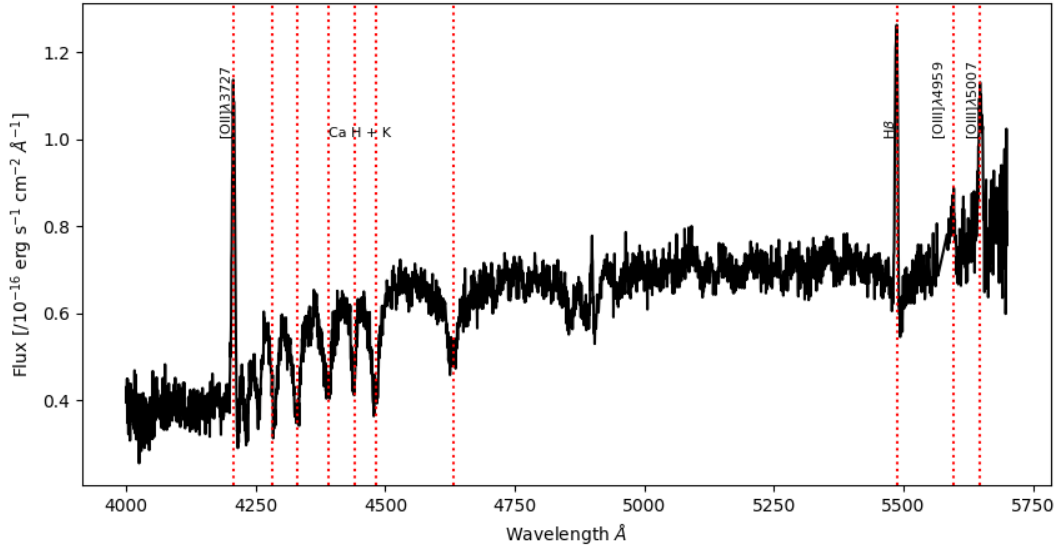


Fig. 5: One-dimensional observed optical spectrum of SDSSJ134420.86+663717.8 nucleus B in the wavelength range 4000–5700 Å. The observed emission and absorption lines have been marked by vertical red dotted lines and named. The aperture size for spectral extraction is 1 arcsec. The wavelength axis depicts the observed wavelength.

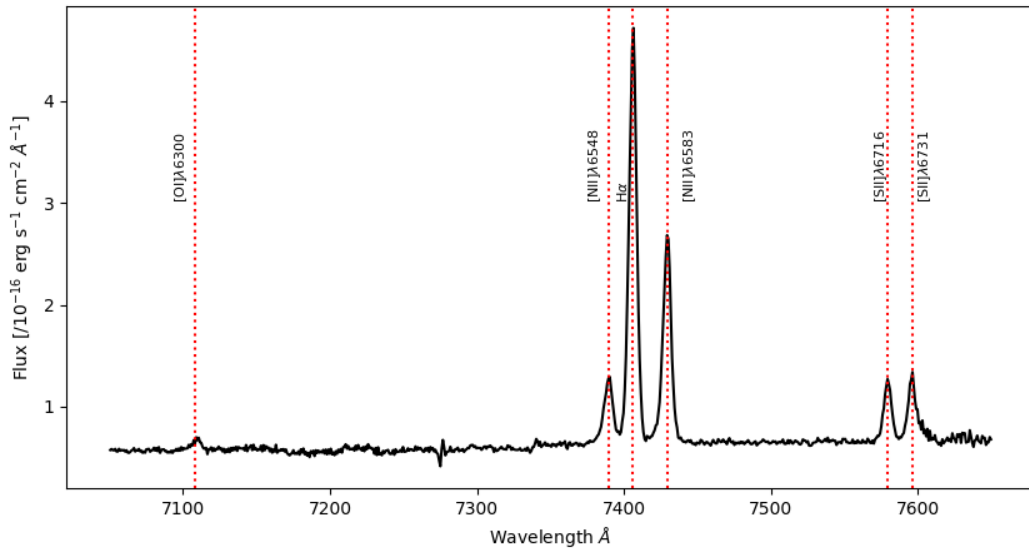


Fig. 6: One-dimensional observed optical spectrum of SDSSJ134420.86+663717.8 nucleus B in the wavelength range 7000–7700 Å. The observed emission and absorption lines have been marked by vertical red dotted lines and named. The aperture size for spectral extraction is 1 arcsec. The wavelength axis depicts the observed wavelength.

tion. Correspondingly, there is a slight broadening seen in some narrow emission lines, however, no split in profiles is noticed. The rotation curve seems to be divided into three distinct parts. The black dots represent the velocities associated with nucleus A, the red dots represent the velocities associated with nucleus B, while the magenta crosses represent the transition phase be-

tween nucleus A and nucleus B. The transition phase is defined as the region between the nuclei along the slit, where the LOS velocity associated with the H α narrow line increases linearly with spatial distance. The velocities are calculated from the shift of the centre of the H α narrow line along the slit using the Gaussian fits explained in Section 3. In blue, we have overplotted the

Table 3: Values for Nucleus B

Emission Line	Observed Wavelength (Å)	Uncertainty in Wavelength (Å)	Flux Value (10^{-16} erg s $^{-1}$ cm $^{-2}$)	Uncertainty in Flux (10^{-16} erg s $^{-1}$ cm $^{-2}$)	FWHM (km sec $^{-1}$)	Uncertainty in FWHM (km sec $^{-1}$)
[O II] λ 3727	4206.95	0.12	1.50	0.27	383	20
H β _{narrow}	5486.34	0.13	1.35	0.16	256	16
[O III] λ 5007	5648.63	0.28	0.62	0.06	429	35
[O I] λ 6300	7108.99	0.64	0.19	0.02	404	65
[N II] λ 6548	7389.56	0.11	1.14	0.04	323	10
H α _{narrow}	7406.12	0.01	7.51	0.32	250	2
[N II] λ 6583	7429.38	0.03	3.78	0.12	265	3
[S II] λ 6716	7579.51	0.11	1.14	0.02	241	9
[S II] λ 6731	7596.16	0.10	1.09	0.07	273	10

Notes. All uncertainties are the 1σ standard error values. The values stated are calculated for an aperture of 1 arcsec.

intensity profile of the H α narrow line along the slit to provide a better understanding about the nature of the rotation curve. The black dashed line represents the level at which there would be no flux from the H α line. The zero on the x-axis was arbitrarily selected to coincide with the point on the slit with the highest intensity of the H α narrow line. The shape of the rotation curve suggests that the galaxies are rotating in opposite directions. This counter-rotation is a feature that can be seen in many cases of interacting galaxies. It arises due to the initial spins of the progenitor galaxies (Barnes 2016). The range of velocities for nucleus A is approximately ± 50 km s $^{-1}$, while for nucleus B, the range of velocities is approximately ± 25 km s $^{-1}$. The shape of the rotation curve shows some asymmetry in the case of galaxy A (since we are no longer dealing with just the central arcsec but rather a longer aperture, we refer to the galaxy associated with nucleus A as galaxy A and the galaxy associated with nucleus B as galaxy B). Asymmetry due to interaction with neighbouring galaxies is a well documented phenomenon (Hodge & Castelaz 2003; Vulcani et al. 2018). Galaxy B has a uniform rotation curve, with no extraordinary features. The transition phase appears to be different from the two other sections, with the LOS velocity increasing almost linearly with spatial distance along the slit. The spatial width of the transition region is approximately equal to the point source function (PSF) of the telescope, thus, we conclude that the transition region has contribution from both of the nuclei. We note that while the flux from the H α line is quite low in the region between the two nuclei, it is never zero. The H α emission line is always present in the transition phase and it is possible to perform Gaussian fitting.

The velocities obtained from the rotation curve can be used to estimate the masses of the central bulges of the galaxies. For this purpose, we used the Baryonic Tully-Fisher relation (BTFR). The original Tully-Fisher relation (Tully & Fisher 1977) is the relation between the luminosity and the rotation velocity of a galaxy, wherein luminosity is considered to be a proxy for total mass of the system. However, luminosity varies with galaxy type, leading to slightly different relations depending on the galaxy being considered. McGaugh et al. (2000); Torres-Flores et al. (2011); McGaugh (2012) (and references therein) show that considering baryonic mass, that is, gas mass as well as stellar mass, leads to a more accurate relation between galactic mass and the rotation velocity. We use the maximum velocity obtained from the rotation curve as seen in Figure 8 to calculate the masses of the bulges in the central 2''. For this purpose, we used the relation stated in Torres-Flores et al. (2011):

$$M_{\text{bar}} = 10^{(2.21 \pm 0.61) V_{\text{max}}^{(3.64 \pm 0.28)}}. \quad (7)$$

The relation yields a baryonic bulge mass of approximately $2 \times 10^8 M_{\odot}$ for galaxy A and a baryonic bulge mass of approxi-

mately $1 \times 10^7 M_{\odot}$ for galaxy B. However, we note that the calculated values of the baryonic bulge masses are an underestimate as we cannot be sure if the slit direction probes the major axis of rotation, and considering that the galaxies are interacting, there is a likelihood of perturbation in the velocities, such that the gradient of the velocity lowers. Additionally, nucleus B could have a higher inclination than nucleus A, making it edge-on to our view as compared to nucleus A, which seems to be face-on based on its spectrum. Taking this into consideration, if we divide the value of the baryonic mass of the bulge of galaxy B with the sine value of its inclination, we get approximately equal bulge mass values of $10^8 M_{\odot}$ for both of the galaxies. The value of the inclination is a rough estimate based on the knowledge we have from the observational results and the results of the simulation (see Section 5 for a detailed description of the simulation). The inclinations were read off the three dimensional model cube and not taken from the list of simulation parameters. We thus conclude that nucleus A and nucleus B have almost equally massive bulges.

4.3. Mass of the central supermassive black holes

The nuclear spectrum can also be used to calculate the mass of the central super-massive black hole of the galaxy. The mass can be calculated in various ways, depending upon the spectral features available, for example, the virial method (explained in detail in the next subsection), the $M_{\text{BH}} - \sigma_*$ relation, the $M_{\text{BH}} - M_{\text{bulge}}$ relation, and the $M_{\text{BH}} - L_{\text{bulge}}$ relation to name a few (Busch (2016) and references therein). In this case, we used the virial method to calculate the mass for nucleus A since we detect broad emission lines, and the $M_{\text{BH}} - \sigma_*$ relation to calculate the mass for nucleus B, since the spectrum for nucleus B shows stellar absorption lines.

4.3.1. Mass of the black hole for nucleus A

The broad lines in the optical spectrum of nucleus A can be used to calculate the mass of the SMBH at its center. The broad lines arise from the broad line region (BLR) around the central SMBH, where gas rotates at high velocities. Consequently, we can use the virial theorem to derive the mass of the central object.

For the case of AGN with broad lines, Equation 8 can be used to calculate the mass of the central black hole in the following form (Peterson 2010),

$$M_{\text{BH}} = f \frac{\Delta V^2 R_{\text{BLR}}}{G}, \quad (8)$$

where ΔV is the velocity of the broad line region gas, usually characterised by the FWHM or the line dispersion (σ) of the

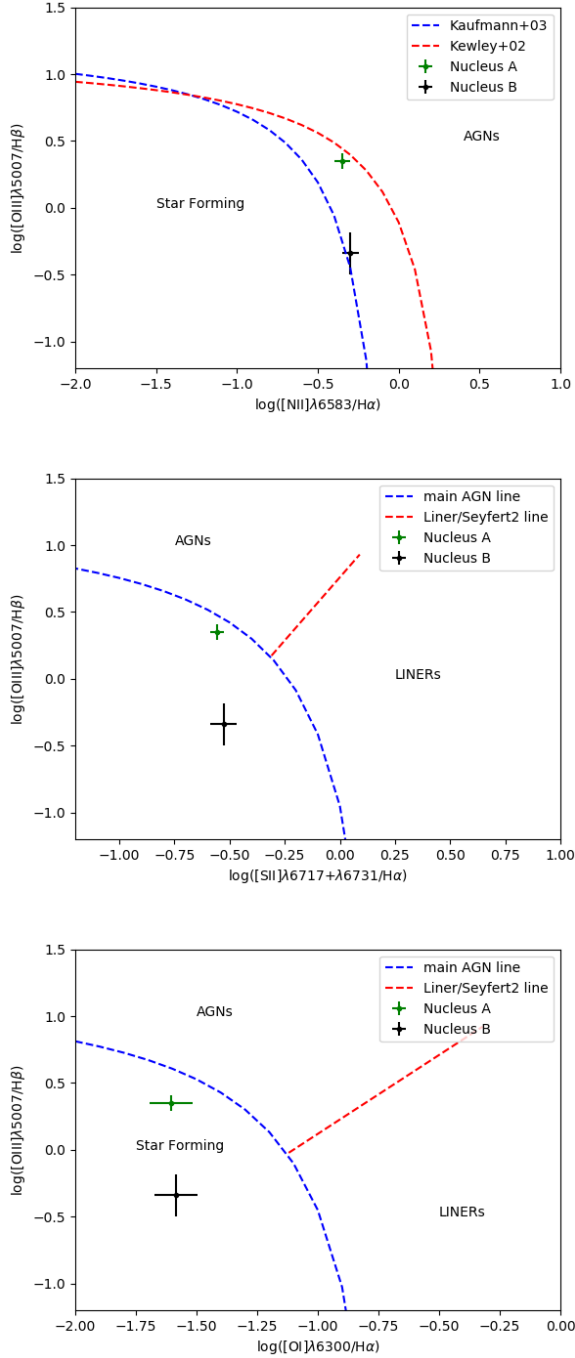


Fig. 7: Plots of $\log([\text{O III}]\lambda 5007/\text{H}\beta)$ vs $\log([\text{N II}]\lambda 6583/\text{H}\alpha)$, $\log([\text{O III}]\lambda 5007/\text{H}\beta)$ vs $\log([\text{S II}](\lambda 6717 + \lambda 6731)/\text{H}\alpha)$ and $\log([\text{O III}]\lambda 5007/\text{H}\beta)$ vs $\log([\text{O I}]\lambda 6300/\text{H}\alpha)$. The green point represents nucleus A and the black point represents nucleus B. The data points have been calculated for an aperture of 1 arcsec.

$\text{H}\beta$ broad line, R_{BLR} is the size of the BLR and G is the gravitational constant. We used the FWHM values obtained from the Gaussian fit procedure to calculate the mass of the central

SMBH. The size of the BLR and the luminosity of the AGN are related to each other by an approximate relation of the form: $R_{\text{BLR}} \propto L^{1/2}$ (Shields & Peterson 1994). Thus, the luminosity of the AGN continuum can be used to represent the extent of the BLR. The dimensionless factor, ' f ', called the virial factor, subsumes within it the effects of everything concerning BLR geometry, its inclination, the kinematics that govern the region, and everything else that is not known to us. The value of ' f ' is different for every individual AGN but is expected to be of the order of unity. An average value of ' f ' can be calculated by normalising the AGN $M_{\text{BH}} - \sigma_*$ relationship to that of quiescent galaxies (Peterson 2010).

Since the $\text{H}\beta$ line in our data falls towards the end of the blue spectrum, where the dichroic splits the light into blue and red components, it is better to use the line width and the luminosity of the $\text{H}\alpha$ line instead. The relations used to relate the luminosity and the FWHM of the $\text{H}\alpha$ line to the continuum luminosity and the FWHM of the $\text{H}\beta$ line are taken from Greene & Ho (2005) and Woo et al. (2015). Finally, the equation used to calculate the mass of the black hole is:

$$M_{\text{BH}} = f \times 10^{6.544} \left(\frac{L_{\text{H}\alpha}}{10^{42} \text{ erg s}^{-1}} \right)^{0.46} \left(\frac{\text{FWHM}_{\text{H}\alpha}}{10^3 \text{ km s}^{-1}} \right)^{2.06} M_{\odot}. \quad (9)$$

The value of f for FWHM-based method was adopted to be 1.12 (Woo et al. 2015). The FWHM of the broad $\text{H}\alpha$ line was taken to be the FWHM of the overall broad component from the $\text{H}\alpha + [\text{N II}]$ complex, while the luminosity was calculated as the sum of the luminosities of the two broad components. With the Hubble constant taken to be $H_0 = 69.6 \text{ km s}^{-1}$, the mass of the central SMBH is calculated to be approximately $2 \times 10^7 M_{\odot}$. We refrain from stating formal error estimates since the relations we used have intrinsic scatter and the value should be taken to be an order of magnitude estimate.

4.3.2. Mass of the black hole for nucleus B

In the absence of broad line features, the $M_{\text{BH}} - \sigma_*$ relation can be used to estimate the mass of the central black hole of a galaxy, where σ_* is the stellar velocity dispersion of the galactic bulge. The $M_{\text{BH}} - \sigma_*$ relation, called the Faber Jackson law for black holes (Merritt 2000), has undergone several changes over the years with regards to the power of σ_* . The relation used here was put forth by McConnell et al. (2011) and takes the form:

$$\frac{M_{\text{BH}}}{10^8 M_{\odot}} \approx 1.9 \left(\frac{\sigma_*}{200 \text{ km s}^{-1}} \right)^{5.1}. \quad (10)$$

The stellar velocity dispersion of the galaxy was found by fitting a stellar template to the optical spectrum of the galaxy using the pPXF package (version v6.7.6), developed by Michele Cappellari (Cappellari 2017; Cappellari & Emsellem 2004). The pPXF package can fit a large set of stellar templates without encountering a template mismatch due to different ranges of wavelength. We used the stellar spectra from the MILES library (Vazdekis et al. 2010) to fit the stellar template to our data. The MILES library consists of synthetic single-age, single-metallicity stellar populations over the full optical spectral range. The value of σ_* obtained from the fitting was $139 \pm 32 \text{ km s}^{-1}$. Plugging this in Equation 10, the mass of the black hole for nucleus B is calculated to be approximately $3 \times 10^7 M_{\odot}$. As with nucleus A, the value for the mass of the central SMBH should be taken as an order of magnitude estimate since the relations we use have intrinsic scatter which deters us from making a formal error estimation.

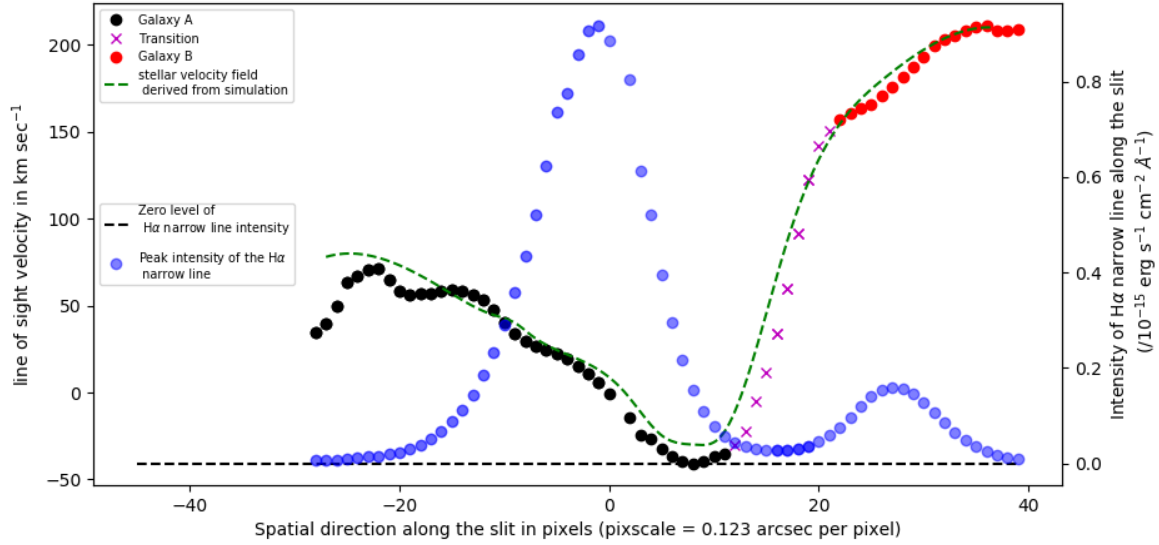


Fig. 8: Line-of-sight velocity in km s^{-1} calculated from the $\text{H}\alpha$ narrow line vs the radial distance from the centre of nucleus A in pixels. The pixel scale is $0.123 \text{ arcsec per pixel}$. Overplotted is the intensity profile of the $\text{H}\alpha$ narrow line. The black dashed line represents the intensity = 0 level for the $\text{H}\alpha$ line. The zero of the x-axis represents the point of highest intensity of the $\text{H}\alpha$ narrow line. The dashed green line represents the stellar velocity field derived from our simulations explained in Section 5.3.2.

4.4. Masses of the galaxies

Finally, we used mass to light ratio to estimate the masses of the individual galaxies. To do this, we used an average mass to light ratio of $\sim 200 h M_{\odot}/L_{\odot}$ from Gonzalez et al. (2019), for close galaxy pairs in the optical regime. We used the continuum luminosities calculated at various distances from the centre to fit Sersic profiles for both of the galaxies, and used these to get integrated values of the luminosities of the entire galaxies. Then we plugged this value of luminosity in the mass to light ratio to estimate the mass of the galaxy. We excluded the central arcsec while fitting the Sersic profile in order to disconsider the contribution from the centre of the galaxy. This yielded values of approximately $2 \times 10^{12} M_{\odot}$ for galaxy A and approximately $6 \times 10^{11} M_{\odot}$ for galaxy B. These values seem to be in agreement with the general galaxy mass estimates. However, we note that as the galaxies are interacting with each other, there must be intermixing of gas, which is not properly accounted for here. This can lead to an overestimation or underestimation of mass as we cannot be sure whether the contribution to luminosity at any particular point comes from one or two galaxies. Consequently, the values of mass quoted here should be taken as order of magnitude estimates.

5. Simulation

While we could ascertain some of the properties of the galaxies from the data available to us, it is interesting to understand the initial conditions of the participant galaxies. For this, simulations play a big role in increasing our understanding. The current morphology of the system provides an inkling regarding the angles at which the galaxies might have approached each other. We must keep in mind, though, that since what we see is the two-dimensional projection of the three-dimensional morphol-

ogy on the plane of the sky, one projection might be explained by many different 3D models. Projection effects could cause tidal tails to cross and might lead to association with the 'incorrect' galaxy, for example, Antennae galaxies have crossing tidal tails. Additionally, one model might be used to explain different structures by introducing different viewing angles, for example, Scharwächter et al. (2004) report a multi-particle model for the QSO 3C48 with conditions similar to those used to interpret the appearance of the Antennae galaxies but with a different viewing angle. Our aim in building the simulation is to model a spatial and kinematical look-alike of SDSS J134420.86+663717.8, and shed some light on one of the possible sets of initial conditions.

5.1. Basis of our simulation

A visual inspection of the image of the object while keeping in mind the properties determined from the analysis in Section 4 supplied a vague idea regarding the initial conditions. The galaxies are at different redshifts and have almost equally massive central SMBHs. The tidal tail of the galaxy at higher redshift appears elongated and extended, while the tidal tail of the galaxy at lower redshift appears to be foreshortened in comparison. The foreshortening might be a result of the viewing angle being such that we look at the tidal tail edge-on. With this in mind, we looked at a model of interacting galaxies presented by Barnes & Hernquist (1996) and Barnes & Hernquist (1998). They presented eight different sets of encounter parameters and studied the outcomes for the case of two equal mass galaxies.

The models consisted of three types of matter, namely stars, dark matter, and interstellar gas. Barnes & Hernquist (1996) assumed that the stars and the dark matter could be described by the collisionless Boltzmann equation, whereas the gas was modelled by the standard laws for a compressible fluid along with gravitational forces, radiative cooling, and shock heating. Pois-

son's equation was used to obtain the gravitational field generated by the stars, dark matter, and gas. The bulge to disk to halo mass ratio was taken to be 1:3:16, with the gas contributing 10% of the disk mass. We focused on one of the eight scenarios presented in Barnes & Hernquist (1996): encounter A, as, coincidentally, the outcome of this scenario resembles SDSS J134420.86+663717.8 most closely.

The parameters for this parabolic encounter are: pericentric separation $R_p = 0.2$, $i_1 = 71$, $\omega_1 = 30$, $i_2 = 0$, $\omega_2 = 0$, and total number of particles $N = 10,112$. The parameters, ' i ' and ' ω ', describe the inclination of the orbit to the spin plane of the galaxy, and the angle between the node and the point of closest approach to the center of the disk without being disrupted, respectively, as defined and used by Toomre & Toomre (1972). They used a length unit of 40 kpc and a time unit of 250 Myr. The paper (Barnes & Hernquist 1996) shows pictorial representations of the objects at various time steps and explains each step in careful detail. Figure 9 shows their simulated result that resembles SDSS J134420.86+663717.8 most closely. A comparison with Figure 1 reveals striking similarities in their morphology. However, there was still some difference in the morphology of the Barnes and Hernquist Model (hereafter referred to as the B&H Model) and the SDSS image, for example, the line connecting the two nuclei in the B&H Model should have a slight tilt to resemble the SDSS image, the tip of the tidal tail associated with nucleus B is on the same level as nucleus B in the B&H Model, while this is not the case in the SDSS image, the tidal tail associated with nucleus A is much longer in the B&H Model as compared to the SDSS image. Moreover, both of the tidal tails are equally prominent. This is not the case for SDSS J134420.86+663717.8. Having been thus convinced about the similarities and the differences between the B&H Model and the SDSS image, we used these parameters as a starting point in our N-body simulation to see if it would yield a better result with some modifications and help shed some light on the initial conditions of the two galaxies. We started with the parameters used by Barnes & Hernquist (1996) and kept modifying them until we reached a point where the result of the simulation looked most alike SDSS J134420.86+663717.8. We present our results in the next section.

5.2. N-body simulation

In their paper, Toomre & Toomre (1972) used three body calculations between the two central masses and each of the particles in the disk to demonstrate that bridges and tails can form due to tidal kinematic interactions. We used their model as a base, but in order to obtain more detailed knowledge of the orbital elements and the orientation of the hosts, we employed N-body calculations. A predictor-corrector method was used and implemented based on the description of the code and the algorithms in Aarseth (2003).

5.2.1. Method

If we consider particles to be subject to gravitational forces only, the forces would vary smoothly with respect to time. In such a case, a polynomial fit could be applied to the force (or acceleration), and force at time $t_0 + \Delta t$ could be predicted via extrapolation. N-body simulations have been used to study a wide range of problems, for example: tidal disruptions of dwarf spheroidal galaxies orbiting the Milky Way (Oh et al. 1995).

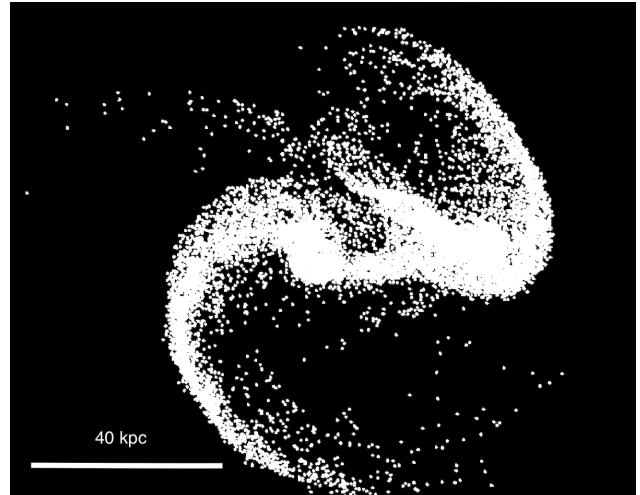


Fig. 9: Simulated SDSSJ134420.86+663717.8 look-alike ≈ 375 Myr after the first collision. Comparison with Figure 1 shows striking similarities between SDSSJ134420.86+663717.8 and the model. Two distinct nuclei are visible, along with the extensive tidal tail associated with nucleus B, which is the nucleus to the left in the image above. Credit: (Barnes & Hernquist 1996)

Instead of initialising each point individually, we used twelve parameters to set the starting conditions of the system: accuracy parameter η , softening parameter or Plummer constant ϵ , number of galaxies, number of particles N , outer radius, central mass, galactic mass ratios, velocity factors, rotations, translations, velocity transformations, and the output time step. The initial structure of our galaxies was that of two disc galaxies, with an outer disc which has the same mass as the central bulge. We set the number of particles N , number of rings, a radius of the outer ring, and a mass of the entire galaxy to generate our galaxy-like structure. For this case, we used an outer radius of 30 kpc, with twenty particles in the outer ring and ten particles in the inner ring, and an additional particle as the galactic centre, that is, bulge, molecular zone, and inner portion of the disc. The outer particles were spaced equally in an outer ring of radius $R = 30$ kpc, while the ten inner particles were spaced equally in an inner ring at radius 15 kpc, such that all particles had the same arc length separation to their respective 'left' and 'right' neighbours. The mass of the central particle was taken to be $10^{11} M_{\odot}$ and is equal to the mass of all other particles. We do not explicitly consider a description of an extended mass distribution at the centre, like a bulge or a central molecular zone, due to the small number of particles, but approximate the mass distribution of the cloud through our central particle. This assumption, therefore, does not contradict our bulge mass estimates of approximately $10^8 M_{\odot}$ for both of the galaxies, since the bulge mass values were derived for the central $2''$, while the central particle here spans approximately $5''$ in diameter. The values of the galaxy masses are in good agreement with the values obtained dynamically in Section 4.4. We initialised the galaxies with velocities of 50 pc Myr^{-1} for the blue (galaxy A) galaxy and -125 pc Myr^{-1} for the red (galaxy B) galaxy. We chose these values based on the velocity difference calculated from the rotation curve. However, we also tried larger and smaller values for the velocities of both galaxies in various combinations and concluded that the velocity values obtained from the observed data yield the most 'lookalike' results,

Table 4: Initialisation conditions for the simulation

Variable	Value	Units
Number of galaxies	2	n.a
N	[20,10]	n.a
Outer radius	30	kpc
Central mass	10^{11}	M_{\odot}
Galaxy mass ratios	[1, 1]	n.a
Rotations around x-axis	$[-17\pi/36, \pi/18]$	radians
Rotations around y-axis	[0, 0]	radians
Rotations around z-axis	$[-\pi/18, 0]$	radians
Galaxy 1 velocity factors	[1.32, 1.03]	n.a
Galaxy 2 velocity factors	[1.32, 1.03]	n.a
Galaxy 1 translation	[-30, -25, 0]	kpc
Galaxy 2 translation	[+30, +25, 0]	kpc
Galaxy 1 group velocity	[50, 5, 1]	pc/Myr
Galaxy 2 group velocity	[-125, -5, -1]	pc/Myr

spatially. Table 4 lists the starting parameters used to implement the simulation.

5.2.2. Limitations

The major limitation of our code is the rather small number of particles used to define our galaxies. However, we note that the total number of particles considered by us ($3 < N_{\text{total}} < 100$) is within the range of 'typical particle number for applications' specified in Aarseth (2003) (pg. 107). We will now present two different factors to demonstrate the accuracy of our results, that is, conservation of energy and stability of a galaxy without tidal forces.

Let us first consider the latter point: to be able to state with any certainty that the structure of the final simulation is due to galactic tidal interactions, we should check how the galaxy behaves in the absence of tidal forces. We define stable galaxies with three different characteristic times: t_{start} : time at which we initialise the system, t_{symmetry} : time at which the galaxy first loses its initial structure, and t_{chaos} : time at which the galaxy first loses its symmetry. After t_{chaos} we cannot be certain that the galactic superstructures are caused by only tidal forces, they could as well be caused by the chaotic motion of the galaxies themselves. We refrain from crossing t_{chaos} ($t_{\text{chaos}} = 2500$ Myr in our case) in our analysis to guarantee the integrity of our results. Beyond t_{chaos} , the system loses symmetry.

Going back to the former point concerning the conservation of energy, we consider the total energy of the system for the duration of the simulation. Figure 10 shows the time evolution of the energy of a single stable galaxy. There is a significant loss in accuracy after 3000 Myr. We do not consider any values beyond this time for our merger simulation, as we consider this point to be an absolute break-down for the accuracy of our simulation. For $t < 3000$ Myr, the maximum energy change is $1.81 \times 10^{-6}\%$. We can compare this to the maximum energy change before t_{chaos} which is $1.22 \times 10^{-11}\%$. In our analysis we never surpass t_{chaos} .

5.3. Visualisation

Here, we show how the imaging and spectroscopy we present for this galaxy merger is matched by the simulations we performed.

5.3.1. Visualising the results from the simulation

In order to get a clear view of the distribution of matter predicted by the simulations and to have a higher degree of confidence regarding the structures involved, we run the simulation 15 times

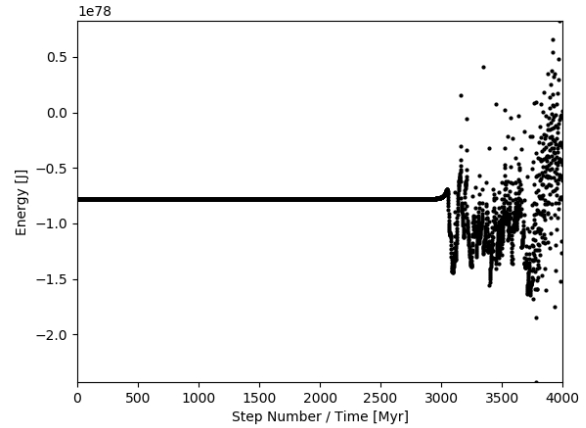


Fig. 10: Time evolution of the energy of a single stable galaxy. There is an absolute break down of accuracy beyond 3000 Myr. Our simulation does not extend beyond 375 Myr in time, which lies well within the time where energy conservation is rather accurate.

(each with 62 particles with 31 particles per galaxy) with minimal alterations to the starting conditions and overlap the resulting data to produce a single image with a total of 930 plotted points such that none of the single particles is of any particular interest.

To provide small alterations to the initial conditions, we rotate the galaxies around their rotation axis by small angles (five increments of $\pi/50$ each), and use three different radii (radial factors of 0.97, 1.00, and 1.03) for each of these five systems. We rotate the 3D Model that we get as the result of the simulation and flatten it so that we can view it at an angle which makes the system comparable to our view of SDSS J134420.86+663717.8. To estimate the inclinations of the galaxies in the result of the simulation, we rotate the Model by 90° around the z-axis, and then rotate it around the y-axis, such that the line of nodes is along the new line-of-sight (see Figure A.1). The rotated cube has an orientation such that it shows the planes of the galaxies to be almost orthogonal not only to each other but also to the new line-of-sight. This allows us to roughly estimate the inclination angles by looking at the original line of sight and the planes of the two galaxies. They are approximately 10° for the red galaxy and approximately 90° for the blue galaxy.

5.3.2. The predicted velocity field

Figure 11a shows the two-dimensional projection of the Model and Figure 11b shows the SDSS image of the galaxies. The comparison shows good similarities between them. The blue-coloured tail resembles the foreshortened tail associated with galaxy A to the south-west in the SDSS image, while the red-coloured tail looks like the arching tidal tail associated with galaxy B to the north-east in the SDSS image. The blue tail loops around the nucleus of the blue galaxy A in the model. The red tail seems to be foreshortened. Moreover, the distance between the nuclei also seems to be similar for both of the images - the simulation result and the data. Additionally, in Figure 11c we show the radial velocities predicted by our model. The north-western

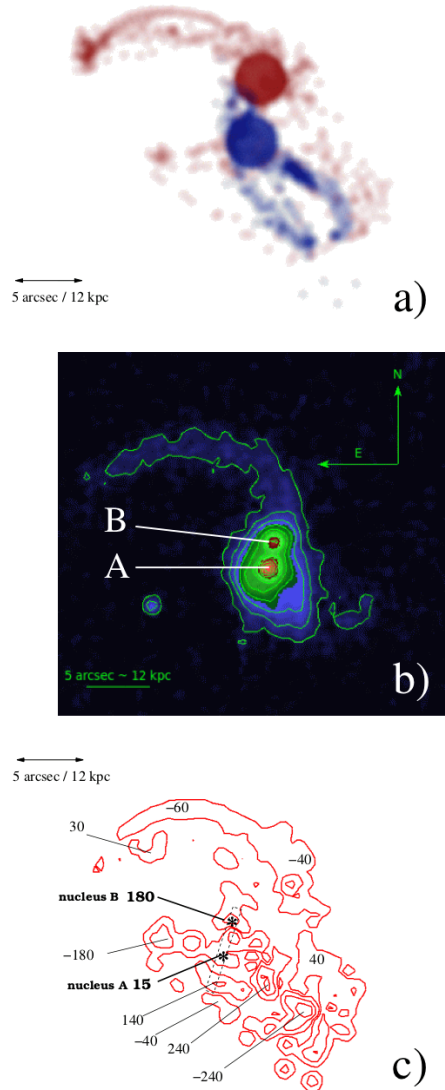


Fig. 11: Comparison of the SDSS image of the galaxies with the result of the simulation. The top panel (a) shows the model obtained using our N-body simulation with the general region of nucleus A (blue) and B (red) highlighted. The middle panel (b) shows the optical SDSS image of galaxies SDSS J134420.86+663717.8, superimposed with contours starting at 10% in steps of 10%. Comparison of the two figures shows striking similarities in their morphology, especially in the shapes of the two tidal arms. In the bottom panel (c), at an angular resolution of about 1 arcsec, we show a smoothed velocity map obtained from the simulated data cubes. Contour levels are -200, -100, -20, 20, 100, 200 km s⁻¹. The dashed rectangular box shows the aperture along which the velocities used to plot the dashed green lines in the rotation curve in Figure 8 were extracted.

tidal arm seems to have a rather uniform velocity distribution of around -60 km s⁻¹, while the region where the tail meets the galaxy B body has velocity of -40 km s⁻¹. The velocity rises in the main body of galaxy B, such that the nuclear region of galaxy B appears to have a velocity of around 180 km s⁻¹ as expected

from the line-of-sight velocity plot in Figure 8. From Figure 11a, we see that the southern part of the structure has a mixture of particles from both of the galaxies, such that the (blue) particles belonging to galaxy A are enveloped on the east and the west by the (red) particles belonging to galaxy B. This is reflected in the velocity map in Figure 11c, as well. We see an envelope of approximately -40 km s⁻¹ to the east and +40 km s⁻¹ to west of the central structure, which shows decreasing velocities going down to -240 km s⁻¹ to the south-west of nucleus A. The velocity distribution along the central part of the galaxy A structure shows a lot of variation, going from -240 km s⁻¹ at the south-west to 240 km s⁻¹ in the middle to 15 km s⁻¹ in the nuclear region. The velocity of the nuclear region for galaxy A is around 15 km s⁻¹. The velocities of the nuclear regions obtained from the model agree with the values estimated from the rotation curve in Figure 8.

5.3.3. Three dimensional projection

Figure 12 shows the three-dimensional projection of the simulated data. The 3D cube has been rotated so that the difference in the morphology of the galaxies based on the viewing angle is apparent. In Figure 12a we show, for completeness, the scenario as seen by the observer in the sky. Galaxy A (blue) to the south-west and galaxy B (red) to the north-east. In Figures 12(b-d), we show, successively, the view from directions in which either one or both the galaxies are seen edge on. We note that the galaxies remain orthogonal to each other even while interacting.

From Figure 12c, we see the blue-coloured system A almost face on. It is evident that the distribution of matter is highly asymmetric, and that the nucleus and a larger mass agglomeration lie almost on opposite sides of a ring-like structure. This corresponds to the images in Figure 11, and in particular in the velocity map in Figure 11c, to the nuclear region of galaxy A and to the very blue-shifted region of that system south of the nucleus A that coincides with the mass agglomeration in the south visible in the top and middle image in Figure 11a and Figure 11b. For the red-coloured system B we also find a highly asymmetric distribution of matter. This system can be seen almost face on in Figure 12b. Here, we have the well pronounced tidal arm to the north and the nuclear region of the B system that is attached to it. At larger distances from the nucleus B, we find highly disturbed matter associations that are offset in velocity from the tidal arm and the nucleus, and that have partially been lifted out of the red galactic disk (see also Figure 12d). Hence, we can understand why in the velocity map in Figure 11c, the highly blue-shifted part of galaxy A, showing extremely negative values of velocities, is embedded in the very extended matter from the B galaxy system, showing redshifted velocities mostly between -40 km s⁻¹ and 40 km s⁻¹.

The striking similarities between the model and the actual galaxies show that we are on the right path, and SDSS J134420.86+663717.8 could indeed be a product of an orthogonal interaction between two spiral galaxies.

6. Conclusions and summary

We present the optical long-slit spectroscopic data of SDSS J134420.86+663717.8, a pair of interacting galaxies. We study their optical spectra and analyse the nature of the two galaxies that form the object. Using diagnostic diagrams and based on the presence of broad Hydrogen recombination lines, we conclude that the mechanism responsible for emission in

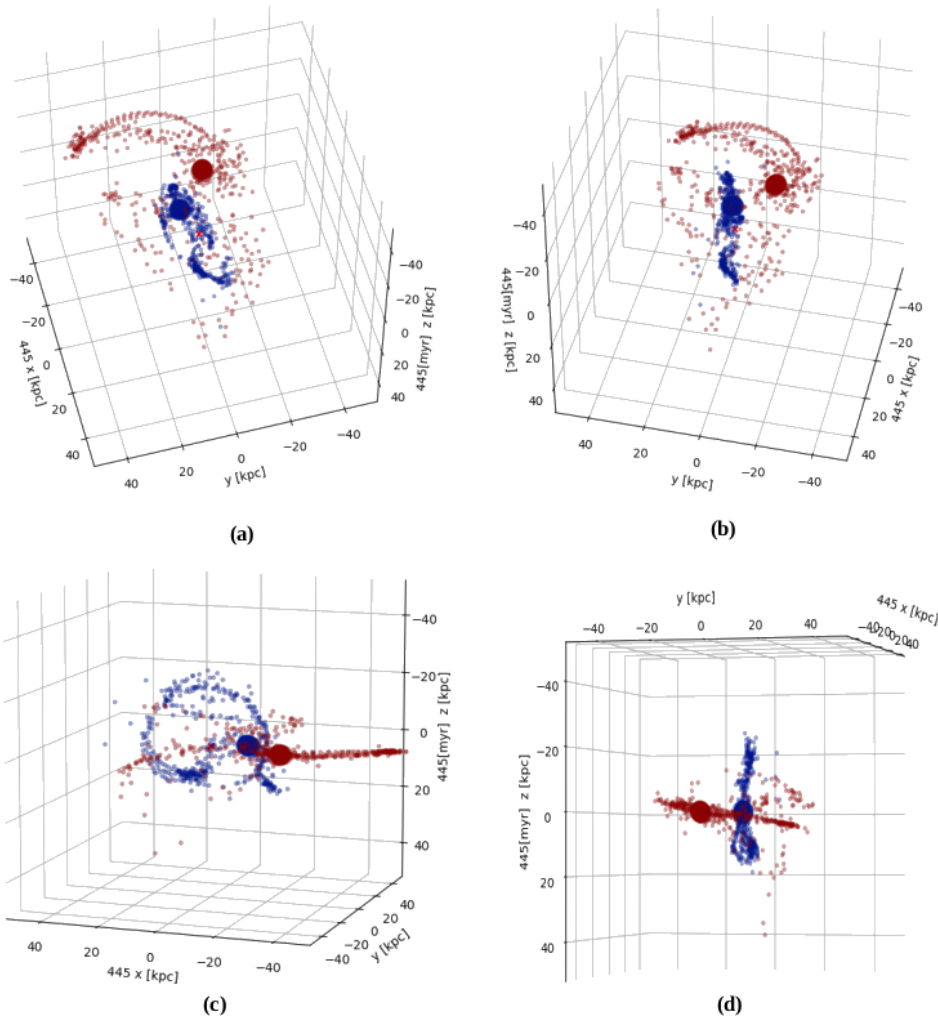


Fig. 12: Three-dimensional projection of the result of the simulation. The 3D plot has been rotated so as to view it from four different perspectives. We can see that the galaxies remain orthogonal to each other during the interaction.

the host of nucleus A is AGN-like, with Seyfert 1 properties, whereas nucleus B appears to be star-forming in nature. There appear to be two broad components for the Hydrogen recombination lines. This hints at a structure in the broad line region. There are almost equally massive SMBH at the centres of both host galaxies, with masses of a few times $10^7 M_{\odot}$. The $H\alpha$ rotation curve of galaxy A shows some asymmetry, while the rotation curve of galaxy B appears to be uniform. There is a transition phase in the $H\alpha$ rotation curve which appears to be different from the rotation curves corresponding to galaxies A and B. We attribute this to contributions from both of the galaxies. Additionally, we use a simple N-body simulation to understand the possible initial conditions of SDSS J134420.86+663717.8. With initial parameters of $R_p = 22.5$ kpc, $i_1 = -85^\circ$, $\omega_1 = -10^\circ$, $i_2 = 10^\circ$, and $\omega_2 = 0^\circ$, the outcome of the simulation resembles our object rather closely. We thus conclude that SDSS J134420.86+663717.8 is an ongoing merger of two almost orthogonal spiral galaxies with approximately equal masses. The galaxies appear to remain orthogonal during the process of interaction.

With almost equally massive hosts, SDSSJ134420.86+663717.8 constitutes a major merger. Major mergers are interesting as they can induce bursts of star-formation and feed the central SMBH, thus triggering an AGN phase (Casteels et al. (2014) and references therein). This appears to be true in the case of SDSSJ134420.86+663717.8. Nucleus A displays AGN behavior and has broad emission lines. Ellison et al. (2019) conclude that there is a connection between AGN triggering and merging at low z (<1) for optical and mid-IR selected AGN. SDSSJ134420.86+663717.8 seems to conform to this conclusion, although, as it is a single case, it cannot be used to support or contradict the general theories pertaining to the evolution of galaxies via mergers or interaction. Additionally, it is difficult to make a general statement for all AGN due to contradictory studies (e.g., Keel et al. (1985); Bessiere et al. (2012); Satyapal et al. (2014); Goulding et al. (2018), against: Gabor et al. (2009); Mechtley et al. (2016); Marian et al. (2019)). This requires a sample chosen based on similar criteria over the electromagnetic range.

Acknowledgements. The authors thank the anonymous referee for their constructive comments and suggestions.

Study of the conditions for star formation in nearby AGN and QSOs is carried out within the Collaborative Research Centre 956, sub-project [A02], funded by the Deutsche Forschungsgemeinschaft (DFG) – project ID 184018867.

Madeleine Yttergren received financial support for this research from the International Max Planck Research School (IMPRS) for Astronomy and Astrophysics at the Universities of Bonn and Cologne.

We made use of the Mods CCD Reduction package to reduce this data. modsCCDRed was developed for the MODS1 and MODS2 instruments at the Large Binocular Telescope Observatory, which were built with major support provided by grants from the U.S. National Science Foundation’s Division of Astronomical Sciences Advanced Technologies and Instrumentation (AST-9987045), the NSF/NOAO TSIP Program, and matching funds provided by the Ohio State University Office of Research and the Ohio Board of Regents. Additional support for modsCCDRed was provided by NSF Grant AST-1108693.

We made use of the NASA/IPAC Extragalactic Database (NED) and of the HyperLeda database.

References

- Aarseth, S. J. 2003, *Gravitational N-Body Simulations*
- Antonucci, R. 1993, *ARA&A*, 31, 473
- Arp, H. 1966, *ApJS*, 14, 1
- Baldwin, J. A., Phillips, M. M., & Terlevich, R. 1981, *PASP*, 93, 5
- Barnes, J. E. 2016, *MNRAS*, 455, 1957
- Barnes, J. E. & Hernquist, L. 1992, *ARA&A*, 30, 705
- Barnes, J. E. & Hernquist, L. 1996, *ApJ*, 471, 115
- Barnes, J. E. & Hernquist, L. 1998, *ApJ*, 495, 187
- Barnes, J. E. & Hernquist, L. E. 1991, *ApJ*, 370, L65
- Bessiere, P. S., Tadhunter, C. N., Ramos Almeida, C., & Villar Martín, M. 2012, *MNRAS*, 426, 276
- Boller, T., Bertoldi, F., Dennefeld, M., & Voges, W. 1998, *A&AS*, 129, 87
- Busch, G. 2016, *arXiv e-prints*, arXiv:1611.07872
- Cappellari, M. 2017, *MNRAS*, 466, 798
- Cappellari, M. & Emsellem, E. 2004, *PASP*, 116, 138
- Casteels, K. R. V., Conselice, C. J., Bamford, S. P., et al. 2014, *MNRAS*, 445, 1157
- Clutton-Brock, M. 1972a, *Ap&SS*, 16, 101
- Clutton-Brock, M. 1972b, *Ap&SS*, 17, 292
- Cole, S., Lacey, C. G., Baugh, C. M., & Frenk, C. S. 2000, *MNRAS*, 319, 168
- Condon, J. J., Cotton, W. D., Greisen, E. W., et al. 1998, *AJ*, 115, 1693
- Cox, T. J., Jonsson, P., Somerville, R. S., Primack, J. R., & Dekel, A. 2008, *MNRAS*, 384, 386
- Cutri, R. M., Wright, E. L., Conrow, T., et al. 2013, *Explanatory Supplement to the AllWISE Data Release Products*, Tech. rep.
- Di Matteo, T., Khandai, N., DeGraf, C., et al. 2012, *ApJ*, 745, L29
- Di Matteo, T., Springel, V., & Hernquist, L. 2005, *Nature*, 433, 604
- Dultzin-Hacyan, D., Krongold, Y., Fuentes-Guridi, I., & Marziani, P. 1999, *ApJ*, 513, L111
- Ellison, S. L., Mendel, J. T., Scudder, J. M., Patton, D. R., & Palmer, M. J. D. 2013, *MNRAS*, 430, 3128
- Ellison, S. L., Viswanathan, A., Patton, D. R., et al. 2019, *MNRAS*, 487, 2491
- Eneev, T. M., Kozlov, N. N., & Sunyaev, R. A. 1973, *A&A*, 22, 41
- Fan, L., Han, Y., Fang, G., et al. 2016, *ApJ*, 822, L32
- Fanidakis, N., Baugh, C. M., Benson, A. J., et al. 2012, *MNRAS*, 419, 2797
- Gabor, J. M., Impy, C. D., Jahnke, K., et al. 2009, *ApJ*, 691, 705
- Glikman, E., Simmons, B., Mailly, M., et al. 2015, *ApJ*, 806, 218
- Gonzalez, E. J., Rodriguez, F., Garcia Lambas, D., et al. 2019, *A&A*, 621, A90
- Gordon, Y. A., Owers, M. S., Pimbblet, K. A., et al. 2017, *MNRAS*, 465, 2671
- Goulding, A. D., Greene, E., Bezanson, R., et al. 2018, *PASJ*, 70, S37
- Greene, J. E. & Ho, L. C. 2005, *ApJ*, 630, 122
- Greene, J. E. & Ho, L. C. 2007, *ApJ*, 667, 131
- Groves, B. & Kewley, L. 2008, in *Astronomical Society of the Pacific Conference Series*, Vol. 390, *Pathways Through an Eclectic Universe*, ed. J. H. Knapen, T. J. Mahoney, & A. Vazdekis, 283
- Hewlett, T., Villforth, C., Wild, V., et al. 2017, *MNRAS*, 470, 755
- Hirschmann, M., Somerville, R. S., Naab, T., & Burkert, A. 2012, *MNRAS*, 426, 237
- Hodge, J. C. & Castelaz, M. W. 2003, *arXiv e-prints*, arXiv:0305022
- Hopkins, P. F., Bundy, K., Croton, D., et al. 2010a, *ApJ*, 715, 202
- Hopkins, P. F., Croton, D., Bundy, K., et al. 2010b, *ApJ*, 724, 915
- Hopkins, P. F. & Hernquist, L. 2009, *ApJ*, 694, 599
- Hopkins, P. F., Hernquist, L., Cox, T. J., et al. 2005b, *ApJ*, 630, 705
- Hopkins, P. F., Hernquist, L., Martini, P., et al. 2005a, *ApJ*, 625, L71
- Jiang, N., Wang, H., Mo, H., et al. 2016, *ApJ*, 832, 111
- Jog, C. J. 2002, *A&A*, 391, 471
- Johansson, P. H., Burkert, A., & Naab, T. 2009, *ApJ*, 707, L184
- Kauffmann, G., Heckman, T. M., Tremonti, C., et al. 2003, *MNRAS*, 346, 1055
- Kauffmann, G., White, S. D. M., & Guiderdoni, B. 1993, *MNRAS*, 264, 201
- Keel, W. C., Kennicutt, R. C., J., Hummel, E., & van der Hulst, J. M. 1985, *AJ*, 90, 708
- Kewley, L. J., Dopita, M. A., Sutherland, R. S., Heisler, C. A., & Trevena, J. 2001, *ApJ*, 556, 121
- Kewley, L. J., Nicholls, D. C., & Sutherland, R. S. 2019, *ARA&A*, 57, 511
- Koulouridis, E., Plionis, M., Chavushyan, V., et al. 2006, *ApJ*, 639, 37
- Lotz, J. M., Davis, M., Faber, S. M., et al. 2008, *ApJ*, 672, 177
- Lotz, J. M., Jonsson, P., Cox, T. J., & Primack, J. R. 2010a, *MNRAS*, 404, 575
- Lotz, J. M., Jonsson, P., Cox, T. J., & Primack, J. R. 2010b, *MNRAS*, 404, 590
- Mantha, K. B., McIntosh, D. H., Brennan, R., et al. 2018, *MNRAS*, 475, 1549
- Marian, V., Jahnke, K., Mechtley, M., et al. 2019, *ApJ*, 882, 141
- Markwardt, C. B. 2009, in *Astronomical Society of the Pacific Conference Series*, Vol. 411, *Astronomical Data Analysis Software and Systems XVIII*, ed. D. A. Bohlender, D. Durand, & P. Dowler, 251
- McConnell, N. J., Ma, C.-P., Gebhardt, K., et al. 2011, *Nature*, 480, 215
- McGaugh, S. S. 2012, *AJ*, 143, 40
- McGaugh, S. S., Schombert, J. M., Bothun, G. D., & de Blok, W. J. G. 2000, *ApJ*, 533, L99
- Mechtley, M., Jahnke, K., Windhorst, R. A., et al. 2016, *ApJ*, 830, 156
- Merritt, D. 2000, in *American Astronomical Society Meeting Abstracts*, Vol. 196, *American Astronomical Society Meeting Abstracts #196*, 21.21
- Mihos, J. C. & Hernquist, L. 1994, *ApJ*, 431, L9
- Mihos, J. C. & Hernquist, L. 1996, *ApJ*, 464, 641
- Moran, E. C., Halpern, J. P., & Helfand, D. J. 1996, *ApJS*, 106, 341
- Moshir, M. & et al. 1990, *IRAS Faint Source Catalogue*, 0
- Newville, M., Stensitzki, T., Allen, D. B., et al. 2016, *LmfIt: Non-Linear Least-Square Minimization and Curve-Fitting for Python*
- Oh, K. S., Lin, D. N. C., & Aarseth, S. J. 1995, *ApJ*, 442, 142
- Oke, J. B. 1990, *AJ*, 99, 1621
- Osterbrock, D. E. & Pogge, R. W. 1985, *ApJ*, 297, 166
- Paturel, G., Petit, C., Prugniel, P., et al. 2003, *A&A*, 412, 45
- Peterson, B. M. 2010, in *IAU Symposium*, Vol. 267, *Co-Evolution of Central Black Holes and Galaxies*, ed. B. M. Peterson, R. S. Somerville, & T. Storchi-Bergmann, 151–160
- Pfleiderer, J. 1963, *ZAp*, 58, 12
- Pfleiderer, J. & Siedentopf, H. 1961, *ZAp*, 51, 201
- Pogge, R. 2019, *rwpgol/modsCCDRed 2.0*, modsCCDRed was developed for the MODS1 and MODS2 instruments at the Large Binocular Telescope Observatory, which were built with major support provided by grants from the U.S. National Science Foundation’s Division of Astronomical Sciences Advanced Technologies and Instrumentation (AST-9987045), the NSF/NOAO TSIP Program, and matching funds provided by the Ohio State University Office of Research and the Ohio Board of Regents. Additional support for modsCCDRed was provided by NSF Grant AST-1108693.
- Pogge, R. W., Atwood, B., Brewer, D. F., et al. 2010, in *Society of Photo-Optical Instrumentation Engineers (SPIE) Conference Series*, Vol. 7735, *Proc. SPIE*, 77350A
- Ricci, C., Bauer, F. E., Treister, E., et al. 2017, *MNRAS*, 468, 1273
- Rich, J. A., Kewley, L. J., & Dopita, M. A. 2014, *ApJ*, 781, L12
- Satyapal, S., Ellison, S. L., McAlpine, W., et al. 2014, *MNRAS*, 441, 1297
- Scharwächter, J., Eckart, A., Pfalzner, S., et al. 2004, *A&A*, 414, 497
- Schneider, D. P., Fan, X., Hall, P. B., et al. 2003, *AJ*, 126, 2579
- Schneider, D. P., Richards, G. T., Fan, X., et al. 2002, *AJ*, 123, 567
- Seibert, M., Wyder, T., Neill, J., et al. 2012, in *American Astronomical Society Meeting Abstracts*, Vol. 219, *American Astronomical Society Meeting Abstracts #219*, 340.01
- Shields, J. C. & Peterson, B. M. 1994, *Comments on Astrophysics*, 17, 241
- Springel, V., Di Matteo, T., & Hernquist, L. 2005, *MNRAS*, 361, 776
- Steinborn, L. K., Hirschmann, M., Dolag, K., et al. 2018, *MNRAS*, 481, 341
- Struck, C. 1999, *Phys. Rep.*, 321, 1
- Toomre, A. & Toomre, J. 1971, in *BAAS*, Vol. 3, 390
- Toomre, A. & Toomre, J. 1972, *ApJ*, 178, 623
- Torres-Flores, S., Epinat, B., Amram, P., Plana, H., & Mendes de Oliveira, C. 2011, *MNRAS*, 416, 1936
- Torrey, P., Vogelsberger, M., Genel, S., et al. 2014, *MNRAS*, 438, 1985
- Treister, E., Schawinski, K., Urry, C. M., & Simmons, B. D. 2012, *ApJ*, 758, L39
- Tully, R. B. & Fisher, J. R. 1977, *A&A*, 500, 105
- Urrutia, T., Lacy, M., & Becker, R. H. 2008, *ApJ*, 674, 80
- Vazdekis, A., Sánchez-Blázquez, P., Falcón-Barroso, J., et al. 2010, *MNRAS*, 404, 1639
- Veilleux, S. & Osterbrock, D. E. 1987, *ApJS*, 63, 295
- Villforth, C., Hamilton, T., Pawlik, M. M., et al. 2017, in *Galaxy Evolution Across Time*, 9
- Vorontsov-Velyaminov, B. A. 1959, *Atlas and Catalog of Interacting Galaxies (1959)*, 0
- Vulcani, B., Poggianti, B. M., Moretti, A., et al. 2018, *ApJ*, 852, 94
- White, S. D. M. & Rees, M. J. 1978, *MNRAS*, 183, 341
- Woo, J.-H., Yoon, Y., Park, S., Park, D., & Kim, S. C. 2015, *ApJ*, 801, 38
- Wright, A. E. 1972, *MNRAS*, 157, 309
- Yabushita, S. 1971, *MNRAS*, 153, 97
- Yan, R., Newman, J. A., Faber, S. M., et al. 2018, *Astrophysics Journal*
- Zuther, J., Fischer, S., & Eckart, A. 2012, *A&A*, 543, A57
- Zwicky, F., Herzog, E., & Wild, P. 1968, *Catalogue of galaxies and of clusters of galaxies*

Appendix A: Estimation of the inclinations of galaxies

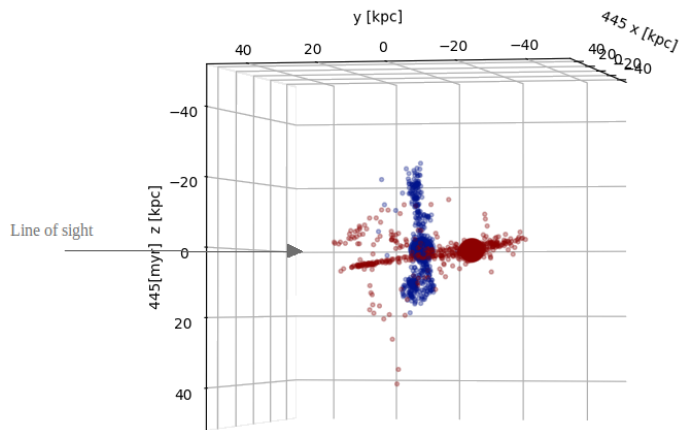


Fig. A.1: 3D model obtained as the result of the simulation is rotated by 90 degrees around the xy -plane, and then rotated about the z -axis such that the line of nodes is the new line of sight for us. The black arrow labelled 'Line of sight' shows the orientation of the plane containing the original line of sight. It can be seen that the galaxies are mutually orthogonal to each other. Additionally, the red galaxy lies along the plane of sight, while the blue galaxy is perpendicular to it.

Paper III (in prep.): The peculiar optical spectrum of Mrk231

Continuing the trend started with the first two projects, the third project of my doctoral work focuses on the optical long-slit spectroscopy study of a late-stage merger, Mrk231. Mrk231 hosts a highly energetic centre that seems to be a consequence of the collision of at least two galaxies. It is extremely bright in the infrared regime and is classified as an ultra-luminous infrared galaxy. Additionally, the optical spectrum of Mrk231 displays several broad absorption and emission lines.

The main goal of this project was to study the central region of Mrk231 and understand the physical processes responsible for the peculiar characteristics in its spectra. Additionally, we carefully examined acquisition images taken at the start of the spectroscopy observations for possible clues about the interaction history of Mrk231 that might help shed light on the unusual nature of its central region.

The results of this project are being prepared to be published in the peer-reviewed journal, *Astronomy & Astrophysics*. A draft of this article is presented below.

The peculiar optical spectrum of Mrk231[★]

Persis Misquitta^{1★★}, Benita Dünnebiel¹, Andreas Eckart^{1,2}

¹ I. Physikalisches Institut, Universität zu Köln, Zùlpicher Str. 77, 50939, Köln, Germany

² Max-Planck Institut für Radioastronomie (MPIfR), Auf dem Hùgel 69, 53121 Bonn, Germany

Received ; accepted

ABSTRACT

Markarian 231 (Mrk231) is one of the closest and one of the brightest ultra-luminous infrared galaxies that is supposed to be in the late stage of galaxy merger. The multi-wavelength spectrum of Mrk231 presents peculiar features and has been the subject of detailed previous study.

In this paper, we focus on the optical long slit spectroscopy study of the central arcsecond of Mrk231, as well as six off-nuclear spectral positions, observed using the multi object double spectrographs at the Large Binocular Telescope. Additionally, acquisition images taken before the spectroscopic observations were examined carefully.

We find that the nuclear as well as off-nuclear spectra of Mrk231 exhibit broad H α emission lines, which could be attributed to high velocity outflows from the nucleus of Mrk231 as well as extreme circum-nuclear starburst. The narrow H α emission line has two additional components in every spectrum, which is indicative of low velocity outflows. The region to the south of the nucleus exhibits weak H β emission compared to the regions to the north that show no or very weak H β emission. The continuum has a stronger blue component in the south compared to the north. The central spectrum has prominent broad absorption lines at a redshift of ~ 0.0262 , which is lower than the redshift of the emission line system, ~ 0.0422 . Broad absorption lines belonging to at least three systems are present in all of the off-nuclear spectra, but the regions to the south have more prominent absorption lines belonging to the system that is at the same redshift as the absorption lines in the central spectrum, while all three systems have absorption lines of similar strength in the regions to the north. A careful examination of the acquisition images of Mrk231 shows that there is diffuse emission in the region adjacent to the northern tail, extending in the north-east direction almost orthogonally, that might be an indication of past interaction of the system with a third galaxy.

Key words. galaxies: interactions - galaxies: active - galaxies: kinematics and dynamics - galaxies: starburst - galaxies: evolution - methods: numerical

1. Introduction

Interacting galaxies provide an excellent environment for both, the rapid growth of supermassive black holes (SMBHs) via accretion as well as enhanced star-formation. Ultra-luminous infrared galaxies (ULIRGs) are proposed to represent an advanced phase of interacting galaxies, where the active galactic nucleus (AGN) is initially dust-enshrouded, before the combination of radiation pressure and supernova explosions sets in to clear the dust, thereby exposing the central optical quasar (Sanders et al. 1988a,b; Veilleux et al. 2009; Hickox & Alexander 2018).

At a redshift of ~ 0.042 (Adams & Weedman 1972; Bok-
senberg et al. 1977; Lipari et al. 2009), Mrk231 is the closest radio-quiet ULIRG to us, and therefore, has been much studied over the years, in various wavelength regimes (e.g., gamma rays: Dermer et al. (1997), X-rays: Eales & Arnaud (1988); Turner (1999); Maloney & Reynolds (2000); Gallagher et al. (2002); Turner & Kraemer (2003); Piconcelli et al. (2013); Teng et al. (2014); Veilleux et al. (2014), ultraviolet (UV): Lipari et al. (1994); Veilleux et al. (2013, 2016); Yang et al. (2018), optical: Boksenberg et al. (1977); Hutchings & Neff (1987); Hamilton

& Keel (1987); Boroson et al. (1991); Lipari et al. (1994); Carilli et al. (1998); Lai et al. (1998); Rupke et al. (2005); Lipari et al. (2009), infrared (IR): Rieke (1976); Cutri et al. (1981); Roche et al. (1983); Armus et al. (1994); Soifer et al. (2000), radio: Baan (1985); Hutchings & Neff (1987); Sanders et al. (1987); Richards et al. (2005); Krips et al. (2008); Fischer et al. (2010), millimetre/sub-millimetre (mm/submm): Papadopoulos et al. (2007); van der Werf et al. (2010); Aalto et al. (2012); Ciccone et al. (2012); Alatalo (2015); González-Alfonso et al. (2018)), since it was first catalogued as object 231 by Markarian (1969), as a galaxy with a strong ultraviolet continuum. One of the earliest optical spectroscopic studies of Mrk231 showed that it has a QSO-like spectrum (Adams & Weedman 1972). Several broad emission lines and multiple-component absorption lines were visible in the spectrum. The absorption lines were shown to be a composite type A stellar spectrum at a redshift similar to the emission lines originating in the nucleus (Adams 1972). Subsequent studies with better resolution revealed at least three absorption line systems, at redshifts of 8000, 6250, and 12900 kms^{-1} (Boksenberg et al. 1977), along with strong Fe II emission (Lipari et al. 1994). Mrk231 is now classified as an Fe II emitting, low ionisation, broad absorption line QSO (FeLoBAL QSO) (e.g., Lipari et al. (2005); Lipari et al. (2009)). Broad absorption line (BAL) systems that have low-ionisation absorption lines as well as emit Fe II are called FeLoBAL QSOs (Becker

[★] This paper uses data taken with the MODS spectrographs built with funding from NSF grant AST-9987045 and the NSF Telescope System Instrumentation Program (TSIP), with additional funds from the Ohio Board of Regents and the Ohio State University Office of Research.
^{★★} e-mail: misquitta@ph1.uni-koeln.de

Table 1: Observational details

Obs. date	PA degrees	Region	No. of exp.	Exp. time s	Total int. time s
28.04.2022	230	Centre	2	700	1400
28.04.2022	230	-2'' offset	2	700	1400
28.04.2022	230	+2'' offset	2	700	1400
28.04.2022	265	Centre	2	700	1400
28.04.2022	265	-2'' offset	2	700	1400
28.04.2022	265	+2'' offset	2	700	1400
29.04.2022	340	Centre	2	350	700
28.04.2022	355	Centre	2	700	1400
28.04.2022	355	-2'' offset	2	700	1400
28.04.2022	355	+2'' offset	2	700	1400

Notes. List of the position angles (PA) used to observe Mrk231 using MODS at the LBT. The date of observation (universal time), region observed, number of exposures, integration time per exposure, and total integration time for each slit position are also listed.

et al. 1997, 2000). The spectrum of FeLoBAL QSOs is supposed to be a superposition of continuous radiation from the accretion disc, the broad emission lines that form in the neighbouring region, and broad absorption lines that form when the continuum passes through a separate region, which is called the broad absorption line region (Branch et al. 2002). The distance between the broad emission and broad absorption line systems might account for the difference in the redshift of the systems. Baan (1985); Klöckner et al. (2003) detect strong hydroxyl (OH) megamaser emission in Mrk231. In order to have (OH) maser emission, there needs to be a potentially extended nuclear source that gives rise to radio continuum and ultraviolet radiation, along with dust to convert the UV radiation into IR that can then be used to pump foreground molecular gas (Baan 1985). A starburst triggered by galaxy-galaxy interaction could give rise to optimal conditions for such masing action to occur. Optical integral field spectroscopy confirmed the presence of an intense and young nuclear starburst (Lipari et al. 2009), leading to the general consensus that the continuum emission in the optical regime arises from the circum-nuclear starburst, while the active nucleus is responsible for the broad emission lines.

With a strong AGN as well as an extreme nuclear starburst, Mrk231 has been found to be the site of nuclear winds, outflows, galactic winds, super giant bubbles, and extreme supernovae and hypernovae (Lipari et al. 2009; Rupke & Veilleux 2011). Galactic winds play an important role in the evolution of galaxies (Veilleux et al. 2005; Fabian 2012). They can help to quench star formation within the galaxy by heating and/or ejecting the cool gas from the host (Veilleux et al. 2016). They are also considered to be the mechanism responsible for the self-regulatory growth of the black hole (BH) and the bulge component of the galaxy (e.g., Di Matteo et al. (2005), Murray et al. (2005), Veilleux et al. (2013)).

In this paper, we present the results from an optical spectroscopic study of Mrk231 carried out by using the multi object double spectrographs (MODS) at the large binocular telescope (LBT). This paper is organised as follows. We present details about the observations and data reduction in Section 2. In Section 3, we present the spectra from different regions of Mrk231, discuss our results in Section 4, and draw conclusions and summarise in Section 5

2. Observations and data reduction

Mrk231 was observed using MODS at the LBT in Tucson, Arizona, USA, on the 28th and 29th of April, 2022. The obser-

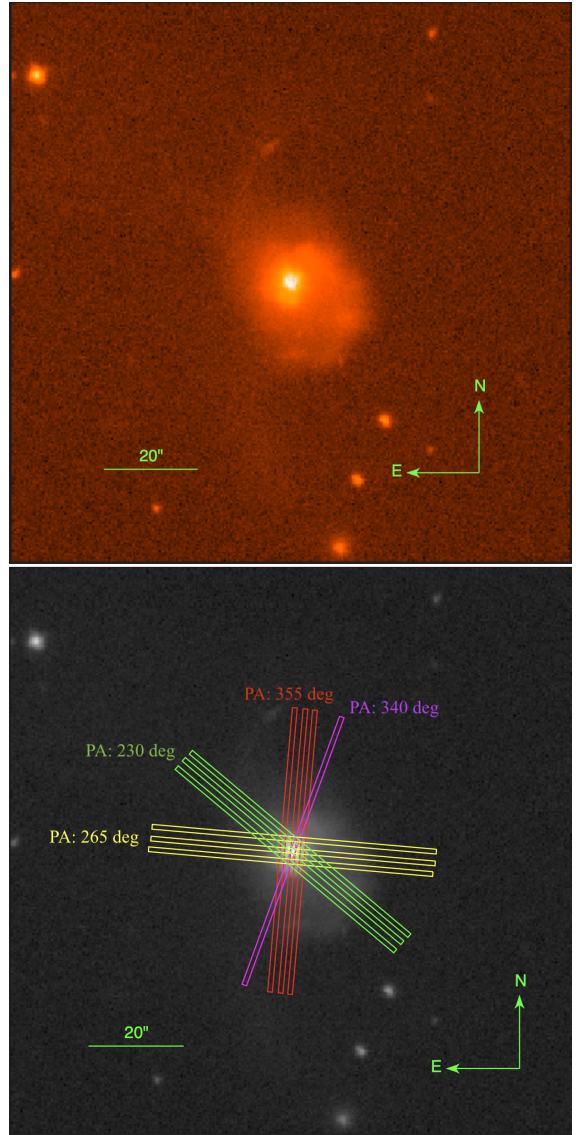


Fig. 1: Top: Coloured SDSS image of Mrk231. Bottom: SDSS image of Mrk231 in grayscale, overlaid with the slit positions used during observations. Green marks a position angle (PA) of 230°, blue marks a PA of 265°, magenta marks a PA of 340°, and red marks a PA of 355°. For PAs 230°, 265° and 355°, we took off-nuclear spectra at offsets of 2'' on either side of the central slit positions. In both images, North is up and East is to the left. The scale is indicated, as well.

ations were performed in binocular mode, with both MODS1 and MODS2 centred on the same source. The spectra have a wavelength coverage in the range 3200-10000 Å. A 1'' wide and 5' long slit was used for the observations. The seeing averaged 1.5''.

The top panel of Figure 1 shows an SDSS image of Mrk231, the source being studied in this paper, in heat colours. The intensely bright centre shows the site of the circum-nuclear starburst and the active galactic nucleus. The less bright host galaxy can be seen surrounding the central region. Additionally, two tidal arms, one moving northwards clockwise from the cen-

tral region and another moving in a counter-clockwise direction southwards from the central region, can be seen. The bottom panel shows the same SDSS image in greyscale, overlaid with the slit positions used for the observation.

Mrk231 was observed using four different position angles (PA) in total. The colour green is used to mark slit positions corresponding to a PA of 230° , yellow marks 265° , magenta marks 340° , and red marks 355° . Three out of the four PAs, 230° , 265° , and 355° , were observed with three slit positions: centre and offsets of $2''$ on either side of the centre. Additionally, all of the slit positions were dithered along the vertical axis by $10''$, culminating in two exposures per slit position and six exposures in total per PA. The integration time per exposure was 700 s. The fourth PA, 340° , was observed with the slit positioned through the centre of the galaxy and a vertical dither of $10''$, with half the exposure time of the exposures at other PAs, giving two exposures for this PA, with a 350 s integration time per exposure. The details of the observations can be found in Table 1.

The two-dimensional spectra were bias corrected using the MODS CCD reduction pipeline (Pogge 2019). Cosmic ray correction, wavelength and flux calibration, and one-dimensional spectral extraction were performed using Pyraf routines, adapted for Python from the IRAF spectral reduction manual¹. Wavelength calibration was performed using two-dimensional spectra of Hg, Ar, Ke, Xe, and Ne lamps observed with the dome of the telescope closed. Flux calibration was performed using the spectrophotometric standard star, BD+33d2642, observed on the first night of the observing run. The spectrophotometric standard star spectra underwent the same data reduction procedure as the science data. MODS1 and MODS2 spectra belonging to each slit position were combined after reduction to improve the signal-to-noise ratio. We were left with ten one-dimensional spectra, corresponding to each slit position, at the end of the data reduction and spectral extraction procedure: four from the centre and six from the offsetted positions. We further combined the four central spectra, since they were extracted over an aperture of $1''$. The resultant seven spectra are presented in the next section (3).

3. Spectra

In this section, we present the one-dimensional spectra extracted from the central $1''$ of Mrk231 and the offsetted positions around PAs 230° , 256° , and 355° , respectively. In each spectrum, the abscissa represents the observed wavelength in Angstroms, while the ordinate shows the flux density in $\text{erg s}^{-1} \text{cm}^{-2} \text{\AA}^{-1}$. The emission and absorption lines are identified and marked, with colour red for emission lines and blue for absorption lines.

3.1. Central $1''$

Figure 2 shows the one-dimensional spectrum of the central $1''$ of Mrk231. The most prominent emission line is the Balmer recombination line, $H\alpha$. Six gaussian components were required to fit the line. Figure 3 shows the Gaussian decomposition of the $H\alpha$ line. The broadest component has a full width at half maximum (FWHM) of $8594.4 \pm 70.3 \text{ km s}^{-1}$. Along with $H\alpha$, we see weak $H\beta$, weak $[\text{O II}]\lambda 3727$, extensive Fe II, and Na I D emission lines. The various emission lines, their line centres, fluxes, and FWHMs can be found tabulated in Table 2. The spectrum also shows one prominent set of absorption lines, the He I $\lambda 3889$, the Ca II H+K, and the Na I D absorption lines. A zoomed-in view

to the Gaussian fitting of the absorption lines in the blue band can be seen in Figure 4. To the left of the prominent blue band absorption lines, three other much weaker absorption lines can be seen. We're unable to ascertain the source of these weak absorption lines. Table 3 lists the line centres, fluxes and FWHMs of the prominent absorption lines. All of the prominent absorption lines are at the common redshift of ~ 0.0262 , while all of the emission lines, except $[\text{O II}]\lambda 3727$, are at the common redshift of 0.0425. $[\text{O II}]\lambda 3727$ is at the redshift of 0.0400. The redshifts across all the regions studied can be found in the Table 4.

3.2. Off-nuclear spectra

Figures 5, 8, 11, 12, 13, and 14 show the one-dimensional spectra extracted over apertures of $1''$ at a distance of $2''$ on either side of the centre of Mrk231 at position angles of 230° , 265° , and 355° each. This corresponds to a distance of $\sim 1.7 \text{ kpc}$ at the redshift of 0.042.

A quick look at the spectra reveals that we can group them into two categories. The first category consists of PA 230° with offset of $-2''$, PA 265° with offset of $-2''$, and PA 355° with offset of $+2''$. These spectra are extracted from regions to the south, south-east, and south-west of the centre of Mrk231. The second category is made up of PA 230° with offset of $+2''$, PA 265° with offset of $+2''$, and PA 355° with offset of $-2''$, and the spectra are extracted from regions to the north, north-east, and north-west of the centre of Mrk231. Spectra belonging to each category share a similar spectral shape and have similar spectral characteristics. In addition to this, all of the spectra share some common features.

3.2.1. General common features of off-nuclear spectra of Mrk231

The spectra show several emission and absorption lines. The most prominent emission line, as with the central spectrum, is the $H\alpha$ recombination line. However, at the distance of $\sim 1.7 \text{ kpc}$ from the centre, along with the centrally present $[\text{O II}]\lambda 3727$, other high ionisation emission lines are also present in the spectrum. These are the $[\text{O III}]\lambda 4959$, $[\text{O III}]\lambda 5007$, $[\text{O I}]\lambda 6300$, $[\text{N II}]\lambda 6548$, $[\text{N II}]\lambda 6583$, $[\text{S II}]\lambda 6716$, and $[\text{S II}]\lambda 6731$ emission lines. The intensity of these spectra is lower than the intensity of the central spectrum by an order of magnitude. At this distance from the centre of the galaxy, the emission from the host galaxy should contribute significantly to the spectrum, with the influence of the central AGN lessening. However, interestingly, for all of the off-nuclear spectra, we need one broad and three narrow components to fit the $H\alpha$ line along with two additional narrow components corresponding to the $[\text{N II}]\lambda 6548$ and $[\text{N II}]\lambda 6583$ emission lines. A zoomed-in view to the Gaussian fitting of the emission lines in the red band of the spectra from PA 230° with offsets of $-2''$ and $+2''$ can be seen in Figures 6 and 9, respectively. The emission lines observed, their line centres, fluxes, and FWHMs from each of the spectra can be found in Tables 5, 7, 9, 11, 13, and 15, respectively.

Along with emission lines, the prominent absorption lines visible in the central spectrum can be seen in these spectra, as well, i.e., the He I $\lambda 3889$, Ca II H+K, and the Na I D absorption lines. The redshift of the absorption line system remains the same as that for the central absorption line system at ~ 0.0262 , as does that of the emission line system at ~ 0.0426 . However, in addition to the absorption lines at redshift of ~ 0.0262 , at least two other absorption line systems are present in the off-nuclear spec-

¹ http://www.astro.iag.usp.br/~jorge/aga5802/spect_iraf_reducao.pdf

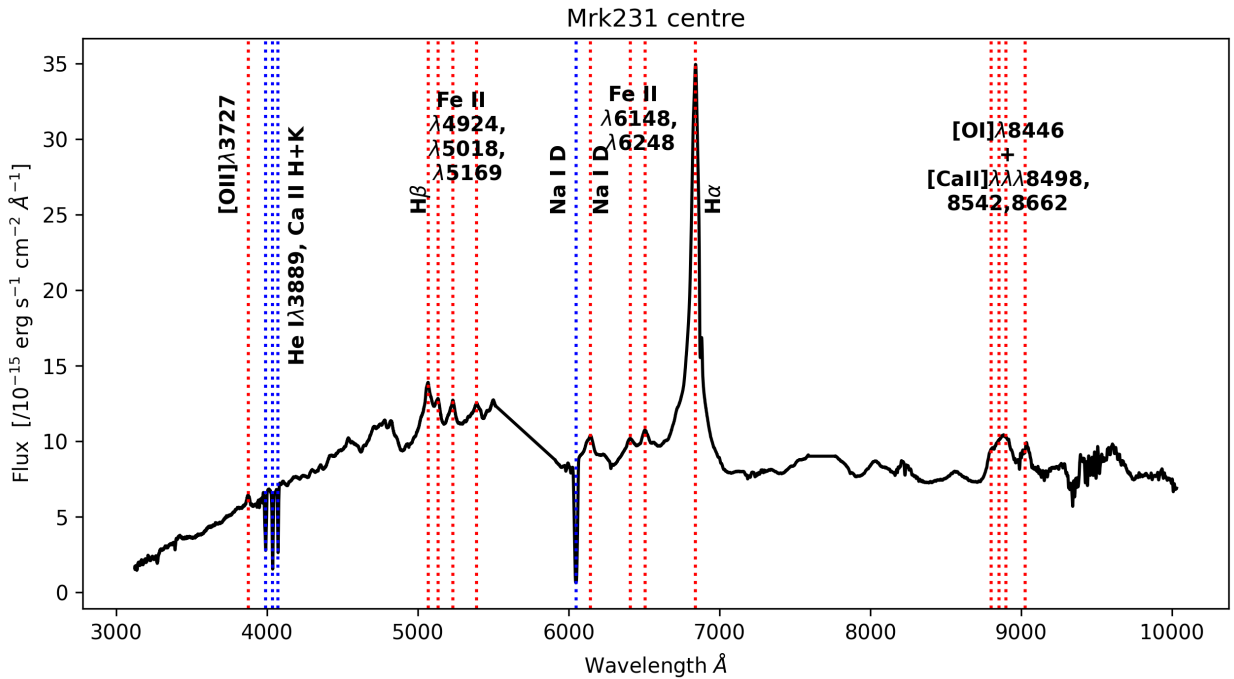


Fig. 2: The averaged one-dimensional observed optical spectrum of the central arcsec of Mrk231. The emission lines observed have been marked by vertical red dotted lines, while the blue vertical dotted lines mark absorption lines. The aperture size for spectral extraction is 1 arcsec. The wavelength axis depicts the observed wavelength.

Table 2: Mrk231 Centre Emission Line Data

Emission Line	Observed Wavelength (Å)	Uncertainty in Wavelength (Å)	Flux Value (10^{-15} erg s $^{-1}$ cm $^{-2}$)	Uncertainty in Flux (10^{-15} erg s $^{-1}$ cm $^{-2}$)	FWHM (km s $^{-1}$)	Uncertainty in FWHM (km s $^{-1}$)
[O II] λ 3727	3874.03	0.23	17.39	0.43	1797.04	44.91
H β _{narrow}	5064.79	0.21	37.56	1.29	1630.08	39.69
H β _{broad}	5074.95	0.44	316.15	3.35	7323.03	76.26
Fe II λ 4924	5135.23	0.27	29.43	1.28	1579.09	49.07
Fe II λ 5018	5226.83	0.24	84.21	1.16	2848.97	36.04
Fe II λ 5169	5384.06	0.40	49.04	1.53	2941.74	72.99
Na I D λ 5893	6146.80	0.33	44.70	0.98	1725.29	25.87
Fe II λ 6148	6406.45	0.44	93.54	1.98	3743.65	66.97
Fe II λ 6248	6506.92	0.33	71.26	1.25	2542.58	40.57
H α _{broad}	6824.18	0.34	1309.35	8.11	8593.78	70.32
H α _{narrow 1}	6796.34	4.29	82.90	30.64	1424.44	180.98
H α _{narrow 2}	6829.78	2.50	549.56	142.72	1485.54	227.36
H α _{narrow 3}	6848.89	0.65	292.17	123.10	1003.96	104.69
H α _{narrow 4}	6862.71	0.11	75.97	10.20	489.60	20.11
H α _{narrow 5}	6882.68	0.13	44.87	1.38	562.28	14.38

Notes. All uncertainties are the 1 σ standard error values. The values stated are calculated for an aperture of 1 arcsec.

tra. One absorption system appears at the redshift of the emission lines at ~ 0.0426 . The second set might be at redshift similar to the weak second set of absorption lines seen in the central spectrum. Figures 7 and 10 present zoomed-in views of the Gaussian fitting of the absorption lines in the blue band of the spectra from PA 230° with offsets of $-2''$ and $+2''$, respectively. The absorption lines observed, their line centres, fluxes, and FWHMs from each of the spectra can be found in Tables 6, 8, 10, 12, 14, and 16, respectively. Additionally, unlike the central spectrum, the redshift for the [O II] λ 3727 emission line is ~ 0.0421 , which is similar to the average redshift of the emission line system.

3.2.2. Differences in the spectral features of off-nuclear spectra of Mrk231

The two categories of off-nuclear spectra of Mrk231 differ from one another in two major aspects. The first is the shape of the continuum. The spectra belonging to category one, i.e., spectra corresponding to regions to the south of the nucleus have lower levels of continuum in the blue band that steepens towards the blue part of the spectrum. The steepening is the highest in the case of PA 355° at offset $+2''$, which corresponds to a spectral extraction region to the south-west/west of the nucleus. The lowest steepening is at PA 265° at offset $-2''$, which corresponds to a spectral extraction region to the south-east of the nucleus. The spectra belonging to category two, i.e., spectra corresponding

Table 3: Mrk231 Centre Absorption Line Data

Emission Line	Observed Wavelength (Å)	Uncertainty in Wavelength (Å)	Flux Value ($10^{-15} \text{ erg s}^{-1} \text{ cm}^{-2}$)	Uncertainty in Flux ($10^{-15} \text{ erg s}^{-1} \text{ cm}^{-2}$)	FWHM (km s^{-1})	Uncertainty in FWHM (km s^{-1})
He I λ 3889	3990.46	0.07	-40.64	0.70	807.43	14.28
Ca II λ 3934	4037.36	0.04	-43.14	0.54	599.65	8.09
Ca II H λ 3969	4072.96	0.05	-29.28	0.50	478.99	8.84
Na I D λ 5893	6048.51	0.11	-196.57	3.66	1044.55	16.37

Notes. All uncertainties are the 1σ standard error values. The values stated are calculated for an aperture of 1 arcsec.

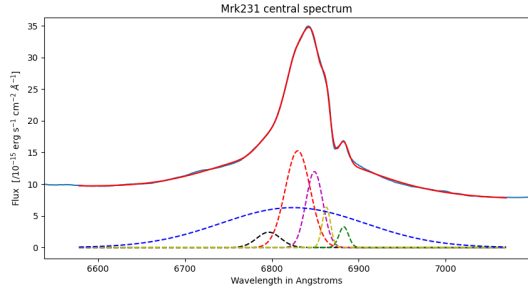


Fig. 3: A zoomed-in view to the spectral decomposition using Gaussian fitting of the $H\alpha$ line in the averaged one-dimensional observed optical spectrum of the central arcsec of Mrk231. Six components were required to get the best fit marked by the solid red line. Dashed blue, black, red, magenta, yellow, and cyan lines show the individual Gaussian components. The aperture size for spectral extraction is 1 arcsec. The wavelength axis (abscissa) depicts the observed wavelength.

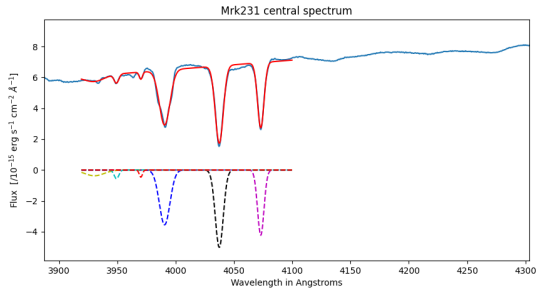


Fig. 4: A zoomed-in view to the spectral decomposition using Gaussian fitting of the absorption lines in the blue channel in the averaged one-dimensional observed optical spectrum of the central arcsec of Mrk231. Six components were required to get the best fit marked by the solid red line. Dashed blue, black, red, magenta, yellow, and cyan lines show the individual Gaussian components. The aperture size for spectral extraction is 1 arcsec. The wavelength axis (abscissa) depicts the observed wavelength.

to regions to the north of the nucleus have flat continua, with a slight tapering off towards the blue end of the spectra.

The second major difference between the spectra belonging to the two categories is the presence/absence of the $H\beta$ emission line. Category one spectra have weak $H\beta$ emission lines, both broad and narrow, but amongst the category two spectra, only PA 265° at offset $+2''$ shows the presence of a weak $H\beta$ emission line. The other two spectra show no indication of $H\beta$ emission. The narrow $H\beta$ emission is the strongest in the case of PA 355° at offset $+2''$.

Table 4: Mrk231 redshifts

PA	Offset	System	Redshift	Velocity (km s^{-1})
Centre		emission	0.0425	12750
Centre		[O II] λ 3727 emission	0.0400	12000
Centre		absorption	0.0262	7860
230°	$-2''$	emission	0.0426	12780
230°	$-2''$	[O II] λ 3727 emission	0.0421	12630
230°	$-2''$	absorption	0.0262	7860
230°	$+2''$	emission	0.0423	12690
230°	$+2''$	[O II] λ 3727 emission	0.0425	12750
230°	$+2''$	absorption	0.0263	7890
265°	$-2''$	emission	0.0424	12720
265°	$-2''$	[O II] λ 3727 emission	0.0424	12720
265°	$-2''$	absorption	0.0261	7830
265°	$+2''$	emission	0.0424	12720
265°	$+2''$	[O II] λ 3727 emission	0.0424	12720
265°	$+2''$	absorption	0.0258	7740
355°	$-2''$	emission	0.0422	12660
355°	$-2''$	[O II] λ 3727 emission	0.0424	12720
355°	$-2''$	absorption	0.0259	7770
355°	$+2''$	emission	0.0424	12720
355°	$+2''$	[O II] λ 3727 emission	0.0428	12840
355°	$+2''$	absorption	0.0258	7740

Notes. All uncertainties are the 1σ standard error values. The values stated are calculated for an aperture of 1 arcsec.

In addition to these two differences, category one spectra seem to have more prominent absorption lines at the redshift of ~ 0.0262 compared to the other two absorption systems, while in the case of category two spectra, all the absorption lines are of similar strength.

4. Discussion

Figures 2, 5, 8, 11, 12, 13, and 14 show the spectra corresponding to the central arcsecond of Mrk231 and six other regions at offsets of $2''$ from the centre. Previous detailed studies of the spectra have shown that the QSO has a major contribution towards the central spectrum, while the spectra from the off-centre regions have contributions from the intense circum-nuclear starburst and the host galaxy. In the following section, we will discuss some of the characteristics of Mrk231 associated with these spectra.

4.1. High velocity outflows in emission lines

One of the most interesting aspects about the spectra of Mrk231 is the presence of broad $H\alpha$ components in regions located at a distance of ~ 1.7 kpc ($2''$) away from the centre of the galaxy. The presence of a broad $H\alpha$ component in the central region of Mrk231 has been studied in previous works. However, we find broad $H\alpha$ components with FWHMs of $\sim 8000 \text{ km s}^{-1}$ at a distance of ~ 1.7 kpc away from the centre. The line centres of all of the broad $H\alpha$ components from the offsetted slit positions are blue-shifted compared with the central broad $H\alpha$ component. In

Table 5: Mrk231 PA 230°offset -2'' Emission Line Data

Emission Line	Observed Wavelength (Å)	Uncertainty in Wavelength (Å)	Flux Value (10^{-16} erg s $^{-1}$ cm $^{-2}$)	Uncertainty in Flux (10^{-16} erg s $^{-1}$ cm $^{-2}$)	FWHM (km s $^{-1}$)	Uncertainty in FWHM (km s $^{-1}$)
[O II] λ 3727 _{blue wing}	3874.78	1.17	12.44	1.88	1259.86	178.85
[O II] λ 3727	3884.94	0.18	8.92	1.54	503.48	47.10
H β _{narrow}	5067.37	0.19	1.31	0.15	215.50	27.23
H β _{broad}	5059.92	1.83	62.25	3.04	6020.85	243.69
[O III] λ 4959	5136.19	0.33	0.34	0.12	126.75	47.31
[Fe II] λ	5136.82	1.54	18.92	2.26	3244.81	228.35
[O III] λ 5007	5219.38	0.23	1.13	0.17	217.27	33.34
[Fe II] λ	5221.92	0.77	21.32	1.17	3086.79	148.22
[O I] λ 6300	6568.07	0.76	2.31	0.41	485.80	88.15
[N II] λ 6548	6826.12	0.27	16.11	3.16	529.58	39.55
H α _{broad}	6818.69	1.10	187.37	3.40	8705.19	194.47
H α _{narrow 1}	6821.35	4.32	61.47	14.14	1937.74	216.82
H α _{narrow 2}	6844.51	0.16	67.16	8.77	826.65	31.56
H α _{narrow 3}	6883.62	0.29	5.10	0.42	394.41	31.38
[N II] λ 6583	6862.86	0.09	33.33	1.49	467.73	10.49
[S II] λ 6716	7002.48	0.32	4.09	0.32	373.58	33.42
[S II] λ 6731	7017.77	0.40	2.47	0.29	306.93	41.04

Notes. All uncertainties are the 1σ standard error values. The values stated are calculated for an aperture of 1 arcsec.

Table 6: Mrk231 PA 230°offset -2'' Absorption Line Data

Absorption Line	Observed Wavelength (Å)	Uncertainty in Wavelength (Å)	Flux Value (10^{-15} erg s $^{-1}$ cm $^{-2}$)	Uncertainty in Flux (10^{-15} erg s $^{-1}$ cm $^{-2}$)	FWHM (km s $^{-1}$)	Uncertainty in FWHM (km s $^{-1}$)
System I ($z = 0.0265$)						
He I λ 3889	3990.80	0.09	-31.73	0.61	1019.98	18.04
Ca II λ 3934	4036.34	0.08	-21.72	0.68	570.04	15.24
Ca II λ 3969	4072.19	0.07	-13.83	0.39	464.57	13.01
Na I λ 5893	6049.34	0.13	-33.42	0.50	1047.58	15.97
System II ($z = 0.0422$)						
He I λ 3889	4052.69	0.57	-13.91	1.12	1366.50	126.73
Ca II λ 3934	4097.55	0.62	-2.25	0.38	607.83	111.29
Ca II λ 3969	4136.75	0.31	-10.96	0.52	1094.48	55.84

Notes. All uncertainties are the 1σ standard error values. The values stated are calculated for an aperture of 1 arcsec.

Table 7: Mrk231 PA 230°offset +2'' Emission Line Data

Emission Line	Observed Wavelength (Å)	Uncertainty in Wavelength (Å)	Flux Value (10^{-16} erg s $^{-1}$ cm $^{-2}$)	Uncertainty in Flux (10^{-16} erg s $^{-1}$ cm $^{-2}$)	FWHM (km s $^{-1}$)	Uncertainty in FWHM (km s $^{-1}$)
[O II] λ 3727	3885.11	0.09	8.56	0.30	445.55	16.99
[O III] λ 5007	5217.93	0.26	1.86	0.16	378.31	35.65
[O I] λ 6300	6566.45	0.29	2.11	0.21	316.61	33.35
[N II] λ 6548	6824.00	0.20	8.64	1.11	448.86	27.70
H α _{broad}	6817.31	1.18	121.97	2.35	8993.43	209.91
H α _{narrow 1}	6820.92	3.28	44.72	7.60	2001.64	171.09
H α _{narrow 2}	6841.92	0.11	42.86	4.99	841.43	29.82
H α _{narrow 3}	6881.96	0.27	3.53	0.29	386.66	29.21
[N II] λ 6583	6861.16	0.06	24.42	0.94	443.80	8.74
[S II] λ 6716	7000.34	0.17	4.30	0.20	328.70	17.57
[S II] λ 6731	7015.16	0.21	3.06	0.19	304.06	21.81

Notes. All uncertainties are the 1σ standard error values. The values stated are calculated for an aperture of 1 arcsec.

Table 8: Mrk231 PA 230°offset +2'' Absorption Line Data

Absorption Line	Observed Wavelength (Å)	Uncertainty in Wavelength (Å)	Flux Value (10^{-15} erg s $^{-1}$ cm $^{-2}$)	Uncertainty in Flux (10^{-15} erg s $^{-1}$ cm $^{-2}$)	FWHM (km s $^{-1}$)	Uncertainty in FWHM (km s $^{-1}$)
System I ($z = 0.0262$)						
He I λ 3889	3994.73	0.21	-9.63	0.47	1100.20	45.81
Ca II λ 3934	4037.87	0.22	-3.24	0.31	503.49	40.10
Ca II λ 3969	4073.45	0.18	-2.03	0.18	357.19	32.77
Na I λ 5893	6047.31	0.14	-17.53	0.28	1042.78	17.21
System II ($z = 0.0422$)						
He I λ 3889	4052.48	0.43	-7.08	0.50	1227.47	88.84
Ca II λ 3934	4099.71	0.35	-2.28	0.27	601.51	68.05
Ca II λ 3969	4137.01	0.26	-9.53	0.42	1274.83	52.21

Notes. All uncertainties are the 1σ standard error values. The values stated are calculated for an aperture of 1 arcsec.

Table 9: Mrk231 PA 265°offset -2'' Emission Line Data

Emission Line	Observed Wavelength (Å)	Uncertainty in Wavelength (Å)	Flux Value (10^{-16} erg s $^{-1}$ cm $^{-2}$)	Uncertainty in Flux (10^{-16} erg s $^{-1}$ cm $^{-2}$)	FWHM (km s $^{-1}$)	Uncertainty in FWHM (km s $^{-1}$)
[O II] λ 3727 ^{blue wing}	3874.55	1.08	12.09	1.70	1258.98	166.47
[O II] λ 3727	3884.38	0.17	7.71	1.34	468.03	46.34
H β _{narrow}	5066.68	0.29	0.68	0.15	181.18	42.63
H β _{broad}	5058.45	2.33	54.81	3.44	5599.74	276.38
[O III] λ 4959	5137.45	0.90	0.84	0.32	433.87	145.99
[Fe II] λ	5134.64	2.13	21.37	2.78	3492.75	302.07
[O III] λ 5007	5217.63	0.25	1.46	0.21	265.64	37.37
[Fe II] λ	5221.26	0.94	19.88	1.28	3106.72	176.97
[O I] λ 6300	6568.12	0.65	2.05	0.39	416.56	77.19
[N II] λ 6548	6825.30	0.28	12.20	2.22	502.39	39.12
H α _{broad 1}	6798.84	25.58	159.50	56.63	7752.35	1123.80
H α _{narrow 1}	6821.60	4.17	72.34	18.05	1988.24	236.60
H α _{narrow 2}	6844.59	0.21	82.17	11.51	997.58	41.20
H α _{narrow 3}	6884.39	0.24	6.04	0.56	396.11	29.63
H α _{broad 2}	6921.55	45.33	42.48	15.71	6301.19	2394.62
[N II] λ 6583	6863.24	0.08	32.76	1.41	455.10	10.05
[S II] λ 6716	7002.18	0.31	4.29	0.40	383.88	34.27
[S II] λ 6731	7017.30	0.38	2.74	0.34	325.77	41.04

Notes. All uncertainties are the 1σ standard error values. The values stated are calculated for an aperture of 1 arcsec.

Table 10: Mrk231 PA 265°offset -2'' Absorption Line Data

Absorption Line	Observed Wavelength (Å)	Uncertainty in Wavelength (Å)	Flux Value (10^{-15} erg s $^{-1}$ cm $^{-2}$)	Uncertainty in Flux (10^{-15} erg s $^{-1}$ cm $^{-2}$)	FWHM (km s $^{-1}$)	Uncertainty in FWHM (km s $^{-1}$)
System I ($z = 0.0262$)						
He I λ 3889	3990.10	0.09	-32.01	1.38	1069.90	27.82
Ca II λ 3934	4036.04	0.06	-19.23	0.50	547.81	11.89
Ca II λ 3969	4071.55	0.06	-12.85	0.39	451.679	12.53
Na I λ 5893	6050.11	0.12	-36.57	0.51	1043.53	14.88
System II ($z = 0.0422$)						
He I λ 3889	4052.56	0.36	-11.11	1.02	1202.20	84.39
Ca II λ 3934	4098.11	0.48	-4.10	0.61	819.89	103.22
Ca II λ 3969	4136.09	0.23	-16.13	0.63	1230.15	44.46

Notes. All uncertainties are the 1σ standard error values. The values stated are calculated for an aperture of 1 arcsec.

Table 11: Mrk231 PA 265°offset +2'' Emission Line Data

Emission Line	Observed Wavelength (Å)	Uncertainty in Wavelength (Å)	Flux Value (10^{-16} erg s $^{-1}$ cm $^{-2}$)	Uncertainty in Flux (10^{-16} erg s $^{-1}$ cm $^{-2}$)	FWHM (km s $^{-1}$)	Uncertainty in FWHM (km s $^{-1}$)
[O II] λ 3727	3884.54	0.11	9.17	0.36	492.72	21.62
H β _{narrow}	5067.02	0.21	1.28	0.17	194.79	29.01
[O III] λ 5007	5218.49	0.25	3.38	0.25	410.46	34.49
[O I] λ 6300	6567.20	0.60	2.35	0.46	375.96	71.72
[N II] λ 6548	6824.02	0.27	19.22	3.62	534.58	38.69
H α _{broad}	6814.56	38.94	245.55	143.73	8611.41	1345.81
H α _{narrow 1}	6820.07	4.39	82.82	20.32	1997.05	232.70
H α _{narrow 2}	6842.35	0.13	89.10	11.88	848.83	31.57
H α _{narrow 3}	6882.28	0.26	6.94	0.67	399.29	31.82
[N II] λ 6583	6861.48	0.09	40.88	2.12	477.01	11.80
[S II] λ 6716	7001.15	0.27	4.88	0.45	333.80	29.99
[S II] λ 6731	7015.93	0.36	3.63	0.45	330.96	39.34

Notes. All uncertainties are the 1σ standard error values. The values stated are calculated for an aperture of 1 arcsec.

Table 12: Mrk231 PA 265°offset +2'' Absorption Line Data

Absorption Line	Observed Wavelength (Å)	Uncertainty in Wavelength (Å)	Flux Value (10^{-15} erg s $^{-1}$ cm $^{-2}$)	Uncertainty in Flux (10^{-15} erg s $^{-1}$ cm $^{-2}$)	FWHM (km s $^{-1}$)	Uncertainty in FWHM (km s $^{-1}$)
System I ($z = 0.0262$)						
He I λ 3889	3992.21	0.13	-16.55	0.80	1053.55	33.82
Ca II λ 3934	4037.65	0.10	-8.26	0.30	506.73	17.09
Ca II λ 3969	4072.85	0.10	-5.57	0.25	436.79	19.15
Na I λ 5893	6047.58	0.11	-38.07	0.49	1037.03	13.89
System II ($z = 0.0422$)						
He I λ 3889	4052.03	0.36	-6.50	0.54	1020.97	76.26
Ca II λ 3934	4098.40	0.36	-2.06	0.27	528.50	68.07
Ca II λ 3969	4136.46	0.23	-10.73	0.47	1167.66	46.42

Notes. All uncertainties are the 1σ standard error values. The values stated are calculated for an aperture of 1 arcsec.

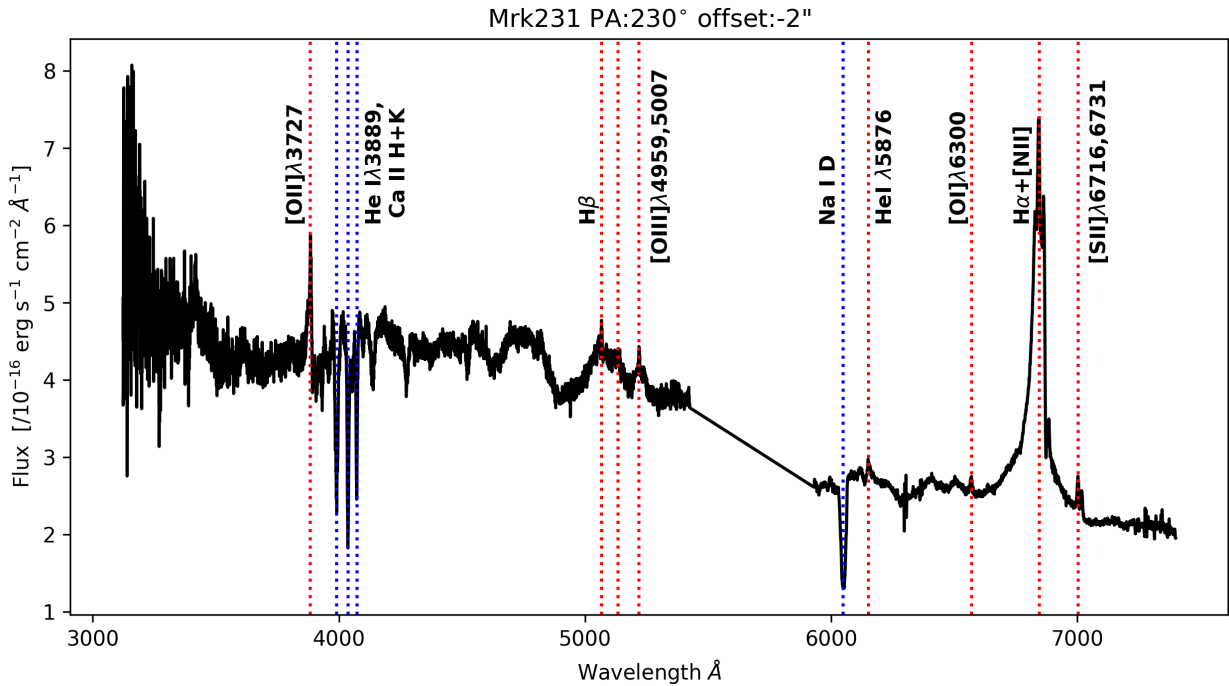


Fig. 5: One-dimensional observed optical spectrum of Mrk231 observed at a PA of 230, with an offset of 2'' to the left of the centre. The emission lines observed have been marked by vertical red dotted lines and named. The aperture size for spectral extraction is 1''. The wavelength axis depicts the observed wavelength.

Table 13: Mrk231 PA 355°offset -2'' Emission Line Data

Emission Line	Observed Wavelength (Å)	Uncertainty in Wavelength (Å)	Flux Value (10^{-16} erg s $^{-1}$ cm $^{-2}$)	Uncertainty in Flux (10^{-16} erg s $^{-1}$ cm $^{-2}$)	FWHM (km s $^{-1}$)	Uncertainty in FWHM (km s $^{-1}$)
[O II]λ3727	3884.98	0.13	5.65	0.27	448.65	23.17
[O III]λ5007	5216.99	0.31	1.38	0.17	138.58	18.40
[O II]λ6300	6565.01	0.38	1.70	0.19	155.37	18.28
[N II]λ6548	6822.46	0.21	8.78	1.13	487.21	28.14
Hα _{broad}	6822.26	0.95	148.18	3.04	9238.43	197.45
Hα _{narrow 1}	6818.76	3.38	43.40	7.74	1967.51	170.27
Hα _{narrow 2}	6841.86	0.18	54.01	5.82	1005.43	34.20
Hα _{narrow 3}	6881.84	0.20	3.73	0.23	378.39	22.23
[N II]λ6583	6860.47	0.06	23.34	0.72	446.03	7.43
[S II]λ6716	6999.08	0.19	3.34	0.18	341.62	20.14
[S II]λ6731	7013.69	0.23	2.29	0.17	296.85	23.95

Notes. All uncertainties are the 1σ standard error values. The values stated are calculated for an aperture of 1 arcsec.

addition to H α , wherever H β is present in the spectrum, it has a broad component, as well. However, the H β line usually needs only one or two components to get a good line fit, while the H α + [N II] complex needs at least six components, i.e., in addition to the four components corresponding to the two [N II] and the broad and narrow H α lines, there are two additional components, one to the left of [N II]λ6548 and another to the right of [N II]λ6583.

Historically, such broad velocity components are usually associated with the BLR of an AGN and to much a lesser extent to outflows or nuclear winds. The BLR typically has a size in the range 0.1-1 pc. However, since Mrk231 is a late-stage merger, with the SMBHs having merged already or in a binary SMBH stage, corresponding BLRs might also be in a state of flux and might be much more extended than normal BLRs in non-colliding systems. The presence of broad H α (and to a lesser

extent, H β) components might also be attributed to some form of nuclear wind/outflows. Rupke & Veilleux (2011) report neutral gas outflow with velocities of about ~ 1000 km s $^{-1}$, extending in all directions from the centre of Mrk231 up to at least 3 kpc. Our data shows that the top two Balmer lines, at least, could be a part of the outflow.

Galactic winds have been also associated with Mrk231. Lřpari et al. (2005) present one- and two-dimensional spectra of Mrk231. They report the existence of four or five nuclear superbubbles or shells with radii $\sim 2.9, 1.5, 1.0, 0.6,$ and 0.2 kpc, and suggest that these giant bubbles could be generated by massive supernova/hypernova explosions associated with an extreme nuclear starburst that could be a stage in the evolution of a young QSO. While, extreme starburst might contribute towards the high velocities observed in the extended regions in Mrk231, starburst ULIRGs don't display such high velocities, in general. There-

Table 14: Mrk231 PA 355°offset -2'' Absorption Line Data

Absorption Line	Observed Wavelength (Å)	Uncertainty in Wavelength (Å)	Flux Value (10^{-15} erg s $^{-1}$ cm $^{-2}$)	Uncertainty in Flux (10^{-15} erg s $^{-1}$ cm $^{-2}$)	FWHM (km s $^{-1}$)	Uncertainty in FWHM (km s $^{-1}$)
System I ($z = 0.0262$)						
He I λ 3889	3993.42	0.22	-9.22	0.47	1117.84	47.33
Ca II λ 3934	4036.75	0.18	-3.57	0.26	507.59	33.44
Ca II λ 3969	4072.24	0.20	-2.22	0.19	414.76	36.90
Na I λ 5893	6047.34	0.15	-18.25	0.31	1062.62	18.35
System II ($z = 0.0422$)						
He I λ 3889	4052.76	0.45	-5.59	0.44	1219.07	98.44
Ca II λ 3934	4099.87	0.48	-2.35	0.31	781.85	95.93
Ca II λ 3969	4137.08	0.25	-7.83	0.38	1126.16	50.03

Notes. All uncertainties are the 1σ standard error values. The values stated are calculated for an aperture of 1 arcsec.

Table 15: Mrk231 PA 355°offset +2'' Emission Line Data

Emission Line	Observed Wavelength (Å)	Uncertainty in Wavelength (Å)	Flux Value (10^{-16} erg s $^{-1}$ cm $^{-2}$)	Uncertainty in Flux (10^{-16} erg s $^{-1}$ cm $^{-2}$)	FWHM (km s $^{-1}$)	Uncertainty in FWHM (km s $^{-1}$)
[O II] λ 3727 _{blue wing}	3876.18	1.01	12.65	1.52	1390.80	148.60
[O II] λ 3727	3885.87	0.10	10.62	1.10	456.27	28.56
H β _{narrow}	5068.76	0.07	4.40	0.17	237.34	10.06
[O III] λ 5007	5219.93	0.13	3.22	0.24	284.49	20.11
[Fe II] λ	5231.78	1.63	6.01	0.72	2000.66	210.44
[O I] λ 6300	6566.11	0.47	1.61	0.25	311.60	52.54
[N II] λ 6548	6823.60	0.20	2.24	0.27	210.15	23.74
H α _{broad}	6809.78	1.55	101.64	2.69	7745.62	188.56
H α _{narrow 1}	6835.15	0.23	87.84	1.57	1964.55	28.97
H α _{narrow 2}	6839.23	0.04	14.47	0.34	251.34	5.26
H α _{narrow 3}	6880.62	0.45	0.93	0.21	202.74	48.40
[N II] λ 6583	6860.51	0.05	14.73	0.36	290.79	6.12
[S II] λ 6716	7000.06	0.20	4.40	0.25	319.71	20.14
[S II] λ 6731	7014.78	0.25	3.10	0.25	299.79	26.51

Notes. All uncertainties are the 1σ standard error values. The values stated are calculated for an aperture of 1 arcsec.

Table 16: Mrk231 PA 355°offset +2'' Absorption Line Data

Absorption Line	Observed Wavelength (Å)	Uncertainty in Wavelength (Å)	Flux Value (10^{-15} erg s $^{-1}$ cm $^{-2}$)	Uncertainty in Flux (10^{-15} erg s $^{-1}$ cm $^{-2}$)	FWHM (km s $^{-1}$)	Uncertainty in FWHM (km s $^{-1}$)
System I ($z = 0.0262$)						
He I λ 3889	3992.00	0.08	-27.51	0.55	920.59	16.53
Ca II λ 3934	4038.15	0.07	-19.95	0.71	553.77	13.38
Ca II λ 3969	4073.80	0.06	-13.51	0.30	460.99	11.05
Na I λ 5893	6044.79	0.14	-19.715	0.31	1059.84	17.37
System II ($z = 0.0422$)						
He I λ 3889	4051.51	0.72	-9.45	0.92	1267.45	134.00
Ca II λ 3934	4098.44	0.59	-1.85	0.32	553.38	105.41
Ca II λ 3969	4136.35	0.38	-10.52	0.58	1297.52	70.86

Notes. All uncertainties are the 1σ standard error values. The values stated are calculated for an aperture of 1 arcsec.

fore, there is a strong possibility that the ionised gas outflow we see in our data has contribution from the AGN, as well.

4.2. Low velocity outflows in emission lines

Along with an ever present broad component, the H α + [N II] blend requires two additional narrow components in each spectrum to have a reasonable resulting best-fit, when performing Gaussian fitting. The most obvious of these components is the bump to the right (red-wards) of the H α + [N II] blend. Along with the red bump, Lípari et al. (2005) report the presence of a blue bump. The blue bump is also seen in our data, although it is less conspicuous (See Figures 6 and 9 for a zoomed in view to the H α + [N II] complex from the offsetted positions at a PA of 230°). Lípari et al. (2005) attribute this spectral feature to outflowing clouds associated with the stellar shells. The outflowing clouds could be a part of the narrow line region (NLR). However, while the multiple narrow H α components are present in

all of the spectra, we only see blue asymmetry in the [O II] λ 3727 emission line in the case of spectra taken at PAs of 230°, at an offset of -2'', 265°, at an offset of -2'', and 355°, at an offset of +2'', respectively. That is, the [O II] λ 3727 line shows blue-shifted components with FWHMs in the range 1200-1400 km s $^{-1}$ to the south of the nucleus, but not to the north. Additionally, we see no asymmetry in the [O III] λ 5007 emission line in any of the spectra.

4.3. Strong Fe II emission

The central spectrum of Mrk231 is characterised by strong Fe II emission, with FWHMs ≥ 1500 km s $^{-1}$. The observed emission lines are marked and indicated in Figure 2 and data related to the emission lines can be found in Table 2. We see no clear indication for the presence of Fe II emission lines in the off-nuclear spectra. This is as expected, considering that while the presence of an AGN is not a necessary criterion for Fe II emission, H II

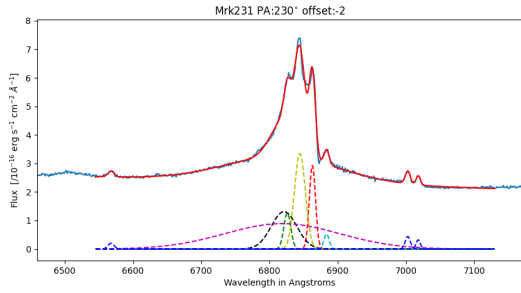


Fig. 6: A zoomed-in view to the spectral decomposition using Gaussian fitting of the $H\alpha$ line in the averaged one-dimensional observed optical spectrum of the central arcsec of Mrk231. Six components were required to get the best fit marked by the solid red line. Dashed blue, black, red, magenta, yellow, and cyan lines show the individual Gaussian components. The aperture size for spectral extraction is 1 arcsec. The wavelength axis (abscissa) depicts the observed wavelength.

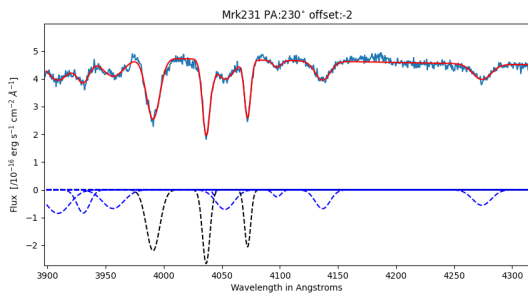


Fig. 7: A zoomed-in view to the spectral decomposition using Gaussian fitting of the absorption lines in the blue channel in the averaged one-dimensional observed optical spectrum of the central arcsec of Mrk231. Six components were required to get the best fit marked by the solid red line. Dashed blue, black, red, magenta, yellow, and cyan lines show the individual Gaussian components. The aperture size for spectral extraction is 1 arcsec. The wavelength axis (abscissa) depicts the observed wavelength.

regions generally don't show strong Fe II emission since, in the presence of dust, iron is depleted on to grains (de Boer et al. 1972). Fe II emission in AGNs seems to arise in the outermost part of the BLR, very close to the surrounding dust (Gaskell et al. 2022). L pari et al. (2005) and Lipari et al. (2009) suggest that BAL QSOs with Fe II low ionisation are young and composite/transition QSOs, where outflows and galactic winds are clearing the nuclear dust that is created by the extreme nuclear starburst, in the form of giant bubbles and supernova/hypernova explosions.

4.4. Broad absorption line system

Mrk231 spectra show several absorption lines in addition to the emission lines. The most prominent of these are the He I λ 3889, the Ca II H and K, and the Na I D absorption lines. With the exception of the central spectrum, all other spectra from offsetted positions show multiple systems of absorption lines. The strongest set of absorption lines are at a redshift of $\sim 7860 \text{ km s}^{-1}$ ($z \sim 0.0262$), while another set of absorption lines lies at a redshift of $\sim 12\,600 \text{ km s}^{-1}$ ($z \sim 0.042$), which corresponds with the redshift of the emission lines. Along with these two, He I λ 3889

and Ca II H+K seem to be absorbed at another lower redshift. The absorption lines are more prominent in the spectra from the centre and at PAs of 230° , at an offset of $-2''$, 265° , at an offset of $-2''$, and 355° , at an offset of $+2''$, respectively, i.e., to the south of the nucleus. He I λ 3889 and Na I D absorption lines are broad, with $\text{FWHM} \gtrsim 1000 \text{ km s}^{-1}$, except for the central spectrum where $\text{FWHM}_{\text{He I } \lambda 3889} \sim 800 \text{ km s}^{-1}$. Additionally, $\text{FWHM}_{\text{He I } \lambda 3889} > \text{FWHM}_{\text{Na I D}}$, with the exception of the central spectrum, and spectra from PA 230° at an offset of $-2''$ and PA 355° at an offset of $+2''$ where $\text{FWHM}_{\text{He I } \lambda 3889} < \text{FWHM}_{\text{Na I D}}$.

The He I λ 3889 line arises from a metastable level 23 eV above the ground state. Absorption from a high lying metastable level could be an indication that the absorbing clouds are associated with the nuclear activity in Mrk231 (Boksenberg et al. 1977). The redshift of the absorption line system would then represent the velocity, relative to the emission line system, with which the absorbing material is approaching the Earth.

4.5. Mass of the SMBH

While there is an extreme nuclear starburst in Mrk231, the central spectrum is majorly dominated by emission from the central non-thermal AGN. The broad emission line components in the central spectrum of Mrk231 could be used to estimate the mass of the central SMBH.

While both $H\alpha$ and $H\beta$ have broad components in the central spectrum, the $H\alpha$ emission might have some contribution from the nuclear starburst. Therefore, we chose to use the $H\beta$ emission line to estimate the mass of the central SMBH. We used the virial mass formula based on the $H\beta$ emission line put forth by Greene & Ho (2005).

$$M_{\text{BH}} = (3.6 \pm 0.2) \times 10^6 \left(\frac{L_{H\beta}}{10^{42} \text{ erg s}^{-1}} \right)^{0.56 \pm 0.02} \left(\frac{\text{FWHM}_{H\beta}}{10^3 \text{ km s}^{-1}} \right)^2 M_{\odot}. \quad (1)$$

Where $L_{H\beta}$ is the luminosity of the broad $H\beta$ emission line in the units of erg s^{-1} and $\text{FWHM}_{H\beta}$ is the FWHM of the broad $H\beta$ emission line in the units of km s^{-1} . The thus estimated mass of the SMBH at the centre of Mrk231 comes out to be $(2.3 \pm 0.2) \times 10^8 M_{\odot}$. This is in very good agreement with the value, $M_{\text{BH}} = 2.3 \times 10^8 M_{\odot}$, put forth by Leighly et al. (2014) using the broad $P\alpha$ line.

4.6. Presence of a diffuse third tail

A careful analysis of the DSS (Figure 15) and SDSS (Figure 16) images of Mrk231 reveals the presence of diffuse emission adjacent to the northern tidal arm and at an angle to it. We were unable to extract any useful spectra from this region, but before starting spectroscopy observations, acquisition images were taken with the red channel of MODS at every position angle, and the region with the diffuse emission fell into the field of view. The exposure time for the acquisition image at PA of 230° was 60s, while the acquisition images at other three PAs were only exposed for 30s each. These acquisition images were rotated and stacked after being bias corrected (Figure 17). Overlaying contours at arbitrarily chosen levels, we see that there is an overdensity of emission, higher than the background, adjacent to the northern tidal tail, extending almost orthogonally outward from its base in the north-east direction. We see this extension in all

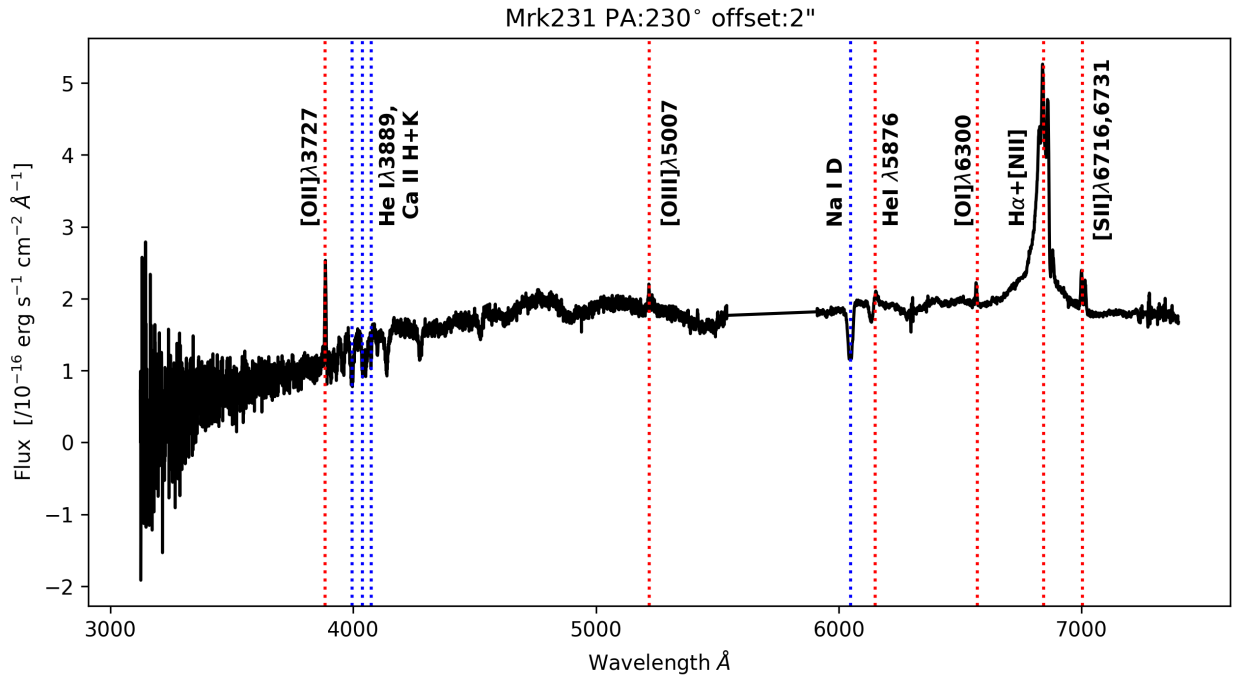


Fig. 8: One-dimensional observed optical spectrum of Mrk231 observed at a PA of 230, with an offset of 2'' to the right of the centre. The emission lines observed have been marked by vertical red dotted lines and named. The aperture size for spectral extraction is 1''. The wavelength axis depicts the observed wavelength.

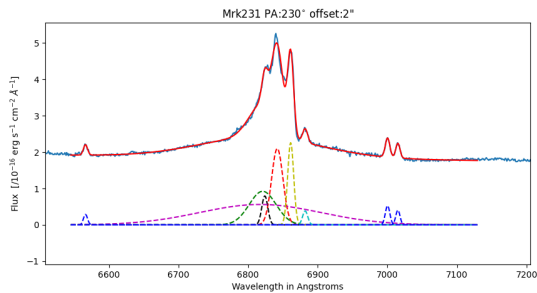


Fig. 9: A zoomed-in view to the spectral decomposition using Gaussian fitting of the $H\alpha$ line in the averaged one-dimensional observed optical spectrum of the central arcsec of Mrk231. Six components were required to get the best fit marked by the solid red line. Dashed blue, black, red, magenta, yellow, and cyan lines show the individual Gaussian components. The aperture size for spectral extraction is 1 arcsec. The wavelength axis (abscissa) depicts the observed wavelength.

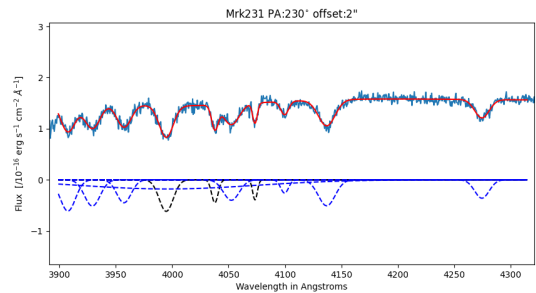


Fig. 10: A zoomed-in view to the spectral decomposition using Gaussian fitting of the absorption lines in the blue channel in the averaged one-dimensional observed optical spectrum of the central arcsec of Mrk231. Six components were required to get the best fit marked by the solid red line. Dashed blue, black, red, magenta, yellow, and cyan lines show the individual Gaussian components. The aperture size for spectral extraction is 1 arcsec. The wavelength axis (abscissa) depicts the observed wavelength.

four of our acquisition images, taken in the red band but at different PAs, and stacking the images together makes it easier to see this.

4.7. Mrk231 as a triple merger

If we consider the morphology of Mrk231 and disregard the presence of the diffuse emission, a similarity emerges between the structure of Mrk231 and the Antennae galaxies (NGC4038/NGC4039), although we note that unlike the NGC4038/NGC4039 pair, where both of the galaxies are clearly

distinguishable, Mrk231 seems to be at a later stage of the merger where the progenitor galaxies can no longer be distinguished. In the absence of the diffuse emission, the progenitor galaxies could have been understood to have similar starting conditions as NGC4038 and NGC4039, but the presence of this diffuse emission introduces an asymmetry to the morphology of Mrk231. While the presence of one or two tidal tails is ubiquitous in cases involving an interaction of two galaxies (Toomre & Toomre 1972), the existence of an asymmetry seems to be rare.

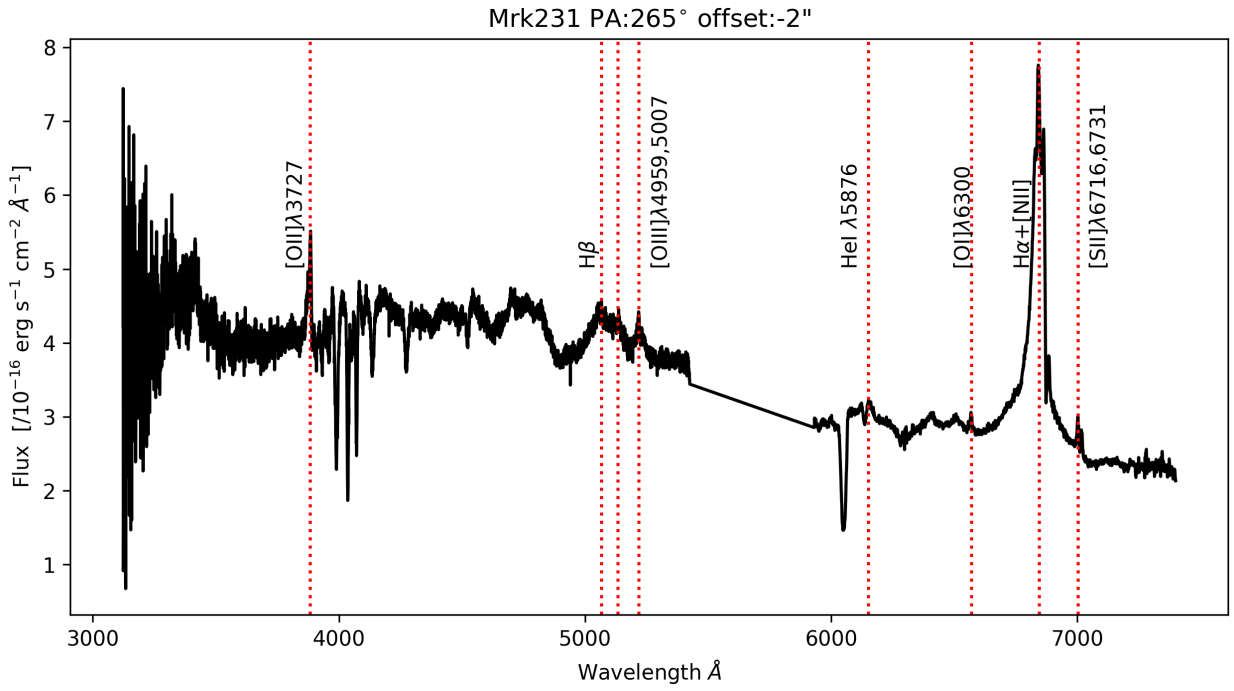


Fig. 11: One-dimensional observed optical spectrum of Mrk231 observed at a PA of 265, with an offset of 2'' to the left of the centre. The emission lines observed have been marked by vertical red dotted lines and named. The aperture size for spectral extraction is 1''. The wavelength axis depicts the observed wavelength.

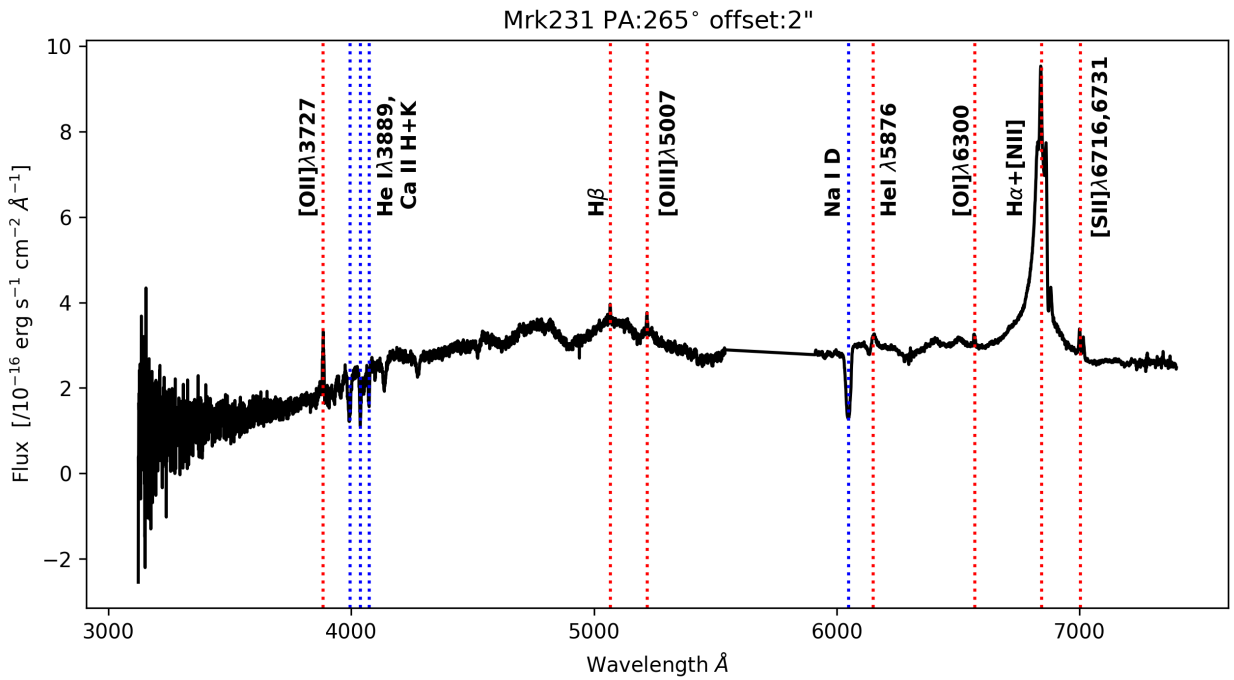


Fig. 12: One-dimensional observed optical spectrum of Mrk231 observed at a PA of 265, with an offset of 2'' to the right of the centre. The emission lines observed have been marked by vertical red dotted lines and named. The aperture size for spectral extraction is 1''. The wavelength axis depicts the observed wavelength.

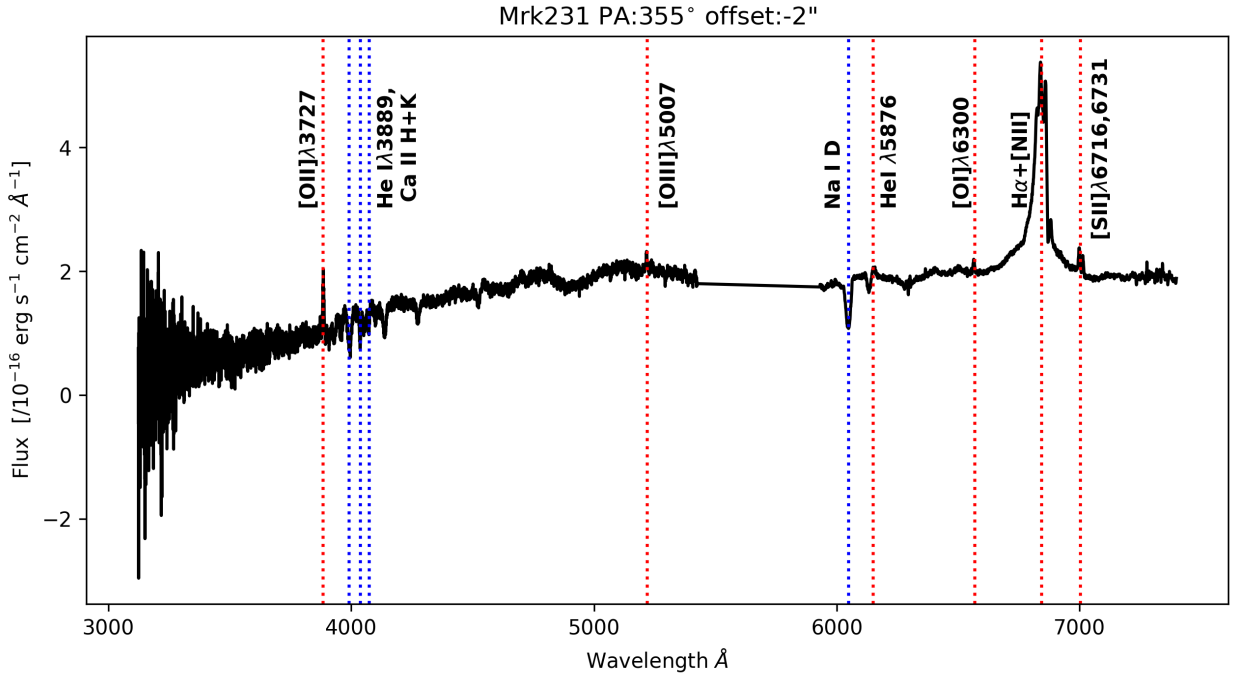


Fig. 13: One-dimensional observed optical spectrum of Mrk231 observed at a PA of 355, with an offset of 2" to the left of the centre. The emission lines observed have been marked by vertical red dotted lines and named. The aperture size for spectral extraction is 1". The wavelength axis depicts the observed wavelength.

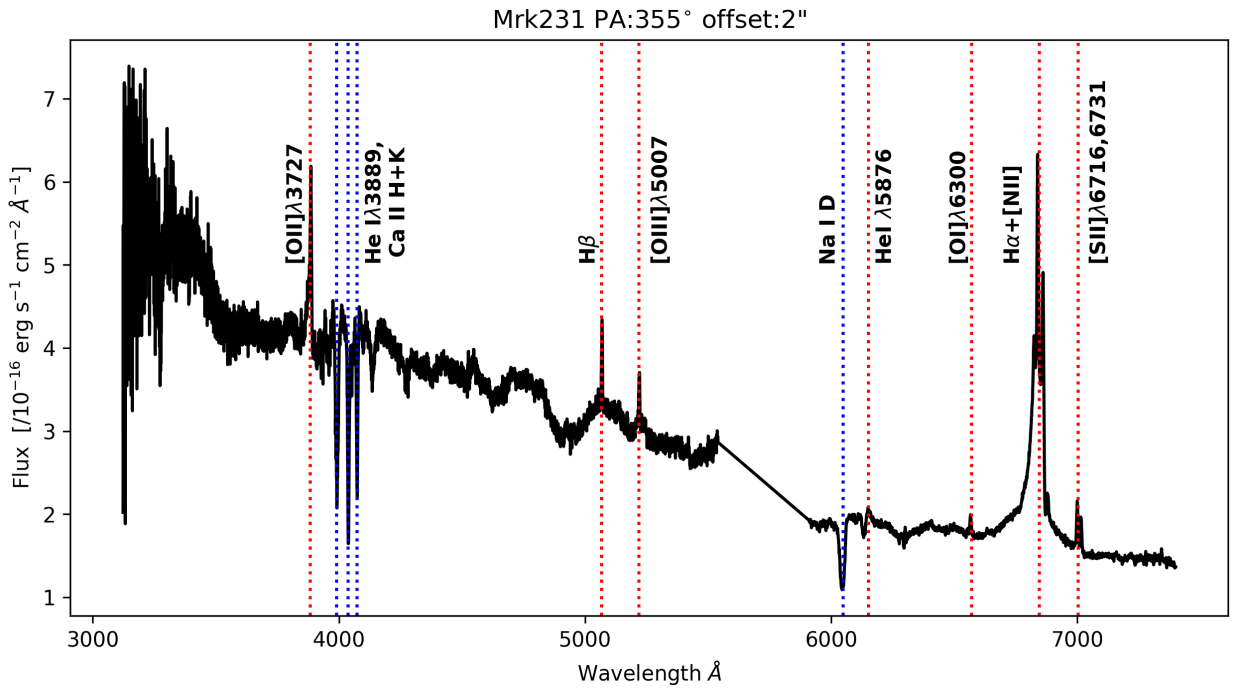


Fig. 14: One-dimensional observed optical spectrum of Mrk231 observed at a PA of 355, with an offset of 2" to the right of the centre. The emission lines observed have been marked by vertical red dotted lines and named. The aperture size for spectral extraction is 1". The wavelength axis depicts the observed wavelength.

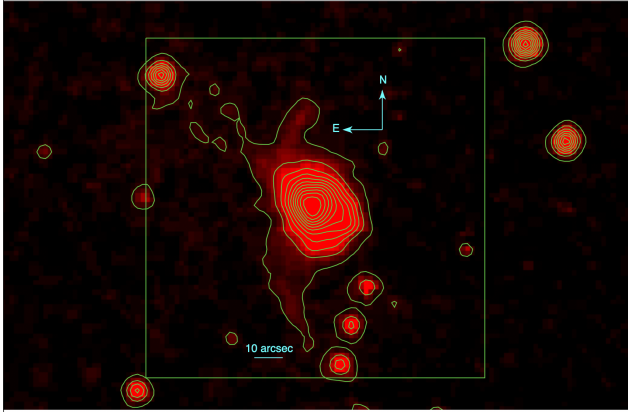


Fig. 15: Optical DSS image of Mrk231 overlaid with arbitrarily selected contours. The green box indicates the field of view of the SDSS survey for comparison with Figure 16. Scale and compass are marked.

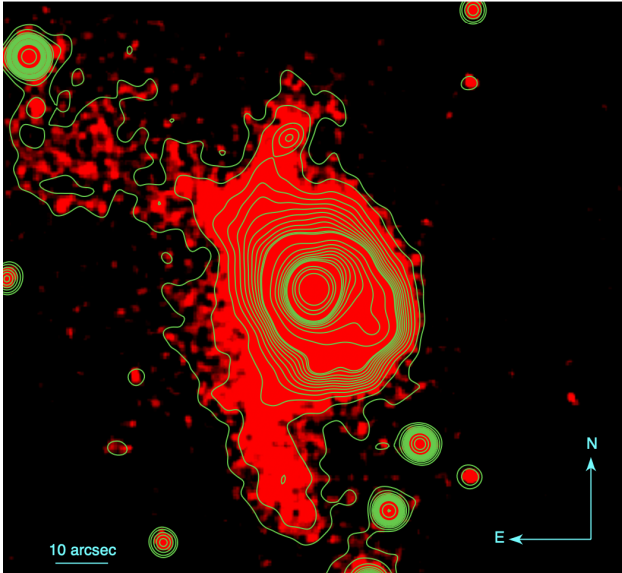


Fig. 16: Optical SDSS image of Mrk231 overlaid with arbitrarily selected contours. Scale and compass are marked.

Such asymmetry could come about if we consider a past interaction with another galaxy, perhaps a dwarf. In that case, the diffuse emission could be a tidal remnant of the minor interaction. Some superficial similarities may be observed with the morphology of the triple merger systems like NGC3341 and SDSS J084905.51+111447.2. However, both NGC3341 and SDSS J084905.51+111447.2 (Pfeifle et al. 2019) seem to have three cores corresponding to the three merging galaxies, even if their discs seem to have been stripped in the case of NGC3341 (Barth et al. 2008), while, in the case of Mrk231, we don't observe the cores corresponding to the second and third galaxies.

Investigating if Mrk231 really is a product of a triple galactic merger would be of great scientific interest. Since the cores corresponding to the galaxies are no longer distinguishable, they might already be a post-merger stage. Interactions of galaxies are typically thought to have lifetimes of several million years, however, the presence of a third SMBH is thought to speed up

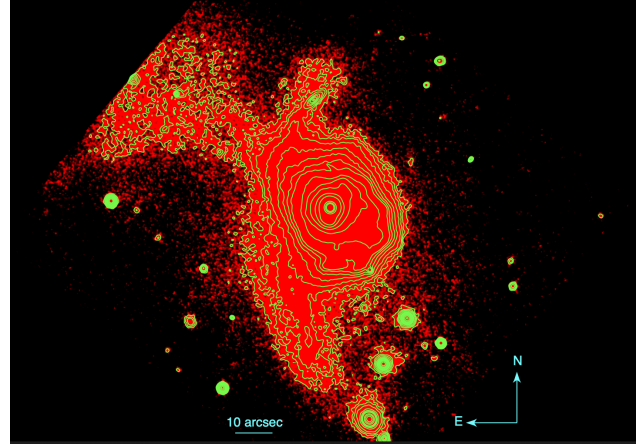


Fig. 17: Optical image of Mrk231 assembled by rotating and stacking the four acquisition images taken by the LBT before commencing with the spectroscopy observations. The presence of diffuse emission adjacent to the northern tidal tail and at an angle to it can be clearly seen. Scale and compass are marked.

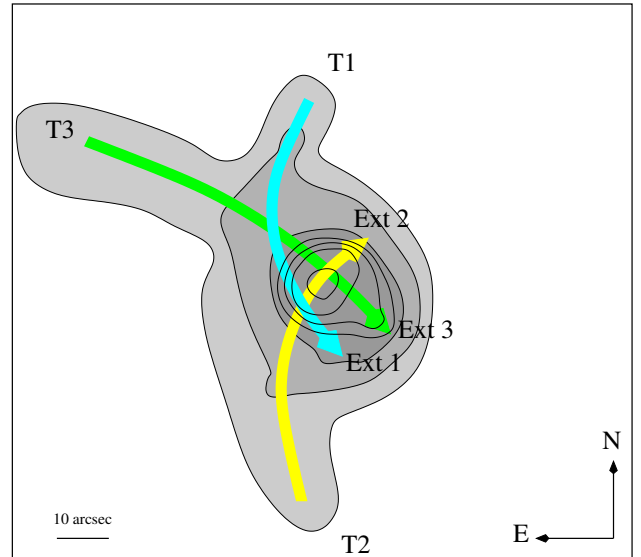


Fig. 18: A sketch showing the possible three galaxy interaction of Mrk231. The contours and the shaded regions are adapted from the LBT acquisition image, Figure 17. Cyan, yellow, and green arrows indicate the paths followed by the three galaxies. Scale and compass are marked.

the process (Ryu et al. 2018), and could be a way to get around the 'final parsec problem' (Milosavljević & Merritt 2003), that is thought to stall a SMBH binary at parsec scales and prevent merging. Since Mrk231 is at a low redshift, it would be possible to conduct a more extensive study on it and check if, for example, continuum or velocity information might be available from the region of diffuse emission.

4.8. Possible merger scenario

The presence of a diffuse third tail and in particular the detection of the additional component to the northeast suggests that Mrk231 is a triple merger. However, a complete simula-

tion would require velocity data from the tidal tails and the main body of the AGN host. In comparison to mergers like the NGC4038/NGC4039 pair, we suggest the following scenario for the triple merger: The extensions visible on low and intermediate intensity levels of the host galaxy indicate the presence of extensions that may be linked to the corresponding tidal tails. The main structure is dominated by two merging systems that are responsible for the tails T1 and T2 (see sketch in Figure 18). These tails may have counterparts in Ext1 and Ext2 on the opposite sides of the nucleus. This structure resembles an almost face on binary merger. A third component that we identify as the additional component to the northeast as a tidal tail T3, resembles a merger component on an almost edge-on orbit that may find its counterpart on the opposite site of the nucleus in the extended component Ext3. Hence the orbital plane of this merger component T3/Ext3 would be almost perpendicular to the binary merger T1/Ext2 and T2/Ext2. A verification of this merger hypothesis requires velocity information that may be provided by planned JWST IFU observations and detailed modeling as we did e.g., for SDSS J134420.86+663717.8 (Misquitta et al. 2020).

5. Conclusions and summary

Mrk231 is a Seyfert 1 ULIRG and a FeLoBAL QSO, with small-scale high velocity outflows as well as large-scale low velocity outflows. In terms of the evolutionary model that favours the path from a merger to a QSO (Sanders et al. 1988a), the mechanism to remove the screen of dust shrouding the nuclei of ULIRGs, thereby revealing the hidden bright QSO, could be provided by fast BAL outflows (Rupke et al. 2005). LoBAL QSOs could, thus, be an intermediate evolutionary phase between a merger and a non-obscured QSO. When two equally massive, gas-rich galaxies undergo an interaction, the gas and dust content within these galaxies is either used to fuel the growth of the central SMBH or it is used in the intense starburst triggered by the collision. In the case of Mrk231, both of these events seem to be taking place simultaneously.

The central region of Mrk231 exhibits peculiar behaviour and has been the study of much previous work. The optical spectrum of the central arcsecond of the galaxy consists of a continuum, overlaid by a very broad $H\alpha$, several Fe II, $H\beta$, Na I D, and weak $[O II]\lambda 3727$ emission lines, as well as strong $He I\lambda 3889$, Ca II H and K, and Na I D absorption lines. The broad $H\alpha$ emission and the $He I\lambda 3889$, Ca II H and K, and Na I D absorption lines are persistently observed in the spectra extracted from regions at a distance of $2''$ (~ 1.7 kpc) from the centre. Additionally, we see a constant presence of a blue-shifted as well reddened narrow $H\alpha$ bumps at wavelengths shorter and longer than $[N II]\lambda 6583$ in all of our spectra. The emission lines and broad absorption lines belong to significantly distinct redshift systems, with the emission lines having a redshift of ~ 0.042 , while the main broad absorption lines correspond to a redshift of ~ 0.0262 . This is typical of BAL systems, where the BAL seem to be produced within clouds associated with the nucleus of the galaxy rather than intervening interstellar medium.

Along with peculiar spectral characteristics, careful inspection of the acquisition images from the observations presented in this work, as well as archival SDSS and DSS images of Mrk231 shows that there is diffuse emission adjacent to the northern tidal arm and almost orthogonal to it, that might be indicative of a past interaction with a third (dwarf) galaxy. As such, Mrk231 presents itself as a good candidate to be investigated further to

understand the source of the diffuse emission and to check if it indeed is a product of a triple galactic merger.

Acknowledgements. Study of the conditions for star formation in nearby AGN and QSOs is carried out within the Collaborative Research Centre 956, sub-project [A02], funded by the Deutsche Forschungsgemeinschaft (DFG) – project ID 184018867.

We made use of the Mods CCD Reduction package to reduce this data. Mod-sCCDRed was developed for the MODS1 and MODS2 instruments at the Large Binocular Telescope Observatory, which were built with major support provided by grants from the U.S. National Science Foundation’s Division of Astronomical Sciences Advanced Technologies and Instrumentation (AST-9987045), the NSF/NOAO TSIP Program, and matching funds provided by the Ohio State University Office of Research and the Ohio Board of Regents. Additional support for modsCCDRed was provided by NSF Grant AST-1108693.

We made use of the NASA/IPAC Extragalactic Database (NED) and of the HyperLeda database.

References

- Aalto, S., Garcia-Burillo, S., Muller, S., et al. 2012, *A&A*, 537, A44
 Adams, T. F. 1972, *ApJ*, 176, L1
 Adams, T. F. & Weedman, D. W. 1972, *ApJ*, 173, L109
 Alatalo, K. 2015, *ApJ*, 801, L17
 Armus, L., Surace, J. A., Soifer, B. T., et al. 1994, *AJ*, 108, 76
 Baan, W. A. 1985, *Nature*, 315, 26
 Barth, A. J., Bentz, M. C., Greene, J. E., & Ho, L. C. 2008, *ApJ*, 683, L119
 Becker, R. H., Gregg, M. D., Hook, I. M., et al. 1997, *ApJ*, 479, L93
 Becker, R. H., White, R. L., Gregg, M. D., et al. 2000, *ApJ*, 538, 72
 Boksenberg, A., Carswell, R. F., Allen, D. A., et al. 1977, *MNRAS*, 178, 451
 Boroson, T. A., Meyers, K. A., Morris, S. L., & Persson, S. E. 1991, *ApJ*, 370, L19
 Branch, D., Leighly, K. M., Thomas, R. C., & Baron, E. 2002, *ApJ*, 578, L37
 Carilli, C. L., Wrobel, J. M., & Ulvestad, J. S. 1998, *AJ*, 115, 928
 Cicone, C., Feruglio, C., Maiolino, R., et al. 2012, *A&A*, 543, A99
 Cutri, R. M., Aitken, D. K., Jones, B., et al. 1981, *ApJ*, 245, 818
 de Boer, K. S., Hoekstra, R., van der Hucht, K. A., et al. 1972, *A&A*, 21, 447
 Dermer, C. D., Bland-Hawthorn, J., Chiang, J., & McNaron-Brown, K. 1997, *ApJ*, 484, L121
 Di Matteo, T., Springel, V., & Hernquist, L. 2005, *Nature*, 433, 604
 Eales, S. A. & Arnaud, K. A. 1988, *ApJ*, 324, 193
 Fabian, A. C. 2012, *ARA&A*, 50, 455
 Fischer, J., Sturm, E., González-Alfonso, E., et al. 2010, *A&A*, 518, L41
 Gallagher, S. C., Brandt, W. N., Chartas, G., Garmire, G. P., & Sambruna, R. M. 2002, *ApJ*, 569, 655
 Gaskell, M., Thakur, N., Tian, B., & Saravanan, A. 2022, *Astronomische Nachrichten*, 343, e210112
 González-Alfonso, E., Fischer, J., Bruderer, S., et al. 2018, *ApJ*, 857, 66
 Greene, J. E. & Ho, L. C. 2005, *ApJ*, 630, 122
 Hamilton, D. & Keel, W. C. 1987, *ApJ*, 321, 211
 Hickox, R. C. & Alexander, D. M. 2018, *ARA&A*, 56, 625
 Hutchings, J. B. & Neff, S. G. 1987, *AJ*, 93, 14
 Klöckner, H.-R., Baan, W. A., & Garrett, M. A. 2003, *Nature*, 421, 821
 Krips, M., Neri, R., García-Burillo, S., et al. 2008, *ApJ*, 677, 262
 Lai, O., Rouan, D., Rigaut, F., Arsenault, R., & Gendron, E. 1998, *A&A*, 334, 783
 Leighly, K. M., Terndrup, D. M., Baron, E., et al. 2014, *ApJ*, 788, 123
 Lipari, S., Colina, L., & Macchetto, F. 1994, *ApJ*, 427, 174
 Lipari, S., Sanchez, S. F., Bergmann, M., et al. 2009, *MNRAS*, 392, 1295
 Lipari, S., Terlevich, R., Zheng, W., et al. 2005, *MNRAS*, 360, 416
 Maloney, P. R. & Reynolds, C. S. 2000, *ApJ*, 545, L23
 Markarian, B. E. 1969, *Astrofizika*, 5, 286
 Milosavljević, M. & Merritt, D. 2003, *ApJ*, 596, 860
 Misquitta, P., Bowles, M., Eckart, A., et al. 2020, *A&A*, 639, A30
 Murray, N., Quataert, E., & Thompson, T. A. 2005, *ApJ*, 618, 569
 Papadopoulos, P. P., Isaak, K. G., & van der Werf, P. P. 2007, *ApJ*, 668, 815
 Pfeifle, R. W., Satyapal, S., Manzano-King, C., et al. 2019, *ApJ*, 883, 167
 Piconcelli, E., Miniutti, G., Ranalli, P., et al. 2013, *MNRAS*, 428, 1185
 Pogge, R. 2019, rwpogge/modsCCDRed 2.0, modsCCDRed was developed for the MODS1 and MODS2 instruments at the Large Binocular Telescope Observatory, which were built with major support provided by grants from the U.S. National Science Foundation’s Division of Astronomical Sciences Advanced Technologies and Instrumentation (AST-9987045), the NSF/NOAO TSIP Program, and matching funds provided by the Ohio State University Office of Research and the Ohio Board of Regents. Additional support for modsCCDRed was provided by NSF Grant AST-1108693.
 Richards, A. M. S., Knapen, J. H., Yates, J. A., et al. 2005, *MNRAS*, 364, 353
 Rieke, G. H. 1976, *ApJ*, 210, L5

- Roche, P. F., Aitken, D. K., & Whitmore, B. 1983, MNRAS, 205, 21P
- Rupke, D. S., Veilleux, S., & Sanders, D. B. 2005, ApJ, 632, 751
- Rupke, D. S. N. & Veilleux, S. 2011, ApJ, 729, L27
- Ryu, T., Perna, R., Haiman, Z., Ostriker, J. P., & Stone, N. C. 2018, MNRAS, 473, 3410
- Sanders, D. B., Soifer, B. T., Elias, J. H., et al. 1988a, ApJ, 325, 74
- Sanders, D. B., Soifer, B. T., Elias, J. H., Neugebauer, G., & Matthews, K. 1988b, ApJ, 328, L35
- Sanders, D. B., Young, J. S., Scoville, N. Z., Soifer, B. T., & Danielson, G. E. 1987, ApJ, 312, L5
- Soifer, B. T., Neugebauer, G., Matthews, K., et al. 2000, AJ, 119, 509
- Teng, S. H., Brandt, W. N., Harrison, F. A., et al. 2014, ApJ, 785, 19
- Toomre, A. & Toomre, J. 1972, ApJ, 178, 623
- Turner, T. J. 1999, ApJ, 511, 142
- Turner, T. J. & Kraemer, S. B. 2003, ApJ, 598, 916
- van der Werf, P. P., Isaak, K. G., Meijerink, R., et al. 2010, A&A, 518, L42
- Veilleux, S., Cecil, G., & Bland-Hawthorn, J. 2005, ARA&A, 43, 769
- Veilleux, S., Meléndez, M., Tripp, T. M., Hamann, F., & Rupke, D. S. N. 2016, ApJ, 825, 42
- Veilleux, S., Rupke, D. S. N., Kim, D. C., et al. 2009, ApJS, 182, 628
- Veilleux, S., Teng, S. H., Rupke, D. S. N., Maiolino, R., & Sturm, E. 2014, ApJ, 790, 116
- Veilleux, S., Trippe, M., Hamann, F., et al. 2013, ApJ, 764, 15
- Yang, L., Dai, X., Lu, Y., Zhu, Z.-H., & Shankar, F. 2018, MNRAS, 480, 5504

Appendix A: A

5 Summary, conclusions and outlook

The work presented in this thesis is based on three projects undertaken to understand the nature of interacting galaxies. The first project, Chapter 2, focuses on a sample of ten pairs/triplets of interacting galaxies, the second project, Chapter 3, is about the pair of interacting galaxies, SDSS J134420.86+663717.8, while the third project, Chapter 4, deals with the radio quiet ULIRG, Markarian 231 (Mrk231). All three projects are based on optical long-slit spectroscopy data obtained using the MODS at the LBT. The main goal of this thesis is to extract and analyse the optical long-slit spectroscopy data of colliding galaxies to study their properties and understand the effects that interactions might have on their evolution. Additionally, efforts have been made toward accessing and analysing archival data where possible, and a simple N-body code was adapted to simulate a morphological and kinematic look-alike of SDSS J134420.86+663717.8 in Chapter 3 to understand the initial conditions of the progenitor galaxies.

This chapter summarises the results from all three projects and attempts to place these results in the context of what is already known about galaxy interactions. Finally, an outlook for the further scope of this research is provided.

5.1 Summary

The following section gives a brief summary of each of the individual projects that form this thesis.

5.1.1 SDSS-FIRST-LBT sample

Figure 5.1 shows the sample of ten pairs/triplets of interacting galaxies selected to be observed using MODS. This sub-sample was selected from a larger sample of 500 galaxies presented by Vitale et al. (2015) and Zajaček et al. (2019). Vitale et al. (2015) focused on a sample of 119 SDSS-FIRST selected galaxies, with the selection criteria of FIRST flux, $F_{1.4\text{GHz}} \geq 100$ mJy, and redshift, $0.04 \leq z \leq 0.4$. Zajaček et al. (2019) presented a more extensive sample by relaxing the FIRST flux criterion to 10 mJy \leq



Figure 5.1: SDSS-FIRST selected sample of ten mergers. See Chapter 2 (Figure 1) for a more detailed image.

$F_{1.4\text{GHz}} \leq 100$ mJy, thereby adding an additional 381 sources to the original sample. The naming convention for the sources used in Chapter 2 follows from the naming convention used in Vitale et al. (2015) and Zajaček et al. (2019), the high FIRST flux sources covered by Vitale et al. (2015) are denoted by the suffix *H* followed by a number, while the sources from the Zajaček et al. (2019) have a lower FIRST flux and are denoted by *L*. Along with archival SDSS and FIRST data, Vitale et al. (2015) and Zajaček et al. (2019) observed all of the 500 sources at 4.85 GHz and 10.45 GHz using the 100-m Effelsberg radio telescope, and present spectral slopes based on the FIRST, 4.85 GHz, and 10.45 GHz fluxes.

Observations with MODS at the LBT were conducted such that the position angle used for the observation covered the nuclei of both of the galaxies in the case of the eight galaxy pairs. For one of the remaining two triplets, L115, it was possible to cover all three nuclei in one position angle, but two position angles were required to cover the three nuclei for the last triplet, L127. A 1'' wide slit was used for all of the observations. Once the spectra were extracted, the emission lines in the spectra were fitted using Gaussian models to estimate their fluxes, line centres, and full widths at half maximum (FWHMs). This in turn helped us to estimate properties like the masses of the central SMBHs, ionisation ratios, bolometric luminosities, Eddington luminosities, and Eddington ratios, and plot diagnostic diagrams. Combining this with the FIRST luminosities and spectral slopes estimated using the FIRST and 4.85 GHz fluxes helped to understand the nature of the ionising source. Additionally, mid-infrared WISE data was used to plot a colour-colour diagram that helped distinguish AGNs from star-forming regions.

The main results of the study are summarised below:

1. Out of the two or three galaxies involved in the interaction in every source in the sample, only one is detected in the radio regime. On plotting optical diagnostic

diagrams (Chapter 2, Figures 5 and 6), it becomes clear that all of the FIRST detected sources lie in the transition/composite region, while the sources not detected by FIRST span all regions of the diagnostic diagram, i.e., star-forming, transition/composite, Seyfert 2, and LINER. This implies that the field that is ionising the nuclear region of the FIRST detected sources must come from a combination of AGN and star-forming regions, solely star-forming regions would not be able to account for the strength of the ionising field.

2. The radio spectral slopes estimated using FIRST and Effelsberg 4.85 GHz continuum fluxes of all of the radio detected sources are ≥ -0.7 , which implies that they are either flat or inverted (Chapter 2, Section 4). Radio emission from star-forming regions is usually faint and dominated by synchrotron emission with steep spectral slopes. Thus, it is less likely that the radio emission seen in the radio-detected sources from the sample originates in star-forming regions. The more likely explanation is that the radiation stems from self-absorbed cores or jets associated with the nucleus of the galaxies. While thermal bremsstrahlung emitted by accelerated electrons has a flat spectrum, at the redshift range covered by the sample, the contribution from non-thermal radiation dominates over the much fainter thermal bremsstrahlung.
3. Using the FWHMs of the broad $H\alpha$ emission lines detected in the nuclear spectra of the sources or by taking into account the stellar velocity dispersions of the nuclear regions, it was possible to estimate the masses of the central SMBHs hosted by the galaxies in the sample (Chapter 2, Sections 6.1 and 6.6). SMBH masses could not be reliably estimated for only three out of the 22 galaxies in the sample, namely, L024B, L125A, and L127C. While the SMBH masses of the entire sample span a range of $\sim 9 \times 10^5 - 9 \times 10^8 M_{\odot}$, the radio-detected galaxies are seen to host the more massive SMBH in the pair/triplet, and these SMBHs have masses in the range $10^7 - 10^8 M_{\odot}$, which are typical values for AGNs like Seyferts.
4. Bolometric luminosity of the sources could be estimated using their 5100 \AA luminosity and the masses of the SMBHs were used to estimate the Eddington luminosity of the sources, where applicable. These, in turn, could be used to estimate the Eddington ratios of the galaxies (Chapter 2, Section 6.4). While the radio-detected galaxies have Eddington ratios in the range $[-4, -2]$, the galaxies not detected in radio have Eddington ratios in the range $[-3, 0]$. The low values of the Eddington ratio are indicative of a lessening of radiative efficiency, which in turn signals a transition from the standard radiatively efficient, optically thick, geometrically thin accretion disc to a radiatively inefficient advection-dominated accretion flow (ADAF) in the inner regions.
5. Archival mid-infrared data observed using the WISE survey (Chapter 2, Section 5) was used to plot a mid-infrared colour-colour diagram (Chapter 2, Figure 16). While the $W2 - W3$ colours of most of the galaxies are high enough to indicate active star formation as opposed to retired galaxies, only two of them, H011A/B and L084B, have high enough $W1 - W2$ to show a significant contribution from an AGN (Chapter 2, Section 6.7).

The work done in Chapter 2 confirms that the interacting galaxies in the SDSS-FIRST-LBT sample have an enhanced level of activity, with at least one galaxy in the pair/triplet having radio emission associated with non-thermal radiation from the nuclear region of the galaxy. These radio detected galaxies also host the more massive SMBH in the pair/triple, and have ionising ratios high enough to indicate contribution from AGN as well star-forming regions.

5.1.2 SDSS J134420.86+663717.8

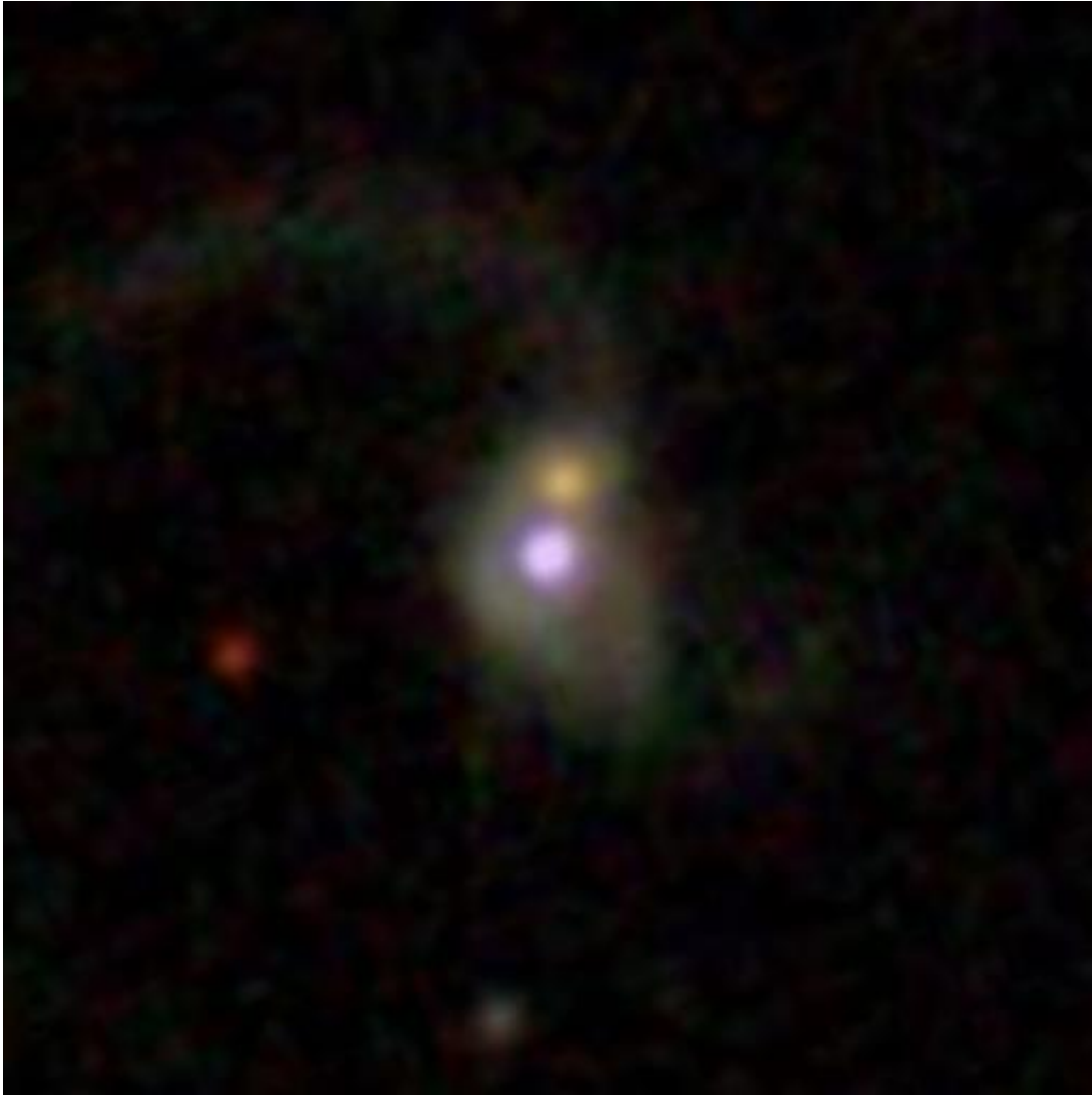


Figure 5.2: SDSS image of the merging pair, SDSS J134420.86+663717.8. See Chapter 3 (Figure 1) for a more detailed image.

Figure 5.2 shows the SDSS survey image of the pair of interacting galaxies, SDSS J134420.86+663717.8. It is located at an intermediate redshift of ~ 0.128 and has been observed at a wide range of wavelengths by surveys like IRAS, WISE, 2MASS, ROSAT, and the Palomar Schmidt 48-inch telescope survey. It consists of two interacting galaxies, designated A (lower in Figure 5.2) and B (upper in Figure 5.2), that are at a

projected separation of ~ 3 arcsec and appear distinct. Nucleus A has an SDSS spectrum and has been classified as a Seyfert 1 galaxy and an infrared luminous galaxy. Nucleus B had no published optical spectrum prior to this work.

The galaxies were observed using MODS at the LBT with a position angle of -12 degrees, chosen to cover both of the nuclei using a $1''$ wide slit. The objective of this project was to extract and analyse the optical long-slit spectra corresponding to both of the nuclei and thereby deduce the properties of the galaxies. Further, a simple N-body simulation was used to understand the initial conditions of the progenitor galaxies.

A careful examination revealed several Balmer lines in the blue band spectrum of nucleus A (Chapter 3, Figure 2). Additionally, both the $H\alpha$ and $H\beta$ emission lines show broad components (Chapter 3, Figures 2, 3, and 4). Broad Hydrogen recombination lines are indicative of the presence of an AGN. On the other hand, nucleus B has a weaker spectrum compared to nucleus A, with fewer emission lines and the presence of stellar absorption lines, especially in the blue band (Chapter 3, Figures 5 and 6). Additionally, no broad components are present in the spectrum of nucleus B.

Plotting the ionisation ratios on optical diagnostic diagrams (Chapter 3, Figure 7), reveals that both nucleus A and nucleus B lie in the transition/composite region on the standard diagnostic plot, however, nucleus A has higher ionisation ratios than nucleus B. The masses of the central SMBHs are estimated to be $2 \times 10^7 M_{\odot}$ for nucleus A and $3 \times 10^7 M_{\odot}$ for nucleus B (Chapter 3, Section 4.3). Galaxy masses were estimated by fitting Sersic profiles for both of the galaxies, yielding a mass of $2 \times 10^{12} M_{\odot}$ for galaxy A and $6 \times 10^{11} M_{\odot}$ for galaxy B (Chapter 3, Section 4.4). Gas rotation curves for both the nuclear regions were plotted using the line centres of the narrow $H\alpha$ line along the slit (Chapter 3, Section 4.2 and Figure 8). Galaxy A is seen to have a maximum observed rotation velocity of $\sim \pm 50 \text{ km s}^{-1}$ while the maximum observed rotation velocity of galaxy B is $\sim \pm 25 \text{ km s}^{-1}$. The velocities obtained from the rotation curve were used in the Baryonic Tully-Fisher relation (Torres-Flores et al. 2011) to estimate the lower limit of the baryonic bulge masses which came out to be $\sim 2 \times 10^8 M_{\odot}$ for galaxy A and $1 \times 10^7 M_{\odot}$ for galaxy B. This is a lower limit since it is not possible to ensure that the major axis of rotation is being probed and there is a high likelihood of perturbation in velocities resulting in a lowered gradient of rotation velocity as the galaxies are interacting.

A careful examination of the tidal tails of galaxies A and B shows that the planes of the galaxies might be orthogonal to each other. Taking this into consideration, two galaxies were initialised orthogonal to each other, with masses of $2 \times 10^{11} M_{\odot}$ each. Galaxy A was initialised with a velocity of 50 pc Myr^{-1} and galaxy B with a velocity of -125 pc Myr^{-1} , based on the velocity difference from the rotation curve. The result of the simulation bears striking resemblance to SDSS J134420.86+663717.8 (Chapter 3, Figure 11). A rotation curve using the line-of-sight (LoS) velocities extracted from the simulation was plotted along with the observed rotation curve (Chapter 3, Figure 8). The simulated rotation curve agrees fairly well with the observed rotation curve. While it is important to remember that this is not a unique solution, it is still of interest that for the selected set of parameters, the resulting model bears a striking resemblance with the observed source, both morphologically and kinematically.

5.1.3 Markarian 231



Figure 5.3: SDSS image of Mrk231. See Chapter 4 (Figure 1) for a more detailed image.

Figure 5.3 shows the SDSS image of Mrk231. Mrk231 is the nearest radio-quiet ULIRG and is a late stage merger based on its morphology. Along with being ultra-luminous in the infrared regime, the nucleus of Mrk231 also has a very bright optical spectrum with very strong and broad $H\alpha$ and multiple Fe II emission. Along with this, the optical spectrum of Mrk231 is interesting because it has strong and broad absorption lines (BAL) in the blue band of its optical spectrum corresponding to a redshift much lower ($z_{\text{BAL}} \sim 0.0262$) than the redshift of the emission line system ($z_{\text{systemic}} \sim 0.0422$). These spectral characteristics make Mrk231 an Fe II emitting low ionisation broad absorption line (FeLoBAL) QSO. In FeLoBAL QSOs, the broad absorption line clouds are thought to be located at a distance from the broad emission line clouds, thereby accounting for the difference in redshift. The covering factor of the BAL clouds might be low, which could explain the rarity of the occurrence of FeLoBALs.

Mrk231 was observed with MODS at the LBT using four different position angles. Figure 1 (bottom panel) from Chapter 4 shows the four position angles. Along with the position angles, the additional slit positions observed are also indicated. Detailed information about the observations can be found in Chapter 4 (Section 2). Altogether, spectral extraction results in seven spectra: one averaged central spectrum and six off-nuclear spectra taken at offsets of $2''$ on either side of the centre at three out of the four position angles. The positions of the slits were such that in the end, there are three spectra from regions to the north of the nucleus and three spectra from regions to the south of the nucleus. Along with the spectra, acquisition images were obtained for each of the position angles. These were processed using the data reduction techniques and examined carefully.

The following points summarise the main results of this work:

1. Broad $H\alpha$ emission is present in all of the off-nuclear spectra along with the expected nuclear spectrum. At a distance of $2''$ from the centre, this corresponds to a distance of $\sim 1.7\text{kpc}$ at the redshift of ~ 0.042 . The existence of broad $H\alpha$ components in the spectra from regions at a scale of more than a kpc from the centre of an AGN is a peculiar occurrence. Such high velocities exist at parsec scales in the broad line region (BLR) of an AGN. This implies that either the BLR in the late stage merger is more extended than a normal BLR or that the high velocities must be an outflow of some kind. The centre of Mrk231 is a site of intense circum-nuclear starburst and has star formation rates $\geq 100 M_{\odot} \text{ yr}^{-1}$. However, it is unlikely that such high velocities are driven solely by star-formation and supernovae explosions, implying that there might be contribution from the nucleus as well (Chapter 4, Section 4.1).
2. Outflows are also seen in narrow $H\alpha$ emission line, which has two additional narrow components in every spectrum: the reddened one is clearly visible as a bump on the right side of the $H\alpha + [\text{N II}]$ complex, while the blue bump is not clearly visible but can be seen in the spectral decomposition of the $H\alpha + [\text{N II}]$ complex (Chapter 4, Section 4.2 and Figures 3,6, and 9). These seem to be low velocity outflows, probably associated with the intense star-burst, however, we see no corresponding outflows in $[\text{O III}]\lambda 5007$.
3. The spectra from regions to the south of the nucleus are stronger than the spectra from regions to the north. They show $H\beta$ emission in their spectrum, have more prominent $z \sim 0.0262$ absorption lines, and a spectrum steeped towards the red band compared to the north which shows little to no $H\beta$ emission, absorption lines of similar strength belonging to different redshift systems (Chapter 4, Section 4.4), and flatter spectra. Previous findings show that the region to the south of the nucleus is a site of intense star-burst.
4. The mass of the central SMBH is estimated to be $(2.3 \pm 0.2) \times 10^8 M_{\odot}$ using the broad $H\beta$ line observed in the central spectrum, which agrees quite well with the literature value of $2.3 \times 10^8 M_{\odot}$ (Leighly et al. 2014) (Chapter 4, Section 4.5).
5. A careful examination of the acquisition images shows that there is diffuse emission in the region adjacent to the northern tidal tail that extends almost orthogonally

from the base of the northern tidal tail in a north-east direction. This could likely be the remnant of a previous interaction or perhaps an old tidal tail. This implies that the interaction history of Mrk231 might be more complicated than previously thought, which could play a role in helping to understand the strange nature of this source.

5.2 Concluding remarks

The previous section 5.1 summarises the three projects undertaken as a part of this doctoral thesis. The underlying connection between the three projects is that all of the sources observed and studied are engaged in interactions. Now that the results of these studies are at hand, it is possible to draw some conclusions regarding the similarities and differences between these sources as well as take into consideration what is known about interacting galaxies from previous studies.

5.2.1 Mergers as a step in galactic evolution

Mergers of galaxies are thought to have played a very important role in the process of galaxy evolution at high redshift. The hierarchical clustering model of galaxy evolution states that galaxies evolved via mergers of smaller bodies (Gott & Rees 1975; White & Rees 1978). In the early stages of the universe after the Big Bang, as galaxies started forming, they were spaced close to each other, leading to a high probability of interactions. As the universe expands, galaxies move farther away from each other, thereby reducing the probability of interaction. In terms of cosmic time scales, this implies that if the collision rate were to be measured, it would be higher at an intermediately higher redshift, peaking around $z \sim 2-3$ ('cosmic high noon'), and lower on either side of this peak redshift. Several studies have been conducted to estimate merger rates over redshift ranges and have found that indeed there is a larger incidence of mergers at earlier times that tends to decrease toward the present epoch (Mantha et al. (2018) and references therein). However, the selection criteria must be chosen carefully to avoid having a biased sample.

In recent years, the initial assumption that mergers are the predominant mechanism to facilitate galaxy evolution at high redshift has been challenged by studies involving increasingly better telescopes (e.g., Genzel et al. (2008); Dekel et al. (2009); Kaviraj et al. (2011); Conselice et al. (2013); Dullo & Graham (2013); Graham et al. (2015); Lofthouse et al. (2017)). Therefore, it is important to consider other processes of galaxy evolution, as well. However, high-excitation radio galaxies predominantly show signs of disturbance which are indicative of a merger (Ramos Almeida et al. 2012b; Pierce et al. 2019). An interesting point to consider is the launching of strong radio jets from the vicinity of an AGN. This could be associated with the spin of the SMBH (Blandford & Znajek 1977), which in turn could be linked to the accretion process of the AGN. In AGN where the accretion is inefficient, the material accreted is not sufficient to change the angular momentum of the SMBH. However, if the accretion process were violent and efficient, then the change in the angular momentum induced by the infalling material would cause the spin of the SMBH to change, which would in turn launch a powerful

radio jet. A gas-rich major merger could, in principle, fulfill the necessary conditions to trigger such a spin change in a SMBH.

The interesting questions to consider, then, are do all mergers trigger AGN? In the AGN triggered by interactions, how frequent are radio loud AGN? In which phase of the interaction does the SMBH start accreting material? Do the SMBHs of all of the galaxies involved in the interaction get triggered? If not, then are there any correlations between the SMBHs that do start accretion? When does the radio-loud phase start? When does it end?

Let's consider the interacting sources in all of the three projects from the perspective of these questions. Out of all of our 25 galaxies (22 from the SDSS-FIRST-LBT sample, 2 belonging to the SDSS J134420.86+663717.8 pair, and 1 corresponding to Mrk231), only one, H011A, is radio loud. While H011 has the shortest projected pair separation in the SDSS-FIRST-LBT sample, and so it might be tempting to conclude that there is a correlation there, Mrk231 is classified as radio quiet, even though it seems to be in a later stage of merger, such that the two nuclei are no longer distinguishable. In comparison with Mrk231, the two nuclei of H011 still appear distinct. Although, it is important to note that despite being radio quiet, Mrk231 has a core and two lobes, extended over ~ 40 pc (Neff & Ulvestad 1988; Ulvestad et al. 1999a). Under higher resolution, the core can be resolved into two distinct compact components with a separation of ~ 1 pc: a variable core and an inner jet (Ulvestad et al. 1999b; Reynolds et al. 2009, 2017, 2020). It has also been deduced that Mrk231 is becoming radio-loud (Reynolds et al. 2017). H011, on the hand, shows signs of being a restarted radio loud AGN (Marecki et al. 2006). Active accretion of material on to a SMBH is thought to be episodic, rather than a once-in-a-lifetime event (e.g., Franceschini et al. (1998); Schoenmakers et al. (2000); Saripalli & Mack (2007)). Along with these two sources associated with an AGN, nine out of the other 20 galaxies from the SDSS-FIRST-LBT survey are detected in the radio regime by FIRST, although their fluxes are low enough to be considered radio-quiet. Based on their radio spectral slopes, it seems likely that this radio emission is associated with the nuclei of the galaxies and not star formation. The radio emission also seems to be associated with the more massive SMBH in the pair or triplet of interacting galaxies. All of the nuclei associated with the radio emission have ionisation ratios high enough to require contribution from both an AGN and star-forming regions. Although, SDSS J134420.86+663717.8 does not fall in the region covered by FIRST, the spectrum of nucleus A displays broad emission lines, indicating the presence of an AGN, while nucleus B is less energetic.

Therefore, based on the work carried out in this thesis, it can be concluded that while the radio-loud phase is not triggered in most of our interacting galaxies, the central regions of the galaxies are certainly involved in some energetic phenomenon that might increase in strength as the merger advances and more fuel is available in the nuclear regions of galaxies. This energetic phenomenon might be enhanced star formation as well as increased accretion onto the central SMBH. It is also interesting to note that it's usually one nucleus of the two or three involved in an interaction that shows signs of being more energetic than the other. From the SDSS-FIRST-LBT sample, the more energetic nucleus is usually the more massive one.

5.3 Outlook

Interacting galaxies have been the subject of many studies over the last several decades, starting from early studies by, for example, [Toomre & Toomre \(1972\)](#); [Barnes & Hernquist \(1991, 1996\)](#); [Hopkins et al. \(2005\)](#), to recent works like [Kawaguchi et al. \(2020\)](#); [McAlpine et al. \(2020\)](#); [Shah et al. \(2022\)](#); [Sivasankaran et al. \(2022\)](#). However, forming a coherent and cohesive theory has proven to be elusive. This could, in part, be due to the highly varied selection criteria employed while forming samples for study. Another reason could be because our database is constantly improving as better telescopes and more advanced simulations are developed. While much progress has been done, there is still much we don't know about galaxy interactions and the role they play in galaxy evolution.

In this regard, the coming decades will surely be highly interesting. With the launch of the James Webb Space Telescope (JWST) on December 25, 2021, a new arena of data collection has been opened up. Cycle 1 projects like the COSMOS-Webb Cosmic Origin Survey ([Kartaltepe et al. 2021](#); [Casey et al. 2022](#)) will image several thousands of galaxies for extended periods of time (COSMOS-Webb will observe half a million galaxies in the near infrared (NIR) and 32000 in the mid-infrared (MIR) over ~ 208 hours). This will enable researchers to conduct spectroscopic follow-ups. Specific to this thesis, Mrk231 is one of the sources that are planned to be observed as a part of the Cycle 1 guaranteed time observations (GTO) ¹, wherein the nucleus, southern star-forming shell, and the background of Mrk231 will be observed using NIR and MIR spectroscopy. Along with JWST, at least two thirty-metre telescopes are planned to start operating in the upcoming decade - the European Southern Association's (ESO) Extremely Large Telescope (ELT) on Cerro Armazones in Chile and the Thirty Meter Telescope (TMT) on Mauna Kea in the USA. While the TMT will have a 30 metre wide mirror, the diameter of the ELT mirror is planned to span 39 metres. They will operate at infrared and optical wavelengths. Access to higher resolution data over a wide range of redshift will surely help to improve our understanding of galaxy evolution.

¹<https://www.stsci.edu/jwst/phase2-public/1268.pdf>

Bibliography

- Antonucci, R. 1993, *ARA&A*, 31, 473
- Bañados, E., Venemans, B. P., Mazzucchelli, C., et al. 2018, *Nature*, 553, 473
- Balick, B. & Brown, R. L. 1974, *ApJ*, 194, 265
- Barnes, J. E. & Hernquist, L. 1996, *ApJ*, 471, 115
- Barnes, J. E. & Hernquist, L. E. 1991, *ApJ*, 370, L65
- Best, P. N. & Heckman, T. M. 2012, *MNRAS*, 421, 1569
- Blandford, R. D. & Znajek, R. L. 1977, *MNRAS*, 179, 433
- Blanton, M. R. & Moustakas, J. 2009, *ARA&A*, 47, 159
- Bridge, C. R., Appleton, P. N., Conselice, C. J., et al. 2007, *ApJ*, 659, 931
- Casey, C. M., Kartaltepe, J. S., Drakos, N. E., et al. 2022, arXiv e-prints, arXiv:2211.07865
- Chiaberge, M., Gilli, R., Lotz, J. M., & Norman, C. 2015, *ApJ*, 806, 147
- Conselice, C. J., Mortlock, A., Bluck, A. F. L., Grützbauch, R., & Duncan, K. 2013, *MNRAS*, 430, 1051
- de Vaucouleurs, G. 1948, *Annales d'Astrophysique*, 11, 247
- DeGraaff, R. B., Blakeslee, J. P., Meurer, G. R., & Putman, M. E. 2007, *ApJ*, 671, 1624
- Dekel, A., Birnboim, Y., Engel, G., et al. 2009, *Nature*, 457, 451
- Dullo, B. T. & Graham, A. W. 2013, *ApJ*, 768, 36
- Eckart, A., Hüttemann, A., Kiefer, C., et al. 2017, *Foundations of Physics*, 47, 553
- Einstein, A. 1915, *Sitzungsberichte der Königlich Preussischen Akademie der Wissenschaften*, 778

- Ellison, S. L., Patton, D. R., & Hickox, R. C. 2015, *MNRAS*, 451, L35
- Faber, S. M. & Jackson, R. E. 1976, *ApJ*, 204, 668
- Faber, S. M., Willmer, C. N. A., Wolf, C., et al. 2007, *ApJ*, 665, 265
- Fixsen, D. J. 2009, *ApJ*, 707, 916
- Franceschini, A., Vercellone, S., & Fabian, A. C. 1998, *MNRAS*, 297, 817
- Freeman, K. C. 1970, *ApJ*, 160, 811
- Gallagher, John S., I. & Hunter, D. A. 1984, *ARA&A*, 22, 37
- Genzel, R., Burkert, A., Bouché, N., et al. 2008, *ApJ*, 687, 59
- Gerola, H. & Seiden, P. E. 1978, *ApJ*, 223, 129
- Gerola, H., Seiden, P. E., & Schulman, L. S. 1980, *ApJ*, 242, 517
- Gordon, Y. A., Pimbblet, K. A., Kaviraj, S., et al. 2019, *ApJ*, 878, 88
- Gott, J. R., I. & Rees, M. J. 1975, *A&A*, 45, 365
- Graham, A. W. 2013, in *Planets, Stars and Stellar Systems. Volume 6: Extragalactic Astronomy and Cosmology*, ed. T. D. Oswalt & W. C. Keel, Vol. 6, 91–140
- Graham, A. W., Dullo, B. T., & Savorgnan, G. A. D. 2015, *ApJ*, 804, 32
- GRAVITY Collaboration, Abuter, R., Amorim, A., et al. 2018, *A&A*, 615, L15
- Greene, J. E., Strader, J., & Ho, L. C. 2020, *ARA&A*, 58, 257
- Hardcastle, M. J. & Croston, J. H. 2020, *NewAR*, 88, 101539
- Hardcastle, M. J., Evans, D. A., & Croston, J. H. 2007, *MNRAS*, 376, 1849
- Hopkins, P. F., Hernquist, L., Cox, T. J., et al. 2005, *ApJ*, 630, 705
- Hopkins, P. F., Somerville, R. S., Hernquist, L., et al. 2006, *ApJ*, 652, 864
- Hubble, E. P. 1925, *Popular Astronomy*, 33, 252
- Hubble, E. P. 1926, *ApJ*, 64, 321
- Jogee, S., Miller, S. H., Penner, K., et al. 2009, *ApJ*, 697, 1971
- Kartaltepe, J., Casey, C. M., Bagley, M., et al. 2021, *COSMOS-Webb: The Webb Cosmic Origins Survey*, JWST Proposal. Cycle 1, ID. #1727
- Kaviraj, S. 2014, *MNRAS*, 440, 2944
- Kaviraj, S., Tan, K.-M., Ellis, R. S., & Silk, J. 2011, *MNRAS*, 411, 2148
- Kawaguchi, T., Yutani, N., & Wada, K. 2020, *ApJ*, 890, 125

- Kellermann, K. I., Sramek, R., Schmidt, M., Shaffer, D. B., & Green, R. 1989, *AJ*, 98, 1195
- Kormendy, J. 1982, *ApJ*, 257, 75
- Kormendy, J. 2013, in *Secular Evolution of Galaxies*, ed. J. Falcón-Barroso & J. H. Knapen, 1
- Kormendy, J. & Kennicutt, Robert C., J. 2004, *ARA&A*, 42, 603
- Krup, E. C. 2003, *Echoes of the Ancient Skies* (Dover Publications)
- Laing, R. A., Jenkins, C. R., Wall, J. V., & Unger, S. W. 1994, in *Astronomical Society of the Pacific Conference Series*, Vol. 54, *The Physics of Active Galaxies*, ed. G. V. Bicknell, M. A. Dopita, & P. J. Quinn, 201
- Lambas, D. G., Tissera, P. B., Alonso, M. S., & Coldwell, G. 2003, *MNRAS*, 346, 1189
- Leighly, K. M., Terndrup, D. M., Baron, E., et al. 2014, *ApJ*, 788, 123
- Lin, C. C. & Shu, F. H. 1964, *ApJ*, 140, 646
- Lin, L., Koo, D. C., Willmer, C. N. A., et al. 2004, *ApJ*, 617, L9
- Lin, L., Patton, D. R., Koo, D. C., et al. 2008, *ApJ*, 681, 232
- Lindblad, B. 1925, *ApJ*, 62, 191
- Lofthouse, E. K., Kaviraj, S., Conselice, C. J., Mortlock, A., & Hartley, W. 2017, *MNRAS*, 465, 2895
- Lotz, J. M., Jonsson, P., Cox, T. J., & Primack, J. R. 2010, *MNRAS*, 404, 590
- Maller, A. H., Katz, N., Kereš, D., Davé, R., & Weinberg, D. H. 2006, *ApJ*, 647, 763
- Mantha, K. B., McIntosh, D. H., Brennan, R., et al. 2018, *MNRAS*, 475, 1549
- Marecki, A., Thomasson, P., Mack, K. H., & Kunert-Bajraszewska, M. 2006, *A&A*, 448, 479
- McAlpine, S., Harrison, C. M., Rosario, D. J., et al. 2020, *MNRAS*, 494, 5713
- Misquitta, P., Bowles, M., Eckart, A., et al. 2020, *A&A*, 639, A30
- Misquitta, P., Eckart, A., Zajaček, M., & Yttergren, M. 2023, *A&A*, 671, A18
- Moore, B., Lake, G., & Katz, N. 1998, *ApJ*, 495, 139
- Mueller, M. W. & Arnett, W. D. 1976, *ApJ*, 210, 670
- Naab, T., Khochfar, S., & Burkert, A. 2006, *ApJ*, 636, L81
- Neff, S. G. & Ulvestad, J. S. 1988, *AJ*, 96, 841
- Netzer, H. 2013, *The Physics and Evolution of Active Galactic Nuclei*

- Nikolic, B., Cullen, H., & Alexander, P. 2004, *MNRAS*, 355, 874
- Pace, C. & Salim, S. 2014, *ApJ*, 785, 66
- Padovani, P. 2017, *Nature Astronomy*, 1, 0194
- Parsa, M., Eckart, A., Shahzamanian, B., et al. 2017, *ApJ*, 845, 22
- Pedersen, O. 1993, *Early Physics and Astronomy* (Cambridge University Press)
- Peterson, B. M. 2006, in *Physics of Active Galactic Nuclei at all Scales*, ed. D. Alloin, Vol. 693, 77
- Pierce, J. C. S., Tadhunter, C. N., Ramos Almeida, C., Bessiere, P. S., & Rose, M. 2019, *MNRAS*, 487, 5490
- Pogge, R. 2019, *rw-pogge/modsCCDRed 2.0*, *modsCCDRed* was developed for the MODS1 and MODS2 instruments at the Large Binocular Telescope Observatory, which were built with major support provided by grants from the U.S. National Science Foundation's Division of Astronomical Sciences Advanced Technologies and Instrumentation (AST-9987045), the NSF/NOAO TSIP Program, and matching funds provided by the Ohio State University Office of Research and the Ohio Board of Regents. Additional support for *modsCCDRed* was provided by NSF Grant AST-1108693.
- Ramos Almeida, C., Bessiere, P. S., Tadhunter, C. N., et al. 2012a, *MNRAS*, 419, 687
- Ramos Almeida, C., Bessiere, P. S., Tadhunter, C. N., et al. 2012b, *MNRAS*, 419, 687
- Reynolds, C., Punsly, B., Kharb, P., O'Dea, C. P., & Wrobel, J. 2009, *ApJ*, 706, 851
- Reynolds, C., Punsly, B., Miniutti, G., O'Dea, C. P., & Hurley-Walker, N. 2017, *ApJ*, 836, 155
- Reynolds, C., Punsly, B., Miniutti, G., O'Dea, C. P., & Hurley-Walker, N. 2020, *ApJ*, 891, 59
- Reynolds, C., Ueda, Y., Awaki, H., et al. 2014, *arXiv e-prints*, arXiv:1412.1177
- Ryden, B. 2003, *Introduction to cosmology*
- Sabater, J., Best, P. N., & Heckman, T. M. 2015, *MNRAS*, 447, 110
- Sahu, K. C., Anderson, J., Casertano, S., et al. 2022, *ApJ*, 933, 83
- Sandage, A. 2005, *ARA&A*, 43, 581
- Saripalli, L. & Mack, K. H. 2007, *MNRAS*, 376, 1385
- Schmidt, M. 1963, *Nature*, 197, 1040
- Schoenmakers, A. P., de Bruyn, A. G., Röttgering, H. J. A., van der Laan, H., & Kaiser, C. R. 2000, *MNRAS*, 315, 371
- Sérsic, J. L. 1963, *Boletín de la Asociación Argentina de Astronomía La Plata Argentina*, 6, 41

- Shah, E. A., Kartaltepe, J. S., Magagnoli, C. T., et al. 2022, *ApJ*, 940, 4
- Shu, F. H. 2016, *ARA&A*, 54, 667
- Sivasankaran, A., Blecha, L., Torrey, P., et al. 2022, *MNRAS*, 517, 4752
- Soria, R., Graham, A. W., Fabbiano, G., et al. 2006, *ApJ*, 640, 143
- Stewart, K. R., Bullock, J. S., Wechsler, R. H., Maller, A. H., & Zentner, A. R. 2008, *ApJ*, 683, 597
- Toomre, A. & Toomre, J. 1972, *ApJ*, 178, 623
- Torres-Flores, S., Epinat, B., Amram, P., Plana, H., & Mendes de Oliveira, C. 2011, *MNRAS*, 416, 1936
- Tran, K.-V. H., van Dokkum, P., Franx, M., et al. 2005, *ApJ*, 627, L25
- Tully, R. B. 1987, *ApJ*, 323, 1
- Tully, R. B., de Marseille, O., & Fisher, J. R. 1975, in *Bulletin of the American Astronomical Society*, Vol. 7, 426
- Ulvestad, J. S., Wrobel, J. M., & Carilli, C. L. 1999a, *ApJ*, 516, 127
- Ulvestad, J. S., Wrobel, J. M., Roy, A. L., et al. 1999b, *ApJ*, 517, L81
- Urry, C. M. & Padovani, P. 1995, *PASP*, 107, 803
- van den Bergh, S. 2012, *ApJ*, 754, 68
- Vitale, M., Fuhrmann, L., García-Marín, M., et al. 2015, *A&A*, 573, A93
- Westman, R. S. 2011, *The Copernican Question* (Los Angeles: University of California Press)
- White, S. D. M. & Rees, M. J. 1978, *MNRAS*, 183, 341
- Zajaček, M., Busch, G., Valencia-S., M., et al. 2019, *A&A*, 630, A83

List of Figures

1.1	Tuning fork style schematic of the Hubble sequence used to classify galaxies morphologically. Credit: Wikipedia	6
1.2	Processes of galaxy evolution updated from Kormendy (1982) and from Kormendy & Kennicutt (2004) . Processes are divided vertically into fast (top) and slow (bottom). Fast evolution happens on a free-fall (dynamical) timescale. Slow means many galaxy rotation periods. Processes are divided horizontally into ones that happen internally in one galaxy (left) and ones that are driven by environment (right). Credit: Kormendy (2013)	10
1.3	Different stages of a merger of galaxies. The images depict the interaction of galaxies Abell 901 and Abell 902, and are illustrated using different images of various galaxies taken by the Hubble Space Telescope. Image credit: NASA, ESA, the Hubble Heritage Team (STScI/AURA)-ESA/Hubble Collaboration and A. Evans (University of Virginia, Charlottesville/NRAO/Stony Brook University), K. Noll (STScI), and J. Westphal (Caltech).	12
1.4	Event Horizon Telescope images of the SMBH at the centres of the giant elliptical galaxy M87 (left) and the Milky Way (right). The images show radio emission from a heated accretion ring orbiting the compact object. The dark centre is the event horizon and its shadow. The images were released in 2019 and 2022, respectively, by the Event Horizon Telescope Collaboration.	14
1.5	The unified AGN model described by Urry & Padovani (1995) . The various components of the AGN are indicated. Credit: Reynolds et al. (2014)	16
5.1	SDSS-FIRST selected sample of ten mergers. See Chapter 2 (Figure 1) for a more detailed image.	92
5.2	SDSS image of the merging pair, SDSS J134420.86+663717.8. See Chapter 3 (Figure 1) for a more detailed image.	94
5.3	SDSS image of Mrk231. See Chapter 4 (Figure 1) for a more detailed image.	96

List of Acronyms

ADAF	Advection Dominated Accretion Flow
ADS	Astrophysics Data System
AO	Adaptive Optics
AGN	Active Galactic Nucleus
ALMA	Atacama Large Millimeter Array
BH	Black Hole
BLR	Broad Line Region
CCD	Charge-Coupled Device
CMB	Cosmic Background Radiation
EHT	Event Horizon Telescope
FoV	Field of View
FIR	Far-infrared
GC	Galactic Center
IR	Infrared
LBT	Large Binocular Telescope
M33	Triangulum galaxy
MIR	Mid-infrared
MW	Milky Way
MODS	Multi Object Double Spectrographs
NIR	Near-Infrared
NLR	Narrow Line Region
RIAF	Radiatively Inefficient Accretion Flow
RQ	Radio Quiet

RL Radio Loud

pc parsec

SED Spectral Energy Distribution

Sgr A* Sagittarius A*

SMBH Supermassive Black Hole

submm submillimeter

UV Ultraviolet

Acknowledgements

No man is an island entire of itself, writes the poet John Donne in his Meditation XVII from *Devotions upon Emergent Occasions*. This has been particularly true for me in the duration of my doctoral work. A PhD is often solitary work, we have some vague questions that we try to understand and then attempt to answer in the duration of time we have at hand. Therefore, oftentimes, it is a very isolating experience. However, I have been very fortunate to have been surrounded by some extremely amazing people.

A huge thank you to Prof. Andreas Eckart, who has been my academic advisor since my Master's thesis, for giving me the opportunity to conduct my doctoral research in his group. His zest for life, generosity of spirit, and immense knowledge, academic and otherwise, are inspirational and motivational, and I shall be forever grateful that I had the opportunity to have his guidance.

A big thank you to the other two members of my Thesis Advisory Committee (TAC), Prof. Jochen Heidt and Dr. Alvaro Sánchez-Monge. The annual TAC meetings were always a joy because my committee members were very supportive and interested in my work, which really helped to build my confidence in the projects.

Observations with the LBT were a big part of my PhD life and they helped me to understand the data better. I am very grateful to Prof. Jochen Heidt for our discussions, they helped me understand and plan the observations in a better and more efficient manner. A big thank you to Prof. Roland Gredel and Prof. Jochen Heidt for organising the LBTB observations and for giving me the opportunity to be the primary observer for several observing runs. I am also very grateful to the telescope operators and science support members at the LBT for helping us with our observations, especially Dr. Dave Thompson who served as the local observer for most of our observations. It was a true pleasure to observe with him, especially towards the last observing run when I became comfortable enough with the process to ask general observation questions.

I am very grateful towards Prof. Lucas Labadie and Prof. Andreas Zilges for accepting to be the second reviewer and Chair of my PhD exam committee, respectively.

A big thank you to Dr. Petra Neubauer-Günther for always being there with helpful suggestions and advise, especially for her help during my first years at the Institute. I am always amazed by how she can remember the names of almost all the students with whom she has had contact. I am also very grateful for all the kindness, help, and support extended by Steffi Simone, Bettina Krause, Tanja Bodendorf, and Huyen Nguyen. A big thank you to Dr. Susanne Herbst, Dr. Isabelle Breloy, and Dr. Matteo Cacco for help regarding SFB matters. I'm especially thankful towards Dr. Isabelle Breloy for always staying on top of my TAC meetings and reminding me gently when it was time and towards Dr. Matteo Cacco for patiently handling all of my travel expense documentation.

I am grateful that I managed to have some normal office time before the pandemic struck and changed the definition of normal for all of us. The daily Mensa lunches, the impromptu coffee/tea breaks, the Christmas and birthday dinners, the conferences in Prague, Schloss Wahn, and Brno, and the short time span when we had *Tanja-Tuesdays* were always joyous occasions to let off some steam and relax. For all of this, I am thankful to all the current and former members of the *Eckart* and *Labadie* groups.

It has been a true joy to share the office 220 with some wonderful colleagues who became even better friends - Rebecca, Marzieh, Nastaran, Harshitha, and Elaheh. Especially Elaheh and Harshitha with whom I share the office since the start of the pandemic, they have been a true support system, always motivating and kind, ever ready to commiserate in moments of grief, encourage in moments of doubt, and celebrate the joys and triumphs - I am so very grateful for the both of them.

Many thanks to the colleagues and friends who proofread my thesis - Aparna, Basel, Elaheh, Lukas, Nachiketa, Matthias, Madeleine, and Rebecca, for making the time and for your patience. A big thank you to Raphael Büchel for his help with translating the abstract and to Lukas for reviewing it and providing suggestions.

I have been fortunate enough to have some truly wonderful friends who have made my life richer by their presence. A big thank you to Giulia Pignataro and Dr. Shashwata Ganguly for sticking by me through all the thicks and thins. It has been a pleasure to share most of my happy, sad, scary, doubtful, and triumphant moments over the last seven years with the two of you. The same applies to Rebecca Saalfeld, for her warm, kind, and loving presence in my life. I am also very grateful for my friendship with Dr. Madeleine Yttergren, with whom I am able to share thoughts about research, books, art, and life in general - it's a joy to have her in my life. Another amazing friend to be grateful for is Aparna Venkat, especially for her way of helping me look at the positive in every situation. A huge thank you to Nachiketa Patil, for always being there and for bearing all of my babbling and philosophising. He has an innate capability to make me laugh when joy seems to be the furthest thing from my mind, and to make me stop and consider a difficult situation from a more rational perspective, for which I shall be forever grateful.

And finally, I owe my deepest gratitude to my wonderful parents, Dolcy and Thomas Misquitta. Whatever I am today, whatever I hope to be, it's because of their loving influence in my life. *Papa*, thank you so much for encouraging my reading habits, for our intense debates/discussions, for our annual vacations, our chess matches, and especially

for your patience and open-mindedness. *Mumma*, I am so very grateful and glad that I'm your daughter. Thank you for always being so understanding and encouraging, for the kindness of your spirit, and for making the time in the midst of your very busy days when I was a teenager to have long, daily conversations with me. They helped me to develop belief in myself, which is ultimately the one thing that helped me feel safe and overcome the moments of doubt that invariably come along the way in long-term projects.

Selbständigkeitserklärung

„Hiermit versichere ich an Eides statt, dass ich die vorliegende Dissertation selbstständig und ohne die Benutzung anderer als der angegebenen Hilfsmittel und Literatur angefertigt habe. Alle Stellen, die wörtlich oder sinngemäß aus veröffentlichten und nicht veröffentlichten Werken dem Wortlaut oder dem Sinn nach entnommen wurden, sind als solche kenntlich gemacht. Ich versichere an Eides statt, dass diese Dissertation noch keiner anderen Fakultät oder Universität zur Prüfung vorgelegen hat; dass sie - abgesehen von unten angegebenen Teilpublikationen und eingebundenen Artikeln und Manuskripten - noch nicht veröffentlicht worden ist sowie, dass ich eine Veröffentlichung der Dissertation vor Abschluss der Promotion nicht ohne Genehmigung des Promotionsausschusses vornehmen werde. Die Bestimmungen dieser Ordnung sind mir bekannt. Darüber hinaus erkläre ich hiermit, dass ich die Ordnung zur Sicherung guter wissenschaftlicher Praxis und zum Umgang mit wissenschaftlichem Fehlverhalten der Universität zu Köln gelesen und sie bei der Durchführung der Dissertation zugrundeliegenden Arbeiten und der schriftlich verfassten Dissertation beachtet habe und verpflichte mich hiermit, die dort genannten Vorgaben bei allen wissenschaftlichen Tätigkeiten zu beachten und umzusetzen. Ich versichere, dass die eingereichte elektronische Fassung der eingereichten Druckfassung vollständig entspricht.“

Teilpublikationen/eingebundene Artikel:

- SDSS-FIRST selected interacting galaxies. An optical long slit spectroscopy study using MODS at the LBT
- Interactions among intermediate redshift galaxies. The case of SDSS J134420.86+663717.8

Eingebundene Manuskripte in Vorbereitung:

- The peculiar optical spectrum of Mrk231

18.12.2022, Persis Misquitta

A handwritten signature in black ink, reading "Persis" in a cursive script, followed by a long horizontal line extending to the right.

Lebenslauf

Persis Misquitta

Curriculum Vitae

Gerolsteiner Straße 38
50937 Cologne
Germany

✉ [regular] misquitta@ph1.uni-koeln.de



Personal data

Date of birth **27.11.1993**
Place of birth **Vasai, India**
Nationality **Indian**

Education

02.2019– Present **Doctoral candidate**, *I.Physikalisches Institut*, University of Cologne, Germany
10.2015– 11.2018 **Master of Science**, *University of Cologne*, Cologne, Germany
Primary area of specialisation: Astrophysics
07.2011– 06.2014 **Bachelor of Science**, *St.Xavier's College (Autonomous)*, Mumbai, India
Major: Physics, minors: Mathematics and Chemistry

Publications

- 2020 **Persis Misquitta**, Andreas Eckart, Michal Zajaček, Madeleine Yttergren, SDSS-FIRST selected interacting galaxies
A&A, accepted for publication: 30.11.2022
- 2020 **Persis Misquitta**, Micah Bowles, Andreas Eckart, Madeleine Yttergren, Gerold Busch, Monica Valencia-S., and Nastaran Fazeli, Interactions among intermediate redshift galaxies: The case of SDSS J134420.86+663717.8
A&A, volume 639, A30, July 2020
- 2021 **Madeleine Yttergren**, **Persis Misquitta**, Á. Sánchez-Monge, M. Valencia-S., A. Eckart, A. Zensus, T. Peitl-Thiesen, Gas and stellar dynamics in Stephan's Quintet: Mapping the kinematics in a closely interacting compact galaxy group
arXiv e-prints, arXiv:2109.13757, September 2021
- 2020 **Nastaran Fazeli**, Andreas Eckart, Gerold Busch, Madeleine Yttergren, Françoise Combes, **Persis Misquitta**, and Christian Straubmeier, Near-infrared observations of the gas structure and kinematics in the circumnuclear region of NGC 1672
A&A, volume 638, A36, June 2020
- 2020 **Nastaran Fazeli**, Andreas Eckart, Gerold Busch, Françoise Combes, **Persis Misquitta**, and Christian Straubmeier, Central kiloparsec of NGC 1326 observed with SINFONI. A nuclear molecular disc inside the starburst ring
A&A, volume 638, A53, June 2020